ISSN: 2687 - 4539

CHAOS

THEORY AND APPLICATIONS

IN APPLIED SCIENCES AND ENGINEERING

Special Issue: Dissemination and Research in the Study of Complex Systems and Their Applications (EDIESCA 2023)

VOLUME 6, ISSUE 2, JUNE 2024 (SPECIAL ISSUE)

AN INTERDISCIPLINARY JOURNAL OF NONLINEAR SCIENCE

Chaos Theory and Applications (CHTA) ISSN: 2687-4539
Volume: 6 – Issue No: 2 (June 2024)
Special Issue: Dissemination and Research in the Study of Complex Systems and Their Applications (EDIESCA 2023)
https://dergipark.org.tr/en/pub/chaos/issue/85190

Editorial Board Members

ISSN: 2687-4539

Chaos Theory and Applications (CHTA)
Volume: 6 – Issue No: 2 (June 2024)
Special Issue: Dissemination and Research in the Study of Complex Systems and Their Applications (EDIESCA 2023)
https://dergipark.org.tr/en/pub/chaos/issue/85190

Contents:

CHAOS
Theory and Applications
in Applied Sciences and Engineering

e-ISSN: 2687-4539
RESEARCH ARTICLE
Vol.6 / No.2 / 2024 / pp.73-82
Special Issue (EDIESCA 2023)
https://doi.org/10.51537/chaos.1376123

Predicting Tipping Points in a Family of PWL Systems: Detecting Multistability via Linear Operators Properties

J.L. Echenausía-Monroy [§,1], **J.R. Cuesta-García** [§,2], **H.E. Gilardi-Velázquez** [α,3], **Sishu Shankar Muni** [β,γ,4] **and J. Álvarez** [§,5]

[§]Applied Physics Division, Center for Scientific Research and Higher Education at Ensenada, CICESE. Carr. Ensenada-Tijuana 3918, Zona Playitas, Ensenada, 22860, B. C., Mexico, [α]Facultad de Ingeniería, Universidad Panamericana. Josemaría Escrivá de Balaguer 101, Aguascalientes, Aguascalientes, 20296, Mexico, [β]School of Digital Sciences, Digital University Kerala, Technocity campus, Mangalapuram, Kerala, India, [γ]Indian Institute of Information Technology and Management Kerala, Technopark road, Kerala, India.

ABSTRACT The study of dynamical systems is based on the solution of differential equations that may exhibit various behaviors, such as fixed points, limit cycles, periodic, quasi-periodic attractors, chaotic behavior, and coexistence of attractors, to name a few. In this paper, we present a simple and novel method for predicting the occurrence of tipping points in a family of Piece-Wise Linear systems (PWL) that exhibit a transition from monostability to multistability with the variation of a single parameter, without the need to compute time series, i.e., without solving the differential equations of the system. The linearized system of the model is analyzed, the stable and unstable manifolds are taken to be real vectors in space, and the changes suffered by these vectors as a result of the modification of the parameter are examined using such simple metrics as the magnitude of a vector or the angle between two vectors in space. The results obtained with the linear analysis of the system agree well with those obtained with the numerical resolution of the dynamical system itself. The work presented here is an extension of previous results on this topic and contributes to the understanding of the mechanisms by which a system changes its stability by fragmenting its basin of attraction. This, in turn, enriches the field by providing an alternative to numerical resolution to identify quantitative changes in the dynamics of complex systems without having to solve the differential equation system.

KEYWORDS
Nonlinear dynamics
Chaotic system
Multistability
PWL system
Bifurcation
Tipping point

INTRODUCTION

In a world governed by complex systems that describe behaviors as mundane as our social interactions to the interconnected workings of our brains as the control center of the human body, the ability to anticipate the moment when a system reaches a point of no return is critical (Scheffer *et al.* 2001; Lenton *et al.* 2008; Jung and Ager 2023). This is a strategic advantage that can be applied to a wide range of disciplines. In this context, we should think of a complex system as an entity consisting of multiple parts whose individual behavior is known and which interact with each other. The behavior of the complex system, in turn, is not equal to the sum of the behaviors of the individual parts, resulting in structures that are generally characterized by nonlinearities (Ott 2002; Echenausía-Monroy *et al.* 2022; Keleş *et al.* 2023).

In the study and characterization of dynamical systems lies one of the central problems: exploring the asymptotic properties of the model when the parameter is continuously changed (Guan *et al.* 2005). A variety of behaviors that a dynamical system can exhibit include equilibrium points, limit cycles, periodic oscillations, chaotic behavior, quasi-periodic behavior, and even the coexistence of attractors can occur, to name a few examples (Ott 2002; Awal and Epstein 2021).

Even if a system exhibits only one type of behavior, the continuous change of system parameters or the influence of external disturbances can lead the system to the point of no return mentioned above. This point is called *tipping point*, where the dynamic behavior of the system changes abruptly and sometimes irreversibly (Biggs *et al.* 2009; Lane 2011). These two types of bifurcations can

Manuscript received: 15 October 2023,
Revised: 18 November 2023,
Accepted: 22 November 2023.

[1]echenausia@cicese.mx (**Corresponding author**)
[2]jcuesta@cicese.mx
[3]hgilardi@up.edu.mx
[4]sishushankarmuni@gmail.com
[5]jqalvar@cicese.mx

be distinguished from a bifurcation point because the tipping point refers to an abrupt and irreversible change in dynamic behavior. In contrast, the bifurcation point can describe changes in equilibrium points, for example, but does not necessarily imply a dynamic change. Examples of this type of abrupt modification in behavior include power outages in electricity grids or the occurrence of massive congestion in urban transportation systems. It is therefore crucial to have tools that allow us to predict the occurrence of these bifurcation points, for example, to make public health decisions regarding the spread of a disease that could lead to a pandemic, to predict a financial crisis, or to measure the tolerance of an ecosystem on the verge of collapse (Rial *et al.* 2004; Jiang *et al.* 2019; O'Regan *et al.* 2020; Lohmann *et al.* 2021; Wunderling *et al.* 2023).

Such a change in parameters in a complex system can lead to transitions between different behaviors, for example, a double limit cycle can bifurcate into the occurrence of chaotic states. These transitions may also involve the occurrence of coexisting states, which is referred to as multistability (Gilardi-Velázquez *et al.* 2018; Echenausía-Monroy *et al.* 2020; Fang *et al.* 2022; Safavi and Dayan 2022). This nearly universal phenomenon describes a range of behaviors from optical illusions to chemical reactions, the use of words, and even emotions. The coexistence of states in complex systems entails the existence of more than one basin of attraction. For a given parameter of the system, the dynamics may oscillate at near of a stable attractor (equilibrium points, periodic orbit, chaotic attractor) for certain initial conditions, but converge to another for a different set of, albeit very similar, initial conditions.

Since Lorenz's work (Lorenz 1963), many research has been done on how to characterize and find the existing behaviors in a dynamic system with complex behavior. One of the most commonly used forms for this is bifurcation diagrams, both for the existence of fixed points and for changes in their stability, but describing only local behaviors. In the case of systems with complex behavior, there are no tools that allow to describe the types of behavior through the analysis of vector fields, but only through the analysis of time series (Nazarimehr *et al.* 2018).

Currently, the search for new ways to predict tipping points in dynamical systems has attracted the attention of the scientific community, as it is seen as an advantage for decision making in critical situations (Moore 2018; Peng *et al.* 2019). In this search and the development of techniques capable of anticipating the occurrence of abrupt dynamic changes, tools based on the analysis of time series are used. This technique is based either on the storage of time series of the phenomenon under study or on the system of equations that describes it. Various statistical and mathematical techniques are used to detect patterns, trends, or changes in the behavior of the system that may indicate that the dynamic behavior is approaching a tipping point. In these cases, early warning signals may be observed, such as increased variance, autocorrelation, or a slowing of recovery rates in response to system perturbations, also known as resilience (Nazarimehr *et al.* 2018; Chen *et al.* 2020; Moghadam *et al.* 2022). Bifurcation theory has also been used to study how the qualitative behavior of a system changes as its parameters vary. By analyzing bifurcation points, it is possible to identify critical thresholds at which inflection points are likely to occur. Similarly, the use of Lyapunov exponents is a popular tool for identifying when a dynamical system is about to change its behavior (Tsakonas *et al.* 2022).

In some cases where the descriptor model leads to a numerical simulation with high computational costs, surrogate or reduced-order models can be used to approximate the behavior of the system and predict inflection points, just as network-based approaches have been used to detect changes in the network structure that might indicate an impending tipping point (Jiang *et al.* 2018).

Although there is a wealth of literature with different approaches to identifying and predicting tipping points in dynamical systems, in most cases there is one constant: time series analysis, which is effective but involves a high computational cost. We have recently published a paper that addresses the prediction of inflection points in a single-parameter Piece Wise Linear (PWL) system that generates multiple scrolls based on the study of the linear operator of the system. This approach shows a relation between vector field properties and the occurrence of coexisting states, with which is possible to predict the tipping points when the system undergoes a change in its global stability due to the variation of one parameter, which causes the system to go from monostability to multistability. The method described in (Echenausía-Monroy *et al.* 2022b) is based on the study of the stable and unstable manifolds of the system as real vectors in three-dimensional space which characterizes the changes in their magnitudes so that the points at which an abrupt change in the dynamics of the system can be identified. While the results are interesting, they are limited to a monoparametric family of attractors that are not able to predict the emergence of multistable dynamics in a system like the one published in (Gilardi-Velázquez *et al.* 2017), where the multi-scroll system has three distinct parameters.

In the present work, the results shown in (Echenausía-Monroy *et al.* 2022b) are generalized to a multiparametric family of oscillators, which are described by three dynamical parameters that change the size, order, and the Lyapunov exponent of the dynamics. In this paper, metrics of vector fields such as the magnitude of a vector and the angle between two vectors in space are used to characterize the variations of real vectors associated with the varieties of the multiple scroll system. The proposed method allows the prediction of tipping points through the eigenspace associated to the vector field, *i.e.*, without the need to solve the system of differential equations, which brings a significant reduction in computational costs. Since the numerical resolution of the system is eliminated, these results can be extended to systems with a larger number of variables without increasing the computational cost.

The remainder of the work consists of the following sections: Section 2 presents the necessary groundwork used in this paper and delineates the problem to be solved. Section 3 describes the methodology used, while the results are discussed in Section 4. The conclusions are explained at the end of the work.

PRELIMINARIES

Consider a third-order Piece-Wise Linear system defined as follows:

$$\dot{\boldsymbol{X}} = \boldsymbol{M}\boldsymbol{X} + g(\boldsymbol{X}), \tag{1}$$

where $\boldsymbol{M}$ is a non-singular linear operator, $\boldsymbol{X}$ is the state vector, $g : \mathbb{R}^n \to \mathbb{R}^n$ is a real commutation function based on a state variable and defined for a set of constant vectors as shown in Eq. (2), where $B_i = [b_1, \ldots, b_l] \in \mathbb{R}^n$ for $h = 1, 2, \ldots, l$ is a set of vectors with real entries. On the other hand, $\Omega_1, \ldots, \Omega_l$ denote a polytopic partition of the state space, also called switching domains, such that $\bigcup_{h=1}^{l} \Omega_h = \mathbb{R}^n$ and $\Omega_h \bigcap (\Omega_m)^0 = \emptyset$, where the notation $(\Omega_m)^0$ denotes the interior of Ω_m. Moreover, in each domain $\Omega_h \subset \mathbb{R}^n$, the system has equilibrium points located at $\boldsymbol{\chi}_h^* = -\boldsymbol{M}^{-1} g(\boldsymbol{X})$,

where $\boldsymbol{M}$ is the linear operator of the system, and it is easy to see that there are as many equilibria as domains Ω_h.

$$g(\boldsymbol{X}) = \begin{cases} B_1 & \text{if} \quad \boldsymbol{X} \in \Omega_1, \\ B_2 & \text{if} \quad \boldsymbol{X} \in \Omega_2, \\ \vdots & \vdots \\ B_l & \text{if} \quad \boldsymbol{X} \in \Omega_l. \end{cases} \tag{2}$$

The interest of this work is to characterize the behavior of PWL systems with the same number of scrolls as equilibrium points. To this end, the eigenvalues of *Eq. (1)* must be described by an Unstable Dissipative System type 1 (UDS I) (Campos-Cantón *et al.* 2010; Campos-Cantón 2015), characterized by having unstable saddle points for the following conditions:

- The linear operator $\boldsymbol{M}$ must have a negative real eigenvalue and a pair of complex conjugates with a real positive component.
- The eigenvalues $\boldsymbol{\lambda} \in \mathbb{C}^{1\times 3}$ of $\boldsymbol{M}$ must satisfy: $\sum_{i=1}^{3} \lambda_i < 0$.

Under these conditions, this article examines a jerk-inspired oscillator generated by:

$$\boldsymbol{M} = \begin{bmatrix} 0 & 1 & 0 \\ 0 & 0 & 1 \\ -\alpha_1 & -\alpha_2 & -\alpha_3 \end{bmatrix}, \; \boldsymbol{X} = \begin{bmatrix} x_1 \\ x_2 \\ x_3 \end{bmatrix}, \; g(\boldsymbol{X}) = \begin{bmatrix} 0 \\ 0 \\ \alpha_1 b(x_1) \end{bmatrix}, \tag{3}$$

$$b(x_1) = \begin{cases} -2 & \text{if} \quad \boldsymbol{X} \in \Omega_1 = \{\boldsymbol{X} \in \mathbb{R}^n : x_1 < -1\}, \\ 0 & \text{if} \quad \boldsymbol{X} \in \Omega_2 = \{\boldsymbol{X} \in \mathbb{R}^n : -1 \leq x_1 < 1\}, \\ 2 & \text{if} \quad \boldsymbol{X} \in \Omega_3 = \{\boldsymbol{X} \in \mathbb{R}^n : x_1 \geq 1\}, \end{cases} \tag{4}$$

where x_i are the state variables, α_i, $i = 1, 2, 3$ are the dynamical parameters corresponding to the family of oscillators that also modify the Lyapunov exponent, the order and the size of the attractor (Echenausía-Monroy *et al.* 2018), where $b(x_1)$ is a function that generates a commutation based on a state variable that induces multiple scrolls in the x_1-dimension.

Since this work focuses on the system responding to the configuration of eigenvalues defined as UDS I, which in turn are defined by the combination of the system parameters, mathematical analysis as described in (Anzo-Hernández *et al.* 2018) is used to determine the proper values:

Proposition 1 *(Anzo-Hernández* et al. *2018) Consider the family of affine linear systems given by Eq. (1,3), and the linear operator* $\boldsymbol{M}$ *with parameters* $\alpha_1, \alpha_2, \alpha_3 \in \mathbb{R}^+$. *If* $\alpha_1 > 0, 0 < \alpha_2 < \dfrac{\alpha_1}{\alpha_3}$, *and* $\alpha_3 > 0$, *then the system described by Eqs. (1,3) is based on an Unstable Dissipative System type 1 (UDS-I).*

Proof 1 *(Anzo-Hernández* et al. *2018) Suppose that* $\alpha_1, \alpha_2 > 0$. *Since* $\alpha_3 = Trace(\boldsymbol{M}) = \sum_{i=1}^{3} \lambda_i < 0$, *where* λ_i, $i = 1, 2, 3$, *is each of the eigenvalues of* $\boldsymbol{M}$, *the system Eq. (1,3) is dissipative. Moreover, with* $\alpha_1 = det(\boldsymbol{M})$, *the system Eq. (3) has saddle equilibrium points determined by the characteristic polynomial of the linear operator* $\boldsymbol{M}$, $\lambda^3 + \alpha_3\lambda^2 + \alpha_2\lambda + \alpha_1 = 0$, *which for* $\alpha_2 < \dfrac{\alpha_1}{\alpha_3}$ *by the Hurwitz polynomial criterion implies instability. Since* α_1, α_2 *and* α_3 *are positive real constants and the characteristic polynomial has no positive characteristic values by Descartes' sign rule, it has only one negative eigenvalue by which the equilibrium point is saddle fixed. Then the eigen spectrum is given by a negative real eigenvalue and a pair of complex conjugate eigenvalues with a positive real part.*

Considering Proposition 1, a multi-scroll jerk inspired system with parameters $\alpha_1 = 10.5$, $\alpha_2 = 7$; $\alpha_3 = 0.7$ for Eq. (3) and the commutation function described by Eq. (4) satisfies the UDS I conditions, generating the attractor shown in Figure 1. The red dots indicate the location of the equilibrium point, and the vertical lines indicate the location of the commutations delimiting each of the system domains, or polytopic partitions.

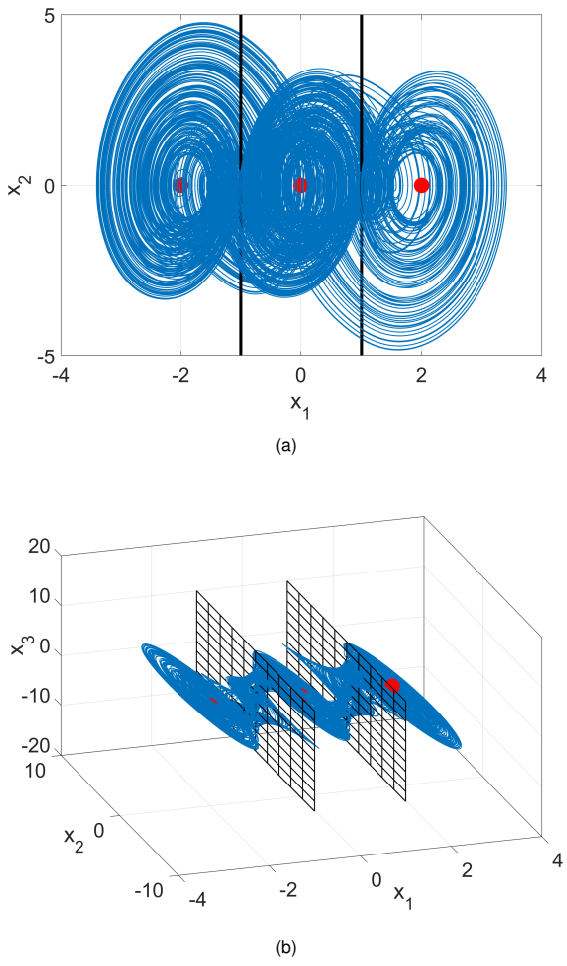

Figure 1 Attractor generated by Eq. (3) and Eq. (4) for $\alpha_1 = 10.5$, $\alpha_2 = 7$; $\alpha_3 = 0.7$ seen in the projection (a) $x_1 - x_2$ and (b) in phase space. The red dots denote the equilibrium points, while the black vertical lines (plane) represent the commutation surfaces.

Remark 1 *Note that the* α_i *values used in Figure 1 are the same as described in (Gilardi-Velázquez* et al. *2017), but with a restricted commutation function, since the authors use the "round to the nearest integer" function as commutation law in the work described, generating an infinite number of equilibrium points.*

In (Gilardi-Velázquez *et al.* 2017), the authors show that a multi-scroll system like the one described in Eq. (3) (for $\alpha_1 = 10.5$, $\alpha_2 = 7$, $\alpha_3 = 0.7$) is able to go from monostability to multistability by changing a bifurcation parameter that affects the third equation of the descriptor system. The resulting system of equations is shown in Eq. (5), where the parameter μ is a positive constant that scales with the dynamical parameters of the system, changing its stability and allowing the transition between monostability and the coexistence of stable single-wing attractors.

$$\begin{aligned} \dot{x_1} &= x_2, \\ \dot{x_2} &= x_3, \\ \dot{x_2} &= \mu[-\alpha_1 x_1 - \alpha_2 x_2 y - \alpha_3 x_3 + \alpha_1 b(x_1)]. \end{aligned} \tag{5}$$

Through numerical simulations, it is possible to identify the points at which the system changes its global stability by fragmenting its basin of attraction, from the generation of a 3-scroll attractor (as in Figure 1) to the generation of a single-wing attractor capable of living stably at each of the equilibrium points of the system. If we use a bifurcation diagram, by μ variation (see Figure 2(a)), and count the number of scrolls that the dynamics generates by changing the parameter μ, we obtain the graph shown in Figure 2(b), where the starting point of the multistable dynamics is $1.03 \leq \mu \leq 2.14$. For $\mu \geq 2.14$, all dynamics are eliminated from the system and converge to the equilibrium point.

Remark 2 *Although the results shown in Figure 2 are not identical to those previously published in (Gilardi-Velázquez* et al. *2017), they are not the main result of this work, but they are necessary to understand the contribution of the paper, which is why they are kept in the Preliminary remarks section.*

Problem Statement

In our previous study (Echenausía-Monroy *et al.* 2022b), we presented an innovative approach to predict tipping points in Piece Wise-Linear (PWL) systems by using linear algebra techniques to analyze the magnitude of manifolds within a monoparametric family of oscillators ($\alpha_1 = \alpha_2 = \alpha_3$). The focus of that research was primarily on identifying these tipping points for a particular class of oscillators. In this current work, we have extended, refined our methodology and generalized its applicability to multiparametric families of multi-scroll PWL oscillators. Our main goal remains the same: to predict the occurrence of tipping points in PWL systems transitioning from monostability to the occurrence of multistable behavior without the need to compute time series, i.e., without solving the differential equations of the system. To achieve this, we have developed an innovative approach that analyzes the angular relationships between real vectors associated with stable and unstable manifolds.

This study builds on our previous research, but it is important to emphasize that the problem, while conceptually related, applies to a broader range of dynamical systems. We improve and generalize the methodology so that it is applicable to different families of multiparametric oscillators. This advance is crucial to gain deeper insights into the transition from monostability to multistability in complex systems without relying on numerical resolution or bifurcation parameter change detection.

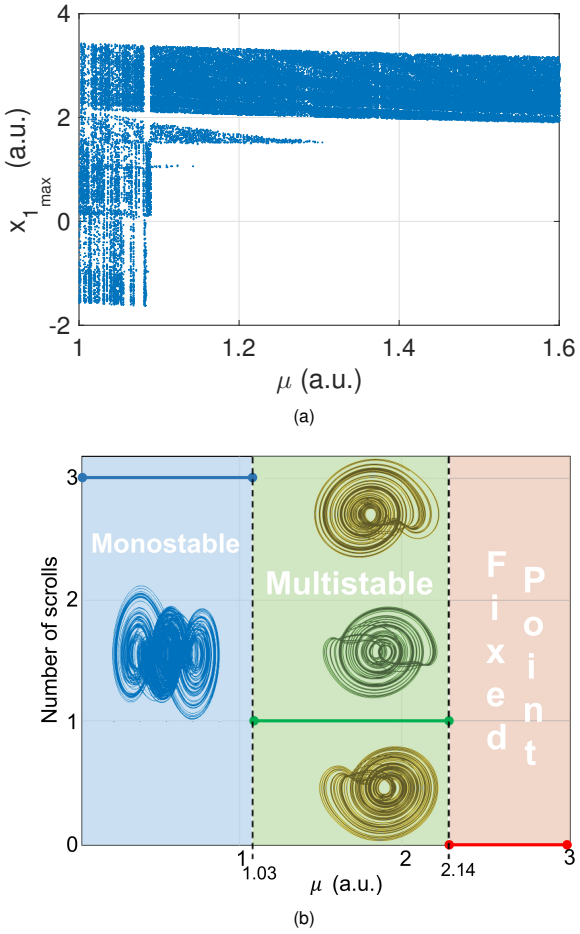

Figure 2 Numerical simulation of the system described by Eqs. (4,5) for $\alpha_1 = 10.5$, $\alpha_2 = 7$; $\alpha_3 = 0.7$ by μ variation. (a) Bifurcation diagram of the local maxima in x_1 by tracking the attractor (using the final state as the initial condition for parameter variation for the initial conditions $x_i = [-0.1\ 0.1\ 0.1]'$). (b) Summary of the behavior shown in the bifurcation diagram.

METHODOLOGY

Matrix algebra, or linear algebra as it is treated in college textbooks, focuses on the study and manipulation of algebraic structures called *vectors* and *matrices*. At its core, it deals with the properties and operations associated with these objects and is used to solve a variety of problems in fields ranging from physics and engineering to computer science and statistics. It has its origins in civilizations such as the Babylonians and Greeks, who were concerned with problems of systems of linear equations by matrix representation, and developed into a mathematical discipline with the contributions of notable mathematicians such as Leonhard Euler and Joseph-Louis Lagrange (Kleiner 2007).

As mentioned in the previous sections, the methodology used in this paper is based on the notion of the changes suffered by the stable and unstable manifolds of the multi-scroll system, which are conceived as real vectors in space. By conceptualizing them as vectors in space, we can quantify their changes by examining their magnitude and the angle that exists between these in the plane or in space.

The determination of the manifolds and their subsequent con-

struction as vectors is done using the linear operator of the descriptor system by computing the eigenvalues and eigenvectors of the model, graphing them in space, and determining their three-dimensional coordinates. As example, and considering Proposition 1, a multi-scroll jerk inspired system with parameters $\alpha_1 = 10.5$, $\alpha_2 = 7$, $\alpha_3 = 0.7$, $\mu = 1$ for Eq. (5) and the commutation function described by Eq. (4) satisfies the UDS I conditions, generating the attractor shown in Figure 1. For this combination of α_i values, the linear system to study is described by Eq. (6), being its eigenvalues described in (7):

$$\boldsymbol{M} = \begin{bmatrix} 0 & 1 & 0 \\ 0 & 0 & 1 \\ -\mu\alpha_1 & -\mu\alpha_2 & -\mu\alpha_3 \end{bmatrix}, \tag{6}$$

$$\begin{aligned} \Lambda &= \{\lambda_{1,2,3}\}, \\ &= \{-1.3372, 0.3186 \pm 2.784\,\mathrm{i}\}, \end{aligned} \tag{7}$$

and their corresponding eigenvectors are equal to:

$$\begin{aligned} \vartheta &= \{\vartheta_{1,2,3}\}, \\ &= \left\{ \begin{pmatrix} 0.4087 \\ -0.5466 \\ 0.7309 \end{pmatrix} \begin{pmatrix} -0.1160 \pm 0.0269\,\mathrm{i} \\ 0.0379 \pm 0.3316\,\mathrm{i} \\ 0.9351 \end{pmatrix} \right\}. \end{aligned} \tag{8}$$

The stable and unstable manifolds of the multiscroll system are defined such that $\vartheta = [\vartheta_i]$, for $i = 1, 2, 3$ is a set of column eigenvectors, where $\boldsymbol{M}\vartheta_i = \lambda_i\vartheta_i$, where λ_i are the system eigenvalues. Under this assumption, the stable manifold is defined by E_s^* =Span$\{\vartheta_1\}$ and the unstable manifold by E_u^* =Span$\{\vartheta_{2,3}\}$, and to represent these manifolds, we consider the real part of both as $E_s = \mathrm{Re}\{E_s^*\}$ and $E_u = \mathrm{Re}\{E_u^*\}$. With this in mind, it is possible to plot the attractor shown in Figure 1 along with the real vectors associated with the stable and unstable manifolds as shown in Figure 3.

Note that Figure 3 shows both manifolds (E_u, E_s) as real vectors in space that always intersect the equilibrium point and are bounded by the commutations induced by the nonlinear function. Under this premise, it is possible to analyze the behavior of these vectors by characterizing their variation and calculating their magnitude change induced by the parameter μ in the system. For this purpose, consider the points A, B, C, and D (see Fig. 3(b)), which have three-dimensional coordinates, intersections with the commutation surfaces, and intersections with the equilibrium point; the associated real vectors can be constructed as follows:

$$\begin{aligned} \vec{M}_s &= \vec{DB} = D - B, \\ \vec{M}_u &= \vec{AC} = A - C, \end{aligned} \tag{9}$$

where the vectors associated with both manifolds have coordinates in space and their magnitude is then defined as:

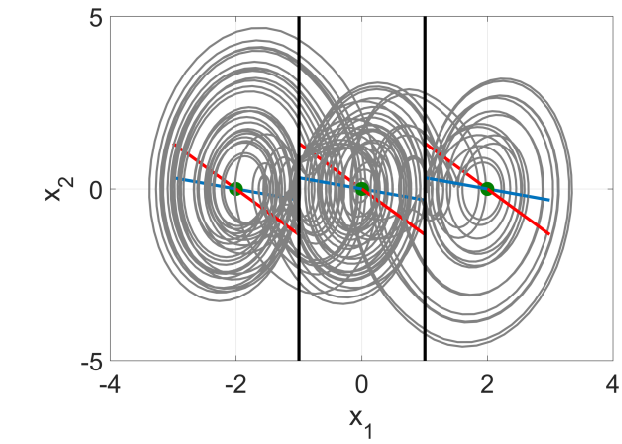

(a)

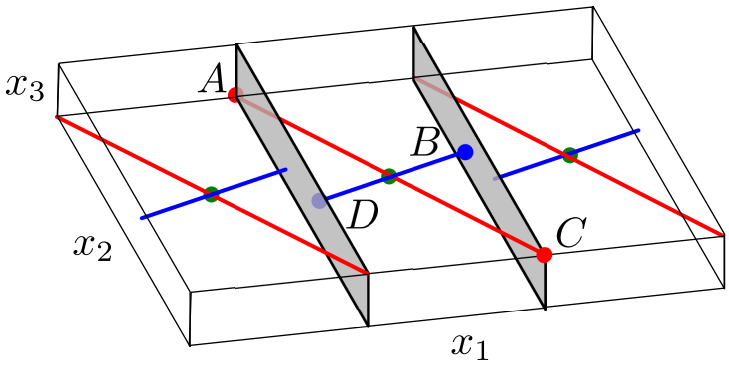

(b)

Figure 3 (a) Attractor generated by Eq. (3,5) for $\mu = 1$, $\alpha_1 = 10.5$, $\alpha_2 = 7$, $\alpha_3 = 0.7$, where the real vector associated with the stable manifold is shown in blue and the one associated with the unstable manifold is shown in red. (b) Real vectors associated with the system manifolds in phase space, omitting the trajectory shown in (a).

$$\begin{aligned} ||\vec{M}_s|| &= \sqrt{(x_{1s_1} - x_{1s_2})^2 + (x_{2s_1} - x_{2s_2})^2 + (x_{3s_1} - x_{3s_2})^2}\,, \\ ||\vec{M}_u|| &= \sqrt{(x_{1u_1} - x_{1u_2})^2 + (x_{2u_1} - x_{2u_2})^2 + (x_{3u_1} - x_{3u_2})^2}\,. \end{aligned} \tag{10}$$

In the same way as for the magnitude of the real vectors associated with the stable and unstable manifolds, it is possible to calculate the cross product between these vectors, defined as shown in Eq. (11), where θ is the angle between the vectors $\vec{M}_s$ and $\vec{M}_u$.

$$||\vec{M}_s \times \vec{M}_u|| = ||\vec{M}_s||\,||\vec{M}_u||\sin(\theta), \tag{11}$$

Remark 3 *Both metrics described previously, the magnitude of the vectors described in Eq. (10) and the cross product between the vectors shown in Eq. (11), are defined for a set of parameters α_i and μ. In this work, the variations of the two metrics are analyzed based on the effect induced by the bifurcation parameter μ, and these variations are illustrated in Figure 4.*

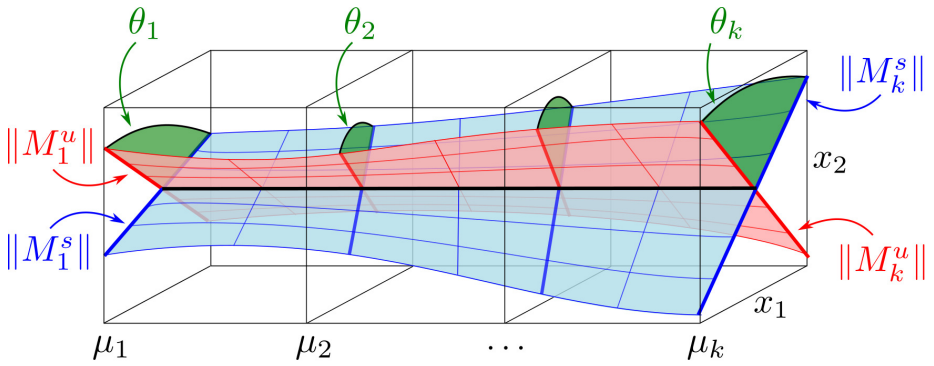

Figure 4 Illustration of the variations of the real vectors associated with the stable and unstable manifolds as the parameter μ changes, considering the vector magnitude ($||\vec{M}_{u,s}||$) and the angle between vectors (θ).

In addition, Appendix A presents an analytical method for characterizing the angles between real vectors in the system. This approach uses both the eigenvalues and the eigenvectors of the system under analysis.

RESULTS AND DISCUSSION

In the same spirit that (Echenausía-Monroy *et al.* 2022b), the eigenspace changes are analyzed along the variation of the parameter μ in the linear operator of the system described by Eq. (5). For each value of μ, the real vectors associated with the stable and unstable manifolds are computed, and in turn, the magnitude of these vectors is calculated. These changes are plotted (for both the stable and unstable manifolds), and points are searched for where these curves intersect. The intersections describe (from what has been reported) the regions where the system shows qualitative changes in its behavior, indicating the occurrence of multistable states, associated with the tipping points in the system. Figure 5 shows the curves obtained for the parametric variations of the magnitudes of the vectors $\vec{M}_s$ (solid lines) and $\vec{M}_u$ (dashed lines). Each of the magnitudes is calculated for the three-dimensional space and in each of the system projections, resulting in 4 curves for each of the vectors.

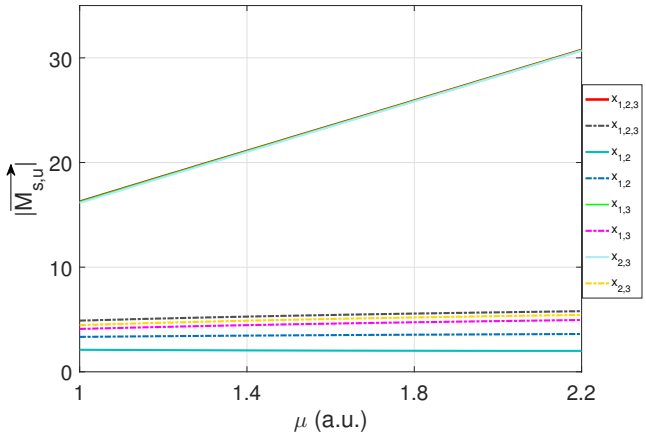

Figure 5 Behavior of the magnitudes of vectors $\vec{M}_s$ and $\vec{M}_u$ throughout the change of parameter μ. The values used are the same as in the attractor in Figure 1 ($\alpha_1 = 10.5$, $\alpha_2 = 7$, $\alpha_3 = 0.7$), and the subindex indicate the projection in which the magnitude is calculated (see Remark 4).

Remark 4 *In the results presented in this section, the notation $x_{\mathbb{I}}$, $\theta_{\mathbb{I}}$ is used, where the subindex $\mathbb{I}$ indicates whether the result was computed in the three-dimensional plane $\mathbb{I} = 1,2,3$ or in one of the state-space projections ($\mathbb{I} = 1,2$, $\mathbb{I} = 1,3$, $\mathbb{I} = 2,3$). Then for each metric used (vector magnitude and angle between vectors) there are 4 values.*

Analyzing the behavior of Figure 5, it becomes clear that there are no intersections in the curves describing the changes in the magnitudes of the real vectors associated with the manifolds of the system under study. The linear operator of the system described by Eq. (5) for the values $\alpha_1 = 10.5$, $\alpha_2 = 7$, $\alpha_3 = 0.7$ serves as a reference point. The absence of the appearance of intersections, as seen in Figure 10 of (Echenausía-Monroy *et al.* 2022b), is due to the fact that in this work we analyze the behavior of the whole family of oscillators described by different parameters α_i. The above mentioned article it was worked with a family of attractors described in the UDS I-value section ($\alpha_1 = \alpha_2 = \alpha_3$), which allows visualization of intersection points between the magnitudes of $\vec{M}_s$ and $\vec{M}_u$ as a function of μ.

In this sense, and maintaining the goal of being able to predict the occurrence of multistable states of the system in the context of a linear analysis without having to analyze the time series, the cross product between vectors is used. This vector operation results in a new vector that is perpendicular to the analyzed vectors. With the vectors $\vec{M}_s$ and $\vec{M}_u$, a perpendicular vector between them is obtained, which in turn gives the angle between the analyzed vectors (θ). This is the value used to characterize the variations of the linear operator, as described in Eq. (11). Figure 6 shows the results obtained by graphing the angle between the vectors of the variations obtained by the cross product. Appendix A presents an analytical method to describe the angles between real vectors within the system. This method relies on both the eigenvalues and eigenvectors of the system under study. It provides an alternative to the visual representation of changes in the system.

Analyzing the behavior of the curves of the angles between the vectors $\vec{M}_s$ and $\vec{M}_u$ in space and in each of the projections, we can identify three intersections. The first one for $\mu = 1.038$; it occurs when the angle between the vectors in both projections $x_{1,2} - x_{1,3}$ reaches the same value, where the plane $x_{1,2}$ is the one where the attractor projection reveals the multistable behavior.

The second intersection point appears for $\mu = 1.158$ when the angle between the vectors reaches the same value for both the projection $x_{1,2}$ and the plane $x_{2,3}$. The last interesting point appears for $\mu = 1.5$ when the angle between the vectors in the three-dimensional space reaches the same value as the angle between the vectors in the plane where the coexistence of the attractors is

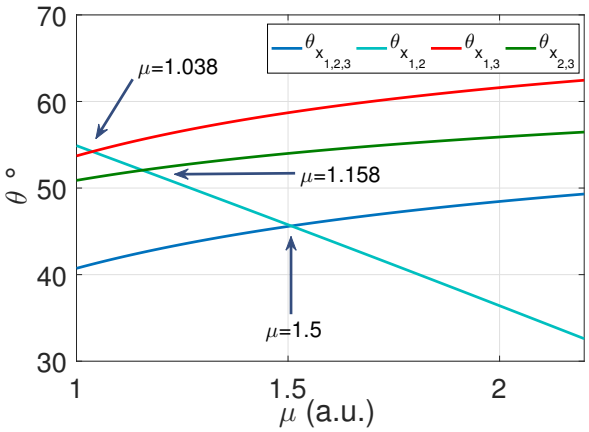

Figure 6 Behavior of the angle between the vectors $\vec{M}_s$ and $\vec{M}_u$ when varying the parameter μ, determined with the cross product. The values used are $\alpha_1 = 10.5,\ \alpha_2 = 7,\ \alpha_3 = 0.7$, which are the same as in the attractor in Figure 1.

appreciated ($x_{1,2}$).

Remark 5 *The first intersection point, where the angles between the varieties converge to the same value, is consistent with what was determined by the analysis of the time series (see Figure 2).*

Comparing the behavior of the angles between the vectors (Figure 6) with the bifurcation diagram shown in Figure 1, we can see that the first intersection between the curves corresponds to the value of μ at which the system breaks its global stability and the coexisting states arise. But it is impossible to ignore the fact that these angular curves have three intersection points. To investigate this behavior, Figure 7 shows the attractors obtained for the values of μ given in the angular curves, where the vectors reach interesting values. The time series used for these figures were calculated for 2^{18} points for an integration step $\tau = 0.01$ with RK4.

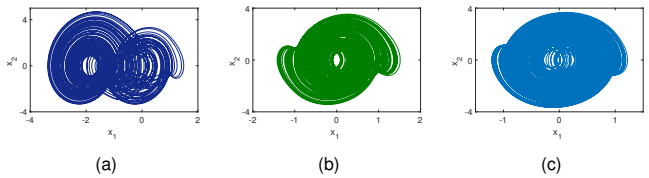

Figure 7 Multistable behavior of the system described by Eqs. (3,5) for the values used corresponds to that of the attractor in Figure 1 $\alpha_1 = 10.5,\ \alpha_2 = 7,\ \alpha_3 = 0.7$ and initial conditions $x_{1i} = -1,\ x_{2i,3i} = 0.1$. (a) $\mu = 1.038$, (b) $\mu = 1.158$, (c) $\mu = 1.5$.

After analyzing the dynamic behavior of the multi-scroll system described by Eqs. (3,5), we can say that the intersection points between the curves of the angles between the vectors correspond to three points where the dynamics of the system undergoes a change, or tipping points:

- $1 < \mu < 1.15$ The system exhibits the coexistence of attractors, but the dynamics is such that there is a basin of attraction with 6 possible attractors, as shown in the (Echenausía-Monroy *et al.* 2022a) obtained by using fractional derivatives. The global monostability has been slightly modified. There is the possibility of i) attractors of a single-wing living in each of the equilibrium points, ii) two symmetric double-scroll attractors, and iii) a small region in the initial conditions for which the system remains monostable.
- $1.15 < \mu < 1.5$ The basins of attraction of the multistable system have become larger, the monostable attractor is almost improbable, and the probability of the occurrence of a double-scroll attractor is small.
- $1.5 < \mu < 2.14$ The system exhibits only the coexistence of attractors of one wing, which live stably in each of the polytopic partitions of the system, which in turn have a single associated equilibrium point.
- $\mu > 2.14$ The system exhibits only the coexistence of stable equilibrium points, in accordance with Proposition 1.

CONCLUSION

The work developed and presented here addresses the problem of predicting the occurrence of inflection points, also called tipping points, in a multi-scroll system moving from monostability to coexistence of attractors. The implemented methodology is based on the study of the linear operator of the descriptor model. Without having to solve the system of equations and/or analyze time series, the points at which the dynamics change such that the coexistence of attractors occurs were predicted.

Using simple techniques of matrix algebra, such as the magnitude of a vector and the cross product between vectors, the linear operator of the system was analyzed. The results obtained are in agreement with those published in other papers on time series analysis. More importantly, considering Proposition 1, the developed method is applicable to the whole family of oscillators described by Eq. (5), and the linear operator depicted in (9). At the same time, it is worth noting that the result can be extrapolated to any number of scrolls in phase space as long as a nonlinear function with equidistant equilibrium points at the center of each of the polytopic partitions is used.

Although the analysis and metrics used are simple and easy to implement, it is worth noting that this allows us to better understand the transition between monostability and coexistence with attractors in dynamical systems. If we develop a tool to relate the angles between the stable and unstable manifolds to the dynamical transitions of the oscillator, then the points where the angles between said manifolds reach the same values in the projection $x_{1,2}$ with the projection $x_{2,3}$ are the points where the system breaks its stability. It is important to emphasize that the projection in which the multistability is estimated is in the plane $x_{1,2}$. It is worth noting that, contrary to what was reported in (Echenausía-Monroy *et al.* 2022b), the methodology proposed in this article is not able to predict the point at which the system changes the stability of its equilibrium points and transforms them into attractive foci points.

In addition, throughout Appendix A, the approach to analytically describe the angle between the real vectors in the system is described by using both the eigenvalues and the eigenvectors of the analyzed system. This is an alternative to the graphical method of visualizing the varieties of the system as real vectors, and enriches the contribution of the paper. It should be emphasized that with the results shown in this paper it is possible to predict the occurrence of multistable states in jerky systems given by Eq. (5) for any nonlinear function $b(x_1)$ such that there are as many scrolls as equilibrium points, regardless of whether the parameters of the system are the same ($\alpha_1 = \alpha_2 = \alpha_3$) or different ($\alpha_1 \neq \alpha_2 \neq \alpha_3$), as long as the system satisfies the conditions to be classified as UDS I.

Future work must be able to apply the obtained results to other systems to confirm the generality of the developed technique, or

otherwise implement new tools for predicting tipping points in dynamical systems without having to solve the systems of equations. Overall, this study advances our understanding of inflection points in dynamical systems and provides a solid foundation for future research in this field since the prediction of tipping points is critical in numerous contexts, from ecology to economics.

APPENDIX: ANGULAR EQUIVALENCE

Next we will develop an equivalent form to Eq. (11) to determine the angle between the manifolds.

Let $\vartheta_1 \in \mathbb{R}$ and $\vartheta_2 = \overline{\vartheta_3} \in \mathbb{C}$ are the eigenvectors of the matrix $\boldsymbol{M}$ given in (6). We define the vectors $\boldsymbol{v}_i = \mathrm{Re}\{\vartheta_i\}$ for $i = 1,2$ and form the set $V = \{\boldsymbol{v}_1, \boldsymbol{v}_2\}$. Let $\boldsymbol{\chi} = (\chi_1, \chi_2, \chi_3) \in \mathbb{R}^3$ be the equilibrium point of the system described by Eq. (1) for the region $\Omega_2 \subset \mathbb{R}^3$, and the parameter $\gamma_d^i \in \mathbb{R}$ defined as:

$$\gamma_d^i = \{\gamma \in \mathbb{R} : \chi_1 + \gamma v_{i1} = d\},$$

where $\boldsymbol{v}_i = (v_{i1}, v_{i2}, v_{i3}) \in V$. Then, the points A, B, C, and D illustrated in Figure 3 can be described as follows:

$$\begin{aligned} A &= \boldsymbol{\chi} + \gamma_{-1}^2 \boldsymbol{v}_2, \quad B = \boldsymbol{\chi} + \gamma_{+1}^1 \boldsymbol{v}_1, \\ C &= \boldsymbol{\chi} + \gamma_{+1}^2 \boldsymbol{v}_2, \quad D = \boldsymbol{\chi} + \gamma_{-1}^1 \boldsymbol{v}_1. \end{aligned} \tag{12}$$

Explicitly, the parameter can be obtained as follows:

$$\gamma_d^i = \frac{d - \chi_1}{v_{i1}},$$

and since the equilibrium point for the region Ω_2 is the origin, we have $\boldsymbol{\chi} = \mathbf{0} \in \mathbb{R}^3$. Thus, the parameters are:

$$\gamma_{-1}^i = \frac{-1}{v_{i1}}, \quad \gamma_{+1}^i = \frac{+1}{v_{i1}}, \tag{13}$$

where it can be observed that $\gamma_{+1}^i = -\gamma_{-1}^i, i = 1,2$.

If we use the same construction as in Eq. (9), but substitute the points from (12), we get the following:

$$\begin{aligned} &\boldsymbol{M}_s = \vec{DB} = D - B = (\boldsymbol{\chi} + \gamma_{-1}^1 \boldsymbol{v}_1) - (\boldsymbol{\chi} + \gamma_{+1}^1 \boldsymbol{v}_1) = \dots \\ &\gamma_{-1}^1 \boldsymbol{v}_1 - \gamma_{+1}^1 \boldsymbol{v}_1 = (\gamma_{-1}^1 - \gamma_{+1}^1)\boldsymbol{v}_1, \\ &\boldsymbol{M}_u = \vec{AC} = A - C = (\boldsymbol{\chi} + \gamma_{-1}^2 \boldsymbol{v}_2) - (\boldsymbol{\chi} + \gamma_{+1}^2 \boldsymbol{v}_2) = \dots \\ &\gamma_{-1}^2 \boldsymbol{v}_2 - \gamma_{+1}^2 \boldsymbol{v}_2 = (\gamma_{-1}^2 - \gamma_{+1}^2)\boldsymbol{v}_2. \end{aligned} \tag{14}$$

Substituting (13) into Eq. (14), we have that

$$\boldsymbol{M}_s = 2\gamma_{-1}^1 \boldsymbol{v}_1, \quad \boldsymbol{M}_u = 2\gamma_{-1}^2 \boldsymbol{v}_2. \tag{15}$$

Without loss of generality, let's assume that $\gamma_{-1}^1, \gamma_{-1}^2 > 0$, and therefore

$$\|\boldsymbol{M}_s\| = 2\gamma_{-1}^1 \|\boldsymbol{v}_1\|, \quad \|\boldsymbol{M}_u\| = 2\gamma_{-1}^2 \|\boldsymbol{v}_2\|. \tag{16}$$

To calculate the angle between the vectors $\boldsymbol{M}_s$ and $\boldsymbol{M}_u$, the dot product (denoted by $\cdot$) can be implemented as follows:

$$\boldsymbol{M}_s \cdot \boldsymbol{M}_u = \|\boldsymbol{M}_s\| \|\boldsymbol{M}_u\| \cos(\theta).$$

When substituting (15) and (16) into the above equation, you get:

$$(2\gamma_{-1}^1)(2\gamma_{-1}^2)(\boldsymbol{v}_1 \cdot \boldsymbol{v}_2) = (2\gamma_{-1}^1)(2\gamma_{-1}^2)\|\boldsymbol{v}_1\| \|\boldsymbol{v}_2\| \cos(\theta),$$

and therefore:

$$\cos(\theta) = \frac{1}{\langle \boldsymbol{v}_1 \rangle \langle \boldsymbol{v}_2 \rangle} \sum_{i \in \mathbb{I}} v_{1i} v_{2i},$$

where

$$\langle \boldsymbol{v}_j \rangle = \left(\sum_{i \in \mathbb{I}} v_{ji}^2 \right)^{1/2},$$

for $j = 1,2$ and with $\mathbb{I} \subseteq \{1,2,3\}$ a collection of indices. Note that $\langle \boldsymbol{v}_j \rangle \equiv \|\boldsymbol{v}_j\|$ when $\mathbb{I} = \{1,2,3\}$. Then the angle between vectors is defined by:

$$\cos(\theta_{\mathbb{I}}) = \frac{1}{\langle \boldsymbol{v}_1 \rangle \langle \boldsymbol{v}_2 \rangle} \left| \sum_{i \in \mathbb{I}} v_{1i} v_{2i} \right|.$$

Explicity, we will have:

$$\begin{aligned} \cos(\theta_{1,2}) &= \frac{|v_{11}v_{21} + v_{12}v_{22}|}{\sqrt{v_{11}^2 + v_{12}^2}\sqrt{v_{21}^2 + v_{22}^2}}, \\ \cos(\theta_{1,3}) &= \frac{|v_{11}v_{21} + v_{13}v_{23}|}{\sqrt{v_{11}^2 + v_{13}^2}\sqrt{v_{21}^2 + v_{23}^2}}, \\ \cos(\theta_{2,3}) &= \frac{|v_{12}v_{22} + v_{13}v_{23}|}{\sqrt{v_{12}^2 + v_{13}^2}\sqrt{v_{22}^2 + v_{23}^2}}, \\ \cos(\theta_{1,2,3}) &= \frac{|v_{11}v_{21} + v_{12}v_{22} + v_{13}v_{23}|}{\sqrt{v_{11}^2 + v_{12}^2 + v_{13}^2}\sqrt{v_{21}^2 + v_{22}^2 + v_{23}^2}}. \end{aligned} \tag{17}$$

Now suppose that the matrix M given in (6) has the eigenvalues $\lambda_1 = p \in \mathbb{R}$, and $\lambda_{2,3} = a \pm ib$ with $a, b \in \mathbb{R}$. Then the eigenvectors of the matrix M can be written as:

$$\begin{pmatrix} \vartheta_1, \vartheta_2, \vartheta_3 \end{pmatrix} = \begin{pmatrix} 1 & 1 & 1 \\ p & a - \mathrm{i}b & a + \mathrm{i}b \\ p^2 & -b^2 - 2\mathrm{i}ab + a^2 & -b^2 + 2\mathrm{i}ab + a^2 \end{pmatrix},$$

while their real part is as follows:

$$\begin{pmatrix} \boldsymbol{v}_1 & \boldsymbol{v}_2 \end{pmatrix} = \begin{pmatrix} 1 & 1 \\ p & a \\ p^2 & a^2 - b^2 \end{pmatrix}.$$

Substituting the aboved described into Eq. (17), we get:

$$\begin{aligned} \cos(\theta_{1,2}) &= \frac{|1 + pa|}{\sqrt{1 + p^2}\sqrt{1 + a^2}}, \\ \cos(\theta_{1,3}) &= \frac{|1 + p^2(a^2 - b^2)|}{\sqrt{1 + p^4}\sqrt{1 + (a^2 - b^2)^2}}, \\ \cos(\theta_{2,3}) &= \frac{|pa + p^2(a^2 - b^2)|}{\sqrt{p^2 + p^4}\sqrt{a^2 + (a^2 - b^2)^2}}, \\ \cos(\theta_{1,2,3}) &= \frac{|1 + pa + p^2(a^2 - b^2)|}{\sqrt{1 + p^2 + p^4}\sqrt{1 + a^2 + (a^2 - b^2)^2}}. \end{aligned} \tag{18}$$

Regardless of which way is chosen, via eigenvectors as described in Eqs. (17) or using the eigenvalues as in Eqs. (18), analysis of these expressions when the parameter μ is varied yields the same plot as in Figure 6.

Acknowledgments

J.L.E.M. thanks CONAHCYT for financial support (CVU-706850), and to J.A.G. for the opportunity to do a postdoctoral fellowship at CICESE.

Availability of data and material

The data used to support the findings of the study are included within the article.

Conflicts of interest

The authors declare that there is no conflict of interest regarding the publication of this paper.

Ethical standard

The authors have no relevant financial or non-financial interests to disclose.

LITERATURE CITED

Anzo-Hernández, A., H. Gilardi-Velázquez, and E. Campos-Cantón, 2018 On multistability behavior of unstable dissipative systems. Chaos: An Interdisciplinary Journal of Nonlinear Science **28**: 033613.

Awal, N. M. and I. R. Epstein, 2021 Period-doubling route to mixed-mode chaos. Physical Review E **104**: 024211.

Biggs, R., S. R. Carpenter, and W. A. Brock, 2009 Turning back from the brink: detecting an impending regime shift in time to avert it. Proceedings of the National academy of Sciences **106**: 826–831.

Campos-Cantón, E., 2015 Switched systems based on unstable dissipative systems. IFAC-PapersOnLine **48**: 116–121.

Campos-Cantón, E., J. G. Barajas-Ramirez, G. Solis-Perales, and R. Femat, 2010 Multiscroll attractors by switching systems. Chaos: An Interdisciplinary Journal of Nonlinear Science **20**.

Chen, L., F. Nazarimehr, S. Jafari, E. Tlelo-Cuautle, and I. Hussain, 2020 Investigation of early warning indexes in a three-dimensional chaotic system with zero eigenvalues. Entropy **22**: 341.

Echenausía-Monroy, J., J. Cuesta-García, and J. Ramirez-Pena, 2022 The wonder world of complex systems. Chaos Theory and Applications **4**: 267–273.

Echenausía-Monroy, J., H. Gilardi-Velázquez, N. Wang, R. Jaimes-Reátegui, J. García-López, *et al.*, 2022a Multistability route in a pwl multi-scroll system through fractional-order derivatives. Chaos, Solitons & Fractals **161**: 112355.

Echenausía-Monroy, J., S. Jafari, G. Huerta-Cuellar, and H. Gilardi-Velázquez, 2022b Predicting the emergence of multistability in a monoparametric pwl system. International Journal of Bifurcation and Chaos **32**: 2250206.

Echenausía-Monroy, J. L., J. García-López, R. Jaimes-Reátegui, D. López-Mancilla, and G. Huerta-Cuellar, 2018 Family of bistable attractors contained in an unstable dissipative switching system associated to a snlf. Complexity **2018**.

Echenausía-Monroy, J. L., G. Huerta-Cuellar, R. Jaimes-Reátegui, J. H. García-López, V. Aboites, *et al.*, 2020 Multistability emergence through fractional-order-derivatives in a pwl multi-scroll system. Electronics **9**: 880.

Fang, S., S. Zhou, D. Yurchenko, T. Yang, and W.-H. Liao, 2022 Multistability phenomenon in signal processing, energy harvesting, composite structures, and metamaterials: A review. Mechanical Systems and Signal Processing **166**: 108419.

Gilardi-Velázquez, H. E., R. d. J. Escalante-González, and E. Campos-Cantón, 2018 Bistable behavior via switching dissipative systems with unstable dynamics and its electronic design. IFAC-PapersOnLine **51**: 502–507.

Gilardi-Velázquez, H. E., L. Ontañón-García, D. G. Hurtado-Rodriguez, and E. Campos-Cantón, 2017 Multistability in piecewise linear systems versus eigenspectra variation and round function. International Journal of Bifurcation and Chaos **27**: 1730031.

Guan, S., C.-H. Lai, and G. Wei, 2005 Bistable chaos without symmetry in generalized synchronization. Physical Review E **71**: 036209.

Jiang, J., A. Hastings, and Y.-C. Lai, 2019 Harnessing tipping points in complex ecological networks. Journal of the Royal Society Interface **16**: 20190345.

Jiang, J., Z.-G. Huang, T. P. Seager, W. Lin, C. Grebogi, *et al.*, 2018 Predicting tipping points in mutualistic networks through dimension reduction. Proceedings of the National Academy of Sciences **115**: E639–E647.

Jung, H. and J. W. Ager, 2023 A tipping point for solar production of hydrogen? Joule **7**: 459–461.

Keleş, Z., G. Sonugür, and M. Alçin, 2023 The modeling of the rucklidge chaotic system with artificial neural networks. Chaos Theory and Applications **5**: 59–64.

Kleiner, I., 2007 *A history of abstract algebra*. Springer Science & Business Media.

Lane, S. N., 2011 The tipping point: How little things can make a big difference. Geography **96**: 34–38.

Lenton, T. M., H. Held, E. Kriegler, J. W. Hall, W. Lucht, *et al.*, 2008 Tipping elements in the earth's climate system. Proceedings of the national Academy of Sciences **105**: 1786–1793.

Lohmann, J., D. Castellana, P. D. Ditlevsen, and H. A. Dijkstra, 2021 Abrupt climate change as a rate-dependent cascading tipping point. Earth System Dynamics **12**: 819–835.

Lorenz, E. N., 1963 Deterministic nonperiodic flow. Journal of atmospheric sciences **20**: 130–141.

Moghadam, N. N., R. Ramamoorthy, F. Nazarimehr, K. Rajagopal, and S. Jafari, 2022 Tipping points of a complex network biomass model: Local and global parameter variations. Physica A: Statistical Mechanics and its Applications **592**: 126845.

Moore, J. C., 2018 Predicting tipping points in complex environmental systems. Proceedings of the National Academy of Sciences **115**: 635–636.

Nazarimehr, F., S. Jafari, S. M. R. Hashemi Golpayegani, M. Perc, and J. C. Sprott, 2018 Predicting tipping points of dynamical systems during a period-doubling route to chaos. Chaos: An Interdisciplinary Journal of Nonlinear Science **28**.

Ott, E., 2002 *Chaos in dynamical systems*. Cambridge university press.

O'Regan, S. M., E. B. O'Dea, P. Rohani, and J. M. Drake, 2020 Transient indicators of tipping points in infectious diseases. Journal of the Royal Society Interface **17**: 20200094.

Peng, X., M. Small, Y. Zhao, and J. M. Moore, 2019 Detecting and predicting tipping points. International Journal of Bifurcation and Chaos **29**: 1930022.

Rial, J. A., R. A. Pielke, M. Beniston, M. Claussen, J. Canadell, *et al.*, 2004 Nonlinearities, feedbacks and critical thresholds within the earth's climate system. Climatic change **65**: 11–38.

Safavi, S. and P. Dayan, 2022 Multistability, perceptual value, and internal foraging. Neuron .

Scheffer, M., S. Carpenter, J. A. Foley, C. Folke, and B. Walker, 2001 Catastrophic shifts in ecosystems. Nature **413**: 591–596.

Tsakonas, S., M. Hanias, and L. Magafas, 2022 Application of the moving lyapunov exponent to the s&p 500 index to predict major

declines. Journal of Risk .
Wunderling, N., A. von der Heydt, Y. Aksenov, S. Barker, R. Bastiaansen, *et al.*, 2023 Climate tipping point interactions and cascades: A review. EGUsphere **2023**: 1–45.

How to cite this article: Echenausía-Monroy, J. L., Cuesta-García, J.R., Gilardi-Velázquez, H.E., Muni, S.S., and Alvarez-Gallegos, J. Predicting Tipping Points in a Family of PWL Systems: Detecting Multistability via Linear Operators Properties *Chaos Theory and Applications*, 6(2), 73-82, 2024.

CHAOS
Theory and Applications
in Applied Sciences and Engineering

e-ISSN: 2687-4539
RESEARCH ARTICLE
Vol.6 / No.2 / 2024 / pp.83-89
Special Issue (EDIESCA 2023)
https://doi.org/10.51537/chaos.1376471

Analysis of the Dynamics of a ϕ^6 Duffing Type Jerk System

A. Bucio-Gutiérrez [α,1], **E. S. Tututi-Hernández** [α,2] **and U. Uriostegui-Legorreta** [α,3]
[α]Facultad de Ciencias Físico Matemáticas, UMSNH, Av. Francisco J. Múgica S/N, 58030, Morelia, Michoacán, México.

ABSTRACT

A theoretically and numerically analysis on Duffing Jerk systems with a sixth-order type potential and a sixth-order potential smoothed by a Gaussian function are carried out in this work. This kind of systems can modelate the response in circuits which may be used in cryptography. The Jerk system is transformed into a dynamical system of dimension three. Choosing the set of values for the parameters to guaranty that Jerk systems are Duffing type with triple well potential. The dynamics and stability of the resulting system are analyzed, through phase space, bifurcation diagrams and Lyapunov exponents by varying the relevant parameters, finding the existence of a strange attractor. The dynamics of system with potential smoothed was studied by varying the smoothing parameter α, finding that this parameter can be used to controlling chaos, since the exponential factor keeps the same fixed points and it regulates smoothly the amplitude of the potential.

KEYWORDS

Jerk system
Duffing system
Bifurcation diagrams
Lyapunov exponent

INTRODUCTION

In recent years, Jerk systems have been the subject of great interest in the specialized community (Louodop *et al.* 2017; Kengne *et al.* 2020). In fact, the wide range of applications in fields such as control engineering (Raineri and Bianco 2019), biomechanics (Sharker *et al.* 2019) and robotics (Chen and Zhang 2016) in which it is necessary a third order derivative for the description of the system. This type of systems are, in general, described by the following equation

$$\dddot{x} = J\left(\ddot{x}, \dot{x}, x\right), \tag{1}$$

where the J stands for "Jerk" (Louodop *et al.* 2017), which represents a measure of the "abruptness" or "smoothness" of movement (from a classical perspective).

Jerk systems can describe phenomena and behaviors more complex than traditional second-order systems, which makes them useful in modeling and controlling systems that experience rapid changes or nonlinearities. Among the Jerk systems the most notable are those that present chaotic behavior. In an autonomous Jerk system, this chaotic behavior is achieved by considering a certain degree of nonlinearity in J and because an increase in this nonlinearity does not necessarily lead to a greater degree of chaos in the system (Patidar and Sud 2005). However, it is possible to work with systems with subjectively simple nonlinearities.

In physical models, Jerk-type arrangements can be used to model, for example, the Nosé-Hoover dynamic system in thermostated dynamic which exhibits time-reversible Hamiltonian chaos (Posch *et al.* 1986). Furthermore, Jerk systems are often implemented in variants of circuits, as they are easy to analyze numerically and experimentally, and can be easily scaled to a wide range of frequencies (Sprott 2011), with hump structure (Folifack Signing *et al.* 2021) and a memristive model with quadratic memductance which is used to build the nonlinear term of a Jerk system (Njitacke *et al.* 2022). Those Jerk systems are used to image encryption.

Due to its applicability in modeling synchronization, one of the most recurring system in the literature on chaos is the non-linear Duffing oscillator (Uriostegui-Legorreta and Tututi-Hernández 2022; Uriostegui and Tututi 2023). Although the Duffing oscillator is a dynamical system of low dimensionality, it can present chaos if it is under an external forcing. Moreover, chaotification (Zhang *et al.* 2009) allows converting the dynamics of autonomous systems to a non-periodic one that presents chaotic motion. Different control methods and chaotification techniques of discrete-time and

Manuscript received: 16 October 2023,
Revised: 25 November 2023,
Accepted: 1 December 2023.

[1]1207258b@umich.mx (**Corresponding author**)
[2]eduardo.tututi@umich.mx
[3]ulises.uriostegui@umich.mx

continuous-time dynamic systems exist in the literature, such as feedback control with temporal delay (Zhou *et al.* 2010) or the cosine chaotification technique (Natiq *et al.* 2019). Furthermore, the chaotic dynamics of the non-linear system can be modulated to obtain a stable state or different types of dynamics (Haluszczynski and Räth 2021)

However, in the first instance it is necessary to identify under what parameters or conditions the system presents a chaotic behavior. For this purpose, it is necessary to find regions of the parameters space that present non-periodical behavior. Thus, methods such as bifurcation diagrams and Lyapunov's spectrum, constituted by Lyapunov's characteristic exponents (LCE), result useful. In last case, a positive LCE is indicative of the presence of a chaotic attractor in the system (Sandri 1996).

In this work, we study both a Duffing Jerk system with sixth-order potential and a Duffing Jerk system with sixth-order potential smoothed by a Gaussian function. The proposed systems are analyzed numerically, showing a change in dynamics by changing the smoothed factor that ranges from presenting chaos to presenting a limit cycle. In addition, we classify the dynamics of the system for different parameters finding that an increase in the smoothed factor leads to restricting the dynamics to two types.

THEORETICAL FRAMEWORK

System

The dynamics of the Jerk system with a potential type ϕ^6 is given by

$$\dddot{x} = -c_1\ddot{x} - c_5c_2\dot{x} + c_5\frac{d}{dx}U(x), \tag{2}$$

being

$$U(x) = \frac{x^2}{2} + \frac{c_3x^4}{4} + \frac{c_4x^6}{6}, \tag{3}$$

the energy potential. Whenever $c_4 > 0$ and $c_3 < 0$, U is triple well potential (Hong *et al.* 2015; Uriostegui-Legorreta and Tututi 2023a,b). Notice that Eq.(2) can be written as an autonomous dynamical system, as follows

$$\begin{aligned}\dot{x} &= y,\\ \dot{y} &= c_5z,\\ \dot{z} &= -c_1z - c_2y + \frac{d}{dx}U(x),\end{aligned} \tag{4}$$

where the c_1, c_2, c_3, c_4 and c_5 parameters are real numbers. Since the system in Eq.(4) is nonlinear and three-dimensional, it could give rise to chaos. In the following it will be established the conditions for chaos.

It is well known that there exists an attractor if the ratio of the contraction of the volume (V) of initial conditions in phase space over time is less than zero(Hilborn *et al.* 2000), that is

$$\frac{1}{V}\frac{dV}{dt} = \frac{\partial\dot{x}}{\partial x} + \frac{\partial\dot{y}}{\partial y} + \frac{\partial\dot{x}}{\partial z} = -c_1 < 0, \tag{5}$$

which is satisfied for $c_1 > 0$. It is known that when $\frac{1}{V}\frac{dV}{dt} < 0$, the volume contracts exponentially thus the system results dissipative and there may be a stable attractor. On the other hand, when $\frac{1}{V}\frac{dV}{dt} > 0$ the volume in phase space expands and there are only unstable fixed points, limit cycles or chaotic repellers; that is, the dynamics diverge if the initial condition is not exactly one of the fixed points. These points (x_0, y_0, z_0) are given by

$$\begin{aligned}\frac{d}{dx}U(x)\,|_{x_0} &= 0,\\ y_0 &= 0,\\ z_0 &= 0.\end{aligned} \tag{6}$$

Hence, the fixed points depend on the parameters of $U(x)$.

To analyze the dynamics, it is necessary obtain the eigenvalues of the Jacobian matrix J of the system, given by

$$J = \begin{pmatrix} 0 & 1 & 0\\ 0 & 0 & c_5\\ \mu(x) & -c_2 & -c_1\end{pmatrix}, \tag{7}$$

with

$$\mu(x) = 1 + 3c_3x^2 + 5c_4x^4. \tag{8}$$

Notice that Eq. (8) is the second derivative with respect to x of the Eq. (3). In this manner, the characteristic polynomial evaluated at each of the fixed points is

$$P(\lambda) = -\lambda^3 - c_1\lambda^2 - c_2c_5\lambda - c_5\mu(x_0), \tag{9}$$

from which, we obtain the type of stability of the fixed points. Notice that Eq. (9) gives three solutions λ_1, λ_2, and λ_3, for which, the dynamics of the system depends on these values. The classification of the stability of system is shown in Table 1 (Francomano *et al.* 2017; Stumpf *et al.* 2011) .

Potential Function $U(x)$

Notice that $\frac{d}{dx}U(x)$ can be written as

$$\frac{d}{dx}U(x) = (x-0)(x-p^+)(x+p^+)(x-p^-)(x+p^-), \tag{10}$$

being

$$p^{\pm}(c_3, c_4) = \pm\sqrt{\frac{1}{2c_4}\left(-c_3 \pm \sqrt{c_3^2 - 4c_4}\right)}, \tag{11}$$

consequently, the fixed points of the system in Eq. (4) are

$$\begin{aligned}x_0 &= 0, p^+, -p^+, p^-, -p^-,\\ y_0 &= 0,\\ z_0 &= 0.\end{aligned} \tag{12}$$

The $p^{\pm}(c_3, c_4)$ in Eq. (11) are, in general, complex functions, so different scenarios can occur: i) all roots are real, ii) one root is real and 4 complex roots (2 complex and its conjugated), iii) 3 real roots and 2 complex roots (1 complex root an its conjugated). It is assume that all the roots are different, otherwise a degenerate case is obtained which is avoided for the interest of the problem.

Then, the conditions for Eq. (11) to be purely real are

$$c_4 \leq \left(\frac{c_3}{2}\right)^2 \tag{13}$$

and

$$\frac{1}{2c_4}\left(-c_3 \pm \sqrt{c_3^2 - 4c_4}\right) \geq 0. \tag{14}$$

In the case of the triple well potential, only the condition in Eq. (13) is necessary. The first condition is bounded by the upper parabola

Table 1 Classification of equilibrium points for 3D system with two complex eigenvalues and one real λ_1.

Equilibrium type	Relation
Asymptotically Stable Focus-Node	$\mathrm{Re}(\lambda_1) < \mathrm{Re}(\lambda_2) = \mathrm{Re}(\lambda_3) < 0$ $\mathrm{Im}(\lambda_2) = -\mathrm{Im}(\lambda_3)$
Unstable Focus-Node	$0 < \mathrm{Re}(\lambda_1) < \mathrm{Re}(\lambda_2) = \mathrm{Re}(\lambda_3)$ $\mathrm{Im}(\lambda_2) = -\mathrm{Im}(\lambda_3)$
Repelling Focus-Saddle	$\mathrm{Re}(\lambda_1) < 0 < \mathrm{Re}(\lambda_2) = \mathrm{Re}(\lambda_3)$ $\mathrm{Im}(\lambda_2) = -\mathrm{Im}(\lambda_3)$
Attracting Focus-Saddle	$\mathrm{Re}(\lambda_3) = \mathrm{Re}(\lambda_2) < 0 < \mathrm{Re}(\lambda_1)$ $\mathrm{Im}(\lambda_3) = -\mathrm{Im}(\lambda_2)$

defined by $c_4 = (c_3/2)^2 : c_3 \in \{-\infty, \infty\} \,/\, \{0\}$. However, it must satisfy at the same time with the second condition, so two cases occur. The first one being with the positive root

$$p^+ \begin{cases} c_4 \leq \left(\frac{c_3}{2}\right)^2, \\ \frac{c_3}{c_4} \leq \frac{\sqrt{c_3^2 - 4c_4}}{c_4}. \end{cases} \tag{15}$$

The region where it is purely real is found graphically by looking at the regions where the imaginary part of p^+ is zero as shown in Figure 1 (a). In the same way, in the second case with the negative root should occur that the imaginary part of p^- must be zero as shown the Figure 1 (b) in te regions delimited by

$$p^- \begin{cases} c_4 \leq \left(\frac{c_3}{2}\right)^2, \\ \frac{c_3}{c_4} \geq -\frac{\sqrt{c_3^2 - 4c_4}}{c_4}. \end{cases} \tag{16}$$

Figures 1 (a) and (b) show the region where $p^{\pm}$ are pure real. That is for $c_3 < 0, c_4 > 0$ and $c_4 < (c_3/2)^2$. In the subsequent discussion it is restricted to the case of the triple well potential.

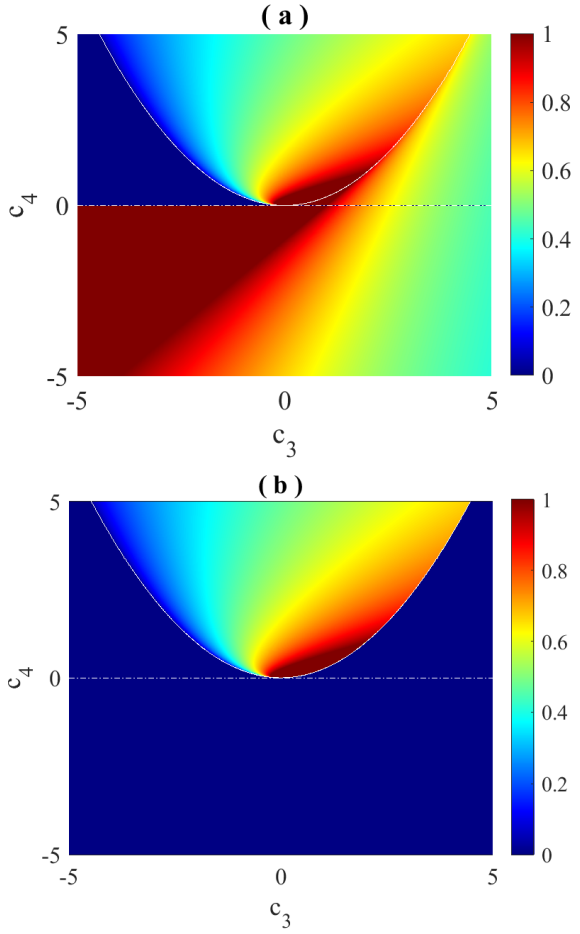

Figure 1 Values of imaginary part of p^+ in (a) and p^- in (b), both normalized to its maximum value.

NUMERICAL ANALYSIS

Bifurcation Diagrams

In order to obtain a dissipative system, it is necessary to take $c_5 > 0$ and $c_2 > 0$ (Louodop *et al.* 2014). To obtain the bifurcation diagrams as function of the c_1, c_2 and c_5 and identify the chaotic regions of the system, we take the values $c_3 = -0.6$ and $c_4 = 0.06$ and take two different initial conditions $\mathbf{x}_1 = (2.7083, 0, 0)$ and $\mathbf{x}_2 = (-2.7083, 0, 0)$, being $\mathbf{x}_i = (x_i, y_i, z_i)$ with $i = 1, 2$, both taken at the same initial time $t = 0$. In Figure 2 it is shown the bifurcation diagrams for the two initial conditions. These bifurcation diagrams were obtained by considering the local maxima of $x(t)$, $y(t)$ and $z(t)$ as a function of the c_1, c_2 and c_5 parameters, respectively, in a interval of time between $[250, 310]$, using a step time of 0.01 in the fourth-order Runge–Kutta method.

Phase Space

As it can be observed from Figure 2 there are regions where the system exhibits chaos. A particular set of values of the parameters

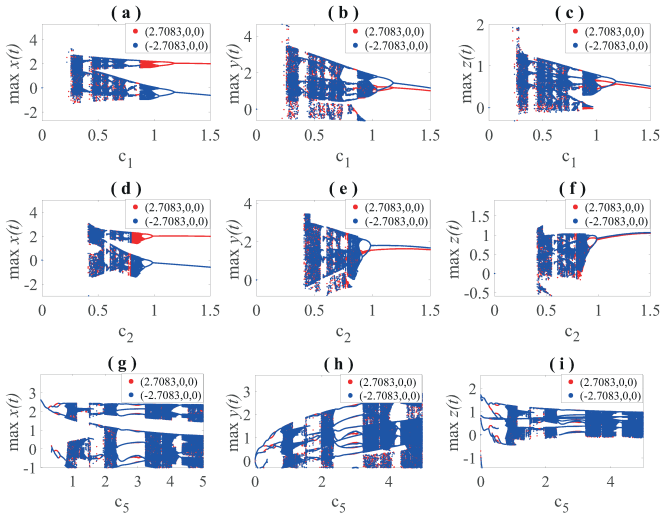

Figure 2 Bifurcation diagrams for the initial conditions $\mathbf{x}_1 = (2.7083, 0, 0)$ in red and $\mathbf{x}_2 = (-2.7083, 0, 0)$ in blue, as function the parameters. The first column (Figures (a), (d) and (g)) is for the x variable. The second column (Figures (b), (e) and (i)) is for the y variable, and finally the third column is for the z variable.

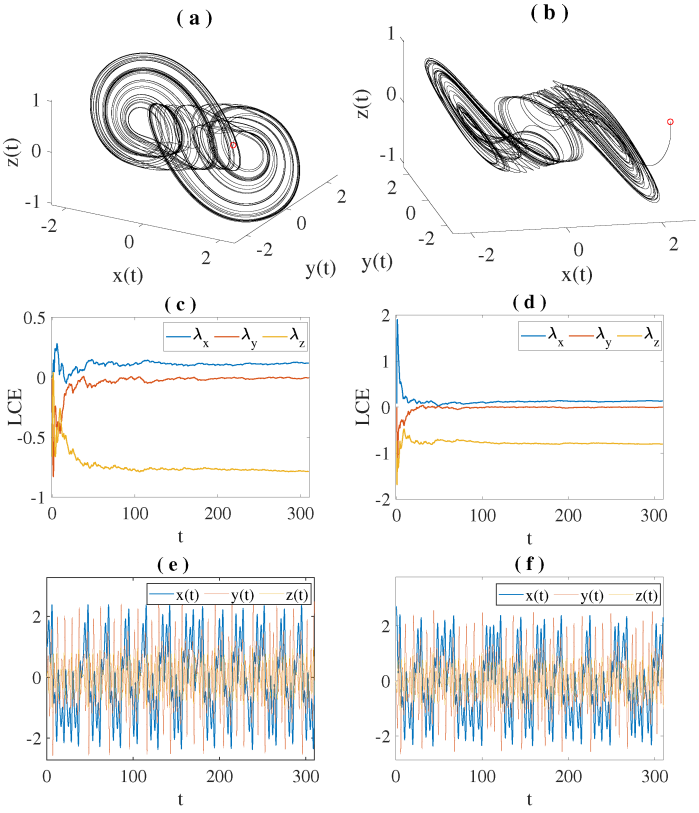

Figure 3 The strange attractors for the Jerk system obtained for the initial conditions of $(1, 0, 0)$ (a) and $(2.7083, 0, 0)$ (b). In (c) and (d) it is displayed the Lyapunov exponents for the corresponding initial conditions. In (e) and (f) it is shown the corresponding time series for the variables x, y and z.

is

$$\begin{aligned} c_1 &= 0.67, \\ c_2 &= 0.7, \\ c_3 &= -0.6, \\ c_4 &= 0.06, \\ c_5 &= 3.55, \end{aligned}$$

which are used for obtain the attractor solutions, shown in figure Figure 3 (a) and (b). The fixed points in Eq. (12) are found by substituting the respective parameters into Eq. (11), resulting the values $x_0 = 0, 2.8083, -1.4537, -2.8083, 1.4537$ with $y_0 = z_0 = 0$. We are interested in corroborating that the solutions obtained with the values of the parameters correspond to strange attractors. To do that it is necessary to obtain the LCE. According to reference (Wolf *et al.* 1985), for a 3-dimensional system, where it is possible to define tree Lyapunov exponents, if one Lyapunov exponent is positive, other equal to zero and the third is negative then it is obtained a strange attractor. It will be used this criterion for the following analysis. In Figures 3 (a) and (b) it is displayed the attractor obtained for the initial conditions of $(1, 0, 0)$ (a) and $(2.7083, 0, 0)$ (b). In Figures 3 (c) and (d) it is shown the Lyapunov exponent for these initial conditions, respectively. The values LCEs, at the time $t = 310$, obtained are $0.1193, -0.0040, -0.7853$ for the first initial condition and $0.1329, -0.0016, -0.8013$ for the second initial condition. Figures 3 (e) and (f) show the time series for the the variables x, y and z in a time interval of $[0, 310]$. As it can be observed the results are not periodic. According to (Wolf *et al.* 1985) the results indicates the presence of strange attractors.

Adding smoothed

Now let us add an exponential term that smooths the derivative of the potential in the system under study, hence the new system is

$$\begin{aligned} \dot{x} &= y, \\ \dot{y} &= c_5 z, \\ \dot{z} &= -c_1 z - c_2 y + \left(\frac{d}{dx} U(x)\right) e^{-\alpha x^2}, \end{aligned} \tag{17}$$

where $\alpha \geq 0$ is the smoothing term. In the case of $\alpha = 0$ it is recovered the former system. Notice that its fixed points, Jacobian and characteristic polynomial of the system described by Eq. (17) do not change in its form, (see Eq.(7)) except for the function

$$\mu_\alpha(x) = \left[1 + (3c_3 - 2\alpha) x^2 + (5c_4 - 2\alpha c_3) x^4 - 2\alpha c_4 x^6\right] e^{-\alpha x^2}. \tag{18}$$

Defining the function

$$\phi_\alpha(x) = \left(\frac{d}{dx} U(x)\right) e^{-\alpha x^2}, \tag{19}$$

whose behavior is illustrated in Figure 4 for different values of α.

With the introduction of the smoothing term, it is possible to obtain bifurcation diagrams varying α in Eqs. (17) to recognize the chaotic regions of the smoothed system. In Figure 5 it is shown the bifurcation diagrams as a function of this parameter. As expected, for small values of α, the system remains chaotic, while for values greater than 0.1, the system becomes non-chaotic, since the nonlinear terms tends to zero for values of α large enough. Despite the presence of regions of non-periodic behavior in the bifurcation diagrams there is a transition to regions of periodicity in which it can be found limit cycles in a region of the parameter

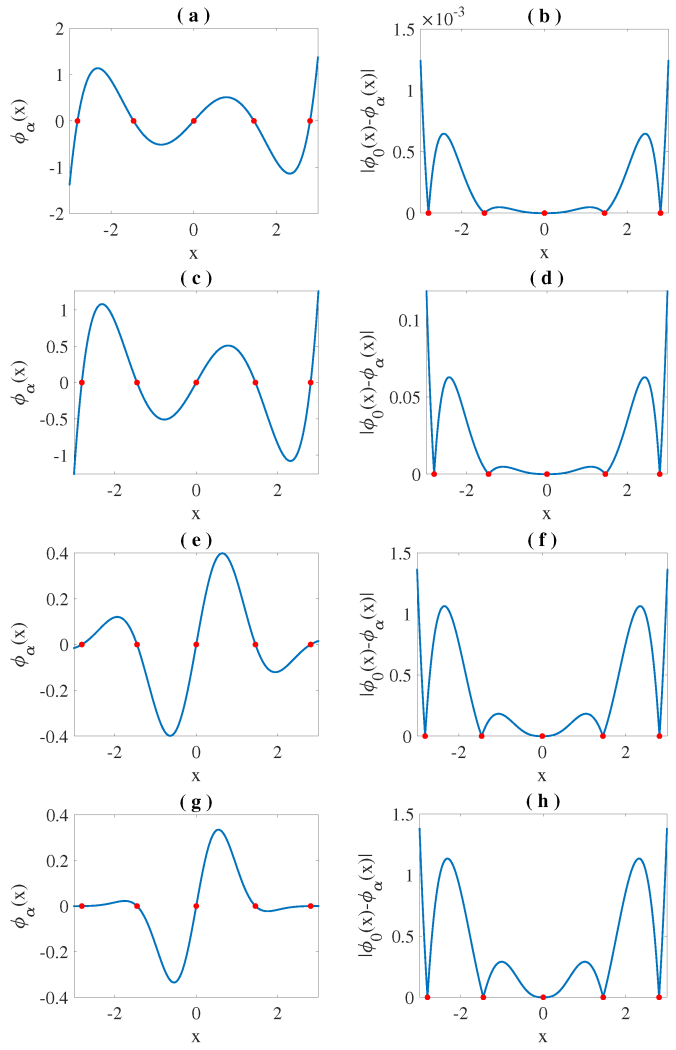

Figure 4 Functions $\phi_\alpha(x)$ (left) and $|\phi_0(x) - \phi_\alpha(x)|$ (right) for $\alpha = 1 \times 10^{-4}$, in (a), $\alpha = 1 \times 10^{-2}$ in (c), $\alpha = 0.5$ in (e) and $\alpha = 1$ in (g). Fixed points in red.

α. In fact, a qualitative analysis is carried out in the phase space of the trajectories at different values of α, finding a limit cycle for a value of $\alpha = 0.5$. This assertion is verified with the values of the LCE obtained for this case $\lambda_x = -0.0094$, $\lambda_y = -0.0458$ and $\lambda_z = -0.6148$ taken at the time $t = 310$. To illustrate this let us take 25 initial conditions distributed over the sphere of radius $r = 0.1$ centered at the point $(1.5, -0.39, 0)$ as it is shown in Figure 6 (a) where it is noticeable that there is a different behavior from the strange attractor of the system without smoothed. Then the radius is reduced to a value of $r = 0.001$, revealing the limit cycle as shows Figure 6 (b). In addition, there are points that are approximately fixed since numerically they are values close to zero.

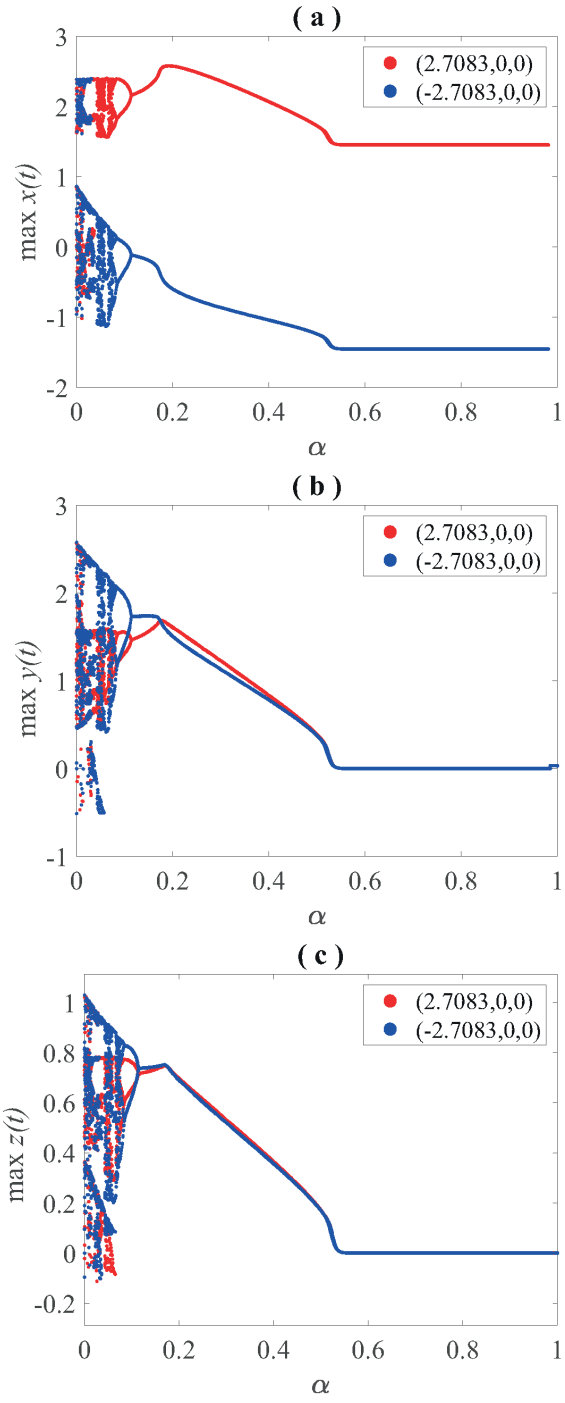

Figure 5 Bifurcation diagrams for the α parameter for the three signals with different initial conditions shown in red and in blue. In the vertical axis it is shown the maxima of corresponding variable.

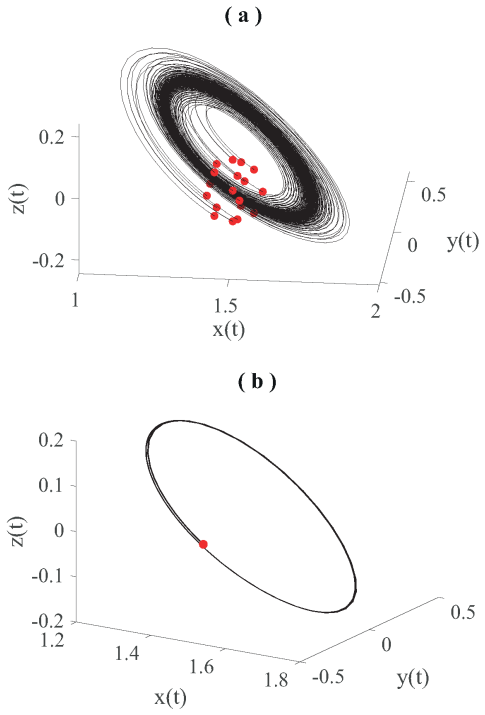

Figure 6 Trajectories in the phase space for smoothed system in Eq. (17) with $\alpha = 0.5$ for initial conditions distributed over the sphere (in red) centered in the point point $(1.5, -0.39, 0)$ with radius $r = 0.1$ in (a) and $r = 0.001$ in (b).

CONCLUSION

Let us briefly discuss the dynamics of the system around the fixed points. Under the values of the parameters c_i, with $i = 1, 2, ..., 5$ previously given, the eigenvalues are found given by the roots of Eq. (9), were it is substituted the function $\mu(x) \to \mu_\alpha(x)$ by using Eq. (18). The eigenvalues are show in Figure 7. According to the classification of the dynamics around fixed points in $3D$ (Francomano *et al.* 2017; Stumpf *et al.* 2011) for the case $\alpha = 0$ (where the distribution of eigenvalues in the complex plane for the different fixed points is shown in Figure 7 (a)), the dynamics are (see Table 1):

$$
\begin{aligned}
(0,0,0) &\quad : \text{Attracting Focus-Saddle.} \\
(p^+,0,0) &\quad : \text{Attracting Focus-Saddle.} \\
(p^-,0,0) &\quad : \text{Repelling Focus-Saddle.} \\
(-p^+,0,0) &\quad : \text{Attracting Focus-Saddle.} \\
(-p^-,0,0) &\quad : \text{Repelling Focus-Saddle.}
\end{aligned}
$$

Note that the dynamics around points $(p^\pm,0,0)$ and $(-p^\pm,0,0)$ is the same. The different types of dynamics are maintained for the values of α shown in Figure 7 (a)-(d) where the imaginary and real parts of the eigenvalues change but remain positive or negative regardless the value of α. Then in (e) of the same figure, the dynamics of the fixed points change to:

$$
\begin{aligned}
(0,0,0) &: \text{Attracting Focus-Saddle.} \\
(p^+,0,0) &: \text{Attracting Focus-Saddle.} \\
(p^-,0,0) &: \text{Asymptotically Stable Focus-Node .} \\
(-p^+,0,0) &: \text{Attracting Focus-Saddle.} \\
(-p^-,0,0) &: \text{Asymptotically Stable Focus-Node .}
\end{aligned}
$$

The results of Figure 7 (f) show that as the value of α increases, the dynamics of the system tend to be only two different types, since the eigenvalues tend to degenerate. Taking a value of $\alpha = 3$ is enough to appreciate this behavior.

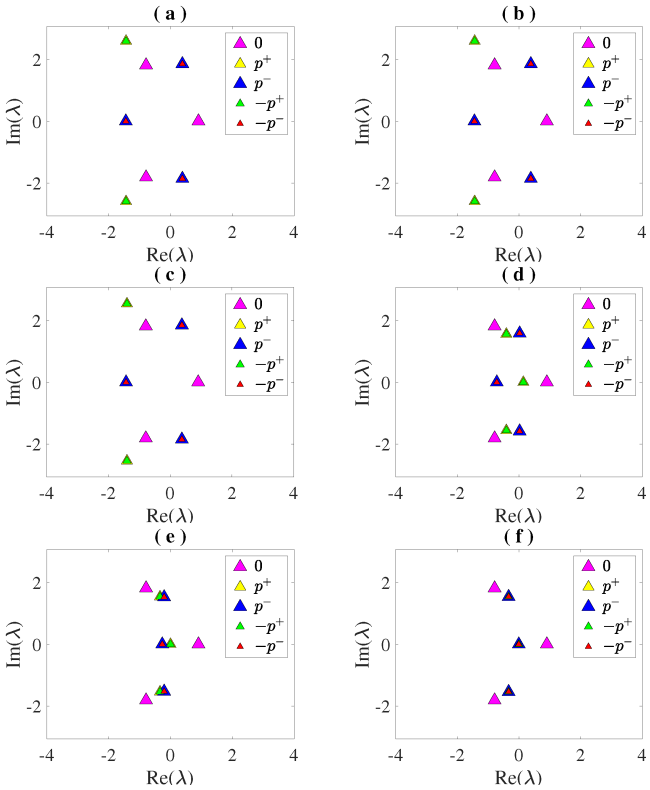

Figure 7 Complex mapping of the eigenvalues λ of the Jerk system for: $\alpha = 0$ (a), $\alpha = 1 \times 10^{-4}$ (b), $\alpha = 1 \times 10^{-2}$ (c), $\alpha = 0.5$ (d), $\alpha = 1$ (e) and $\alpha = 3$ (f). Notice the some eigenvalues coincide for certain values of α, for example for the fixed points p^+ (in yellow) and $-p^+$ (in green).

In this work, a chaotic system, constructed by immersing the Duffing oscillator with a potential type ϕ^6 in a Jerk type system and then adding an exponential smoothed factor to the Duffing potential with a parameter α, that modulates the amplitude of the potential was studied. It was found that for $\alpha = 0$ and for adequate values of the potential there exists a strange attractor, result that was corroborated by using bifurcation diagrams and by analyzing the Lyapunov exponents. By increasing from zero to certain values of α there is found a transition from the chaotic motion to regular one. In some cases the regular motion corresponds to limit cycles.

The way of controlling chaos by means of the function used in this work can also be used in other dynamical system of low- or high-dimensionality.

Expanding upon the current study, future research initiatives may explore other alternative methods for analyzing the dynamics of systems such as the behavior of Lyapunov Exponents as a function of parameters, Poincaré sections, basins of attraction, and exploring different approaches for parameter estimation that induce chaotic behavior in the system. The thorough study of Jerk-type systems with Duffing potential, whose dynamics can transit from periodic to chaotic, provides the opportunity to analyze this behavior in the synchronization of the dynamics of the system to a better understanding on implications and applications of implementing Jerk systems (Uriostegui-Legorreta and Tututi-Hernández

2022; Uriostegui and Tututi 2023; Vaidyanathan *et al.* 2017).

Acknowledgments

This work was supported by Universidad Michoacana de San Nicolás de Hidalgo (UMSNH) and Consejo Nacional de Humanidades Ciencias y Tecnologías (CONAHCYT).

Availability of data and material

Not applicable.

Conflicts of interest

The authors declare that there is no conflict of interest regarding the publication of this paper.

Ethical standard

The authors have no relevant financial or non-financial interests to disclose.

LITERATURE CITED

Chen, D. and Y. Zhang, 2016 Minimum jerk norm scheme applied to obstacle avoidance of redundant robot arm with jerk bounded and feedback control. IET Control Theory & Applications **10**: 1896–1903.

Folifack Signing, V., T. Fozin Fonzin, and M. Kountchou, 2021 Chaotic jerk system with hump structure for text and image encryption using dna coding. Circuits, Systems, and Signal Processing **40**: 4370–4406.

Francomano, E., F. M. Hilker, M. Paliaga, and E. Venturino, 2017 An efficient method to reconstruct invariant manifolds of saddle points. Dolomites Research Notes on Approximation **10**.

Haluszczynski, A. and C. Räth, 2021 Controlling nonlinear dynamical systems into arbitrary states using machine learning. Scientific reports **11**: 12991.

Hilborn, R. C. *et al.*, 2000 *Chaos and nonlinear dynamics: an introduction for scientists and engineers*. Oxford University Press on Demand.

Hong, L., J. Jiang, and J.-Q. Sun, 2015 Fuzzy responses and bifurcations of a forced duffing oscillator with a triple-well potential. International Journal of Bifurcation and Chaos **25**: 1550005.

Kengne, L. K., H. K. Tagne, J. M. Pone, and J. Kengne, 2020 Dynamics, control and symmetry-breaking aspects of a new chaotic jerk system and its circuit implementation. The European Physical Journal Plus **135**: 340.

Louodop, P., M. Kountchou, H. Fotsin, and S. Bowong, 2014 Practical finite-time synchronization of jerk systems: theory and experiment. Nonlinear Dynamics **78**: 597–607.

Louodop, P., S. Saha, R. Tchitnga, P. Muruganandam, S. K. Dana, *et al.*, 2017 Coherent motion of chaotic attractors. Physical Review E **96**: 042210.

Natiq, H., S. Banerjee, and M. Said, 2019 Cosine chaotification technique to enhance chaos and complexity of discrete systems. The European Physical Journal Special Topics **228**: 185–194.

Njitacke, Z. T., C. Feudjio, V. F. Signing, B. N. Koumetio, N. Tsafack, *et al.*, 2022 Circuit and microcontroller validation of the extreme multistable dynamics of a memristive jerk system: application to image encryption. The European Physical Journal Plus **137**: 619.

Patidar, V. and K. Sud, 2005 Bifurcation and chaos in simple jerk dynamical systems. Pramana **64**: 75–93.

Posch, H. A., W. G. Hoover, and F. J. Vesely, 1986 Canonical dynamics of the nosé oscillator: Stability, order, and chaos. Physical review A **33**: 4253.

Raineri, M. and C. G. L. Bianco, 2019 Jerk limited planner for real-time applications requiring variable velocity bounds. In *2019 IEEE 15th International Conference on Automation Science and Engineering (CASE)*, pp. 1611–1617, IEEE.

Sandri, M., 1996 Numerical calculation of lyapunov exponents. Mathematica Journal **6**: 78–84.

Sharker, S. I., S. Holekamp, M. M. Mansoor, F. E. Fish, and T. T. Truscott, 2019 Water entry impact dynamics of diving birds. Bioinspiration & biomimetics **14**: 056013.

Sprott, J. C., 2011 A new chaotic jerk circuit. IEEE Transactions on Circuits and Systems II: Express Briefs **58**: 240–243.

Stumpf, P. P., Z. Sütő, and I. Nagy, 2011 Research in nonlinear dynamics triggered by r&d experiences .

Uriostegui, U. and E. S. Tututi, 2023 Master-slave synchronization in the van der Pol and duffing systems via elastic, dissipative and a combination of both couplings. Journal of Applied Research and Technology **21**: 227–240.

Uriostegui-Legorreta, U. and E. Tututi, 2023a Control and synchronization in the Duffing-van der Pol and Φ^6 duffing oscillators. Indian Journal of Physics pp. 1–13.

Uriostegui-Legorreta, U. and E. S. Tututi, 2023b Master-slave synchronization in the Duffing-van der Pol and Φ^6 duffing oscillators. International Journal of Nonlinear Sciences and Numerical Simulation **24**: 1059–1072.

Uriostegui-Legorreta, U. and E. S. Tututi-Hernández, 2022 Master-slave synchronization in the rayleigh and duffing oscillators via elastic and dissipative couplings. Revista de ciencias tecnológicas **5**.

Vaidyanathan, S., A. Sambas, M. Mamat, and M. S. WS, 2017 Analysis, synchronisation and circuit implementation of a novel jerk chaotic system and its application for voice encryption. International Journal of Modelling, Identification and Control **28**: 153–166.

Wolf, A., J. B. Swift, H. L. Swinney, and J. A. Vastano, 1985 Determining lyapunov exponents from a time series. Physica D: nonlinear phenomena **16**: 285–317.

Zhang, H., D. Liu, and Z. Wang, 2009 Chaotification of nonchaotic systems. Controlling Chaos: Suppression, Synchronization and Chaotification pp. 309–341.

Zhou, J., D. Xu, and Y. Li, 2010 Chaotifing duffing-type system with large parameter range based on optimal time-delay feedback control. In *2010 International workshop on chaos-fractal theories and applications*, pp. 121–126, IEEE.

How to cite this article: Bucio-Gutiérrez, A., Tututi-Hernández, E. S., and Uriostegui-Legorreta, U. Analysis of the Dynamics of a ϕ^6 Duffing Type Jerk System. *Chaos Theory and Applications*, 6(2), 83-89, 2024.

CHAOS
Theory and Applications
in Applied Sciences and Engineering

e-ISSN: 2687-4539
RESEARCH ARTICLE
Vol.6 / No.2 / 2024 / pp.90-110
Special Issue (EDIESCA 2023)
https://doi.org/10.51537/chaos.1375866

Investigating Feed-Forward Back-Propagation Neural Network with Different Hyperparameters for Inverse Kinematics of a 2-DoF Robotic Manipulator: A Comparative Study

Rania Bouzid [a,1], **Hassène Gritli** [a,b,2] **and Jyotindra Narayan** [c,3]

[a]Laboratory of Robotics, Informatics and Complex Systems (RISC Lab, LR16ES07), National Engineering School of Tunis, University of Tunis El Manar, BP. 37, Le Belvédère, 1002 Tunis, Tunisia, [b]Higher Institute of Information and Communication Technologies, University of Carthage, Technopole of Borj Cédria, Route de Soliman, BP 123, Hammam Chatt 1164, Ben Arous, Tunisia, [c]Mechatronics and Robotics Laboratory, Department of Mechanical Engineering, Indian Institute of Technology Guwahati, Guwahati 781039, Assam, India.

ABSTRACT Inverse kinematics is a significant challenge in robotic manipulators, and finding practical solutions plays a crucial role in achieving precise control. This paper presents a study on solving inverse kinematics problems using the Feed-Forward Back-Propagation Neural Network (FFBP-NN) and examines its performance with different hyperparameters. By utilizing the FFBP-NN, our primary objective is to ascertain the joint angles required to attain precise Cartesian coordinates for the end-effector of the manipulator. To accomplish this, we first formed three input-output datasets (a fixed-step-size dataset, a random-step-size dataset, and a sinusoidal-signal-based dataset) of joint positions and their respective Cartesian coordinates using direct geometrical formulations of a two-degree-of-freedom (2-DoF) manipulator. Thereafter, we train the FFBP-NN with the generated datasets using the MATLAB Neural Network Toolbox and investigate its potential by altering the hyperparameters (e.g., number of hidden neurons, number of hidden layers, and training optimizer). Three different training optimizers are considered, namely the Levenberg-Marquardt (LM) algorithm, the Bayesian Regularization (BR) algorithm, and the Scaled Conjugate Gradient (SCG) algorithm. The Mean Squared Error is used as the main performance metric to evaluate the training accuracy of the FFBP-NN. The comparative outcomes offer valuable insights into the capabilities of various network architectures in addressing inverse kinematics challenges. Therefore, this study explores the application of the FFBP-NNs in tackling the inverse kinematics, and facilitating the choice of the most appropriate network design by achieving a portfolio of various experimental results by considering and varying different hyperparameters of the FFBP-NN.

KEYWORDS
Robotic manipulator
Inverse kinematics
Feed-Forward back propagation
Artifical neural network
Hyperparameters
Levenberg-Marquardt algorithm
Bayesian regularization algorithm
Scaled conjugate gradient algorithm
Different datasets
Mean squared error
R-value

INTRODUCTION

Robot kinematics plays a fundamental role in respective robotic research and applications. The progress in inverse kinematics algorithms is of utmost importance for advancing this field, as noted in various studies (Gao *et al.* 2017; Liu *et al.* 2017; Rea Minango and Ferreira 2017). However, conventional approaches for solving inverse kinematics problems frequently face issues with convergence and entail intricate iterative procedures, which can negatively impact the overall efficiency and quality of these algorithms, as highlighted in the work of Reiter *et al.* (2018). Additionally, it has been noted in the research work of Zhao *et al.* (2018) and that of Di Pietro *et al.* (2012) that conventional approaches for solving inverse problems lack a unified equation for describing motion.

Manuscript received: 15 October 2023,
Revised: 30 November 2023,
Accepted: 5 December 2023.

[1]rania.bouzid@istic.ucar.tn
[2]grhass@yahoo.fr (**Corresponding author**)
[3]n.jyotindra@gmail.com

Compared to forward kinematics equations, inverse kinematics equations present more significant challenges. Solving inverse kinematics difficulties is typically more complex than solving forward kinematics ones Bouzid *et al.* (2024d,c). The purpose of forward kinematics is to identify the end-effector's position based on joint angles or positions (Bouzid *et al.* 2023, 2024b). In most cases, this can be accomplished using simple geometric calculations. However, inverse kinematics entails determining the joint angles or positions that match to a desired end-effector position, which requires solving a set of nonlinear equations. This can be computationally intensive, with complex relationships and limits (Bouzid *et al.* 2024d,c).

Many researchers and organizations have conducted thorough research into inverse kinematics algorithms within the field of robotics (Benavente-Peces *et al.* 2014; Narayan *et al.* 2022; Becerra and Kremer 2011; Narayan and Singla 2017a). These algorithms primarily concentrate on four key aspects: geometric algorithms, analytical algorithms, geometric-analytic algorithms, and numerical algorithms. An analytical algorithm for solving kinematics' inverse problems in palletization manipulator robotics was proposed by Xu *et al.* (2017). While this analytical algorithm offers certain practicality to some possible extent, it was found to encounter the probem of yielding multiple analytical solutions for a single pose, thereby complicating the determination of a unique solution. Practical experience has revealed that while applying the algorithm to robotics offers flexibility, the design process tends to become overly convoluted. This often leads to the need for numerous iterations, resulting in inefficiencies (Abbas *et al.* 2019; Narayan *et al.* 2018).

Therefore, to address the problem of computationally expensive analytical and numerical solutions, researchers have started exploring intelligent solutions in the last few years (Li and Savkin 2018; Mahajan *et al.* 2017). The authors in (Duka 2014) generated training data for the Neural Network by randomly choosing joint angle values and then determining the resulting end-effector position, following circular trajectories through forward kinematics. Furthermore, the paper introduces a method to rescale the input and output data to fall within the $[-1,\ 1]$ range, thereby improving the network's performance. In another research by Dash *et al.* (2017), the Levenberg-Marquardt (LM) algorithm was used to train the designed network over a set number of epochs. This study focuses on tackling the problem of solving the inverse kinematics of a 6-DoF system through the application of an artificial neural network (ANN). In the work by Mahajan *et al.* (2017), a neural network model was presented, capable of independently governing the actions of a manipulator, thus obviating the need for external guidance. The neural network was trained through unsupervised learning methods, focusing on a 2-DoF system. The primary focus of the study is to trace a circular path and intercept a moving ball. In the study by Narayan and Singla (2017a), the researchers used the adaptive neuro-fuzzy inference system (ANFIS) with a Gaussian membership function to solve the inverse kinematics problem of a 4-DoF SCARA robot, combining fuzzy inference systems and neural network approaches from prior work.

Li and Savkin (2018) proposed a solution using competitive neural networks to address the inverse kinematics problem in robotics, focusing on the task of a mechanical arm grabbing an object. A MATLAB-based simulation was carried out, as referenced in (Kumar *et al.* 2018), to assess the efficacy of an intelligent technique in rectifying position errors during the execution of a circular trajectory by a 2R robot. By introducing minor variations in link lengths, geometric discrepancies were examined by generating a simulated dataset using the kinematic models derived. Subsequently, the neural network was trained on this dataset to forecast position error values within the operational area of the robot. In (Lathifah *et al.* 2018), authors explored an ANN to solve the problem of an inverse kinematics for a 3-link planar serial robotic manipulator. The trained neural network was tested by considering that the robotic manipulator performs square and/or triangle motions within the admissible working-space (Bouzid *et al.* 2024d). Moreover, the LM algorithm trained the neural network for the inverse kinematics problem's solution. Various network architectures were tested by Handayani *et al.* (2018) to find the optimal solution. The proposed method was evaluated using a simple planar manipulator performing tasks such as drawing a square and a triangle, and the results demonstrate the validity of the neural network trained with the Bayesian Regularization (BR) algorithm for solving the inverse kinematics problem. Theofanidis *et al.* (2018) have introduced a novel neural network-based approach for estimating a kinematically redundant robotic arm's forward kinematics and testing it for different configurations.

The neural network is trained in the work by Dumitriu *et al.* (2020), using the LM algorithm to map the manipulator's joints and the end-effector's position based on forward kinematics calculations. The network is trained for different scenarios, and the Mean Square Error (MSE) is used to evaluate the accuracy of the results. The research work in (Gao 2020) demonstrated that the proposed algorithm of the inverse kinematics, which employs an enhanced BPNN, outperforms better than traditional/classical algorithms for inverse solutions when handling with the inverse kinematics problem in manipulator robots with six degrees of freedom (Bouzid *et al.* 2024d). Aravinddhakshan *et al.* (2021) introduced a neural network-based approach for a 5-DoF manipulator through supervised learning, achieving accurate inverse kinematics and optimizing path planning during pick and place operations. This highlights the effectiveness of neural networks in manipulator control. Furthermore, the research of Köker *et al.* (2004) focused on a three-joint robotic manipulator and utilized simulation software to plan cubic trajectories and define the manipulator's work volume. A key strength highlighted in the study is the neural network's remarkable online performance. In addition, multiple neural networks were employed in (Takatani *et al.* 2019) to learn the inverse kinematics of redundant robotic manipulators using an independent approach, and by studying different structures of the evaluation function (Bouzid *et al.* 2024d). Furthermore, the training data employed in this learning methodology consists of different endpoints, different postures, and different evaluation values of the robotic manipulators. Meanwhile, Ibarra-Pérez *et al.* (2022) emphasizes the challenge of setting structural parameters for neural networks, advocating for optimization-based methods over trial-and-error, saving time and improving performance. Lastly, in the work of Aysal *et al.* (2023), machine learning techniques are found to be a viable option for analyzing the kinematics of a 3-DoF robot arm with an RRR design, mainly using an MLP model to ensure system stability.

In (Wagaa *et al.* 2023), various Deep Learning networks were developed to solve the inverse kinematics of 6-DoF manipulator robots. ANN, Convolutional Neural Network (CNN), Long-Short Term Memory (LSTM), and Gated Recurrent Unit (GRU) are the neural network architectures that have been considered. Furthermore, authors examined the performance of analytical and neural systems in producing robot trajectories using the RoboDK simulator to display simulation results with real-world implications. In (Cagigas-Muñiz 2023), various strategies involving ANNs were

proposed and studied. The results revealed that the proposed original bootstrap sampling and hybrid methods could significantly outperform approaches that just use one ANN. Nevertheless, none of these advancements completely solved the inverse kinematics problem in articulated robots. García-Samartín and Barrientos (2023) addressed the forward kinematics' problem using ANNs and Genetic Algorithms (GA). Using the publicly available Inverse Kinematic (IK) model, both GA and ANN approaches were implemented. Authors showed, compared to another approach, that the proposed methodologies produced equivalent or higher results in terms of accuracy and time. Authors in (Bouzid *et al.* 2023, 2024b) studied the forward kinematics problem of a 2-DoF robotic manipulator via ANNs. Moreover, they tackled in (Bouzid *et al.* 2024a) the same problem for a SCARA manipulator robot. Furthermore, the problem of studying and solving the issues of the inverse kinematics for the manipulator robot was considered in (Bouzid *et al.* 2024d,c). Other solving approaches of the inverse kinematics problem for articulated manipulator robots can be found within these previous references.

The existing literature on the subject reveals a noticeable gap in research related to the comparative analysis of neural networks with different hyperparameters when applied to solving the inverse kinematics of robot manipulators. As a response to this deficiency, our study makes a substantial contribution by introducing a Feed-Forward Back-Propagation Neural Network (FFBP-NN) specifically designed to tackle the inverse kinematics problem of a 2-DoF articulated robotic manipulator. Through the process, we investigated the effectiveness of the FFBP network architecture with three distinct generated datasets: a random-step-size dataset, a fixed-step-size dataset, and a sinusoidal-signal-based dataset with varying frequencies (Bouzid *et al.* 2024d,c, 2023, 2024b). Moreover, for each dataset type, the network architecture is tested with different hyperparameters, such as the number of hidden layers, neurons in the hidden layer, and three different training optimization algorithms, namely the Levenberg-Marquardt (LM) (Ranganathan 2004), the Bayesian regularization (BR) (Kayri 2016), and the Scaled conjugate gradient (SCG) (Møller 1993). The testing and verification phases are achieved in order to evaluate the capacity of the trained neural network to minimize approximation errors and appropriately estimate inverse kinematics.

The rest of this paper is structured like so: Section 2 delves into the mathematical representation of the forward kinematics of manipulator robots with n degrees of freedom, while Section 3 explores the computational aspects of the inverse kinematics for a 2-DoF manipulator robot. Section 4 introduces a novel approach using an FFBP-NN to efficiently solve inverse kinematics problems, detailing the network's architecture. In this previous Section, we provide a brief overview of FFBP-NNs to ensure reader understanding. A flowchart and the hyperparameters used in the proposed FFBP-NNs are also illustrated in this previous same section. Section 5 presents numerical results obtained through the FFBP-NNs' application and initiates a discussion on implications, potential improvements, and broader applications within the field of robotics. The paper concludes with a conclusion and some possible future directions for improvements, presented in Section 6.

FORWARD KINEMATICS OF n-DOF MANIPULATOR ROBOTS

It is worth mentioning first that the terminology DoF stands for "Degree of Freedom". In the context of robotics, mechanics, and other related disciplines, it refers to the number of independent parameters or variables that define the configuration or motion of a system. Thus, in the context of a robot arm, the number of degrees of freedom would represent the number of independent ways the arm can move or rotate.

A Brief Description on Forward Kinematics of n-DoF Manipulator Robots

Forward kinematics of n-DoF manipulator robots is a fundamental concept in robotics that deals with determining the position and orientation of the robot's end-effector (usually a tool or gripper) in the workspace based on the joint angles or variables of the robot's individual links. It is akin to tracing the path of a robot's "hand" as it moves through its various joint configurations. Methods from geometry and linear algebra, trigonometric transformation matrices, and homogeneous coordinate transformations are frequently used in traditional solutions to the forward kinematics problem. Here is a brief overview of the conventional solution approaches for the computation of the forward kinematics of manipulator robots:

1. *Geometric Approach*: It offers a straightforward understanding of how a robot's joints and links affect its end-effector's position and orientation, useful for simpler robots like planar ones but less effective for complex structures with closed-loop chains or redundancy due to accuracy challenges and lack of closed-form solutions (Kim *et al.* 2016).

2. *Trigonometric methods*: While excelling in simplicity and computational efficiency, trigonometric methods are most suitable for planar robots because they provide analytical solutions without iterative techniques (Petrescu *et al.* 2017). However, they may not be as effective for complex robots in three-dimensional spaces or with unconventional joint arrangements, as their assumptions may lead to reduced accuracy. Engineers and roboticists should assess their suitability for specific applications and consider alternative approaches when dealing with intricate systems or non-standard geometries.

3. *Coordinate transformations*: Coordinate transformations have versatile applications in various robotic systems, including 2D and 3D environments with different degrees of freedom (Wang *et al.* 2014). They provide a mathematically rigorous foundation, enhancing complex robots' capabilities and integrating seamlessly with other techniques. However, implementing them can be intricate, especially for robots with many joints and complex link geometries, potentially leading to longer development times and errors. Proficiency in coordinate transformations may require a robust mathematical background, posing a learning curve for some robotic practitioners.

Extending the concept of coordinate transformation, forward kinematics is calculated using Denavit-Hartenberg (DH) parameters and the homogeneous transformation matrix (Denavit and Hartenberg 1955). The DH parameters provide a systematic way to describe the geometric relationship between the robot's successive joints and links (Narayan and Singla 2017a). The Homogeneous Transformation Matrix combines DH parameters to express the transformation from one coordinate frame (associated with a specific joint) to another, effectively mapping the position and orientation of each link concerning the previous one. By multiplying these transformation matrices sequentially from the base link to the end-effector, the forward kinematics algorithm computes the final transformation that represents position of the robot's end-effector in the base coordinate frame.

Furthermore, for each joint/frame, the parameters in this previous homogeneous transformation matrix, noted as ${}^{i}_{i-1}\mathcal{H}$, are defined, according to the DH method, like so (Ganapathy 1984):

- Link length (a): The path of the shared normal defining the difference between the preceding z-axis (that is of the $(i-1)$th frame) and the actual z-axis (that is of the ith frame).
- Link twist (α): The angle about the shared normal between the preceding z-axis and the present z-axis.
- Link offset (d): The path from the previous x-axis to the actual x-axis, along the preceding z-axis.
- Joint angle (θ): The degree of rotational angle about the z-axis between the preceding x-axis and the actual x-axis.

The homogeneous transformation matrix ${}^{i}_{i-1}\mathcal{H}$ from the $(i-1)$th frame to the next one (ith frame) is represented via the following expression (Ganapathy 1984):

$$ {}^{i}_{i-1}\mathcal{H} = \begin{bmatrix} {}^{i}_{i-1}\mathcal{R} & {}^{i}_{i-1}\mathcal{T} \\ \mathcal{O} & 1 \end{bmatrix} \tag{1} $$

where ${}^{i}_{i-1}\mathcal{R}$ and ${}^{i}_{i-1}\mathcal{T}$ are, respectively, the rotation and translation matrices from one frame to the next one. Moreover, the symbol $\mathcal{O}$ stands for the zero matrix with appropriate dimension.

Such homogeneous transformation matrix (1) is explicitly expressed in terms of the DH parameters, θ, d, α and a, as follows:

$$ {}^{i}_{i-1}\mathcal{H} = \begin{bmatrix} \cos(\theta) & -\sin(\theta)\cos(\alpha) & \sin(\theta)\sin(\alpha) & a\cos(\theta) \\ \sin(\theta) & \cos(\theta)\cos(\alpha) & -\cos(\theta)\sin(\alpha) & a\sin(\theta) \\ 0 & \sin(\alpha) & \cos(\alpha) & d \\ 0 & 0 & 0 & 1 \end{bmatrix} \tag{2} $$

The Adopted 2-DoF Robotic Manipulator and its Forward Kinematics

In our study, we utilize a 2-DoF manipulator robotic model as shown in Figure 1. In the kinematic description of the robotic system under consideration, the joints are denoted as joint 1 and joint 2, representing the rotational angles θ_1 and θ_2, respectively. The associated links are labeled as follows: link 0 corresponds to l_0, link 1 to l_1, and link 2 to l_2. This notation establishes a clear and concise representation of the joint angles and link lengths, facilitating the systematic analysis of the robot's kinematics.

By following the steps and the implementation of the geometrical method and validating with the DH method, the forward kinematics equations for the 2-DoF manipulator robot can be obtained as follows (Ghaleb and Aly 2018):

$$ X = l_0 + l_1\cos(\theta_1) + l_2\cos(\theta_1+\theta_2) \tag{3} $$
$$ Y = l_1\sin(\theta_1) + l_2\sin(\theta_1+\theta_2) \tag{4} $$

For our specific scenario, the lengths of the 2-DoF manipulator robot are set as follows: $l_0 = 1\ [m]$, $l_1 = 2\ [m]$, and $l_2 = 3\ [m]$. Note that in these equations (3) and (4), the parameters θ_1 and θ_2 represent the joint angles of the 2-DoF manipulator robot, serving as input parameters for computing the Cartesian coordinates X and Y.

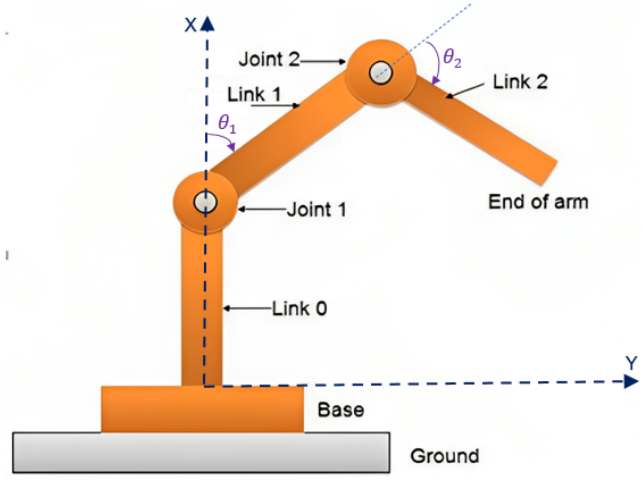

Figure 1 Schematic of a 2-DoF manipulator robot (updated from (Madhuraghava *et al.* 2018)).

INVERSE KINEMATICS OF THE 2-DOF MANIPULATOR ROBOT

In the case of inverse kinematics for the 2-DoF manipulator robot, the problem is formulated to calculate the joint angles necessary to position the end-effector at a specific Cartesian coordinate in the workspace, as shown in Figure 2. Thereafter, an intelligent neural network-based solution is proposed to address the problem formulation.

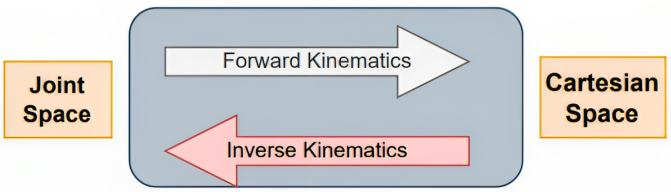

Figure 2 Schema of the Forward/Inverse Kinematics. The left-hand side of the figure represents the manipulator articulation variable. The right-hand side represents the location of the robot end-part.

Problem Formulation

The complexity arises from the nonlinear and intricate mathematical equations governing the connection between joint angles q and the resulting end-effector position Z, modeling the following forward kinematics model (Narayan and Singla 2017b):

$$ Z = \mathcal{F}(q), \qquad q \in \mathbb{R}^n, \qquad Z \in \mathbb{R}^m \tag{5} $$

and therefore the following inverse kinematics model, which is considered to be unknown:

$$ q = \varphi(Z) \tag{6} $$

Here are a few problems associated with the inverse kinematics:

1. *Nonlinearity*: Nonlinear inverse kinematics challenges arise due to complex joint configurations or irregular manipulator robot shapes, necessitating computationally intensive solutions through iterative numerical methods or optimization techniques (Snieder 1998).

2. *High-dimensional Spaces*: As the number of joints in a manipulator robot increases, the dimensionality of the inverse kinematics problem also increases. To tackle this problem, dimension reduction and advanced optimization methods may be required (Petrović 2018).

3. *Joint limits*: Manipulator robots typically have joint limits that restrict the range of motion for each joint. Ensuring that the solutions of the inverse kinematics respect these physical limits is essential to prevent damage to the manipulator robot (Huo and Baron 2008).

Proposed Method

In this research work and to solve the inverse kinematics of the 2-DoF manipulator robot, the proposed approach is articulated around the following points:

- Our research project centers on applying intelligent techniques to tackle inverse kinematics challenges, particularly on ANNs.
- In our investigation, we will explore the use of FFBP-NNs utilizing various training optimizers and diverse numbers of hidden layers.
- We aim to evaluate their effectiveness across three different datasets to enhance our understanding of their capabilities.

FEED-FORWARD BACK-PROPAGATION NEURAL NETWORK FOR SOLVING THE INVERSE KINEMATICS PROBLEM

A Brief Overview on Feed-Forward Back-Propagation Neural Networks

An FFBP-NN stands as a pivotal construct within the expansive realm of ANNs, designed primarily to excel in supervised machine learning endeavors such as classification and regression, prediction of time series, as well as modeling of complex nonlinear dynamical systems (Cimen *et al.* 2019; Martinez-garcia *et al.* 2022; Karaca 2023; Keleş *et al.* 2023; Noorani and Mehrdoust 2022). An FFBP-NN fundamentally comprises a layered architecture where neurons are intricately linked, guiding information in a carefully designed unidirectional path. This complex network structure typically includes an input layer, which receives initial data inputs; a series of hidden layers, one or more in the count, actively involved in intermediate data processing and the extraction of vital features; and, to complete the sequence, an output layer tasked with generating the network's predictions. The core of this neural architecture hinges on two essential components: the allocation of weights to neural connections, which indicates the connection strength, and the inclusion of bias terms at each neuron, discreetly introducing an adjustment to the neuron's activation function output.

The crux of FFBP-NN operation is the feedforward process, wherein data systematically traverses the network's layers. Within each layer, a neuron undertakes the intricate task of computing a weighted sum of its inputs, adding the bias term into the equation, and applying a designated activation function, resulting in an output that cascades to the next layer. These activation functions, spanning the spectrum from sigmoid and hyperbolic tangent to the robust rectified linear unit (ReLU), serve to imbue the network with a capacity for nonlinearity, thereby empowering it to model intricate and non-trivial data relationships effectively. We find the eagerly awaited predictions at the apex of the network, located within the output layer. An essential aspect of this procedure entails the utilization of a loss or cost function, which scrupulously quantifies the gap between these predictions and the pristine target values present in the training dataset. The optimization process, a crucial stage in an FFBP-NN, is guided by the venerable back-propagation algorithm.

This iterative mechanism recalibrates the network's core parameters - the weights and biases - in pursuit of the singular objective: minimizing the loss function. Underpinning this algorithmic operation is the gradient descent technique, a stalwart of optimization methodologies, masterfully guiding parameter adjustments. Central to this process is the learning rate, a hyperparameter wielding influence over the scale of parameter updates, thereby determining the network's convergence rate. With the profound complexity and nuance embedded within FFBP-NNs, hyperparameters serve as vital navigational coordinates in this intricate journey. These encompass many facets, encompassing the count of hidden layers, the number of neurons nested within each layer, the judicious selection of activation functions, and the meticulous tuning of the learning rate. Through these careful adjustments, FFBP-NNs evolve from their nascent state into formidable models, attaining an esteemed position within the pantheon of machine learning paradigms. FFBP-NNs play a pivotal role across multifarious domains, underscoring their enduring relevance and adaptability through their ability to capture, decode, and illuminate intricate data relationships.

Training With Three Different Datasets

The proposed method employs three distinct datasets: (1) a dataset with a fixed step size, (2) another with random step sizes, and (3) a sinusoidal-signal-based dataset featuring varying frequencies. The selection of these datasets aims to thoroughly evaluate the FFBP-NN's performance across various input data types.

It is important to note that we arbitrarily use the parameters, and multiple possible combinations depend on our choices. We have discovered these results through numerical experimentation, but obtaining other values and even more efficient models is possible. We conducted tests over 1000 epochs, exploring using 1 to 5 hidden layers for a given number of layers (as shown in Figure 3), and a specific dataset size.

Fixed-step-size Dataset: This initial dataset served as the main foundation for training ANNs through a FFBP method. This dataset was meticulously curated to evaluate the ANN's performance across various scenarios (Bouzid *et al.* 2023, 2024d,b,c). The dataset creation process involved systematically altering the values of θ_1 and θ_2, incrementing them by a fixed step size h equal to $h = 0.02$, within the interval from $\theta_i^{\min} = -\pi$ to $\theta_i^{\max} = \pi$, for $i = 1, 2$.

Thus, for each articulated variable θ_i, we build the vector of all values of θ_i by sweeping the interval $[\theta_i^{\min} : \theta_i^{\max}]$, for all $i = 1, 2$, for left to right with the fixed step $h = 0.02$. The following expressions are used to build such intervals of the two parameters θ_1 and θ_2.

$$\theta_1^{\text{Range}} = [\theta_1^{\min} : h : \theta_1^{\max}] \tag{7}$$

$$\theta_2^{\text{Range}} = [\theta_2^{\min} : h : \theta_2^{\max}] \tag{8}$$

The size of each vector θ_i^{Range}, with $i = 1, 2$, is equal to $N = \frac{2\pi}{h} + 1 = 315$. It is worth to note that the decrease of the value of the parameter h will lead to the increase of the value of N, and hence of the size of the dataset in question, which is equal in the present case (that is with $h = 0.02$) to $N^2 = 99225$.

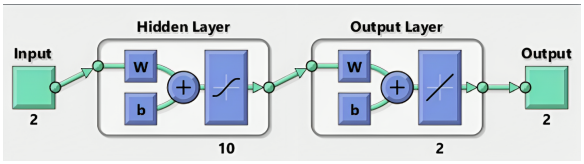

(a)

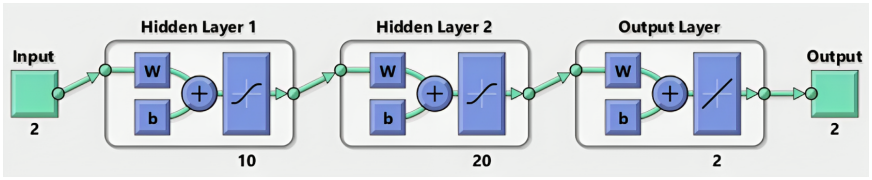

(b)

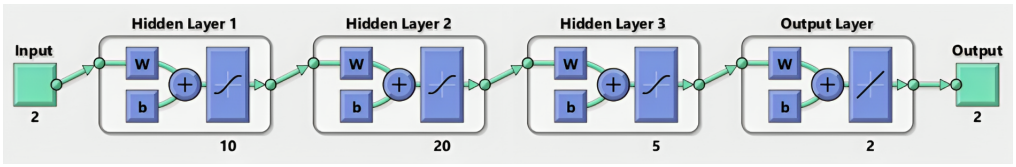

(c)

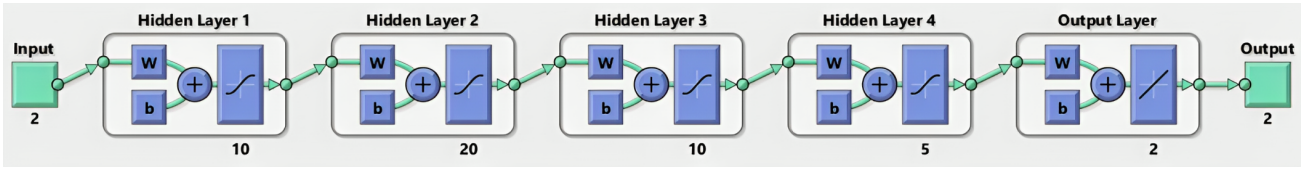

(d)

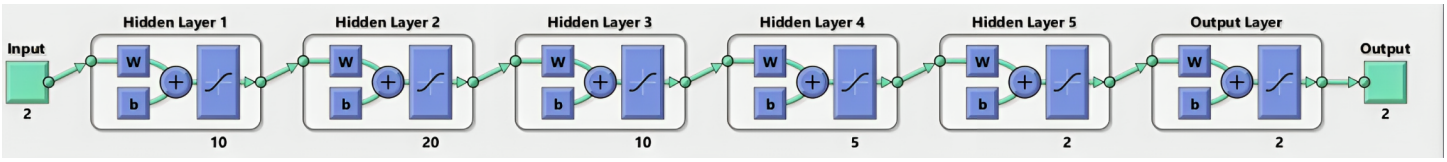

(e)

Figure 3 Different adopted ANN architectures with a different number of neurons in each hidden layer: (a) ANN model with only one hidden layer having 10 neurons, it will be noted as 1 Hidden layer (10), (b) ANN model with two hidden layers where the first hidden layer has 10 neurons, whereas the second hidden layer has only 2 neurons, it will be referred to as 2 Hidden layers (10,2), (c) ANN model with three hidden layers, where the number of neurons in each hidden layer is successively 10, 20 and 2, it will be noted as 3 Hidden layers (10,20,2), (d) ANN model with four hidden layers and where the number of neurons associated to each layer is respectively 10, 20, 5, and 2, and it will be referred to as 4 Hidden layers (10,20,5,2), and (e) ANN model with five hidden layers, and it will be indicated as 5 Hidden layers (10,20,10,5,2).

For each possible combination of these joint angles θ_i in the interval θ_i^{Range}, for all $i = 1, 2$, by sweeping then from left to right, we employed the forward kinematics equations (3) and (4) to compute the corresponding Cartesian coordinates (X and Y). Therefore, the dataset consisted of pairs of input and output data, where the Cartesian coordinates represent the outputs, whereas the inputs are the two joint angles (θ_1 and θ_2).

The main goal is to enable the FFBP-NN to accurately predict joint angles from various end-effector positions. We achieved this by using diverse input and output data in the dataset and the FFBP-NN during training to improve the proposed ANN's ability to generalize and make precise predictions of the positions of the adopted 2-DoF manipulator robot.

Random-step-size Dataset: This dataset was deliberately designed to inject an element of unpredictability and variability into the input data, serving as a test of the FFBP-NN's adaptability and resilience. The primary objective behind creating this dataset was to gauge the FFBP-NN's capacity to handle unforeseen patterns and assess its robustness when confronted with such unanticipated scenarios (Bouzid *et al.* 2023).

To generate the random dataset for the inverse kinematics of the 2-DoF manipulator robot, we harnessed the power of the "rand" function to produce random values for the joint angles, θ_1 and θ_2. Each data point within this dataset was characterized by two joint angles, θ_1 and θ_2, randomly chosen from a non-uniform distribution (Bouzid *et al.* 2023, 2024b). We applied a scaling and shifting technique to ensure that these randomly generated joint angles fell within the desired range of $-\pi$ to π. Specifically, we multiplied the random values by 2π and subtracted π, yielding joint angles that span the entire range from $-\pi$ to π (Bouzid *et al.* 2023, 2024d,b).

The following expression elucidates the computation process

for this random dataset (Bouzid *et al.* 2023, 2024d,b):

$$\theta^{\text{Range}} = \text{rand}(N, 2) \times 2\pi - \pi \tag{9}$$

where N is the desired total number of parameters, which gives hence the size of the dataset. Note that this expression (9) will generate the complete dataset for the two variables θ_1 and θ_2. The output of this equation is then a vector composed of two columns: the first column is for θ_1, whereas the second column is for θ_2.

Then, once the random part/subset of the dataset is generated, we compute the two Cartesian coordinates X and Y of the manipulator robot using the forward kinematics equations (3) and (4). As a result, we obtain a matrix with two columns where the first column is for the X coordinate and the second column is for the Y coordinate. This matrix is therefore saved in the dataset along with the first part composed of the two variables θ_1 and θ_2. Thus, the resulting matrix is composed of four columns and N rows. For this random dataset, we fixed $N = 1000$.

The inherent randomness and variability of this adopted dataset pose a robust challenge to the FFBP-NN, forcing it to adapt and learn from unforeseen patterns. Using previously generated joint angles, we systematically cycled through forward kinematics equations for each data point. This iterative process created a dataset with diverse and random combinations of Cartesian coordinates and joint angles. Each entry in the dataset displayed a unique combination of joint angles associated with Cartesian coordinates, enabling a comprehensive and random exploration of the end-effector positions of the manipulator robot (Bouzid *et al.* 2023, 2024d,b,c).

Sinusoidal-signal-based Dataset: We harnessed the capabilities of the FFBP-NN by introducing a third dataset tailored to evaluate its proficiency in handling sinusoidal signals characterized by varying frequencies. This dataset was pivotal in assessing the performance of the FFBP-NN when confronted with diverse frequency patterns. Our primary goal was to comprehensively examine how effectively the FFBP-NN could discern and predict the intricate cyclic patterns inherent in the input data. This exploration was instrumental in enabling the FFBP-NN to acquire an in-depth understanding of these complex signals and enhance its ability to generalize across a broad spectrum of cyclic patterns (Bouzid *et al.* 2023, 2024d,b,c).

The sinusoidal-signal-based dataset encompassed two sinusoidal signals with distinct characteristics, as outlined in Table 1. Each signal i corresponds to the joint variable θ_i, for $i = 1, 2$.

This dataset facilitates the creation of visualizations for tracking the fluctuations in joint angles θ_1 and θ_2 concerning an angular parameter. These visualizations are constructed using the following equations:

$$\theta_1 = A_1 \times \sin(f_1 \times \xi_1 + \phi_1) \tag{10}$$
$$\theta_2 = A_2 \times \sin(f_2 \times \xi_2 + \phi_2) \tag{11}$$

In these equations (10) and (11), and in order to generate the two sinusoidal signals, the two parameters ξ_1 and ξ_2 are varied within the admissible interval $[-\pi, \pi]$. As a result, another form of the distribution of the values of the two angles θ_1 and θ_2 will be obtained. A such distribution is entirely different to that of the first and second datasets.

When we generate the parameters and equations for the sinusoidal-signal-based dataset, a figure emerges as its representation. This figure encompasses two subplots illustrating the generated curves of our variables, which are θ_1 and θ_2 (see Figure 4). In the initial subplot at the top, the curve is depicted in blue, illustrating the connection between the angle on the x-axis (ξ) and the corresponding joint angle (θ_1) on the y-axis. This subplot provides insights into how the joint angle θ_1 varies with respect to the angle/variable ξ. In the second subplot at the bottom, the curve is presented in magenta. Here, the x-axis (ξ) signifies the angle, while the y-axis represents the joint angle (θ_2). This subplot enables us to examine how the joint angle θ_2 responds to changes in the angle/variable ξ. Collectively, these subplots offer a visual depiction of the sinusoidal-signal-based dataset, highlighting the interplay between angles and their corresponding joint angles, as demonstrated in Figure 4. Additionally, this visual representation aids in understanding the dataset's characteristics.

Table 1 Parameters used for the sinusoidal-signal-based dataset for generating the values of the two angular positions θ_1 and θ_2 of the 2-DoF manipulator robot.

Parameter	Signal 1 of θ_1	Signal 2 of θ_2
Frequency f [Hz]	1.5	10
Phase ϕ [rad]	0	$\pi/4$
Amplitude A [rad]	π	π
Angle ξ [rad]	$[-\pi, \pi]$	$[-\pi, \pi]$
Number of samples N	1000	1000

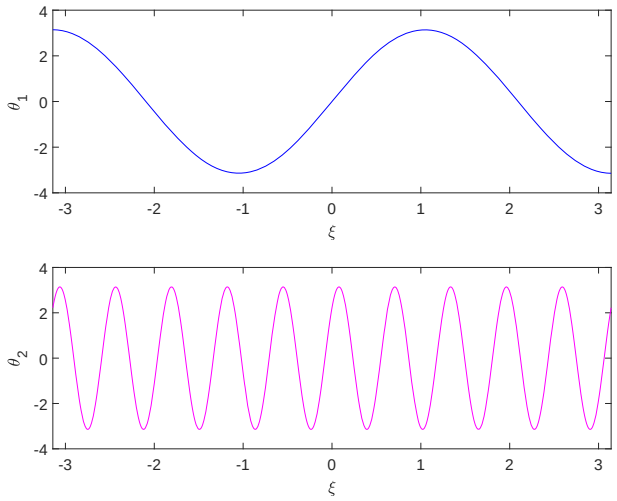

Figure 4 Presentation of the generated signals of the two sinusoidal signals of the two variables θ_1 and θ_2 of the 2-DoF manipulator robot.

Therefore, once the values of two joint angles θ_1 and θ_2 are obtained according to the adopted sinusoidal distributions, we introduce the forward kinematic model, that is equations (3) and (4), for the computation of the Cartesian coordinates X and Y of the 2-DoF manipulator robot. These results of X and Y are then putted together with the generated variables θ_1 and θ_2 to form hence the dataset in question. Such dataset has a size equal to $N = 1000$.

Adopted Training Optimizers for the FFBP-NNs

In the complex world of training neural networks, there are many optimization methods to tweak the inner workings of a model to get better at reducing errors. Within this realm, the tapestry of algorithms is rich, each weaving its own unique pattern in the grand design of optimization. Our work focuses on three of these distinguished algorithms, each bearing its own distinctive character and prowess.

Levenberg-Marquardt (LM) Optimizer: First, the Levenberg-Marquardt (LM) algorithm emerges as a stalwart choice (Ranganathan 2004). Emerging from the challenges of nonlinear least squares problems, this method utilizes a repetitive process of tweaking parameters. It skillfully estimates the Hessian matrix, which plays a crucial role in governing the shape of the error surface, and combines it with a stabilizing factor. This approach excels when dealing with relatively modest-sized networks, achieving rapid and captivating convergences.

Bayesian Regularization (BR) Optimizer: Delving deeper into the optimization domain, the Bayesian Regularization (BR) algorithm emerges as a prudent approach where the role of a Bayes theorem is crucial, steering the training process towards regularization (Kayri 2016). Endowed with prior knowledge concerning the model's parameters, it safeguards against the perilous pitfalls of overfitting. Pioneering a trail where prior probability distributions are important, the algorithm's objective is to unearth the posterior distribution that, with a predestined sense, maximizes the likelihood of the available data. This algorithm offers unwavering performance against noisy or scanty data.

Scaled Conjugate Gradient (SCG) Optimizer: The Scaled Conjugate Gradient (SCG) algorithm takes the stage as an efficient approach where it marries the concepts of conjugate gradients with adaptive step sizes (Møller 1993). The algorithm dynamically scales its step size according to the undulating contours of the error surface. In doing so, it navigates the rugged terrain of optimization with unparalleled grace, achieving swifter convergence. The algorithm's reputation precedes it, proving its mettle in the daunting task of handling large-scale networks. Its legacy lies in computational efficiency and an unwavering commitment to the cause of convergence.

Evaluation Metrics

MSE: In the context of our research, the MSE is used as a the main metric for assessing the accuracy of predictions of the adopted FFBP-NNs. Such metric is calculated using the following expression:

$$\mathrm{MSE} = \frac{1}{n}\sum_{i=1}^{n}(y_i - \hat{y}_i)^2 \tag{12}$$

where n is the number of observations, y_i represents the actual values, and $\hat{y}_i$ represents the predicted values. This equation quantifies the average squared difference between the actual and predicted values. The MSE is a valuable tool in evaluating the performance of predictive models. Such metric will be essentially used to compared between the performance of the different adopted artificial neural networks.

Coefficient of correlation R-value: Moreover, to evaluate the performance of the neural network models, we will use the regression metric, the coefficient of correlation R, called also as the coefficient of determination R^2. Such metric R is expressed and computed according to the following relation (del Rosario Martinez-Blanco *et al.* 2016):

$$\mathrm{R} = \frac{\sqrt{\sum_{i=1}^{n}(\hat{y}_i - \bar{y})^2}}{\sqrt{\sum_{i=1}^{n}(y_i - \bar{y})^2}} \tag{13}$$

where $\bar{y}$ stands for the mean of the actual values.

It is important to note that it is possible to use other metrics to measure the performance of the FFBP-NN models. Such metrics can be the Mean Absolute Error (MAE), the Root Mean Square Error (RMSE), the Mean Absolute Percentage Error (MAPE), the Relative Root Mean Squared Error (rRMSE), the Normalized Mean Square Error (NMSE), the Relative Mean Absolute Error (rMAE), the Mean Biased Error (MBE), the Mean Relative Error (MRE), just to mention a few (del Rosario Martinez-Blanco *et al.* 2016; Darba *et al.* 2022; Keleş *et al.* 2023). In this present work, only the MSE and the R-value are considered as two metrics to evaluate the performance of the FFBP-NN models in solving the inverse kinematics of the 2-DoF manipulator robot.

Solving Methodology of the FFBP-NNs Training Process

In pursuit of transparency and reproducibility, we adopted MATLAB as our primary software platform, harnessing a suite of specialized toolboxes to streamline implementation and experimentation. The Neural Network Toolbox (NNT) within MATLAB played a pivotal role in this pursuit, offering crucial functionalities for the design, training, and simulation of neural networks. The NNT in MATLAB is a versatile collection of tools tailored for a spectrum of applications, ranging from pattern recognition to time-series prediction. Noteworthy features include its support for diverse neural network architectures, encompassing feedforward networks, radial basis networks, and self-organizing maps. The toolbox empowers users to define network structures with ease, specifying layers, nodes, and activation functions. MATLAB's NNT further stands out with its array of training algorithms, including Levenberg Marquardt and Bayesian regularization, allowing us to fine-tune parameters for optimal results. Moreover, its graphical tools facilitate the visualization of neural network architectures, enabling us to analyze performance through plots and confusion matrices.

In this work, and in order to solve the inverse kinematics of the 2-DoF manipulator robot using ANNs models, we followed some specific steps. The flowchart of Figure 5 reveals these different and specific steps followed to train the adopted FFBP-NNs using the proposed datasets arriving to the final step, which is the displaying of simulation results by plotting the MSE, the regression curves and the error histograms.

Hyperparameters for the Training Process

Table 2 reveals the different parameters and hyperparameters used for the training of the proposed FFBP-NNs and their values. For each set of (hyper-)parameters, the training process is executed according to the flowchart presented in Figure 5. The adopted FFBP-NN models are illustrated in Figure 3, where we used an architecture composed of 1, or 2, or 3, or 4, or 5 hidden layers. For each hidden layer, it corresponds the number of neurons.

In this work, two kinds of the activation function have been considered in the training phase: (1) the hyperbolic tangent sigmoid transfer function (tansig) used for all hidden layers, and (2) the linear transfer function (purelin) for the output layer (see (Keleş *et al.* 2023) for for further details about these two activation

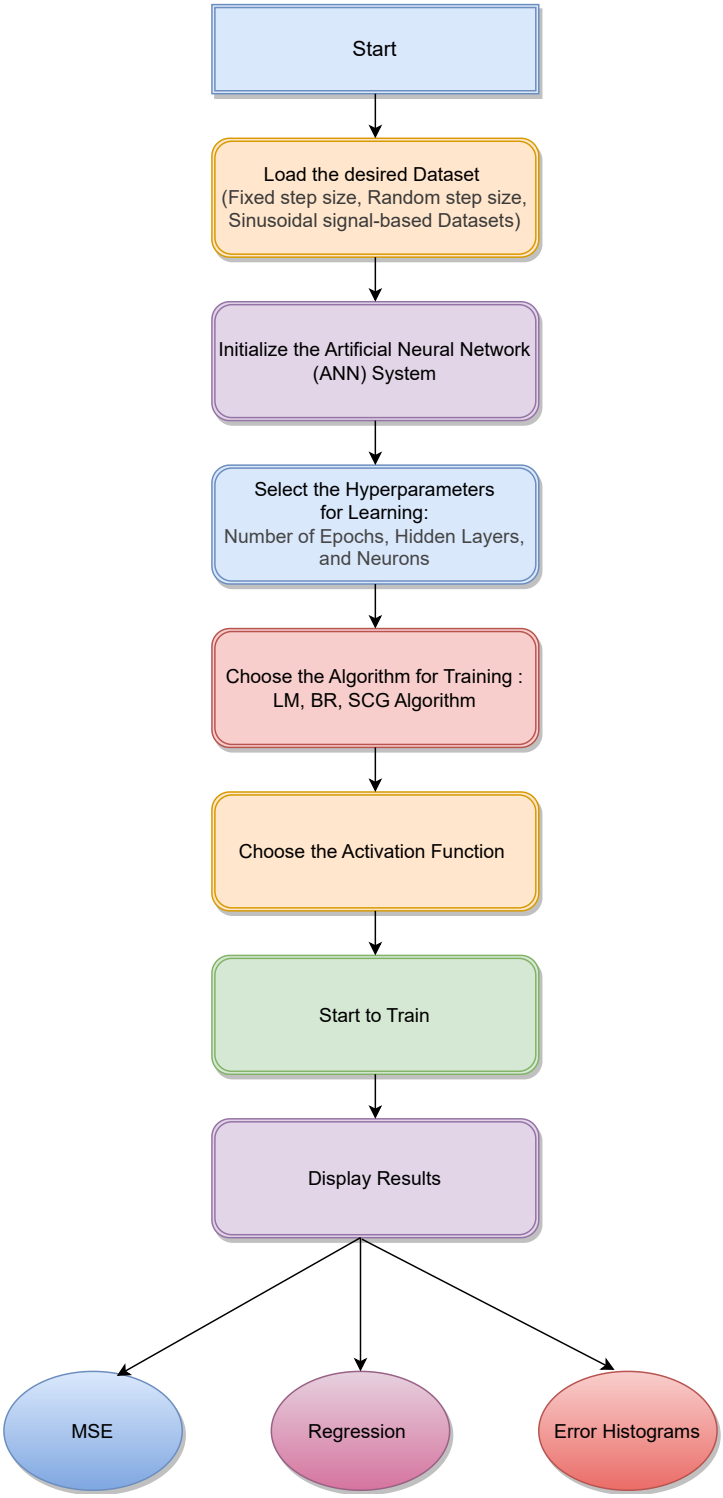

Figure 5 Flowchart describing the procedure for training the FFBP-NN and displaying graphical results.

Table 2 Parameters/hyperparameters, and their adopted values, used for the training process of the proposed FFBP-NNs.

Parameter	Value
Number of inputs	2
Number of outputs	2
Number of hidden layers (NbHLs)	1 or 2 or 3 or 4 or 5
Number of neurons for each layer (NbNs)	NbHLs: 1 — NbNs: 10 NbHLs: 2 — NbNs: 10, 20 NbHLs: 3 — NbNs: 10, 20, 5 NbHLs: 4 — NbNs: 10, 20, 10, 5 NbHLs: 5 — NbNs: 10, 20, 10, 5, 2
Activation function of the hidden layers	tansig
Activation function of the output layer	purelin
Optimizer	LM or BR or SCG
Maximum validation failures	50
Minimum gradient	10^{-6}
Training goal	10^{-6}
Maximum number of epochs	1000

functions). Although it is possible to select the activation function tansig for the output layer; however, no clear enhancement of the results has been observed.

Remark 1. *It is worth to note that in the present work, we have adopted five different architectures of the FFBP-NN, as seen in Figure 3. For each model, we increased the number of the hidden layer, for which the first model has only one hidden layer, whereas the last and fifth one has five hidden layers. However, the number of neurons for each hidden layer is entirely arbitrary. Actually, we tried with other possibilities of the number of neurons, but we have not observed a clear difference in the MSE results. Moreover, the type of the activation functions for the hidden layers and the output layer is fixed for all models. As noted previously, by selecting a tansig activation function for the output layer, we have not noted a clear difference in the simulation results.*

RESULTS AND DISCUSSIONS

In this section, we will show some simulation results of the training of the adopted FFBP-NN architectures using the three optimizers: the Levenberg-Marquardt (LM) optimizer, the Bayesian Regularization (BR) optimizer, and the Scaled Conjugate Gradient (SCG) optimizer. Moreover, the values of the different hyperparameters, along with these optimizers, are given in Table 2. As noted previously, the MSE will be used as the main metric for the evaluation of the performance of the training process and hence of the FFBP-NN models illustrated in Figure 3.

Feed-Forward Back-Propagation Neural Network with the Levenberg-Marquardt (LM) Algorithm

When assessing the training performance of the FFBP-NN using the LM optimization algorithm across a diverse range of datasets – fixed, random, and sinusoidal – it becomes evident that their performance exhibits relatively significant variations. The outcomes of these experiments are visually presented in Figure 6.

In the case of the fixed-step-size dataset, the FFBP-NN model demonstrated its most favorable validation MSE of 2.3255, achieving this at the 116th epoch. This specific neural architecture comprised one hidden layer with 10 neurons. In contrast, when the FFBP-NN model was trained using the random-step-size dataset, its highest validation MSE of 2.2345 was observed at the 75th epoch. The FFBP-NN architecture featured four hidden layers with (10, 20, 5, 2) neurons in this scenario. Lastly, when the FFBP-NN model was trained with a sinusoidal-signal-based dataset, it yielded the best validation MSE of 2.4656 at the 41st epoch. Similarly, this model employed a neural architecture with four hidden layers having (10, 20, 5, 2) neurons, as detailed in the accompanying Table 3.

Comparing these results, it is evident that the FFBP-NN model's performance varies significantly depending on the nature of the dataset used for training. When trained on a dataset with random step-size values, the model demonstrated its best performance regarding the lowest validation MSE. This indicates its ability to generalize and adapt to the irregular patterns within the random dataset. However, when exposed to a dataset based on sinusoidal signals, the performance of the FFBP-NN model declined, as shown by a significantly higher validation MSE. This observation suggests that the model faced difficulties in effectively capturing the complex and oscillatory nature of the sinusoidal data. In contrast, when the model was trained on a dataset with a fixed step size, it exhibited an even higher validation MSE. This indicates that the FFBP-NN model excelled at capturing the inherent patterns within this specific data distribution.

The neural architecture used in these experiments consistently had two hidden layers with varying neuron configurations, except for the sinusoidal dataset, which had four hidden layers. This architectural difference didn't have a straightforward correlation with model performance, as seen in the varying MSE values across the three different datasets. Therefore, the dataset choice significantly impacts the model performance more than the specific neural architecture.

When training an FFBP-NN model in MATLAB for regression, it is common to split the dataset into three subsets: training, validation, and test. The training set is the largest and forms the foundation for model development, involving weight and bias adjustments based on prediction errors and a chosen regression loss function like MSE. The validation set, smaller in size, is used to evaluate the model's performance during training, helping to identify overfitting or underfitting and compute key regression metrics, including MSE. Finally, the test set, a distinct data subset untouched during training or parameter adjustments, rigorously evaluates the model's performance. It tests the model on unseen data, calculating regression metrics to assess its ability to make precise predictions. By dividing data into training, validation, and test sets, an evaluation framework is created to select the best model based on validation performance and provide an unbiased, comprehensive evaluation of the test set for overall efficacy.

The results obtained for regression are graphically represented in Figure 7. The first dataset, using a fixed step size, had regression coefficients of $R = 0.53114$ (training), $R = 0.54541$ (validation), and $R = 0.52057$ (testing), resulting in an overall $R = 0.53171$. In the second dataset with random step sizes, we obtained $R = 0.57484$ (training), $R = 0.55223$ (validation), and $R = 0.55394$ (testing), leading to an overall R of 0.56834. The third dataset, with a sinusoidal signal, performed the best values, with $R = 0.73744$ (training), $R = 0.72915$ (validation), and $R = 0.67531$ (testing), resulting in an overall regression coefficient $R = 0.72444$. These results underscore the importance of tailoring the regression approach to the specific characteristics of each dataset. While the fixed step size and random step size datasets yielded distinct regression coefficients, the sinusoidal-signal-based dataset displayed the highest overall R values, highlighting the adaptability and efficacy of the FFBP-NN with the LM algorithm in handling diverse data types.

The comparative analysis of estimated joint angles from the system output and the FFBP-NN model is shown in Figure 8. We observe a remarkable congruence between the system outputs and the FFBP-NN model outputs in the first set of plots, representing the lowest MSE scenario with a random dataset. The blue and cyan lines represent the system and FFBP-NN model's outputs that appear nearly superimposed, indicating that the model accurately captures the underlying patterns in the random data. This suggests the model's performance is relatively acceptable in a scenario where the data is relatively unstructured and lacks a clear pattern. However, a different picture emerges in the second set of plots depicting the highest MSE with a sinusoidal dataset. Here, the system outputs (in blue) follow a distinct sinusoidal pattern, while the FFBP-NN model's outputs (in cyan) exhibit significant deviations. The model seems to struggle to accurately capture the cyclical nature of the sinusoidal data, resulting in a noticeable discrepancy between the two lines. This highlights the challenges that an FFBP-NN model may encounter when dealing with datasets characterized by complex, periodic, or oscillatory behaviors.

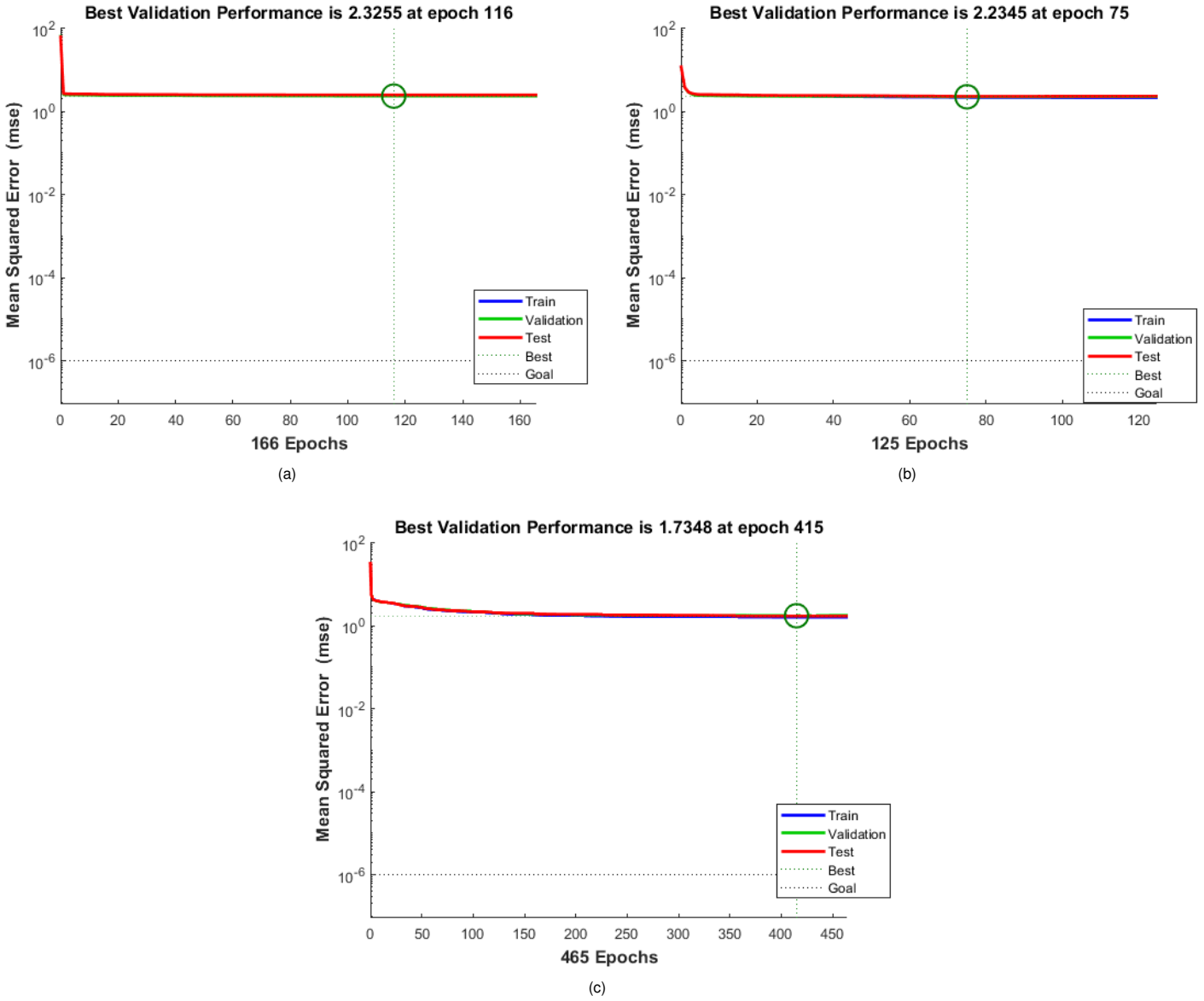

Figure 6 Lowest MSEs obtained with the LM algorithm and for the three different datasets: (a) Lowest MSE (Fixed Dataset, 1 hidden layer), (b) Lowest MSE (Random Dataset, 4 hidden layers), and (c) Lowest MSE (Sinusoidal Dataset, 4 hidden layers).

Table 3 Results of training with the LM algorithm for the three different proposed datasets.

Number of hidden layers (number of neurons in each layer)	FIXED dataset	RANDOM dataset	SINUSOIDAL dataset
1 Hidden layer (10)	MSE: 2.3255 Epoch: 116	MSE: 2.2996 Epoch: 49	MSE: 3.6382 Epoch: 84
2 Hidden layers (10,2)	MSE: 2.3771 Epoch: 43	MSE: 2.2836 Epoch: 192	MSE: 3.1784 Epoch: 243
3 Hidden layers (10,20,2)	MSE: 2.4669 Epoch: 49	MSE:2.2813 Epoch: 78	MSE: 3.1859 Epoch: 29
4 Hidden layers (10,20,5,2)	MSE: 2.501 Epoch: 57	MSE: 2.2345 Epoch: 75	MSE: 2.4517 Epoch: 53
5 Hidden layers (10,20,10,5,2)	MSE: 2.5121 Epoch: 19	MSE: 2.3068 Epoch: 63	MSE: 2.9133 Epoch: 39

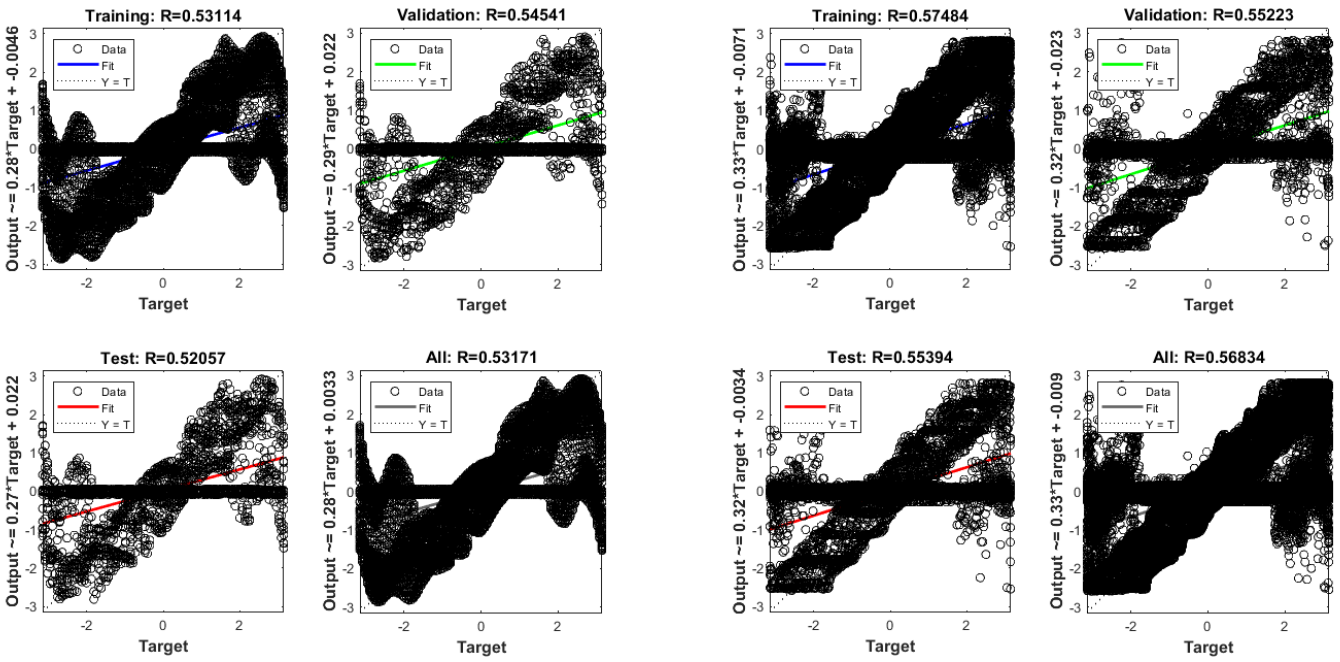

(a) (b)

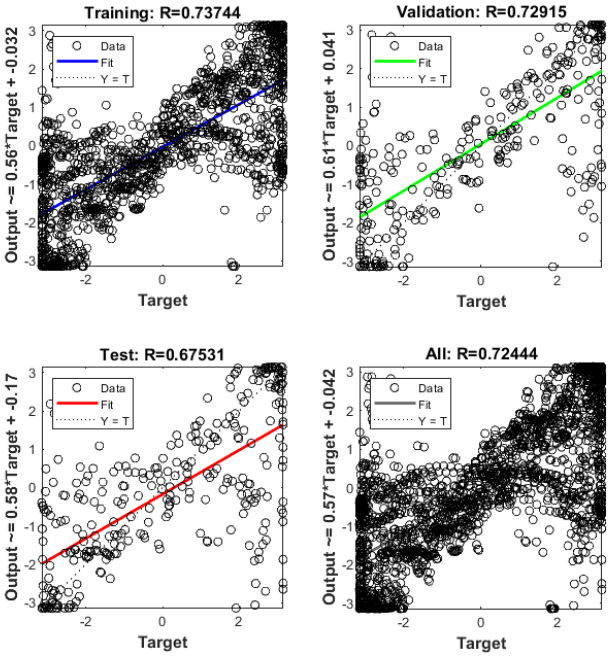

(c)

Figure 7 Regression results obtained by means of the LM algorithm and with the three proposed datasets: (a) Regression (Fixed Dataset, 1 hidden layer), (b) Regression (Random Dataset, 4 hidden layers), and (c) Regression (Sinusoidal Dataset, 4 hidden layers).

Feed-Forward Back-Propagation Neural Network with the Bayesian Regularization (BR) Algorithm

In the subsequent phase of our research, we examined the performance of the FFBP-NN, which had undergone training using the BR algorithm. This analysis encompassed an exploration of various datasets, including those of a fixed, random, and sinusoidal nature. The outcomes of this investigation illuminated pronounced variations in the network's performance, as visually represented in

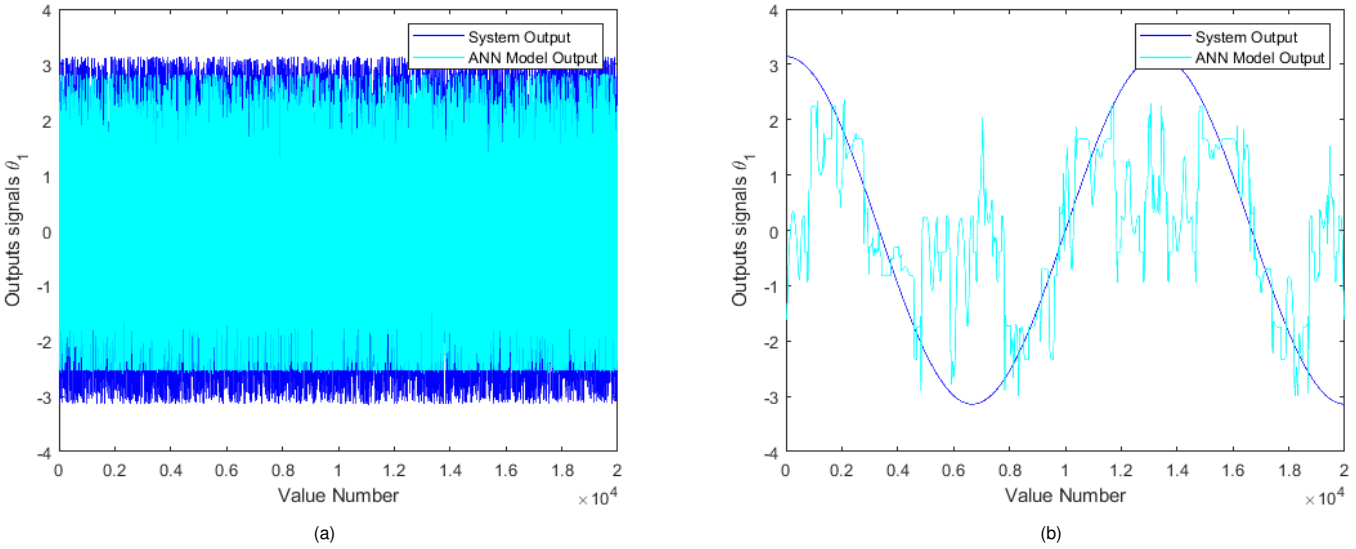

Figure 8 Comparative analysis of actual and estimated outputs obtained by means of the LM Algorithm: (a) Lowest MSE (Random Dataset, 4 hidden layers), and (b) Highest MSE (Sinusoidal Dataset, 1 hidden layer).

Figure 9. Notably, when the FFBP-NN underwent training on the fixed dataset, a remarkable achievement was observed, with the network achieving its most favorable MSE of 2.3348, a milestone reached precisely at epoch 37. The architectural configuration of this particular model featured three hidden layers with neuron configurations specified as (10, 20, 2). This outcome clearly demonstrated the BR algorithm's exceptional effectiveness in curbing overfitting tendencies and reinforcing the network's aptitude for generalization, resulting in notably proficient training outcomes when dealing with the fixed dataset. In a distinct vein, a different set of findings emerged when the FFBP-NN was subjected to training with random data. Specifically, it achieved its lowest recorded MSE, amounting to 2.1682, a noteworthy accomplishment at epoch 68. The architectural blueprint for this particular model diverged from the previous one, featuring a configuration of four hidden layers. This divergence in the network's architecture hinted at its adaptability and robustness, particularly in the face of more erratic and unpredictable data distributions, as with random data. Furthermore, our exploration extended to the training of the FFBP-NN on sinusoidal data. This endeavor yielded an MSE of 2.4632, attained at epoch 79. The architectural design for this specific scenario encompasses four hidden layers.

Our comprehensive comparison of these results underscores the multifaceted nature of the BR algorithm's impact on the FFBP-NN performance, as shown in Table 4. It facilitates the network's generalization and efficacy across various datasets with varying characteristics. The fixed dataset showcases the algorithm's proficiency in handling stable and non-random data patterns, whereas the random dataset demonstrates the network's adaptability to more unpredictable and erratic data distributions. Finally, the sinusoidal dataset reflects the algorithm's capability to address cyclical and periodic patterns, albeit with slightly lower performance than the fixed and random datasets. This nuanced understanding of the algorithm's behavior provides valuable insights for practitioners seeking to optimize neural network training across diverse datasets, emphasizing the significance of tailoring the approach to the specific data context.

When delving into the analysis of regression results for the BR algorithm, it becomes apparent that the primary focus lies on identifying the most optimal MSE value, particularly in the context of random data. The MSE is a pivotal metric in regression tasks, which is a crucial indicator of the model's accuracy in predicting target values. In the case of the BR algorithm, achieving the best possible MSE for random data sets a profound benchmark for the algorithm's performance. The consistent trend toward an MSE value close to 1 underscores the algorithm's capacity to minimize prediction errors and enhance the precision of its forecasts, as shown in Figure 10. Results showed promising performance in one experiment involving fixed step size data for training a three-layer FFBP-NN. The regression coefficient (R) during training reached the value 0.55022, indicating effective learning from the dataset. Validation yielded an R-value of 0.54578, demonstrating the network's generalization ability. Testing produced an R-value of 0.54834, reinforcing the model's real-world applicability. The overall R-value was 0.54922, indicating stability and accuracy in diverse scenarios. The results remained strong in a separate experiment using datasets with random step sizes and a four-layer neural network. The training phase achieved the R-value of 0.56858, showing adaptability to erratic data. Validation maintained high performance with an R of 0.57789. Testing, slightly lower at $R = 0.55223$, still offered reliability for practical use. The overall R-value was 0.56759, highlighting robustness even with challenging data. For a third dataset characterized by sinusoidal patterns, the FFBP-NN excelled. Training achieved an exceptional R of 0.70922, showing the model's ability to capture intricate patterns. Validation and testing displayed strong R-values (0.70532 and 0.70213), confirming suitability for sinusoidal data in real-world scenarios. The overall R-value of 0.70756 affirmed the network's robustness with complex, signal-based datasets.

In our training process, and as shown in Figure 11, we will delve deeper into the insights gained from our neural network model, using the BR algorithm. We will examine two distinct scenarios, each showcasing unique characteristics. In the first set of visual representations, we explore the domain of the lowest MSE. Here,

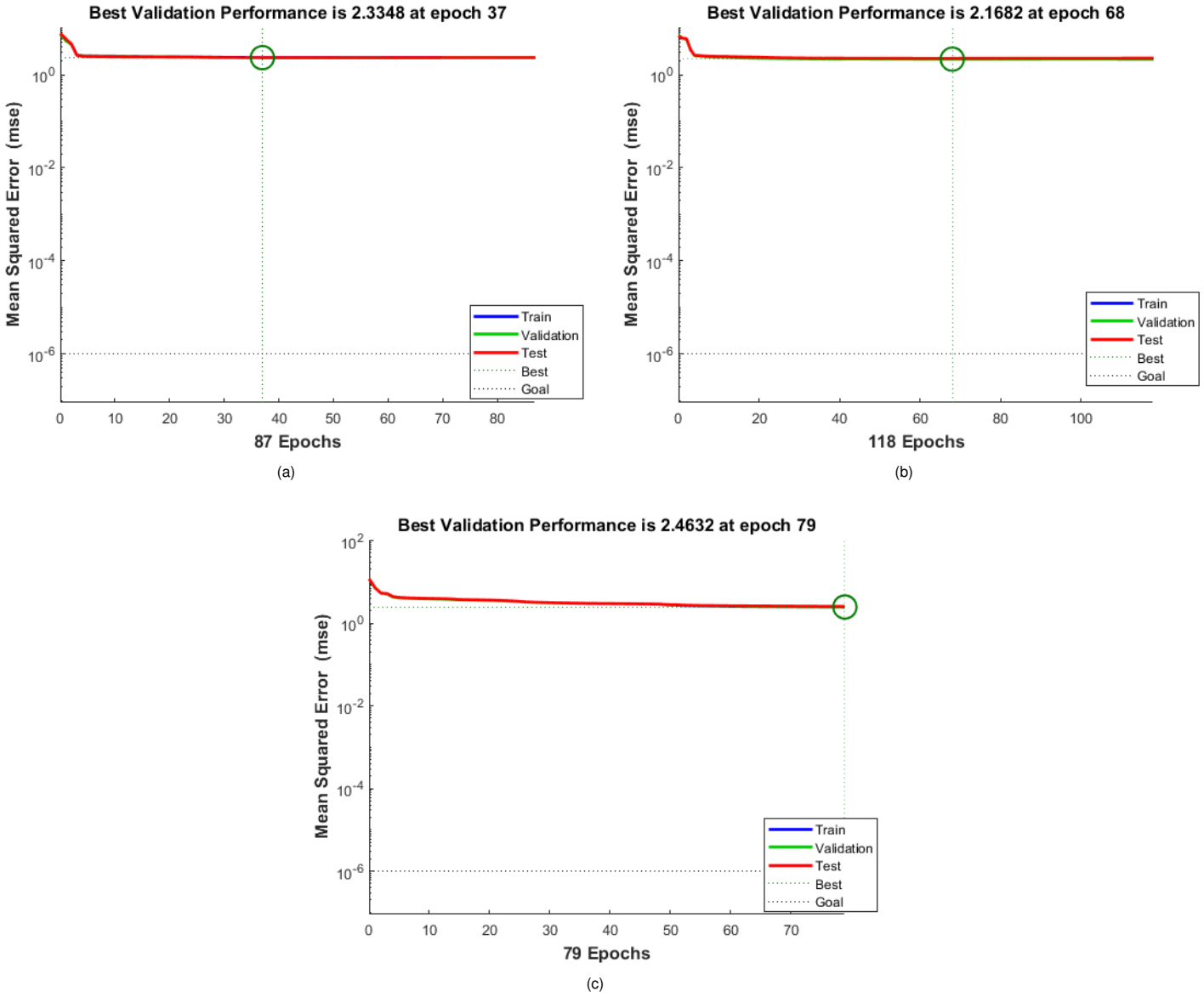

Figure 9 Lowest MSEs obtained using the BR algorithm and for the three generated datasets: (a) Lowest MSE (Fixed Dataset, 3 hidden layers), (b) Lowest MSE (Random Dataset, 4 hidden layers), and (c) Lowest MSE (Sinusoidal Dataset, 4 hidden layers).

Table 4 Results of training obtained with the BR algorithm for the three proposed different datasets.

Number of hidden layers (number of neurons in each layer)	FIXED dataset	RANDOM dataset	SINUSOIDAL dataset
1 Hidden layer (10)	MSE: 2.460 Epoch: 515	MSE: 2.3009 Epoch: 90	MSE: 3.4353 Epoch: 45
2 Hidden layers (10,2)	MSE: 2.4824 Epoch: 33	MSE: 2.1895 Epoch: 308	MSE: 3.1628 Epoch: 152
3 Hidden layers (10,20,2)	MSE: 2.3348 Epoch: 101	MSE: 2.2516 Epoch: 52	MSE: 2.7771 Epoch: 106
4 Hidden layers (10,20,5,2)	MSE: 2.3915 Epoch: 125	MSE: 2.1682 Epoch: 68	MSE: 2.4632 Epoch: 79
5 Hidden layers (10,20,10,5,2)	MSE: 2.4865 Epoch: 88	MSE: 2.3547 Epoch: 33	MSE: 2.8119 Epoch: 41

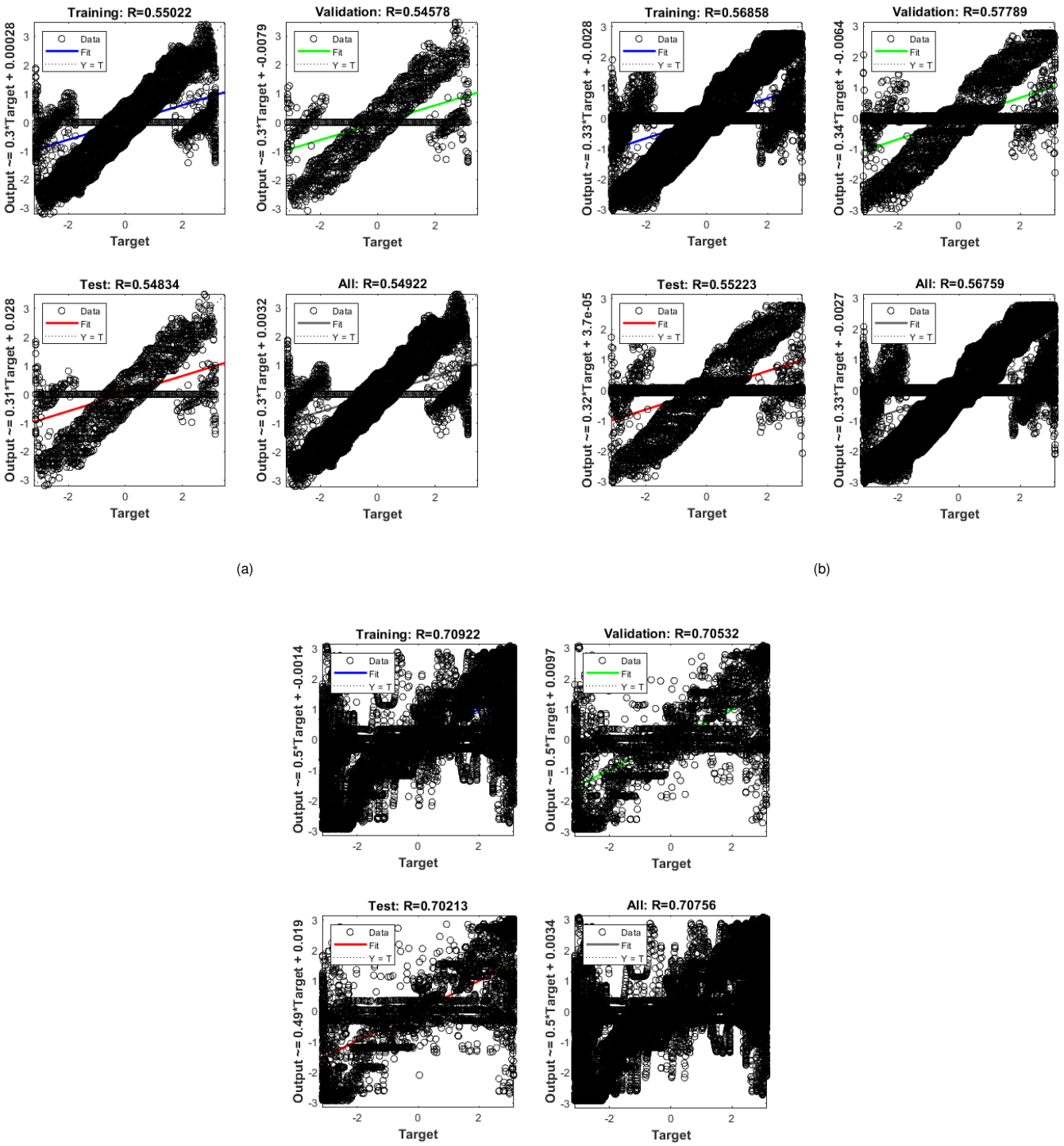

Figure 10 Regression results obtained with the BR algorithm and for the three distinct datasets: (a) Regression (Fixed Dataset, 3 hidden layers), (b) Regression (Random Dataset, 4 hidden layers), and (c) Regression (Sinusoidal Dataset, 4 hidden layers).

our neural network confronts a random dataset. It is immediately evident that there is a remarkable alignment between the system's outputs and the FFBP-NN model's outputs. The blue and cyan lines, representing the outputs, are almost identical, highlighting the model's proficiency in capturing the underlying complexity of the random data. This strong correspondence underscores the model's exceptional performance, especially when data lacks a clear structure or recognizable patterns. On the other hand, we

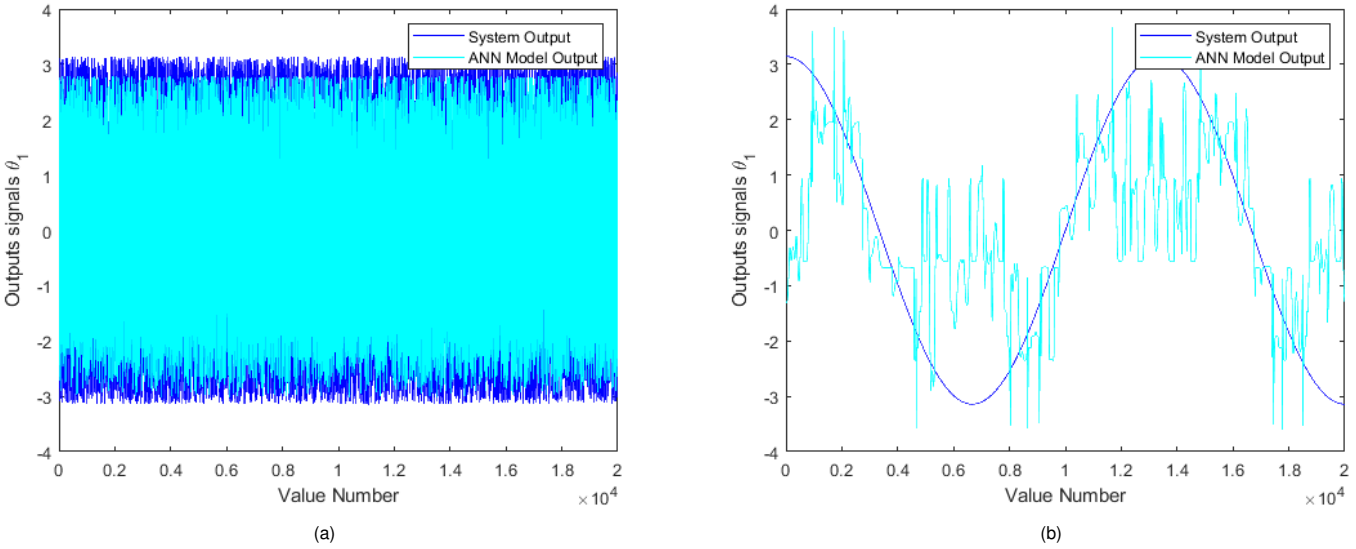

Figure 11 Comparative analysis of actual and estimated outputs obtained with the BR Algorithm and for two different datasets and for two different structures of the FFBP-NN model: (a) Lowest MSE (Random Dataset, 4 hidden layers), and (b) Highest MSE (Sinusoidal Dataset, 1 hidden layer).

shift our focus to the second set of visualizations, where we face the challenges of the highest MSE. In this case, our FFBP-NN model deals with a sinusoidal dataset. Here, the system's outputs, illustrated by the blue curve, gracefully follow the sinusoidal pattern, while the FFBP-NN model's outputs, depicted in cyan, exhibit noticeable deviations. It becomes apparent that the FFBP-NN model struggles to accurately replicate the cyclic nature inherent in sinusoidal data, resulting in significant disparities between the two curves.

Feed-Forward Back-Propagation Neural Network with the Scaled Conjugate Gradient (SCG) Algorithm

The SCG algorithm is highly regarded for its remarkable convergence rate and capability to effectively address intricate optimization challenges. In our investigation, we conducted a comparative analysis of training the FFBP-NN model using the SCG algorithm across different datasets: fixed, random, and sinusoidal. The outcomes exhibited notable variations in their performance, as depicted in Table 5. Specifically, when employing the SCG algorithm with the fixed data, the FFBP-NN model achieved its most favorable MSE of 2.4327 at the 130th epoch. The architectural configuration of this model comprised two hidden layers with respective neuron arrangements of (10, 2). Conversely, training the FFBP-NN model using random data yielded the best MSE of 2.2804 at the 463rd epoch, with a simpler model architecture consisting of 3 hidden layers configured as (10, 20, 2). Additionally, we conducted training on sinusoidal data, resulting in the FFBP-NN model achieving its lowest MSE of 2.4054 at the 835th epoch. The model architecture employed in this scenario also featured four hidden layers, as detailed in Figure 12. Some key observations emerge when comparing the FFBP-NN model's performance with the SCG algorithm across three datasets. The SCG algorithm excelled in optimizing performance on the fixed dataset, achieving a low MSE of 2.4327 at epoch 130, indicating its suitability for well-defined data. Conversely, on the random dataset, while still benefiting from SCG, it reached the lowest MSE of 2.2804 at epoch 463, indicating the challenge of adapting to random data. The SCG algorithm took longer for sinusoidal data to achieve its best MSE of 2.4054 at epoch 835, showing adaptability to different data types with consistent model architecture.

In summary, the SCG algorithm's efficacy in optimization tasks is underscored by its convergence rate, yet its performance is contingent on the characteristics of the dataset. It excels in scenarios with clear data patterns, such as fixed data, while it may require more time and iterations to converge on datasets with randomness or complex patterns, like random and sinusoidal data. Therefore, selecting the appropriate optimization algorithm and model architecture should be a deliberate decision based on the specific characteristics of the dataset and the desired outcomes.

In training FFBP-NN with the SCG algorithm, we conducted regression tasks on three distinct datasets to optimize the MSE. These experiments involved fixing the step size data and utilizing two hidden layers. The results of the first dataset revealed regression coefficients as follows: an R-value of 0.49759 for the training set, an R-value of 0.5263 for the validation set, an R-value of 0.49396 for the test set, and an overall R-value of 0.50141. In the second dataset, we focused on minimizing the MSE using random step size data and expanding to three hidden layers. The corresponding regression statistics were found to be an R-value of 0.55522 for the training set, an R-value of 0.55847 for the validation set, an R-value of 0.55722 for the test set, and an overall R-value of 0.55599. Lastly, when dealing with a dataset based on a sinusoidal signal, the aim was again to minimize the MSE. The regression results for this dataset included an R-value of 0.72855 for the training set, an R-value of 0.7177 for the validation set, an R-value of 0.72493 for the test set, and an overall R-value of 0.72638. These distinct regression analyses shed light on the varying performance of the FFBP-NN trained with the SCG algorithm across different datasets, step sizes, and hidden layer configurations, offering valuable insights for further optimization and model selection, as shown in Figure 13.

A comparative examination was conducted to assess the actual

Table 5 Results obtained after training different FFBP-NN models with the SCG algorithm and for the three different datasets.

Number of hidden layers (number of neurons in each layer)	FIXED dataset	RANDOM dataset	SINUSOIDAL dataset
1 Hidden layer (10)	MSE: 2.5814 Epoch: 158	MSE: 2.4924 Epoch: 90	MSE: 3.7088 Epoch: 537
2 Hidden layers (10,2)	MSE: 2.4327 Epoch: 130	MSE: 2.3492 Epoch: 407	MSE: 3.6975 Epoch: 606
3 Hidden layers (10,20,2)	MSE: 2.5152 Epoch: 188	MSE: 2.2804 Epoch: 463	MSE: 2.6966 Epoch: 998
4 Hidden layers (10,20,5,2)	MSE: 2.4944 Epoch: 269	MSE: 2.2983 Epoch: 213	MSE: 2.4054 Epoch: 835
5 Hidden layers (10,20,10,5,2)	MSE: 2.4609 Epoch: 146	MSE: 2.349 Epoch: 577	MSE: 3.4659 Epoch: 384

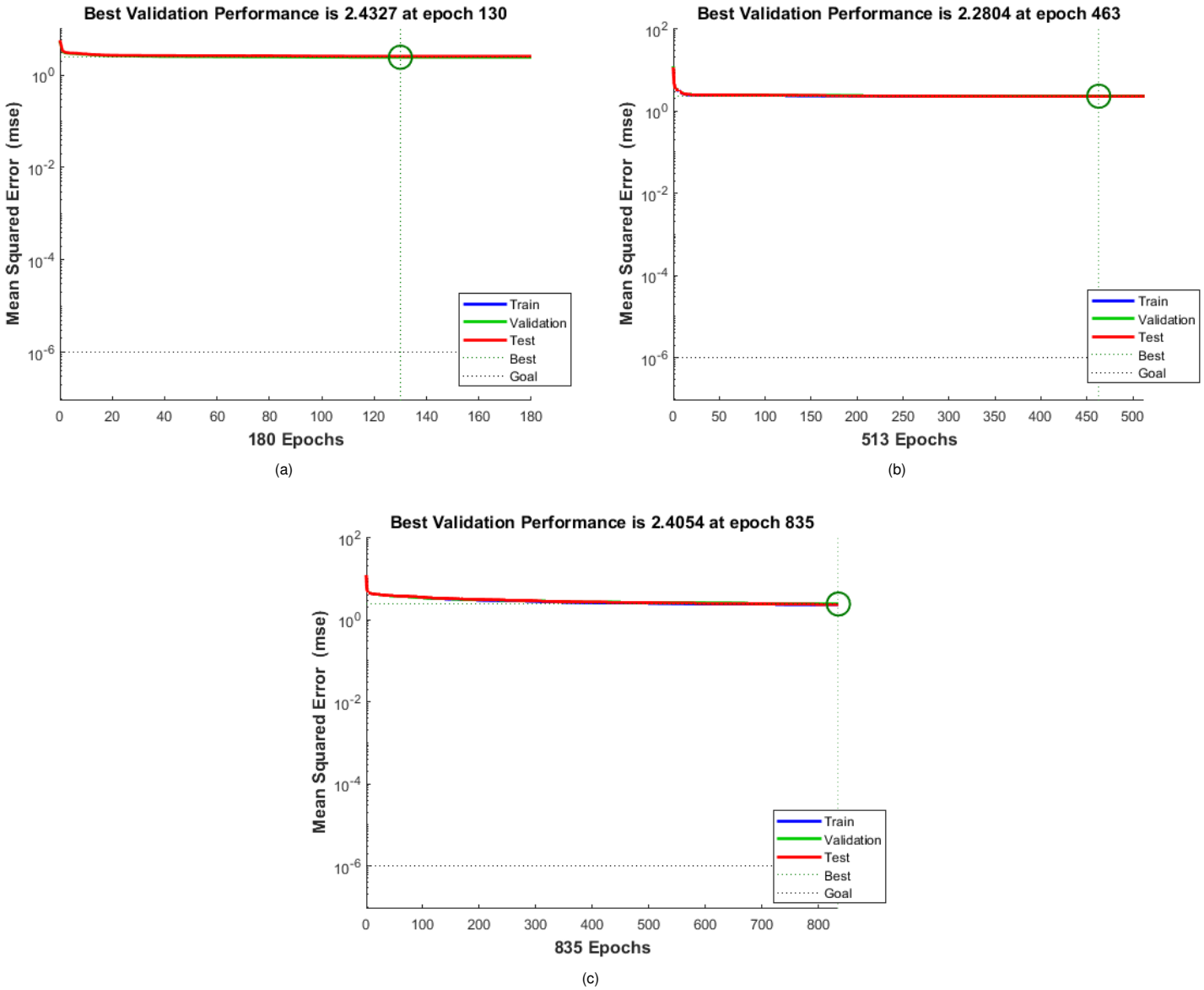

Figure 12 Lowest MSEs obtained by training the FFBP-NN models with the SCG algorithm and for the three different datasets: (a) Lowest MSE (Fixed Dataset, 2 hidden layers), (b) Lowest MSE (Random Dataset, 3 hidden layers), and (c) Lowest MSE (Sinusoidal Dataset, 4 hidden layers).

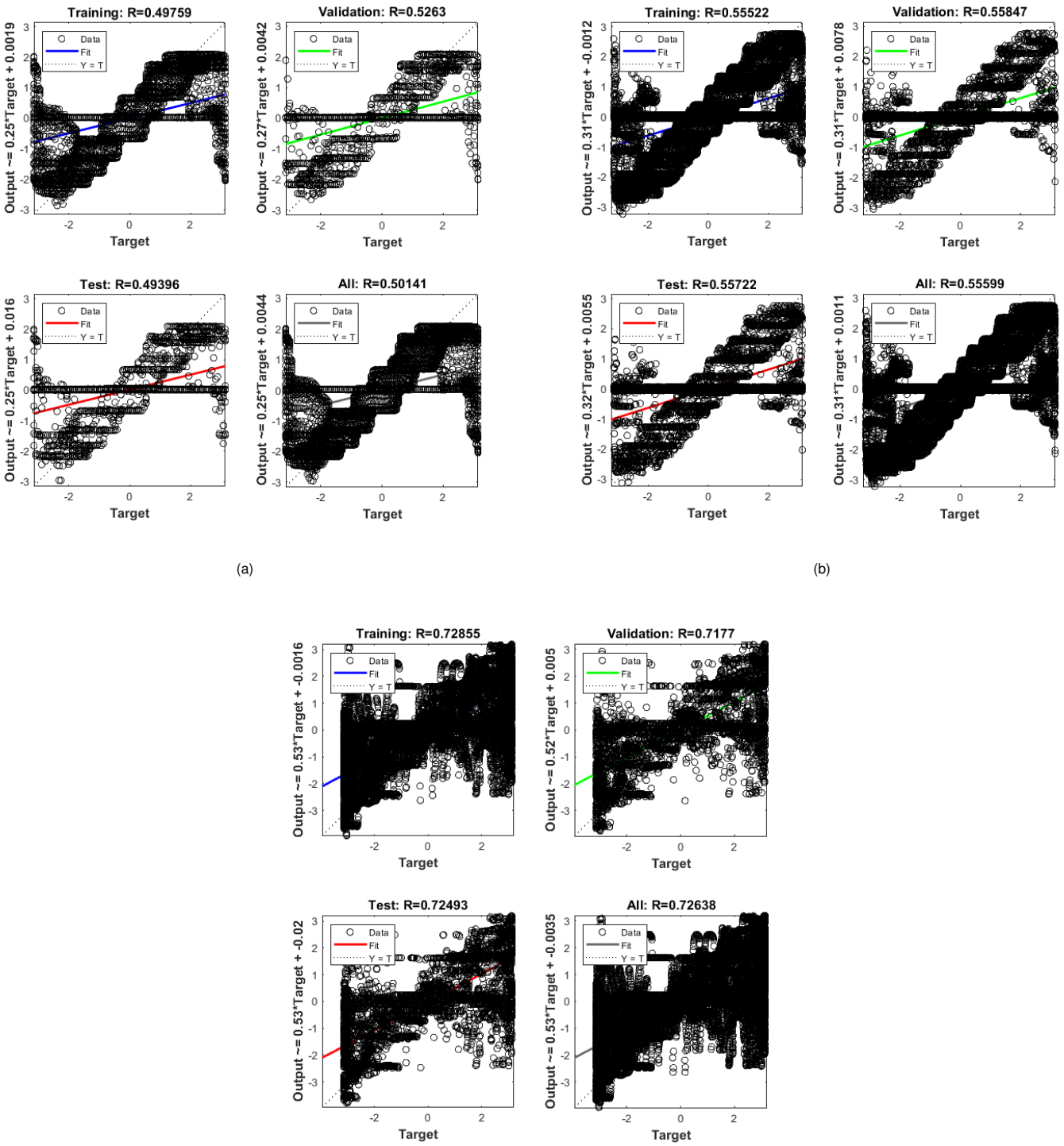

Figure 13 Regression results of some proposed FFBP-NN models obtained with the SCG algorithm and for the three different datasets: (a) Regression (Fixed Dataset, 2 hidden layers), (b) Regression (Random Dataset, 3 hidden layers), and (c) Regression (Sinusoidal Dataset, 4 hidden layers).

and predicted results produced by the SCG Algorithm using two different datasets. When employing the SCG algorithm, it became evident that our neural network excelled when dealing with random data. However, it faced difficulties in accurately reproducing sinusoidal patterns. The analysis comparing the estimated joint angles between the system output and the FFBP-NN model is illus-

trated in Figure 14. In the first series of plots, which represents the scenario with the lowest MSE using a random dataset, a striking similarity is observed between the outputs of the system and the FFBP-NN model. The blue and cyan lines, representing the system and FFBP-NN model outputs, closely overlap, indicating that the model effectively captures the underlying patterns within the random data. This suggests the model performs reasonably well when the data lacks a clear structure and is relatively unorganized. Conversely, a different story unfolds in the second series of plots depicting the scenario with the highest MSE using a sinusoidal dataset. In this case, the system outputs (depicted in blue) follow a clear sinusoidal pattern, while the FFBP-NN model's outputs (depicted in cyan) exhibit noticeable deviations. The model appears to encounter challenges in accurately replicating the cyclical nature of sinusoidal data, resulting in a significant disparity between the two lines. This emphasizes the difficulties of an FFBP-NN model when confronted with datasets characterized by intricate, periodic, or oscillatory behaviors.

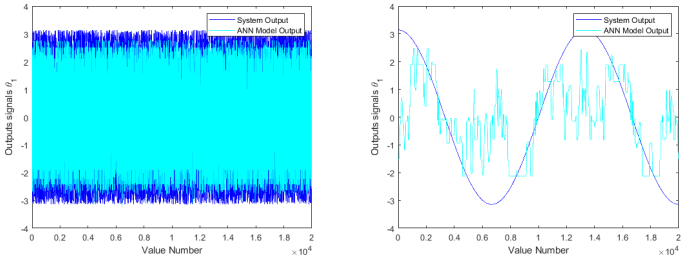

Figure 14 Comparative analysis of actual and estimated outputs obtained with the SCG Algorithm and using two different datasets: (a) Lowest MSE (Random Dataset, 3 hidden layers), and (b) Highest MSE (Sinusoidal Dataset, 1 hidden layer).

CONCLUSION

In conclusion, our work presented a contribution in the fields of robotics and automation through the development and implementation of various Feed-Forward Back-Propagation Neural Network (FFBP-NN) algorithms for the computation of the inverse kinematics of a 2-DoF manipulator robot. A pivotal aspect of our research involves an in-depth exploration of these algorithms, coupled with rigorous experimentation and evaluations to discern their performance characteristics.

We mainly used the MSE metric to evaluate the performance of the different proposed neural network architectures. Based on such metric, our findings highlighted the substantial impact of training with Levenberg-Marquardt (LM) and Bayesian Regularization (BR) algorithms, particularly noting that the optimal results (that correspond to the lowest MSEs) were achieved when trained with random-step-size datasets in the context of a four-hidden-layer configuration. Similarly, for the Scaled Conjugate Gradient (SCG) algorithm, we observed the best outcomes (lowest MSE) when employing random-step-size datasets in a three-hidden-layer setting. This nuanced understanding of algorithmic behavior provides valuable insights for practitioners. Most notably, our work achieves a remarkable milestone by applying FFBP-NN models to address inverse kinematics problems with an unprecedented level of precision and reliability, surpassing the capabilities of traditional methods. These outcomes underscore the transformative potential of FFBP-NN models in tackling complex problems within the realm of robotics.

In future works, it is essential to expand the applicability of the proposed FFBP-NN models by testing them on manipulator robots with greater degrees of freedom, such as SCARA or 6-DoF industrial robots. This evaluation will assess the scalability and adaptability of the FFBP-NN models across diverse robotic platforms.

Furthermore, in order to improve the selection phase of the hyperparameters of the FFBP-NN, the idea is to integrate the metaheuristic optimization algorithms within the training process in order to find the optimal architecture to provide the best accuracy or the lowest MSE. In addition, the objective is to explore and utilize more advanced ANN architectures, such as Recurrent Neural Networks (RNNs) and Convolutional Neural Networks (CNNs), for the modeling of the inverse kinematics of manipulator robots. This exploration can significantly enhance the capabilities of the training process and prediction when operating with a complex structure of the robot and also with a high number of degrees of freedom and then for redundant manipulator robots.

Moreover, the current work can be extended and applied to the control part of manipulator robots using some nonlinear control approaches as those proposed in (Jenhani *et al.* 2022) for the position control of robotic systems, as well as for particular applications like in medical robotics such as exoskeleton systems for pediatric gaits (Narayan *et al.* 2018, 2023).

Availability of data and material

The data used to support the findings of the study are included within the article.

Conflicts of interest

The authors declare that there is no conflict of interest regarding the publication of this paper.

Ethical standard

The authors have no relevant financial or non-financial interests to disclose.

LITERATURE CITED

Abbas, M., J. Narayan, and S. K. Dwivedy, 2019 Simulation analysis for trajectory tracking control of 5-DOFs robotic arm using ANFIS approach. In *2019 5th International Conference On Computing, Communication, Control And Automation (ICCUBEA)*, pp. 1–6.

Aravinddhakshan, S., S. Apte, and S. M. Akash, 2021 Neural network based inverse kinematic solution of a 5 DOF manipulator for industrial application. Journal of Physics: Conference Series **1969**: 012010.

Aysal, F. E., İ. Çelik, E. Cengiz, and Y. Oğuz, 2023 A comparison of multi-layer perceptron and inverse kinematic for RRR robotic arm. Politeknik Dergisi pp. 1–1.

Becerra, G. and R. Kremer, 2011 Ambient intelligent environments and environmental decisions via agent-based systems. Journal of Ambient Intelligence and Humanized Computing **2**: 185–200.

Benavente-Peces, C., A. Ahrens, and J. Filipe, 2014 Advances in technologies and techniques for ambient intelligence.

Bouzid, R., J. Narayan, and H. Gritli, 2023 Feedforward backpropagation artificial neural network for modeling the forward kinematics of a robotic manipulator. In *2023 International Conference on Innovation and Intelligence for Informatics, Computing, and Technologies (3ICT)*, pp. 302–307, Sakheer, Bahrain.

Bouzid, R., J. Narayan, and H. Gritli, 2024a Artificial neural networks for the forward kinematics of a SCARA manipulator: A comparative study with two datasets. In *2024 ASU International Conference in Emerging Technologies for Sustainability and Intelligent Systems (ICETSIS)*, pp. 1792–1797.

Bouzid, R., J. Narayan, and H. Gritli, 2024b Exploring neural networks for forward kinematics of the robotic arm with different length configurations: A comparative analysis. In *2024 IEEE International Conference on Interdisciplinary Approaches in Technology and Management for Social Innovation (IATMSI)*, volume 2, pp. 1–6.

Bouzid, R., J. Narayan, and H. Gritli, 2024c Investigating neural network hyperparameter variations in robotic arm inverse kinematics for different arm lengths. In *2024 Third International Conference on Power, Control and Computing Technologies (ICPC2T)*, pp. 351–356.

Bouzid, R., J. Narayan, and H. Gritli, 2024d Solving inverse kinematics problem for manipulator robots using artificial neural network with varied dataset formats. In *Complex Systems and Their Applications*, edited by E. Campos-Cantón, G. Huerta-Cuellar, E. Zambrano-Serrano, and E. Tlelo-Cuautle, pp. 55–78, Cham, Springer Nature Switzerland.

Cagigas-Muñiz, D., 2023 Artificial neural networks for inverse kinematics problem in articulated robots. Engineering Applications of Artificial Intelligence **126**: 107175.

Cimen, M. E., Z. Garip, M. A. Pala, A. F. Boz, and A. Akgül, 2019 Modelling of a chaotic system motion in video with artificial neural networks. Chaos Theory and Applications **1**: 38 – 50.

Darba, A., N. B. Sushmi, and D. Subbulekshmi, 2022 Performance analysis of FFBP-LM-ANN based hourly GHI prediction using environmental variables: A case study in chennai. Mathematical Problems in Engineering **2022**: 1713657.

Dash, K. K., B. B. Choudury, and S. K. Senapati, 2017 A inverse kinematic solution of a 6-DOF industrial robot using ANN. Indian Journal of Scientific Research **15**: 97–101.

del Rosario Martinez-Blanco, M., V. H. Castañeda-Miranda, G. Ornelas-Vargas, H. A. Guerrero-Osuna, L. O. Solis-Sanchez, *et al.*, 2016 Generalized regression neural networks with application in neutron spectrometry. In *Artificial Neural Networks*, edited by J. L. G. Rosa, chapter 3, IntechOpen, Rijeka.

Denavit, J. and R. S. Hartenberg, 1955 A kinematic notation for lower-pair mechanisms based on matrices. Journal of Applied Mechanics **22**: 215–221.

Di Pietro, A., D. Torresi, M. Zadro, L. Cosentino, C. Ducoin, *et al.*, 2012 The inverse kinematics thick target scattering method as a tool to study cluster states in exotic nuclei. Journal of Physics: Conference Series **366**: 012013.

Duka, A.-V., 2014 Neural network based inverse kinematics solution for trajectory tracking of a robotic arm. Procedia Technology **12**: 20–27.

Dumitriu, D. N., O. D. Melinte, and M. Ionescu, 2020 Neural networks kinematics guidance of lewansoul learm 5r serial manipulator. Acta Electrotehnica **61**.

Ganapathy, S., 1984 Decomposition of transformation matrices for robot vision. Pattern Recognition Letters **2**: 401–412.

Gao, B., Z. Zhu, J. Zhao, and L. Jiang, 2017 Inverse kinematics and workspace analysis of a 3 DOF flexible parallel humanoid neck robot. Journal of Intelligent & Robotic Systems **87**: 211–229.

Gao, R., 2020 Inverse kinematics solution of robotics based on neural network algorithms. Journal of Ambient Intelligence and Humanized Computing **11**: 6199–6209.

García-Samartín, J. F. and A. Barrientos, 2023 Kinematic modelling of a 3RRR planar parallel robot using genetic algorithms and neural networks. Machines **11**.

Ghaleb, N. M. and A. A. Aly, 2018 Modeling and control of 2-DOF robot arm. International Journal of Emerging Engineering Research and Technology **6**: 24–31.

Handayani, A. N., N. Lathifah, H. W. Herwanto, R. A. Asmara, and K. Arai, 2018 Neural network bayesian regularization backpropagation to solve inverse kinematics on planar manipulator. In *2018 Joint 7th International Conference on Informatics, Electronics & Vision (ICIEV) and 2018 2nd International Conference on Imaging, Vision & Pattern Recognition (icIVPR)*, pp. 99–104, IEEE.

Huo, L. and L. Baron, 2008 The joint-limits and singularity avoidance in robotic welding. Industrial Robot: An International Journal **35**: 456–464.

Ibarra-Pérez, T., J. M. Ortiz-Rodríguez, F. Olivera-Domingo, H. A. Guerrero-Osuna, H. Gamboa-Rosales, *et al.*, 2022 A novel inverse kinematic solution of a six-DOF robot using neural networks based on the taguchi optimization technique. Applied Sciences **12**: 9512.

Jenhani, S., H. Gritli, and G. Carbone, 2022 Comparison between some nonlinear controllers for the position control of Lagrangian-type robotic systems. Chaos Theory and Applications **4**: 179 – 196.

Karaca, Y., 2023 Computational complexity-based fractional-order neural network models for the diagnostic treatments and predictive transdifferentiability of heterogeneous cancer cell propensity. Chaos Theory and Applications **5**: 34 – 51.

Kayri, M., 2016 Predictive abilities of Bayesian regularization and Levenberg–Marquardt algorithms in artificial neural networks: a comparative empirical study on social data. Mathematical and Computational Applications **21**: 20.

Keleş, Z., G. Sonugür, and M. Alçın, 2023 The modeling of the rucklidge chaotic system with artificial neural networks. Chaos Theory and Applications **5**: 59 – 64.

Kim, J. S., Y. H. Jeong, and J. H. Park, 2016 A geometric approach for forward kinematics analysis of a 3-sps/s redundant motion manipulator with an extra sensor using conformal geometric algebra. Meccanica **51**: 2289–2304.

Köker, R., C. Öz, T. Çakar, and H. Ekiz, 2004 A study of neural network based inverse kinematics solution for a three-joint robot. Robotics and autonomous systems **49**: 227–234.

Kumar, P. *et al.*, 2018 Artificial neural network based geometric error correction model for enhancing positioning accuracy of a robotic sewing manipulator. Procedia Computer Science **133**: 1048–1055.

Lathifah, N., A. N. Handayani, H. W. Herwanto, and S. Sendari, 2018 Solving inverse kinematics trajectory tracking of planar manipulator using neural network. In *2018 International Conference on Information and Communications Technology (ICOIACT)*, pp. 483–488, IEEE.

Li, H. and A. V. Savkin, 2018 An algorithm for safe navigation of mobile robots by a sensor network in dynamic cluttered industrial environments. Robotics and Computer-Integrated Manufacturing **54**: 65–82.

Liu, W., D. Chen, and J. Steil, 2017 Analytical inverse kinematics solver for anthropomorphic 7-DOF redundant manipulators with human-like configuration constraints. Journal of Intelligent & Robotic Systems **86**: 63–79.

Madhuraghava, P., B. D. Fakruddin, R. V. Subhash, and N. Sunil, 2018 Modelling and structural, analysis of a 6-DOF robot spray coating manipulator. The International Journal of Engineering and Science **7**: 48–56.

Mahajan, A., H. Singh, and N. Sukavanam, 2017 An unsupervised learning based neural network approach for a robotic manipulator. International Journal of Information Technology **9**: 1–6.

Martinez-garcia, J. A., A. M. Gonzalez-zapata, E. J. Rechy-ramirez, and E. Tlelo-cuautle, 2022 On the prediction of chaotic time series using neural networks. Chaos Theory and Applications **4**: 94 – 103.

Møller, M. F., 1993 A scaled conjugate gradient algorithm for fast supervised learning. Neural networks **6**: 525–533.

Narayan, J., M. Abbas, B. Patel, and S. K. Dwivedy, 2023 Adaptive RBF neural network-computed torque control for a pediatric gait exoskeleton system: an experimental study. Intelligent Service Robotics **232**: 726–732.

Narayan, J., S. Banerjee, D. Kamireddy, and S. K. Dwivedy, 2022 Fuzzy membership functions in ANFIS for kinematic modeling of 3R manipulator. In *Handbook of Smart Materials, Technologies, and Devices: Applications of Industry 4.0*, edited by C. M. Hussain and P. Di Sia, pp. 1101 – 119, Springer International Publishing, Cham.

Narayan, J. and A. Singla, 2017a ANFIS based kinematic analysis of a 4-DOFs SCARA robot. In *2017 4th International Conference on Signal Processing, Computing and Control (ISPCC)*, pp. 205–211.

Narayan, J. and A. G. Singla, 2017b *Inverse Kinematic Study of Spatial Serial Manipulators using ANFIS Approach*. Ph.D. thesis, Thapar Institute of Engineering and Technology.

Narayan, J., E. Singla, S. Soni, and A. Singla, 2018 Adaptive neuro-fuzzy inference system–based path planning of 5-degrees-of-freedom spatial manipulator for medical applications. Proceedings of the Institution of Mechanical Engineers, Part H: Journal of Engineering in Medicine **232**: 726–732.

Noorani, I. and F. Mehrdoust, 2022 Parameter estimation of uncertain differential equation by implementing an optimized artificial neural network. Chaos, Solitons & Fractals **165**: 112769.

Petrescu, R. V., R. Aversa, B. Akash, R. Bucinell, J. Corchado, *et al.*, 2017 Inverse kinematics at the anthropomorphic robots, by a trigonometric method. American Journal of Engineering and Applied Sciences **10**: 394–411.

Petrović, L., 2018 Motion planning in high-dimensional spaces. arXiv preprint arXiv:1806.07457 .

Ranganathan, A., 2004 The levenberg-marquardt algorithm. Tutoral on LM algorithm **11**: 101–110.

Rea Minango, S. N. and J. C. E. Ferreira, 2017 Combining the step-nc standard and forward and inverse kinematics methods for generating manufacturing tool paths for serial and hybrid robots. International Journal of Computer Integrated Manufacturing **30**: 1203–1223.

Reiter, A., A. Müller, and H. Gattringer, 2018 On higher order inverse kinematics methods in time-optimal trajectory planning for kinematically redundant manipulators. IEEE Transactions on Industrial Informatics **14**: 1681–1690.

Snieder, R., 1998 The role of nonlinearity in inverse problems. Inverse problems **14**: 387.

Takatani, H., N. Araki, T. Sato, and Y. Konishi, 2019 Neural network-based construction of inverse kinematics model for serial redundant manipulators. Artificial Life and Robotics **24**: 487–493.

Theofanidis, M., S. I. Sayed, J. Cloud, J. Brady, and F. Makedon, 2018 Kinematic estimation with neural networks for robotic manipulators. In *Artificial Neural Networks and Machine Learning–ICANN 2018: 27th International Conference on Artificial Neural Networks, Rhodes, Greece, October 4-7, 2018, Proceedings, Part III 27*, pp. 795–802, Springer.

Wagaa, N., H. Kallel, and N. Mellouli, 2023 Analytical and deep learning approaches for solving the inverse kinematic problem of a high degrees of freedom robotic arm. Engineering Applications of Artificial Intelligence **123**: 106301.

Wang, W., G. Yu, M. Xu, and D. Walker, 2014 Coordinate transformation of an industrial robot and its application in deterministic optical polishing. Optical Engineering **53**: 055102–055102.

Xu, W., Z. Mu, T. Liu, and B. Liang, 2017 A modified modal method for solving the mission-oriented inverse kinematics of hyper-redundant space manipulators for on-orbit servicing. Acta Astronautica **139**: 54–66.

Zhao, D., Y. Bi, and Y. Ke, 2018 Kinematic modeling and inverse kinematics solution of a new six-axis machine tool for oval hole drilling in aircraft wing assembly. The International Journal of Advanced Manufacturing Technology **96**: 2231–2243.

How to cite this article: Bouzid, R., Gritli, H., and Narayan, J. Investigating Feed-Forward Back-Propagation Neural Network with Different Hyperparameters for Inverse Kinematics of a 2-DoF Robotic Manipulator: A Comparative Study *Chaos Theory and Applications*, 6(2), 90-110, 2024.

CHAOS
Theory and Applications
in Applied Sciences and Engineering

e-ISSN: 2687-4539
RESEARCH ARTICLE
Vol.6 / No.2 / 2024 / pp.111-121
Special Issue (EDIESCA 2023)
https://doi.org/10.51537/chaos.1376424

Numerical Analysis of Chaos in a Phononic Crystal Waveguide with Circular Inclusions of Real Materials

A. Bucio-Gutiérrez [α,1], **H. Pérez-Aguilar** [α,2] **and H. E. Alva-Medrano** [β,3]

[α]Facultad de Ciencias Físico Matemáticas, UMSNH, Av. Francisco J. Múgica S/N, 58030, Morelia, Michoacán, México, [β]Tecnológico Nacional de México, Instituto Tecnológico de Morelia, Avenida Tecnológico 1500, 58120, Morelia, Michoacán, México.

ABSTRACT Phononic crystal waveguides (PnCW) have been of great interest due to their properties of manipulating or filtering the acoustic waves with which they interact. Similarly, the presence of the phenomenon of chaos in the classical transport of particles through billiards with analogous geometries has been investigated. With this in consideration, in the present work an acoustic system of a two-dimensional PnCW is modeled, composed of two plane-parallel plates and a periodic arrangement of circular cylindrical inclusions with acoustic surfaces of real materials. In this system, we use the numerical technique of the integral equation, which allows us to obtain the pressure field corresponding to the normal modes in a range of frequencies. In addition, spatial statistical properties of pressure intensity such as the autocorrelation function (ACF) and its standard deviation called correlation length were calculated. The results show that when the correlation length is very small, the system presents disordered patterns of field intensities. Thus under certain conditions, the system under consideration presents a chaotic behavior, similar to the corresponding classical system.

KEYWORDS
Phononic crystal waveguide
Acoustic chaos
Integral equation method
Autocorrelation function

INTRODUCTION

A phononic crystal (PnC) is a periodic material that exhibits a forbidden band structure for certain frequency ranges of acoustic waves (Maldovan 2013). This feature allows effective control of sound propagation, as waves cannot propagate in certain directions or specific frequency ranges. These bands are determined by the geometric parameters and the elastic properties of the material used in the PnC (Khelif *et al.* 2004). The constant study of the properties of PnCs has allowed the development of structures that offer optimal control over wave propagation. Thanks to this, advanced devices such as acoustic diodes, waveguides (Otsuka *et al.* 2013), selective filters, and acoustic superlenses (Chen *et al.* 2018) have been manufactured, among others.

Among these devices, waveguides stand out as they are used in various scientific and technological fields; such as optics, in photonic circuits of nanometric order (Lee *et al.* 2016); and concerning this work, in acoustics, in phononic crystal waveguides (PnCWs). PnCWs are systems composed of a periodic structure formed by two or more fluids, or a combination of solid and fluid, that interact with a pressure field. In fact, the crystalline structures that make up the PnCWs are fundamental in solid state physics (Kittel *et al.* 1996). That is why PnCW systems have emerged as a fascinating area of research in recent years. As these band structures exhibit properties such as the manipulation of acoustic wave propagation, which has shown great potential for the control and direction of acoustic waves in a wide range of applications.

The design of PnCW involves the manipulation of parameters such as geometry, spacing, and material composition (Jia *et al.* 2018). This allows the creation of specific frequency bands where acoustic waves can be confined and guided along predetermined paths. This ability to control sound propagation opens up a wide range of potential applications, ranging from acoustic signal processing devices (El-Kady *et al.* 2008) to noise isolation systems (Torrent and Sánchez-Dehesa 2008).

Similarly, there have been notable advances in the theoretical understanding, simulation, and manufacturing of PnCWs. Exhaustive research has been carried out on multiple waveguide configurations, ranging from one- to two-dimensional and three-dimensional (Pennec *et al.* 2010b; Liu *et al.* 2020). The literature has studied the response of PnC and PnCW systems made of different materials such as quartz whose acoustic response is in the order of

Manuscript received: 16 October 2023,
Revised: 26 November 2023,
Accepted: 5 December 2023.

[1]1207258b@umich.mx (**Corresponding author**)
[2]hiperezag@yahoo.com
[3]hugo.am@morelia.tecnm.mx

kiloHertz (He *et al.* 2020), lead-epoxy unit cell to detect different gases at different temperatures (Zaki *et al.* 2020), gas and water pipelines over the 1-50 kHz (Jing *et al.* 2018), stainless steel with mechanically drilled holes filled with liquid for its characterization by measuring its bulk modulus (Mukhin *et al.* 2022). These advances have allowed a greater understanding of the fundamental principles that govern the behavior of waves in these systems, as well as the development of more sophisticated techniques for their design and manufacture.

Additionally, it is important to note that PnCs share various similarities with photonic crystals (PC). One of these similarities is the simultaneous existence of forbidden bands for both photons and phonons (Pennec *et al.* 2010a). This connection between PnCs and PCs has led us to the hypothesis that the former can also exhibit chaotic dynamics in systems of geometries similar to the latter (Navarro-Urrios *et al.* 2017). These observations open the door to new research and explorations in the field of phononic crystals, in search of better understanding of their behavior and take advantage of their properties for various purposes.

Classical fields (electromagnetic, acoustic, etc.) or quantum amplitude probabilities share the same interesting statistical features when, in the corresponding geometrical or classical limits (wavelength tends to zero), the dynamics of rays or trajectories exhibit chaos (Stöckmann 1999). Wave and quantum chaos are thus now well-documented topics covering a wide variety of physical systems: electrons in quantum dots (Wilkinson *et al.* 1996), cold atoms (Hensinger *et al.* 2001), surface waves (Kudrolli *et al.* 2001), elastodynamics (Weaver 1989), acoustics (de Rosny *et al.* 2000; Ellegaard *et al.* 2001), microwaves (Sridhar 1991; Dembowski *et al.* 2000) and optical cavities (Nöckel and Stone 1997; Doya *et al.* 2002a). In wave cavities for which the limit of rays exhibits chaos, wave function statistics is generally expected to follow the predictions of Random Matrix Theory (RMT). According to this theory, wave functions are uniformly distributed over the whole available phase space which is ergodically explored by the rays, thus locally resulting in a random superposition of plane waves (Berry 1977). Nevertheless, some ergodic modes of chaotic billiard systems are known to show an anomalous increase in intensity along weakly unstable periodic orbits, a phenomenon called scarring (Heller 1984; Kaplan 1998; Ellegaard *et al.* 2001; Doya *et al.* 2002a). Two alternative approaches are generally considered to study the influence of scars on wave statistics in chaotic wave cavities. One is devoted to the analysis of individual scarred eigenstates (Heller 1984), while the other is dynamical as it is based on the evolution of wave packets launched along periodic orbits (Kaplan and Heller 1999), that generally the long time evolution yields a typical specklelike field pattern characterized by the well-known isotropic field autocorrelation function (ACF) (Berry 1977; Doya *et al.* 2002a; Kuhl *et al.* 2005). In this context, it is relevant to highlight that the analysis of the ACF has proven to be a very useful tool for understanding and characterizing both theoretically and experimentally chaotic behavior. This technique has been particularly applied in the study of optical fibers with non-circular cross-sections, where light rays exhibit chaotic dynamics (Doya *et al.* 2002b).

There are advances in the theory of chaotic dynamical systems, particularly the results of Sinai (Sinai 1970) and Ruelle (Ruelle 1991), on wave mechanics experiments that use microwaves for studying the so-called quantum-classical correspondence, a central issue in quantum chaos. The properties of closed Sinai billiard microwave cavities have been discussed in terms of universal predictions from RMT, as well as periodic orbit contributions, which manifest as scars in eigenfunctions and standing wave patterns (Sridhar and Lu 2002). In an equivalent analogy we study the acoustic-classical correspondence of the properties of the eigenvalues and eigenfunctions of the Sinai billiard-shaped cavities and the 2-D n-disk billiards in PnCWs. Consequently, through the ACF, it is possible to obtain precise information about the statistical properties of the acoustic response of the study system. The ACF allows evaluating the similarity of a signal with itself as it moves both in time and space, especially in cases where the stationary case is assumed. In this way, the analysis of the ACF is positioned as a valuable tool to deepen the study of chaotic systems and contribute to a greater understanding of their dynamic behavior.

In our study, we have considered two acoustic systems of two-dimensional PnCWs, one of infinite length and another of truncated length. These systems are composed of two plane-parallel plates and a periodic arrangement of circular cylindrical inclusions with acoustic surfaces of particular materials, as illustrated in Figures 1 and 2. The inclusions play a crucial role in wave behavior, acting as reflectors and diffractors. This leads to a significant modification in the pressure field compared to the case of a PnCW having two plates with acoustic surfaces but no inclusions.

In our numerical simulations, we have used the Integral Equation Method (IEM) (Mendoza-Suárez and Pérez-Aguilar 2016; Villa-Villa *et al.* 2017), which has proven to be a powerful tool for analyzing acoustic response. This method has the advantage of considering interaction between two plane-parallel plates and cylindrical inclusions, allowing more accurate results. Through this technique, we can investigate and understand normal mode behavior in different geometric configurations and frequencies, specifically in our particular systems. This gives us greater ability to analyze the acoustic response of our system and allows us to obtain valuable information about its statistical properties.

METHODOLOGY

Firstly, it is necessary to find the equation that characterizes the problem posed. The wave equation is the central element that determines and conditions the propagation of acoustic waves in a given medium. For this, we consider the continuum theory in a homogeneous medium, which means that its properties in the unperturbed state are the same everywhere. We also consider the case of perfect fluids, as these do not deform nor allow the propagation of transverse mechanical waves, so processes such as energy dissipation due to viscosity are ignored. Therefore, a linear approximation is performed on the continuity equation of mass, the non-viscous force equation and the equation of state around an initial stationary state of the system (Blackstock 2001), obtaining

$$\frac{\partial s}{\partial t} + \nabla \cdot \mathbf{u} = 0, \tag{1a}$$

$$-\nabla p(\mathbf{r}, t) = \rho_0 \frac{\partial \mathbf{u}}{\partial t}, \tag{1b}$$

$$p = Bs, \tag{1c}$$

where $\mathbf{u}$ is the average vectorial velocity of the fluid, B is called the adiabatic volumetric modulus, s is the condensation at any point and p is the acoustic pressure at any point, considered harmonic in time. As acoustics studies the generation and spatio-temporal evolution of small mechanical perturbations (vibrations) in a fluid (sound waves) or in a solid (elastic waves), it is natural to describe the behavior of the acoustic pressure field in the waveguide through the Helmholtz equation, similar to Maxwell equations in electromagnetic system, from Eqs. (1). Thus, applying the diver-

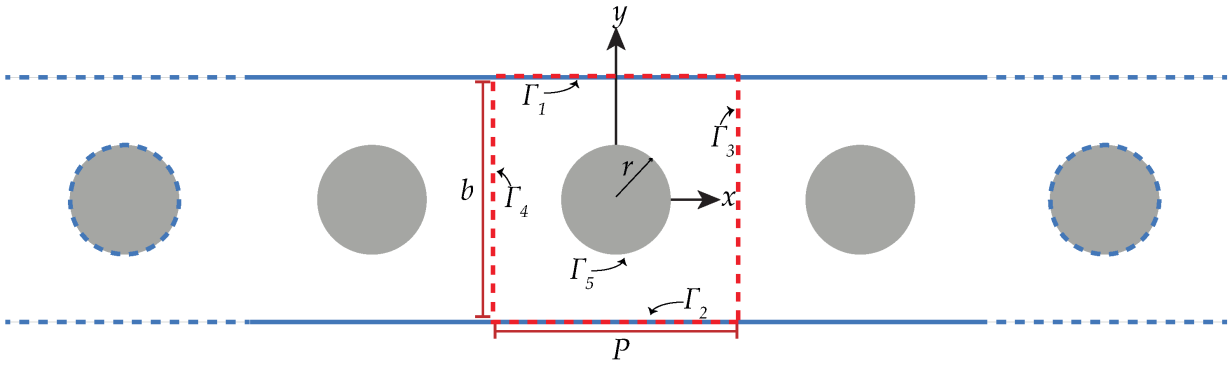

Figure 1 Infinite 2D PnCW system diagram. The system is composed of two plane-parallel plates and a periodic arrangement of circular cylindrical inclusions with acoustic surfaces. The Γ contours define the unit cell of the system with periodicity in the x-direction.

gence to Eq. (1a), we obtain

$$-\nabla^2 p(\mathbf{r},t) = \rho_0 \nabla \cdot \frac{\partial \mathbf{u}}{\partial t}, \tag{2}$$

where ∇^2 is the three-dimensional Laplacian operator. On the other hand, considering the temporal derivative of Eq. (1a) and using $\partial(\nabla \cdot \mathbf{u})/\partial t = \nabla \cdot (\partial \mathbf{u}/\partial t)$, we arrive at

$$\frac{\partial^2 s}{\partial t^2} + \nabla \cdot \frac{\partial \mathbf{u}}{\partial t} = 0. \tag{3}$$

Now, combining Eqs. (2) and (3), can be reduced to

$$\nabla^2 p(\mathbf{r},t) = \rho_0 \frac{\partial^2 s}{\partial t^2}, \tag{4}$$

and substituting Eq. (1c) into Eq. (4) yields the acoustic wave equation,

$$\nabla^2 p(\mathbf{r},t) \quad = \quad \frac{1}{c_m^2}\frac{\partial^2 p(\mathbf{r},t)}{\partial t^2}, \tag{5}$$

where c_m is the longitudinal wave velocity in the acoustic medium given by

$$c_m = \sqrt{\frac{\beta_0}{\rho_0}\gamma}, \tag{6}$$

as the adiabatic bulk modulus has the relation $B = \beta_0\gamma$, with ρ_0 being the constant equilibrium density. Additionally, this is a characteristic property of the fluid and depends on the equilibrium conditions. Eq. (5) is also known as the homogeneous acoustic wave equation for pressures. For a linear acoustic pressure wave in a unit cell $p(\mathbf{r},t)$, considering the harmonic case with time frequency ω; that is, $p(\mathbf{r},t) = p(\mathbf{r})e^{-i\omega t}$, we obtain the stationary wave equation,

$$\nabla^2 p(\mathbf{r}) + k^2 p(\mathbf{r}) = 0, \tag{7}$$

being

$$k^2 = \left(\frac{\omega}{c_m}\right)^2, \tag{8}$$

the magnitude of the wave vector that gives us the dispersion relation as a function of the frequency ω and the wave speed in the medium c_m (for more detailed of acoustic wave equation deduction is suggested see (Ginsberg 2018a)). The only property of the medium that appears in Eq. (8) is the wave speed, which depends on conditions such as laboratory temperature and pressure and is closely related to the opposition that the medium presents to the propagation of the pressure wave. That is why the specific acoustic impedance plays a fundamental role since it is the quotient between the acoustic pressure at a point in the medium and the instantaneous velocity of the particles at that point,

$$Z = \frac{p}{u}. \tag{9}$$

There are three limit cases for the acoustic impedance of a surface (Ginsberg 2018b); when the opposition of the medium is enormous, that is, it is not possible to disturb the medium for any pressure, it is said that the impedance $Z \to \infty$ and the surface is rigid; the opposite case of the soft surface occurs when $Z \to 0$, so a small pressure on surface induces a great speed. The third case is when the quotient of impedance is one, which represents a non-reflective medium. In addition, when impedance is finite and different from zero, a real material will be considered, and since we consider time-harmonic plane waves, the characteristic acoustic impedance is given by (Beranek and Mellow 2012)

$$Z_m = \rho c_m, \tag{10}$$

where the density ρ is the main constitutive parameter that determines the characteristics of the propagation of acoustic waves in the medium. The dispersion relation for real acoustic media for real constitutive media is obtained by substituting Eq. (10) into Eq. (8), given by

$$k = \frac{\rho_r}{Z_r}\frac{\omega}{c_m}, \tag{11}$$

where ρ_r and Z_r are the relative density and relative characteristic acoustic impedance of the medium in relation to air, respectively. Finally, when it comes to a system of this type, it is necessary to consider the boundary conditions at the interfaces between the media involved (Filippi *et al.* 1998),

$$p^{(1)} = p^{(2)}, \tag{12a}$$

$$\frac{c_{m_1}}{Z_{m_1}}\frac{\partial p^{(1)}}{\partial n} = \frac{c_{m_2}}{Z_{m_2}}\frac{\partial p^{(2)}}{\partial n}. \tag{12b}$$

The first condition tells us that the pressure is continuous on the interface, that is, there is no net force on the interface separating the media. The second condition tells us that the normal component of the pressure is continuous and requires that the media involved remain in contact (Kinsler *et al.* 2000).

In extreme cases of infinite or zero impedance (soft or rigid surface) the problem is significantly simplified. When there is a rigid surface, the normal pressure of the particles at the boundary

is zero; that is, the second boundary condition at the interface equals zero. Whereas, when there is a soft surface, the transmitted wave has zero pressure amplitude at the boundary, so the first condition at the interface equals zero (Pike and Sabatier 2001).

Let us also note the similarity between transverse electrical polarization (TE) with a surface considered as limits a perfect electric conductor is equivalent to the case of the soft acoustic surface; that is, a Dirichlet problem. In the same way, the transverse magnetic polarization (TM) is equivalent to the case of the rigid acoustic surface; that is, a Neumann problem (McGurn 2020).

NUMERICAL INTEGRAL METHOD

To calculate the corresponding pressure intensities of the eigenmodes of the system, we use the numerical technique of the IEM for a PnCW (Pérez-Aguilar *et al.* 2013). This technique is used, in particular, to model the interaction of waves that disturb a system with two-dimensional bodies (Pérez *et al.* 2009; Mendoza-Suárez and Pérez-Aguilar 2016). This method has two analogous approaches depending on whether the system is infinite or a finite length. The method is based on Green's second integral theorem in the equation that models our problem, allowing us to obtain a system of coupled integral equations. Subsequently, the discretization of the system of integral equations is carried out, which results in a set of linear equations under boundary conditions that can be represented in a single homogeneous matrix equation $MX = 0$ in the case of the infinite system, and inhomogeneous $MX = A$ for the finite system. It is important to mention that only a finite number of sampling points are taken into account along the contours that define the surface of the two-dimensional system of study, which allows savings in computational resources when numerically calculating line integrals in a discrete approximation form unlike differential methods that require a two-dimensional discrete mesh. Next, we describe the IEM corresponding to a two-dimensional PnCW of infinite and finite length.

Infinite waveguide

In Figure 1, P is the period of the PnCW system in x-direction; b is the distance between the flat plates; r is the radius of the circular inclusion, and the region enclosed by the curves Γ_i for $i = 1, 2, 3$ and 4 can be considered as an unit cell of the system. This region contains the circular inclusion with a profile given by Γ_5. Taking into account that the system is periodic along the direction of the waveguide, it is possible to apply Bloch's theorem (Bloch 1929), which states that the field can be written as a product of a plane wave and a periodic function along its direction of periodicity as

$$p(x + P, y) = p(x, y) \exp(-i\mathbf{K}P), \tag{13}$$

where $\mathbf{K}$ is the one-dimensional Bloch vector. For each j-th medium, the two-dimensional Green's function corresponds, which is the equivalent solution to Eq. (7), so the general form of the Helmholtz integral equation is

$$\frac{1}{4\pi} \oint_\Gamma \left[G\left(\mathbf{r}, \mathbf{r}'\right) \frac{\partial p\left(\mathbf{r}'\right)}{\partial n'} - p\left(\mathbf{r}'\right) \frac{\partial G\left(\mathbf{r}, \mathbf{r}'\right)}{\partial n'} \right] ds' = p(\mathbf{r})\Theta(\mathbf{r}), \tag{14}$$

with

$$G(R) = \frac{i}{4} H_0^1(kR), \tag{15}$$

where $H_0^1(\zeta)$ is the Hankel function of the first kind and zero order, $R = |\mathbf{r} - \mathbf{r}'|$ and $\Theta\left(\mathbf{r}\right) = 1$ if $\mathbf{r}$ is inside the region and $\Theta\left(\mathbf{r}\right) = 0$ otherwise. Given the geometry, the problem must be posed as a system of n equations (one for each region between the interfaces of the different homogeneous media) in which the boundary conditions (Eqs. (12)) must be satisfied.

To solve the Eq. (14) numerically, it is necessary to discretize by dividing curve Γ of the j-th region into curve segments Γ_i of arc length Δs small enough so that the field and its normal derivative are constant. Thus, the integrals of Eq. (14) for the j-th region can be approximated as follows (Mendoza-Suárez *et al.* 2011)

$$\oint_\Gamma \left[G\left(\mathbf{r}, \mathbf{r}'\right) \frac{\partial E\left(\mathbf{r}'\right)}{\partial n'} \right] ds' \approx \sum_n \Phi_n L_{mn}, \tag{16a}$$

$$\oint_\Gamma \left[p\left(\mathbf{r}, \mathbf{r}'\right) \frac{\partial G\left(\mathbf{r}'\right)}{\partial n'} \right] ds' \approx \sum_n \Psi_{n'} N_{mn}, \tag{16b}$$

where the source functions are

$$\Phi_n = \left. \frac{\partial p\left(\mathbf{r}'\right)}{\partial n'} \right|_{\mathbf{r}' = \mathbf{r}'_n}, \tag{17a}$$

$$\Psi_n = \left. p\left(\mathbf{r}'\right) \right|_{\mathbf{r}' = \mathbf{r}'_n}, \tag{17b}$$

and matrix elements are defined as

$$L_{mn} = \int_{s_n - \Delta s/2}^{s_n + \Delta s/2} G\left(\mathbf{r}, \mathbf{r}'\right) ds', \tag{18a}$$

$$N_{mn} = \int_{s_n - \frac{\Delta s}{2}}^{s_n + \frac{\Delta s}{2}} \frac{\partial G\left(\mathbf{r}, \mathbf{r}'\right)}{\partial n'} ds'. \tag{18b}$$

In the previous expressions, the subscript m denotes the observation point and n the integration point. Substituting Eq. (15) in Eqs. (18) to obtain explicit forms, it is also necessary to consider that the Green function has a removable singularity in the two-dimensional case at $\mathbf{r} = \mathbf{r}'$; since this is where the point source that gives rise to this function is located. We then got the fact that Eqs. (18) are respectively (Mendoza-Suárez and Villa-Villa 2006)

$$\begin{aligned} L_{mn} = {} & [1 - \delta_{mn}] \frac{i\Delta s}{4} H_0^{(1)}\left(k_j \left|\mathbf{r}_m - \mathbf{r}_n\right|\right) + \\ & + \left[\frac{i\Delta s}{4} H_0^{(1)}\left(k_j \frac{\Delta s}{2e}\right) \right] \delta_{mn} \end{aligned} \tag{19}$$

and

$$\begin{aligned} N_{mn} = {} & [1 - \delta_{mn}] \frac{i\Delta s k_j}{4} \mathbf{n}_n \cdot \frac{\left(\mathbf{r}_m - \mathbf{r}_n\right)}{\left|\mathbf{r}_m - \mathbf{r}_n\right|_1} H_1^{(1)}\left(k_j \left|\mathbf{r}_m - \mathbf{r}_n\right|\right) + \\ & + \left[\frac{1}{2} + \frac{\Delta s}{4\pi} \mathbf{n}_n \cdot \mathbf{t}'_n \right] \delta_{mn}, \end{aligned} \tag{20}$$

where $\mathbf{n}_n$ is the normal to the contour Γ at the point $\mathbf{r}_n$ and $\mathbf{t}'_n$ is the curvature vector of the surface at the same integration point.

Therefore, we have converted the set of integral equations given by Eq. (14) into a homogeneous system of linear equations,

$$\sum_n \Phi_n L_{mn} - \sum_n p_n N_{mn} \approx p(\mathbf{r})\Theta(\mathbf{r}), \tag{21}$$

which can be represented by matrices such as

$$M\left(\mathbf{K}, \omega\right) X\left(\mathbf{K}, \omega\right) = 0, \tag{22}$$

where $M\left(\mathbf{K}, \omega\right)$ is the representative matrix associated with the system, $X\left(\mathbf{K}, \omega\right)$ are the source functions to be found that depend on the Bloch vector $\mathbf{K}$ and the frequency ω. Since the system of linear equations is homogeneous, a non-trivial solution can be obtained if the determinant of this matrix is zero. It is possible to determine the band structure, defining the function

$$D\left(\mathbf{K}, \omega\right) = \ln\left(\det M\left(\mathbf{K}, \omega\right)\right), \tag{23}$$

which presents local minimum points that will give the numerical dispersion relation $\omega(\mathbf{K})$, that determine the eigenmodes of the system for a specific frequency.

For the idealized cases where soft or rigid acoustic surfaces are present, which are characterized by having zero and infinite impedance respectively, the problem is significantly simplified. For example, in the case of the soft surface, the field is zero so there is no pressure inside the surface, on the other hand, in the case of the rigid surface, the normal derivative of the field is zero, so modes propagate even with the surface (Pike and Sabatier 2001).

Finite waveguide

Because in nature the dimensions of this type of system is finite, we can model a more realistic system taking the case of PnCW characterized by the number of consecutive unit cells to choose, thus we can truncate the infinite system to obtain a finite model of the waveguide as shown in Figure 2. Furthermore, we consider a plane pressure wave of pressure that interacts with the system at normal incidence; so in addition to the theory already mentioned, together with the fact that we are now dealing with matrix inversion problem (that is, a homogeneous matrix system) an incident pressure beam is considered (in region R_0) and calculation of scattered pressure field as response of the waveguide.

Since we have already described the integral numerical method, we use Eq. (14) in such a way that we can express the field in region R_0 as

$$p^{(0)}(\mathbf{r}) = p^{(0)}_{inc}(\mathbf{r}) + \frac{1}{4\pi}\sum_{j=1}^{M}\int_{\mathbf{r}_i}\left[G\left(\mathbf{r},\mathbf{r}'\right)\frac{\partial p\left(\mathbf{r}'\right)}{\partial n'} - p\left(\mathbf{r}'\right)\frac{\partial G\left(\mathbf{r},\mathbf{r}'\right)}{\partial n'}\right]ds'. \tag{24}$$

The terms on the right side correspond to the incident pressure field and the scattered pressure field, respectively. Then, for the other regions, when approximating to the observation point, we obtain

$$p^{(j)}(\mathbf{r})\Theta_j(\mathbf{r}) = \frac{1}{4\pi}\oint_{\mathbf{r}_i}\left[\frac{\rho_{r,j}}{Z_{r,j}}G_j\left(\mathbf{r},\mathbf{r}'\right)\frac{\partial p_j\left(\mathbf{r}'\right)}{\partial n'} - p_j\left(\mathbf{r}'\right)\frac{\partial G_j\left(\mathbf{r},\mathbf{r}'\right)}{\partial n'}\right]\delta_{ji}ds', \tag{25}$$

where $\Theta_j\left(\mathbf{r}\right) = 1$ if $\mathbf{r}$ is inside the j-th medium or zero otherwise, δ_{ji} is the Kronecker delta and $\rho_{r,j}$, $Z_{r,j}$ are the density and impedance of the j-th medium relative to that of air, respectively. With this the inhomogeneous algebraic system is found that has the field and its normal derivative as unknowns.

To deal with the finite PnCW problem with method described above, it is necessary to make assumptions about the incident pressure field. Once the sources $\Psi^{(j)}_n$ and $\Phi^{(j)}_n$ are obtained, with $j = 1, 2, \ldots, M$ bodies (using the notation of Eqs. (17)), the field can be calculated at any point within the pressure regions that constitute the system using the same integral equations. If $\mathbf{r} \in R_0$, that is, the propagation region, the corresponding equation is

$$\Psi^{(0)}_m = \sum_{n=1}^{N} L^{(0)}_{mn}\Phi^{(0)}_n - \sum_{n=1}^{N} N^{(0)}_{mn}\Psi^{(0)}_n - \Psi^{\mathrm{inc}(0)}_m, \tag{26}$$

where, the incident pressure field is expressed as

$$\Psi^{(\mathrm{inc})}(\mathbf{r}) = \Psi_0 e^{i\mathbf{k}\cdot\mathbf{r}}, \tag{27}$$

where Ψ_0 is a constant with appropriate units, $\mathbf{k}$ is the propagation wave vector and $\mathbf{r}$ is the position of each point at which the wave comes into contact. On the other hand, for the other regions $\mathbf{r} \in \mathbf{R}_j$, the associated equation is

$$\Psi^{(j)}_m = \sum_{n=1}^{N} L^{(j)}_{mn}\Phi^{(j)}_n - \sum_{n=1}^{N} N^{(j)}_{mn}\Psi^{(j)}_n. \tag{28}$$

RESULTS

In the programming of the integral equation method, the Message Passing Interface (MPI) protocol was implemented to reduce the computation time for obtaining results. To obtain reliable results in the case of high frequencies, it is necessary to use small discretization intervals Δs. To ensure the accurate approximation of the integral corresponding to the profile that models the system, the intervals must be smaller than the periodicity of the system, which is related to the wavelength $\lambda = 2\pi c_m/\omega$. Thus, it is necessary that $\Delta s \ll \lambda$. Furthermore, since statistical properties envision disordered behavior in systems where chaos phenomenon occurs, we calculated the average of the ACF for several data sets. This tells us the similarity between the behavior of the function at a given point and its behavior at any consecutive point.

Autocorrelation Function

An important mathematical tool for the interpretation of numerical data is the ACF. The ACF defines how data points in a spatial (or temporal) series relate, on average, to previous data points. In other words, it measures the self-similarity of the data set (Vilela *et al.* 2013).

The ACF for a pattern of acoustic pressure field intensity, $I(\mathbf{r})$, in the unit cell is defined as:

$$ACF_j \equiv \sum_{i=1}^{N_p}\frac{\left(I\left(\mathbf{r}_i\right) - \mu\left(I\left(\mathbf{r}_{i-j}\right) - \mu\right)/N_p}{\sigma^2}, \tag{29}$$

being the average value of I,

$$\mu = \sum_{i=1}^{N_p}\frac{I\left(\mathbf{r}_i\right)}{N_p} \tag{30}$$

and the variance,

$$\sigma^2 = \sum_{i=1}^{N_p}\frac{\left(I\left(\mathbf{r}_i\right) - \mu\right)^2}{N_p}, \tag{31}$$

where Np is the number of sampling points with coordinates $(x_i, y\left(x_i\right))$. In this case $y(x)$ being fixed, with $0 < x < P$ in the infinite system and $0 < x < 10P$ in the finite system and the subscript j indicates the value of the ACF with respect to the j-th coordinate point. In this way, autocorrelation was calculated using points located in the upper middle section of the waveguide. The autocorrelations of the intensity patterns that we will show in this work result from correlations between the values of intensity $I(\mathbf{r})$ themselves. The ACF is positive when the relationship between values is linear (they are very similar), it is negative when the relationship is linearly inverse (they are very different) and it is null when there is no linear relationship (Montenegro-García 1989; Legendre 1993). A quantity that could be even more important is the standard deviation of the ACF, known as *correlation length* l_c, which helps us to compare the cases considered since it is a measure used to quantify the dispersion of a set of numerical data (Doya *et al.* 2002a). Due to the oscillatory nature of the ACF, the

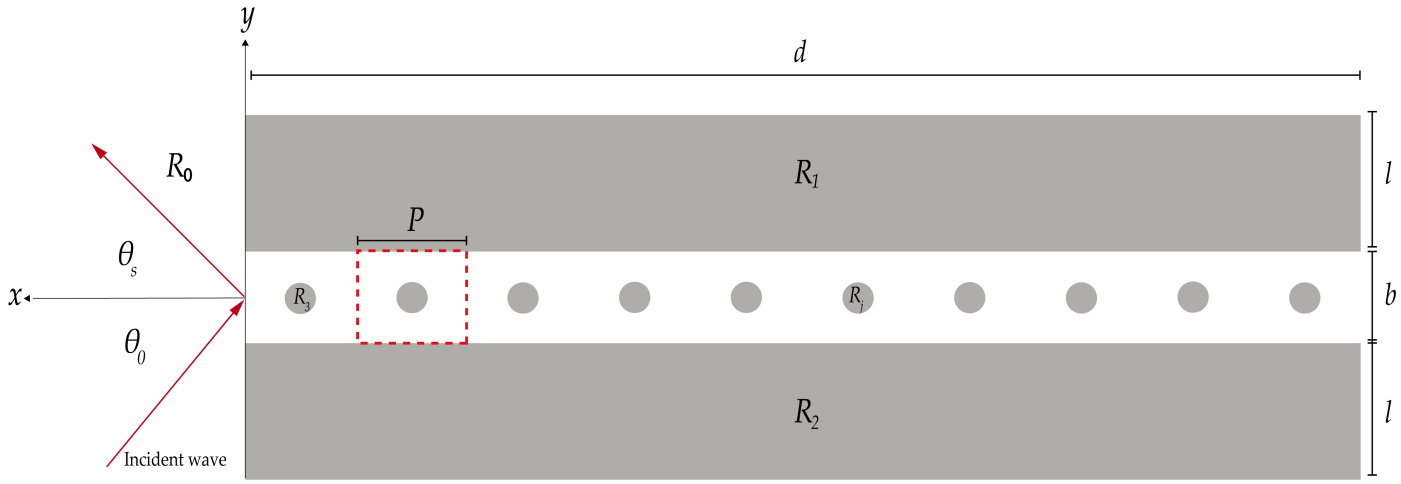

Figure 2 Finite 2D PnCW system diagram.

length of the correlation is related to the typical speckle grain size. Therefore, the decrease in the length of the correlation as the frequency increases is a characteristic feature of chaos or equivalently of the presence of a positive Lyapunov exponent (Sugihara and May 1990).

Infinite PnCW

Let us consider the system illustrated in Figure 1 with a periodicity $P = 2\pi$ μm in one direction, a plate spacing $b = 2\pi$ μm, a periodic arrangement of circular inclusions with a filling fraction f for a sufficiently small discretization step $\Delta s = 0.0126$ μm for better data acquisition. Furthermore, the determinant function $D\,(k_r = 0, \omega_r)$ was calculated for a number of frequencies given by $n_\omega = 400$ choosing a particular propagation mode given by $(k_r = 0, \omega_r)$. The system is modeled in particular for a brass inclusion, however, it is possible to apply the method for different types of materials considering the characteristic acoustic impedance of the inclusion. In the case of brass it is given by a value of $Z = 40$ MRayls, which is a real rigid surface; while the top and bottom plates of the system are composed of an ideal soft acoustic material.

First, the inclusion centered on the unit cell with a filling fraction factor of $f = 0.003$ is considered. The pressure field intensities as well as the ACFs are obtained. The numerical results obtained range for frequencies from 504.8964 MHz to $\omega = 199.308$ GHz (from ultrasound to hypersonic) are shown in Figure 3. Data sets are taken along 1200 different lines parallel to x that are equidistant a distance $\varepsilon > 0$. Each of the ACFs are calculated from $N_P = 3063$ sampling points and the ACFs are averaged showing behavior that tends to zero with increasing frequency. Similarly, pressure field intensity patterns are obtained for a brass inclusion with a larger value of the filling fraction factor $f = 0.3$, leading to different vibration modes as seen in Figure 4. The parameters used and obtained are compiled in Table 1 for both cases.

The numerical results of infinite PnCW with different filling fractions shown in both tables indicate that the value of the correlation length is smaller as the frequency increases. Such decrease in the correlation length deduced from the standard deviation of the spatial ACF with increasing frequency is a characteristic feature of chaos (or equivalently, of the presence of a positive Lyapunov exponent) (Sugihara and May 1990). Furthermore, it complies with the acoustic-classical correspondence of the already known properties of the eigenvalues and eigenfunctions of the Sinai billiard-shaped cavities. This also provides further evidence that the acoustic modes in a PnCW at high frequencies (small wavelengths) is a deterministically chaotic system.

To break the symmetry of the unit cell, the inclusion is placed in the upper right corner of the unit cell for both values of the filling fractions previously considered. Observing in Figures 5 and 6 how field pressure patterns change as the frequency ω increases, we see that modes inside the inclusion in some cases differ greatly from the form held outside it. However, the continuity of the field is maintained by boundary conditions. Table 2 shows the values obtained for both figures.

Table 1 Numerical results of infinite PnCW with centered brass inclusion.

f	ω (MHz)	l_c
0.003	504.8964	0.37695
0.003	16958.3923	0.12054
0.003	66640.7837	0.06492
0.003	199308.6716	0.0555
0.3	509.2547	0.38954
0.3	16957.3781	0.11355
0.3	66640.9522	0.16325
0.3	199229.8121	0.10516

Finite PnCW

Let us now consider a more realistic system, such as the finite PnCW of length $d = 20\pi$ μm, plate spacing $b = 2\pi$ μm, which

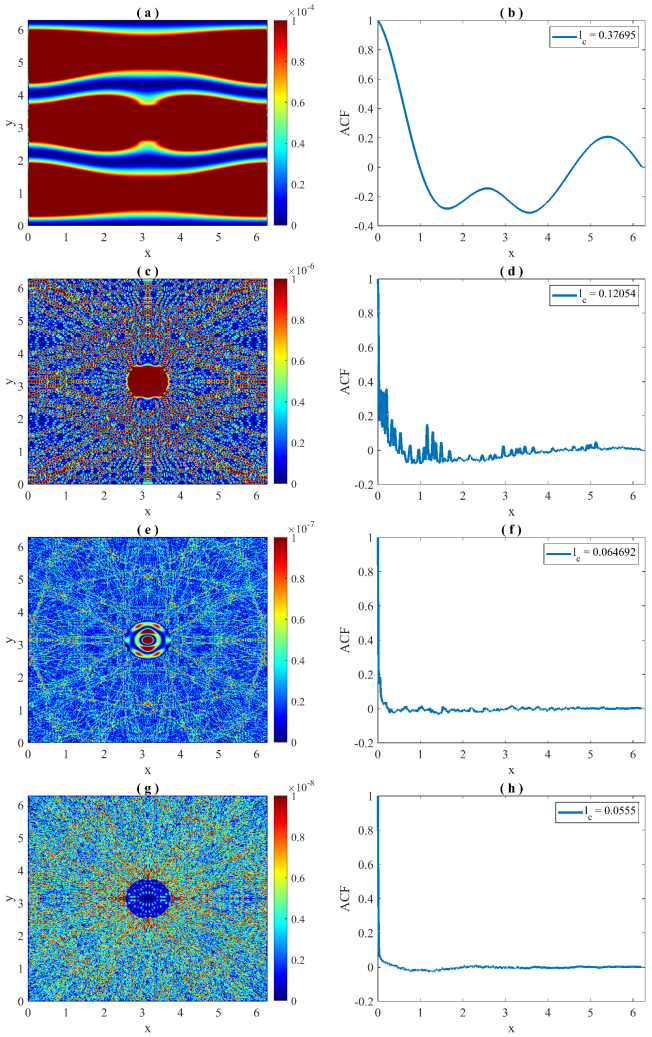

Figure 3 Pressure field intensity patterns and their respective ACFs for an infinite PnCW with small brass inclusion ($f = 0.003$) centered on the unit cell. The frequency values chosen for each field pattern are indicated in Table 1.

Table 2 Numerical results of infinite PnCW with non-centered brass inclusion.

f	ω (MHz)	l_c
0.003	491.8217	0.38589
0.003	16956.8086	0.087289
0.003	66629.7729	0.071931
0.003	199323.604	0.050629
0.3	601.8675	0.31883
0.3	16953.4455	0.132
0.3	66646.2891	0.12757
0.3	199323.604	0.069709

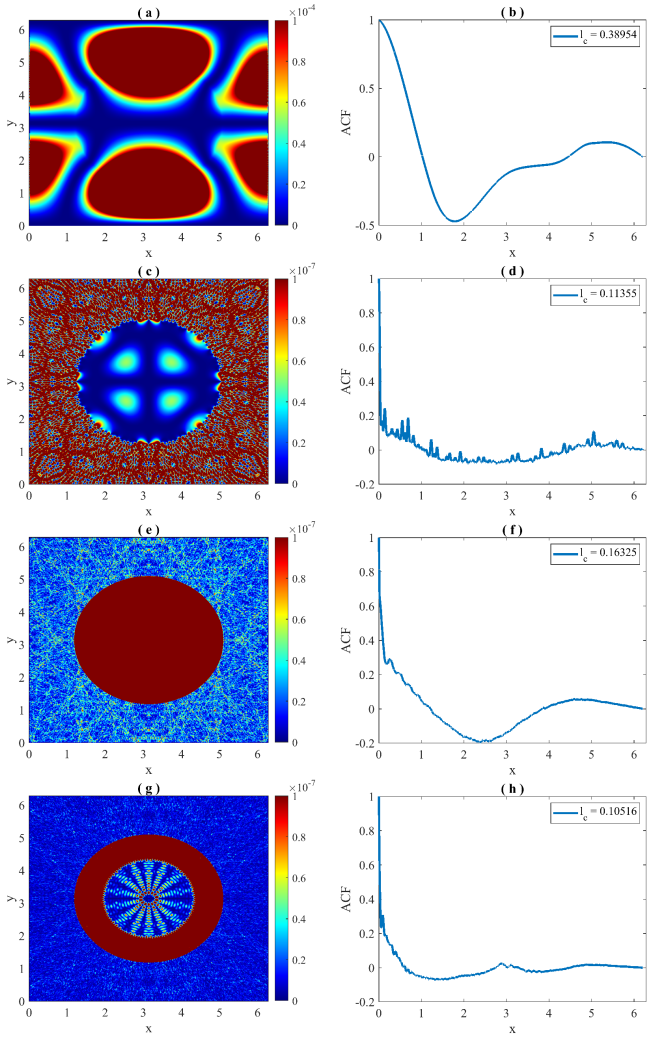

Figure 4 Pressure field intensity patterns and their respective ACFs for an infinite PnCW with a large brass inclusion ($f = 0.3$) centered on the unit cell. The frequency values chosen for each field pattern are indicated in Table 1.

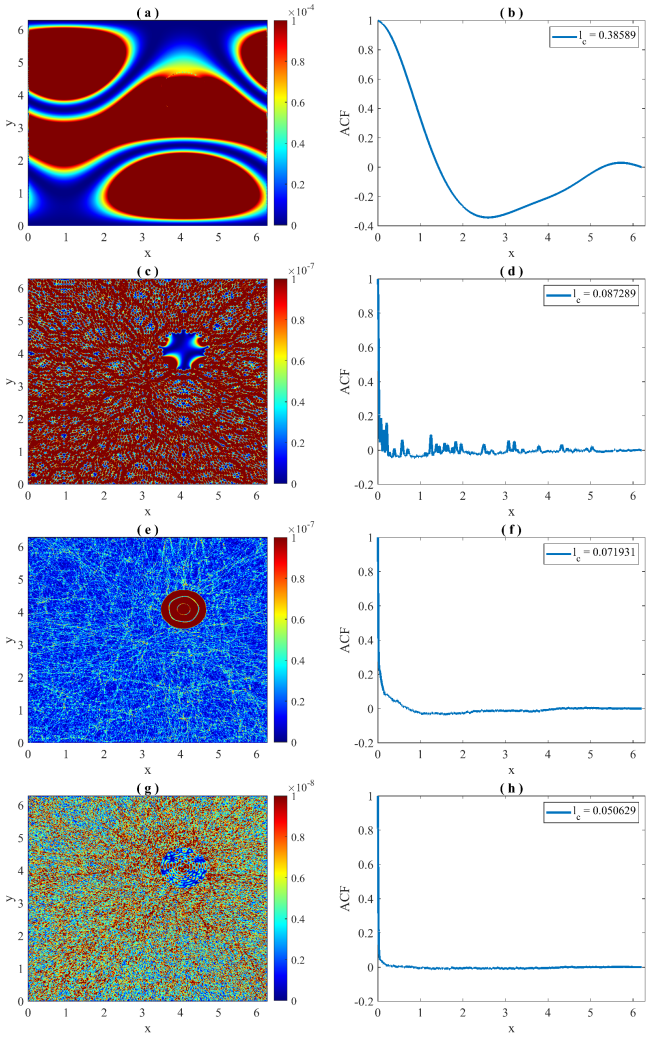

Figure 5 Pressure field intensity patterns and their respective ACFs for an infinite PnCW with small brass inclusion ($f = 0.003$) non centered on the unit cell. The frequency values chosen for each field pattern are indicated in Table 2.

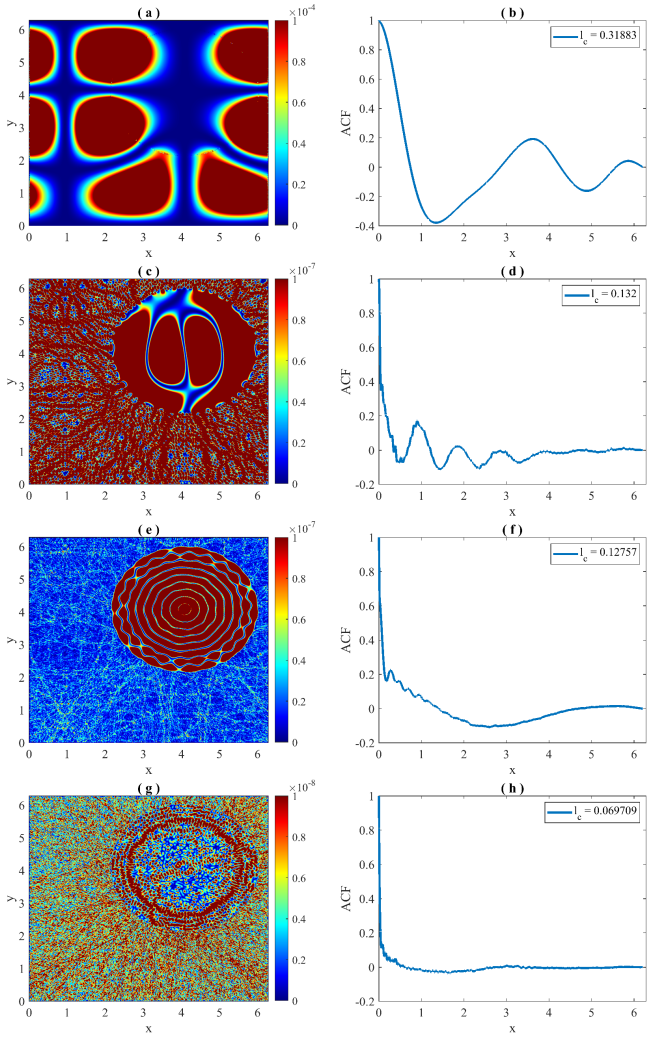

Figure 6 Pressure field intensity patterns and their respective ACFs for infinite PnCW with a large brass inclusion ($f = 0.3$) non centered on the unit cell. The frequency values chosen for each field pattern are indicated in Table 2.

have a thickness of $l = 30$ μm to avoid edge effects and 10 brass inclusions with filling fraction of $f = 0.3$ distributed by a period $P = 2\pi$ and the discretization of the mesh given by $\Delta s = 0.00338$ μm (see Figure 2).

As in the finite system, brass inclusions are considered, while the plates are made of soft acoustic material. The pressure field intensities that were obtained for frequencies from $\omega = 830$ MHz to 66 GHz are shown in Figure 7. The values considered for the case of a finite PnCW are shown in Table 3. The respective ACFs are calculated from $N_P = 6254$ sampling points in the same way over the average of 1200 ACFs of the data set within the PnCW. From the average of the ACFs, the minimum correlation length of $l_c = 0.034718$ corresponding to the highest frequency is obtained. Similar to the case of the infinite system, in both cases the increase in frequency results in a decrease in the correlation length, which we also attribute to the fact that the system response is chaotic.

Table 3 Numerical results of finite PnCW with centered brass inclusion.

f	ω (MHz)	l_c
0.3	830.269	0.20757
0.3	8459.2819	0.087232
0.3	16742.771	0.065393
0.3	33153.8227	0.038081
0.3	66260.371	0.034718

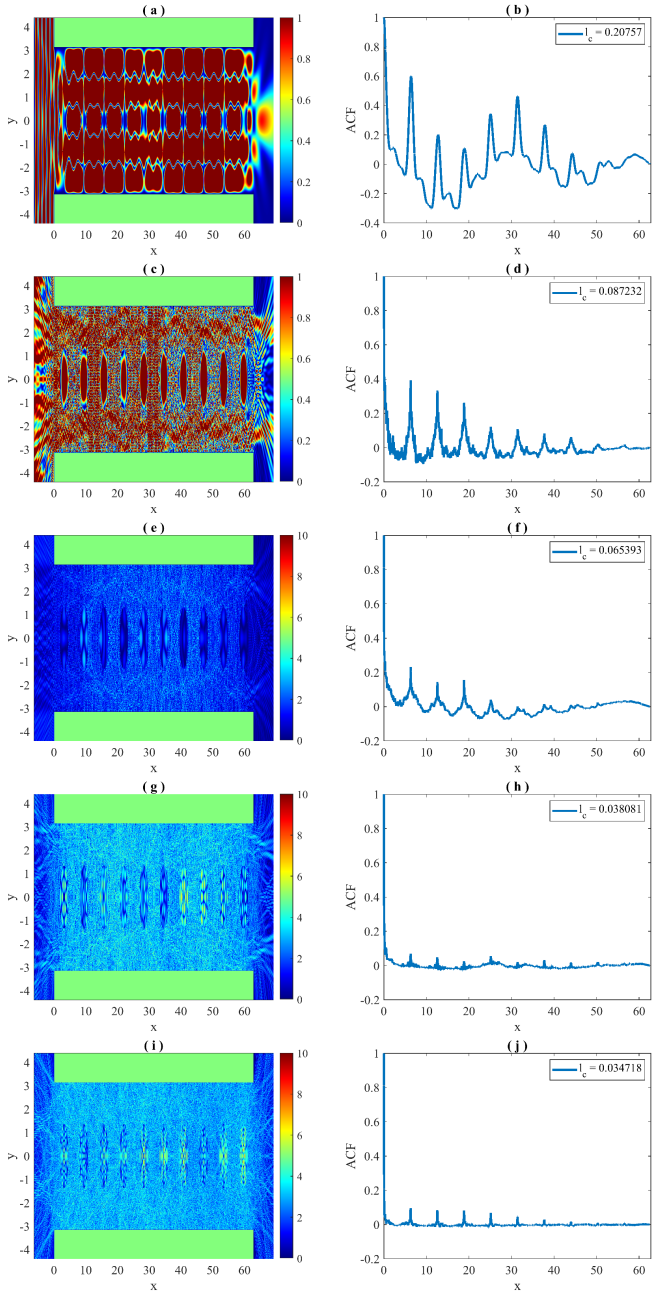

Figure 7 Pressure field intensity patterns and their respective ACFs for a finite PnCW with 10 large brass inclusion ($f = 0.3$) centered on the waveguide. The frequency values chosen for each field pattern are indicated in Table 3.

CONCLUSION

We conducted a theoretical and numerical study to analyze the chaotic effects in phononic crystal waveguides composed of two plane-parallel plates and a periodic arrangement of circular cylindrical inclusions with acoustic surfaces of real materials. We used the numerical integral method to study the acoustic response of the system and examine the chaos phenomenon present in it. In our simulations, we have observed that the periodic arrangement of circular cylindrical inclusions in our acoustic systems has a notable impact on the pressure field intensity patterns as the frequency increases. This effect has been studied using the ACF and it has been observed that the correlation length decays at higher frequencies in both types of systems considered. This behavior is an indication of the presence of chaotic behavior in the system due to non-periodicity and disordered response. These findings support our initial hypothesis and demonstrate that inclusions in the system introduce complex and chaotic dynamics in the propagation of acoustic waves. Our study has also revealed that the size and arrangement of circular cylindrical brass inclusions influence the acoustic response of the system. By changing the radius and position of the inclusions, significant changes in the intensity of the acoustic pressure field can be obtained. In summary, numerical analysis using the Integral Equation Method has allowed us to better understand the behavior of two-dimensional PnCW acoustic systems. This approach offers opportunities for design and optimization of acoustic devices with customized properties, and their application in fields such as sound engineering, acoustic communication, and noise control. Furthermore, the phenomenon of chaotic dynamics in PnCW could give rise to applications such as the detection of defects in crystal geometry with ACF, the transmission and control of acoustic waves with metamaterials (Deymier 2013), or information encryption (Bose and Pathak 2006; Zhou *et al.* 2014).

Acknowledgments

H. Pérez-Aguilar express their gratitude to the Coordinación de la Investigación Científica of the Universidad Michoacana de San Nicolás de Hidalgo for the financial support granted for the development of this research project. Likewise, this work was supported by Tecnológico Nacional de México (TecNM) unit Morelia, and Consejo Nacional de Humanidades Ciencias y Tecnologías (CONAHCYT).

Availability of data and material

Not applicable.

Conflicts of interest

The authors declare that there is no conflict of interest regarding the publication of this paper.

Ethical standard

The authors have no relevant financial or non-financial interests to disclose.

LITERATURE CITED

Beranek, L. L. and T. Mellow, 2012 *Acoustics: sound fields and transducers*. Academic Press.

Berry, M. V., 1977 Regular and irregular semiclassical wavefunctions. Journal of Physics A: Mathematical and General **10**: 2083–2091.

Blackstock, D. T., 2001 Chapter 2 Detailed Development of Acoustical Wave Equations, pp. 65–107 in *Fundamentals of Physical Acoustics*, Acoustical Society of America.

Bloch, F., 1929 Über die quantenmechanik der elektronen in kristallgittern. Zeitschrift für physik **52**: 555–600.

Bose, R. and S. Pathak, 2006 A novel compression and encryption scheme using variable model arithmetic coding and coupled chaotic system. IEEE Transactions on Circuits and Systems I: Regular Papers **53**: 848–857.

Chen, M., H. Jiang, H. Zhang, D. Li, and Y. Wang, 2018 Design of an acoustic superlens using single-phase metamaterials with a star-shaped lattice structure. Scientific reports **8**: 1–8.

de Rosny, J., A. Tourin, and M. Fink, 2000 Coherent backscattering of an elastic wave in a chaotic cavity. Physical review letters **84**: 1693–1695.

Dembowski, C., H.-D. Gräf, A. Heine, R. Hofferbert, H. Rehfeld, *et al.*, 2000 First experimental evidence for chaos-assisted tunneling in a microwave annular billiard. Physical review letters **84**: 867.

Deymier, P. A., 2013 *Acoustic metamaterials and phononic crystals*, volume 173. Springer Science & Business Media.

Doya, V., O. Legrand, and F. Mortessagne, 2002a Light scarring in an optical fiber. Physical Review Letters **88**: 014102.

Doya, V., O. Legrand, F. Mortessagne, and C. Miniatura, 2002b Speckle statistics in a chaotic multimode fiber. Physical Review E **65**: 056223.

El-Kady, I., R. Olsson III, and J. Fleming, 2008 Phononic band-gap crystals for radio frequency communications. Applied Physics Letters **92**: 233504.

Ellegaard, C., K. Schaadt, and P. Bertelsen, 2001 Acoustic chaos. Physica Scripta **2001**: 223–230.

Filippi, P., A. Bergassoli, D. Habault, and J. P. Lefebvre, 1998 *Acoustics: basic physics, theory, and methods*. Elsevier.

Ginsberg, J. H., 2018a Chapter 4 Principles and Equations for Multidimensional Phenomena, pp. 295–346 in *Acoustics: A Textbook for Engineers and Physicists*, Springer.

Ginsberg, J. H., 2018b *Acoustics: A Textbook for Engineers and Physicists*, volume 1. Springer.

He, J., S. Yang, Z. Hileman, R. Wang, D. Homa, *et al.*, 2020 An acoustic waveguide with tight field confinement for high temperature sensing. IEEE Sensors Journal **20**: 14126–14131.

Heller, E. J., 1984 Bound-state eigenfunctions of classically chaotic hamiltonian systems: scars of periodic orbits. Physical Review Letters **53**: 1515–1518.

Hensinger, W. K., H. Häffner, A. Browaeys, N. R. Heckenberg, K. Helmerson, *et al.*, 2001 Dynamical tunnelling of ultracold atoms. Nature **412**: 52–55.

Jia, Z., Y. Chen, H. Yang, and L. Wang, 2018 Designing phononic crystals with wide and robust band gaps. Physical Review Applied **9**: 044021.

Jing, L., Z. Li, Y. Li, and R. D. Murch, 2018 Channel characterization of acoustic waveguides consisting of straight gas and water pipelines. IEEE Access **6**: 6807–6819.

Kaplan, L., 1998 Wave function intensity statistics from unstable periodic orbits. Physical review letters **80**: 2582–2585.

Kaplan, L. and E. Heller, 1999 Measuring scars of periodic orbits. Physical Review E **59**: 6609–6628.

Khelif, A., A. Choujaa, S. Benchabane, B. Djafari-Rouhani, and V. Laude, 2004 Guiding and bending of acoustic waves in highly confined phononic crystal waveguides. Applied physics letters **84**: 4400–4402.

Kinsler, L. E., A. R. Frey, A. B. Coppens, and J. V. Sanders, 2000 *Fundamentals of acoustics*. John Wiley & Sons.

Kittel, C., P. McEuen, and P. McEuen, 1996 *Introduction to solid state physics*, volume 8. Wiley New York.

Kudrolli, A., M. C. Abraham, and J. P. Gollub, 2001 Scarred patterns in surface waves. Physical Review E **63**: 026208.

Kuhl, U., H. Stöckmann, and R. Weaver, 2005 Classical wave experiments on chaotic scattering. Journal of Physics A: Mathematical and General **38**: 10433.

Lee, H. S., D. H. Luong, M. S. Kim, Y. Jin, H. Kim, *et al.*, 2016 Reconfigurable exciton-plasmon interconversion for nanophotonic circuits. Nature communications **7**: 13663.

Legendre, P., 1993 Spatial autocorrelation: trouble or new paradigm? Ecology **74**: 1659–1673.

Liu, J., H. Guo, and T. Wang, 2020 A review of acoustic metamaterials and phononic crystals. Crystals **10**: 305.

Maldovan, M., 2013 Sound and heat revolutions in phononics. Nature **503**: 209–217.

McGurn, A. R., 2020 *Introduction to Photonic and Phononic Crystals and Metamaterials*. Morgan & Claypool Publishers.

Mendoza-Suárez, A. and H. Pérez-Aguilar, 2016 Numerical integral methods to study plasmonic modes in a photonic crystal waveguide with circular inclusions that involve a metamaterial. Photonics and Nanostructures-Fundamentals and Applications **21**: 1–12.

Mendoza-Suárez, A., H. Pérez-Aguilar, and F. Villa-Villa, 2011 Optical response of a perfect conductor waveguide that behaves as a photonic crystal. Progress In Electromagnetics Research **121**: 433–452.

Mendoza-Suárez, A. and F. Villa-Villa, 2006 Numerical method based on the solution of integral equations for the calculation of the band structure and reflectance of one- and two-dimensional photonic crystals. Journal of the Optical Society of America B **23**: 2249–2256.

Montenegro-García, A., 1989 La función de autocorrelación y su empleo en el análisis de series de tiempo. Revista Desarrollo y Sociedad pp. 117–132.

Mukhin, N., M. Kutia, A. Aman, U. Steinmann, and R. Lucklum, 2022 Two-dimensional phononic crystal based sensor for characterization of mixtures and heterogeneous liquids. Sensors **22**: 2816.

Navarro-Urrios, D., N. E. Capuj, M. F. Colombano, P. D. García, M. Sledzinska, *et al.*, 2017 Nonlinear dynamics and chaos in an optomechanical beam. Nature communications **8**: 14965.

Nöckel, J. U. and A. D. Stone, 1997 Ray and wave chaos in asymmetric resonant optical cavities. Nature **385**: 45–47.

Otsuka, P. H., K. Nanri, O. Matsuda, M. Tomoda, D. Profunser, *et al.*, 2013 Broadband evolution of phononic-crystal-waveguide eigenstates in real-and k-spaces. Scientific reports **3**: 3351.

Pennec, Y., B. D. Rouhani, E. El Boudouti, C. Li, Y. El Hassouani, *et al.*, 2010a Simultaneous existence of phononic and photonic band gaps in periodic crystal slabs. Optics express **18**: 14301–14310.

Pennec, Y., J. O. Vasseur, B. Djafari-Rouhani, L. Dobrzyński, and P. A. Deymier, 2010b Two-dimensional phononic crystals: Examples and applications. Surface Science Reports **65**: 229–291.

Pérez, H. I., C. I. Valencia, E. R. Méndez, and J. A. Sánchez-Gil, 2009 On the transmission of diffuse light through thick slits. Journal of the Optical Society of America A **26**: 909–918.

Pérez-Aguilar, H., A. Mendoza-Suárez, E. S. Tututi, and I. F. Herrera-González, 2013 Disordered field patterns in a waveguide with periodic surfaces. Progress In Electromagnetics Research B **48**: 329–346.

Pike, E. R. and P. C. Sabatier, 2001 *Scattering, Two-Volume Set: Scattering and Inverse Scattering in Pure and Applied Science*. Elsevier.

Ruelle, D., 1991 *Chance and Chaos*, volume 110. Princeton University Press.

Sinai, Y. G., 1970 Dynamical systems with elastic reflections. Russian Mathematical Surveys **25**: 137–189.

Sridhar, S., 1991 Experimental observation of scarred eigenfunctions of chaotic microwave cavities. Physical review letters **67**: 785–788.

Sridhar, S. and W. Lu, 2002 Sinai billiards, ruelle zeta-functions and ruelle resonances: microwave experiments. Journal of statistical physics **108**: 755–765.

Stöckmann, H.-J., 1999 *Quantum Chaos: An Introduction*. Cambridge University Press, New York.

Sugihara, G. and R. M. May, 1990 Nonlinear forecasting as a way of distinguishing chaos from measurement error in time series. Nature **344**: 734.

Torrent, D. and J. Sánchez-Dehesa, 2008 Acoustic cloaking in two dimensions: a feasible approach. New Journal of Physics **10**: 063015.

Vilela, M., N. Halidi, S. Besson, H. Elliott, K. Hahn, *et al.*, 2013 Fluctuation analysis of activity biosensor images for the study of information flow in signaling pathways. In *Methods in enzymology*, volume 519, pp. 253–276, Elsevier.

Villa-Villa, F., H. Pérez-Aguilar, and A. Mendoza-Suárez, 2017 The locally corrected Nyström method applied to 3D scalar SIE in acoustic cavities using curvilinear coordinates. Engineering Analysis with Boundary Elements **79**: 110–118.

Weaver, R. L., 1989 Spectral statistics in elastodynamics. The Journal of the Acoustical Society of America **85**: 1005–1013.

Wilkinson, P., T. Fromhold, L. Eaves, F. Sheard, N. Miura, *et al.*, 1996 Observation of 'scarred' wavefunctions in a quantum well with chaotic electron dynamics. Nature **380**: 608–610.

Zaki, S. E., A. Mehaney, H. M. Hassanein, and A. H. Aly, 2020 Fano resonance based defected 1D phononic crystal for highly sensitive gas sensing applications. Scientific Reports **10**: 17979.

Zhou, Y., Z. Hua, C.-M. Pun, and C. P. Chen, 2014 Cascade chaotic system with applications. IEEE transactions on cybernetics **45**: 2001–2012.

How to cite this article: Bucio-Gutiérrez, A., Pérez-Aguilar, H., and Alva-Medrano, H. E. Numerical Analysis of Chaos in a Phononic Crystal Waveguide with Circular Inclusions of Real Materials. *Chaos Theory and Applications*, 6(2), 111-121, 2024.

CHAOS
Theory and Applications
in Applied Sciences and Engineering

e-ISSN: 2687-4539
RESEARCH ARTICLE
Vol.6 / No.2 / 2024 / pp.122-130
Special Issue (EDIESCA 2023)
https://doi.org/10.51537/chaos.1376501

Emergent Behaviors in Coupled Multi-scroll Oscillators in Network with Subnetworks

A. Ruiz-Silva [*,1], **B.B. Cassal-Quiroga** [α,2], **Eber J. Ávila-Martínez** [β,3] **and H.E. Gilardi-Velázquez** [§,4]

*Programa de Ingeniería en Sistemas Biomédicos. Universidad Estatal de Sonora, Unidad Hermosillo, Ley Federal del Trabajo, Col. Apolo, 83100, Hermosillo, Sonora, México, αFacultad de Ciencias, Universidad Autónoma de San Luis Potosí. Av. Chapultepec 1570, Priv. del Pedregal, 78295, San Luis Potosí, S. L. P., México, βInnovaciones Tecnológicas Mercado S.A. de C.V., Av. Sierra Leona 418, Lomas 2a Secc., 78210, San Luis Potosí, S.L.P., México, §Facultad de Ingeniería, Universidad Panamericana, Josemaría Escrivá de Balaguer 101,20296 Aguascalientes, Aguascalientes, Mexico.

ABSTRACT This paper presents the emergence of two collective behaviors in interconnected networks. Specifically, the nodes in these networks belong to a particular class of piece-wise linear systems. The global topology of the network is designed in the form of connected subnetworks, which do not necessarily share the same structure and coupling strength. In particular, it is considered that there are two levels of connection, the internal level is related to the connection between the nodes of each subnetwork; while the external level is related to connections between subnetworks. In this configuration, the internal level is considered to provide lower bounds on the coupling strength to ensure internal synchronization of subnetworks. The external level has a relevant value in the type of collective behavior that can be achieved, for which, we determine conditions in the coupling scheme, to achieve partial or complete cluster synchronization, preserving the internal synchronization of each cluster. The analysis of the emergence of stable collective behavior is presented by using Lyapunov functions of the different coupling. The theoretical results are validated by numerical simulations.

KEYWORDS
Network of subnetworks
Multi-scroll systems
Synchronization
PWL systems

INTRODUCTION

In recent years, there has been a growing interest in the study of networks containing subnetworks, spanning various scientific and technological fields. This is because studying interconnected networks plays a fundamental role in modeling systems composed of multiple interacting components (Huang *et al.* 2008; Mucha *et al.* 2010; Lu *et al.* 2014; Boccaletti *et al.* 2023). Usually, a network of subnetworks is considered to be composed of a large set of interconnected groups, where subnetworks, clusters, or communities can be identified, sharing a common topological or dynamic classification feature (Chen *et al.* 2014; Kenett *et al.* 2015). Furthermore, synchronization in complex dynamic networks has many applications in different fields as secure communications (Méndez-Ramírez *et al.* 2023; Zhou and Wang 2016).

Manuscript received: 6 October 2023,
Revised: 15 November 2023,
Accepted: 4 December 2023.

[1]adriana.ruiz@ues.mx (**Corresponding author**)
[2]bahia.cassal@uaslp.mx
[3]phd.eber.avila.martinez@gmail.com
[4]hgilardi@up.edu.mx

In this field, research approaches can be categorized into two main lines. The first line concentrates on the analysis of the structural or spectral properties of networks of subnetworks, with the primary objective of characterizing the "subnetwork structure" of a complex system. This involves the identification of groups of closely interconnected nodes that can address aspects such as transitivity, degree distribution, the presence of recurring patterns, as well as the spectral characteristics of their Laplacian matrices (De Domenico *et al.* 2013; Cozzo *et al.* 2016; Tang *et al.* 2023; Katakamsetty *et al.* 2023). The second research line focuses on the dynamic properties of networks of subnetworks, where each subnetwork is composed of nodes with similar or identical dynamic properties Kenett *et al.* (2015). In this context, the principal objective is to describe the development of collective motion within these subnetworks, which includes the observation of various patterns of synchronized behavior and other dynamic phenomena (Liu *et al.* 2023; Arellano-Delgado *et al.* 2023; Boccaletti *et al.* 2014, 2023; Lu *et al.* 2014).

Many recent studies have been dedicated to analyzing the emergence of collective behavior in subnetworks, often defining two types of collective behaviors: inner synchronization and outer syn-

chronization. Usually, outer synchronization, also referred to as complete synchronization, happens when all nodes within a network of subnetworks synchronize their dynamics, demonstrating that same behavior or state. In outer synchronization, there is no distinction between nodes or subnetworks of nodes; instead, the entire network functions as a single coherent unit. This synchronization is typically observed in networks with strong couplings or interactions between nodes, where information and dynamics propagate swiftly throughout the network, resulting in a collective behavior where all nodes converge to the same state.

On the other hand, inner synchronization, also referred to as local synchronization or cluster synchronization, occurs when a subnetwork of nodes within a network achieve synchronization of their dynamics while maintaining distinct dynamics between the subnetwork or cluster (Ruiz-Silva and Barajas-Ramírez 2018; Ruiz-Silva 2021). In other words, nodes within each subnetwork synchronize with one another, while nodes in separate subnetworks exhibit distinct behaviors. Inner synchronization is often observed in networks with a modular or hierarchical structure, where nodes within the same module or hierarchy exhibit stronger synchronization with each other compared to nodes outside their respective module or hierarchy. It should be noted that most previous studies on cluster synchronization analyze the collective behavior for networks in which nodes are different systems where different emergent behaviors are mainly related to the nature of the nodes. However, there are few investigations focused on the synchronization problem for a set of dynamical systems that exhibit different collective behaviors in networks with identical nodes, where depending on the correlation between the states and the dynamical systems involved is the type of collective behavior that appears.

The simplest type of synchronization to identify is when states oscillate identically, and when they oscillate differently it is known as generalized synchronization. In particular, we consider piece-wise linear systems, since represent a specific category of dynamic systems that display linear properties within discrete regions of their state space, delimited by potentially nonlinear boundaries. These systems have proven to be valuable tools for modeling a wide range of phenomena in various disciplines, from physics to biology and engineering. In this research, we focus on the analysis of networks whose nodes are piece-wise linear systems, adding a layer of complexity to the interconnected dynamics. The use of this type of system is attributed to its facilitation of stability analysis for network models. Furthermore, there exist prior results regarding the synchronization of these systems in regular network models (Ruiz-Silva *et al.* 2022b; Ávila-Martínez *et al.* 2022; Ruiz-Silva *et al.* 2022a).

In this work, our primary focus is on the exploration of the emergence of collective behaviors in interconnected subnetworks under changes in the nature of coupling scheme, which have been configured with two levels of interconnection. The internal level pertains to individual connections within each subnetwork, while the external level encompasses connections between different subnetworks. It is imperative to highlight that the external level serves a dual role, as it not only facilitates communication between subnetworks but also plays a crucial role in determining the collective behaviors observed in the entire network. Furthermore, in order to simplify the analysis, the nodes are regarded as a specific class of piece-wise linear systems capable to displays infinite scrolls along one-dimensional grid (Gilardi-Velázquez *et al.* 2017).

In particular, we consider a network of identical multiscroll systems where the coupling scheme is linear, bidirectional, and diffusive, for which the emergence of stable collective behavior is analyzed. For this purpose, we consider that systems are coupled by one, two, or three state variables. There is a theoretical analysis to determine the conditions under which synchronization arises using a common Lyapunov function for all the nodes in an unweighted network. The stabilization analysis, in the synchronization problem between clusters in a complex network, is interesting because the individual dynamics of each cluster can have a different qualitative behavior that depends on the initial conditions and its inner coupling, hence the steady state of the synchronous solution. It isn't easy to know it a priori due to sensitivity to initial conditions. Moreover, numerical simulations are used to illustrate the emergent behavior in the networks of multi-scrolls as partial and complete cluster synchronization.

The rest of the document is structured as follows: First, we introduce multi-scroll systems, the subnetwork model, and the construction of the subnetwork network model. Second, we analyze the synchronized behavior for a subnetwork and network of subnetworks using Lyapunov stability theory. Third, we present a case study, followed by numerical simulations that illustrate our result. Finally, we conclude with a discussion of our findings.

PRELIMINARIES

Multi-scroll System

In literature, various approaches have been proposed for generating attractors with multiple scrolls (Campos-Cantón *et al.* 2010; Echenausía-Monroy and Huerta-Cuéllar 2020). It is widely known that the generation of this type of attractor is influenced both by the stability properties of the generated equilibrium points and the choice of an appropriate switching function for implementation. In general terms, it is possible to evaluate the stability of the equilibrium points in these systems by applying the theory of Unstable Dissipative Systems (UDS). This theory is formulated within a three-dimensional manifold encompassing dissipative and conservative components. Consequently, the coexistence of these two components results in the emergence of attractors referred to as multi-scroll attractors (Campos-Cantón *et al.* 2012; Campos-Cantón 2016).

As a previous work (Gilardi-Velázquez *et al.* 2017), we consider that each node is a nonlinear dynamical system defined for a specific class of affine linear systems given by the round function which is defined as follows:

$$\begin{aligned} \dot{\psi}_i &= A\psi_i + B(\psi_i), \\ \begin{bmatrix} \dot{x}_i \\ \dot{y}_i \\ \dot{z}_i \end{bmatrix} &= \begin{bmatrix} y_i \\ z_i \\ -a_{31}x_i - a_{32}y_i - a_{33}z_i \end{bmatrix} + \begin{bmatrix} 0 \\ 0 \\ c * Round\left(\frac{x_i}{0.6}\right) \end{bmatrix}, \end{aligned} \quad (1)$$

where $\psi_i = [x_i, y_i, z_i]^T \in \mathbb{R}^3$ is the state vector of the i-th node, the constant matrix $A = \{a_{ij}\} \in \mathbb{R}^{3\times3}$ is the linear operator of the system, and $B = [b_1, b_2, b_3]^T \in \mathbb{R}^3$ is the affine vector. It should be noted that the behavior of the system (1) is determined by the spectrum of matrix A, which can generate a wide variety of combinations and, therefore, various dynamic behaviors. In particular, (Gilardi-Velázquez *et al.* 2017) introduced a commutation law between different regions of the phase space, reflected in the affine vector B, which is controlled by the $Round(x)$ function. So that the system can show infinite scrolls along one dimension or infinite attractors for a specific bifurcation parameter, in this work we just

consider the parameters for which the systems display infinite scrolls.

Under these conditions, an example of the system described in equation (1) is shown in Figure 1 for $a_{31} = 10.5$, $a_{32} = 7.0$, $a_{33} = 0.7$, and $c = 6.3$ with initial condition $\psi_0 = [3, -0.5, 0.5]^T$. In Figure 1(a) we show the projection of the multi-scroll system onto the planes (x_i, y_i), (x_i, z_i), and (y_i, z_i). Figure 1(b) corresponds to the temporal behavior of the states x_i, y_i, and z_i with arbitrary units (a.u.) time. Additionally, in Figure 2 we show the phase portrait of the resulting attractor.

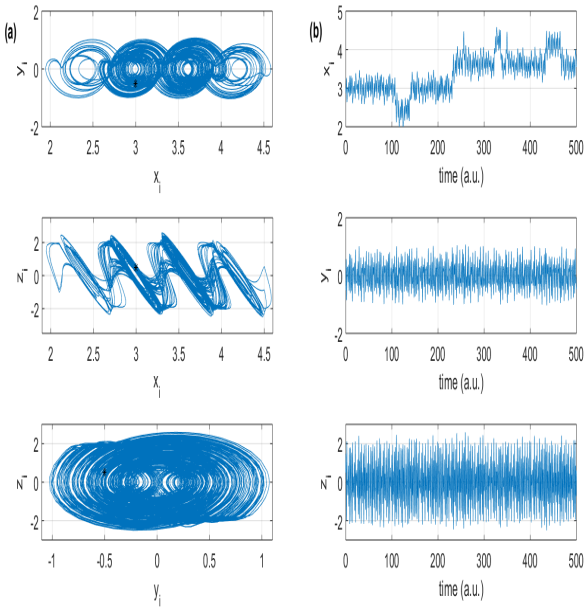

Figure 1 Projection of trajectories of the system (1) onto the the planes (x_i, y_i), (x_i, z_i) and (y_i, z_i), and time series with initial condition $\psi_0 = [3, -0.5, 0.5]^T$ marked by black asterisk.

Subnetworks model

Consider a regular dynamical subnetwork (RDS) formed by a set of r interconnected nodes, where each of the node is a multi-scroll system (1), and the interaction structure between them is modeled by a regular graph. Therefore, the individual dynamics of each node in the subnetwork of the RDS is given by:

$$\dot{\psi}_i^{[k]} = f(\psi_i^{[k]}) + g^{[k]} \sum_{j=1}^{r} \ell_{ij}^{[k]} \Gamma^{[k]} \psi_j^{[k]}, \text{ for } i = 1, 2, \cdots, r. \qquad (2)$$

Here, the supra-index k indicates the label of each subnetwork, $\psi_i^{[k]} = [x_i^{[k]}, y_i^{[k]}, z_i^{[k]}]^T \in \mathbb{R}^3$ is the state vector of i-th node in k-th subnetwork; $f(\psi_i^{[k]}) = A\psi_i^{[k]} + B(\psi_i^{[k]})$ determines the dynamics of an isolated node, i.e., multi-scroll system. The constant $g^{[k]} > 0$ denotes the uniform coupling strength of the subnetwork; $\Gamma^{[k]} \in \mathbb{R}^{3\times3}$ is a zero-one diagonal matrix describing the internal coupling between nodes in the k-th subnetwork. The Laplacian matrix gives its external coupling configuration for each subnetwork, $L^{[k]} = \{\ell_{ij}^{[k]}\} \in \mathbb{R}^{r\times r}$, which is considered to be a regularly connected graph. Furthermore, we assume that each subnetwork

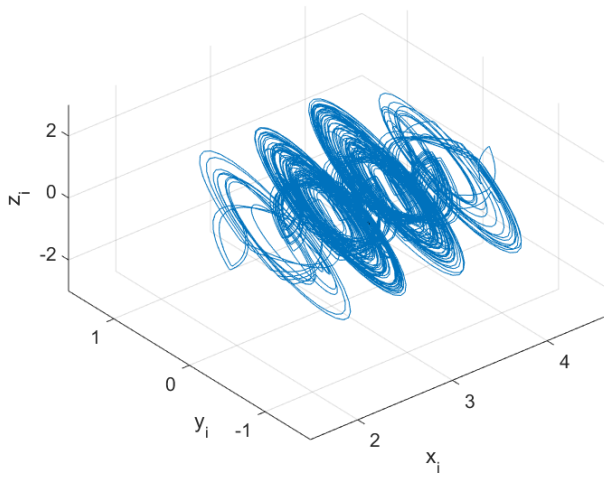

Figure 2 Multi-scroll attractor, in the phase space (x_i, y_i, z_i) with the initial condition $\psi_0 = [3, -0.5, 0.5]^T$.

is connected, *i.e.*, that there are no isolated nodes in the subnetwork. As a result, the Laplacian matrix, $L^{[k]}$, is a symmetric and irreducible matrix, with just one zero eigenvalue and all other eigenvalues strictly negative (Wang and Chen 2002).

Notice that in general, the set of admissible structures $L^{[k]}$ may include all possible patterns of connections. However, it is necessary to determine some restrictions when establishing the model for a network of subnetworks. Although they may be networks with different topologies, they must contain the same number of nodes.

Defining $\chi^k = [\psi_1^{[k]}, \psi_2^{[k]}, \cdots, \psi_r^{[k]}] \in \mathbb{R}^{3r}$ as the state variable of a single subnetwork. Then, (2) can be expressed as

$$\dot{\chi}^{[k]} = F^{[k]}(\chi^{[k]}, g^{[k]}, \Gamma^{[k]}, L^{[k]}). \qquad (3)$$

In what follows we will use the following shorthand notation, $F^{[k]}(\chi^{[k]})$, for the dynamics of the k-th subnetwork, whose elements depend on the coupling matrix, the connection strength and the internal dynamics of the nodes.

Network of subnetworks

Now, consider that M subnetworks are interconnected in a network model. In this context, the dynamical equation of the full system is described as follows

$$\dot{\psi}_i^{[k]} = f(\psi_i^{[k]}) + g^{[k]} \sum_{j=1}^{r} \ell_{ij}^{[k]} \Gamma^{[k]} \psi_j^{[k]} + \sum_{l=1}^{M} d_{kl} H^{[l]} \psi_i^{[l]}, \qquad (4)$$

for $i = 1, 2, \cdots, r$, and $k, l = 1, 2, \cdots, M$. Note that the first two terms on the right-hand side of (4) represent the individual dynamics of each subnetwork, whose elements were described in (2). While the third element to the right-hand side of (4) is related to the coupling among subnetworks.

Hence, $H^{[l]}$ is the inner connection matrix for nodes in different subnetworks, and the $D = \{d_{kl}\} \in \mathbb{R}^{M\times M}$ elements belong to the outer connection matrix for different subnetworks, which is constructed as follows: if a node in the k-th subnetwork is connected with its replica in the l-th subnetwork thus $d_{kl} \neq 0$ (with $k \neq l$), otherwise $d_{kl} = 0$, and $d_{kk} = -\sum_{l=1}^{M} d_{kl}$ for $k, l = 1, 2, \cdots, M$.

In vector form the eq. (4) can be written as:

$$\dot{\chi} = F(\chi) + (D \otimes H)\chi \tag{5}$$

where $\chi = [\chi^{[1]}, \chi^{[2]}, \cdots, \chi^{[M]}]^T \in \mathbb{R}^{3rM}$, is the state equations of the networks of subnetworks, with $\chi^{[k]} \in \mathbb{R}^{3r}$; $D \in \mathbb{R}^{M\times M}$ is the outer connection matrix described in the previous paragraph, while $H = Diag(H^{[1]}, H^{[2]}, \cdots, H^{[M]}) \in \mathbb{R}^{3r\times 3r}$, and $\otimes$ denotes the Kronecker product. It is worth noting that the network model describes all kinds of topologies, where they can consider connection patterns with uniform weights or non-uniform connections.

An example of our proposed structures is shown in Figure 3. In this case, both networks are composed of six subnetworks made up of $r = 4$ nodes, each of the subnetworks is represented by a color, and black lines represent the connections between the subnetworks. In Figure 3(a) all subnetworks have a star structure with a bidirectional coupling. Additionally, the connection between subnetworks is through a bidirectional ring structure. In Figure 3(b) the subnetworks have different topologies, and the connection between subnetworks is shown with some directed links.

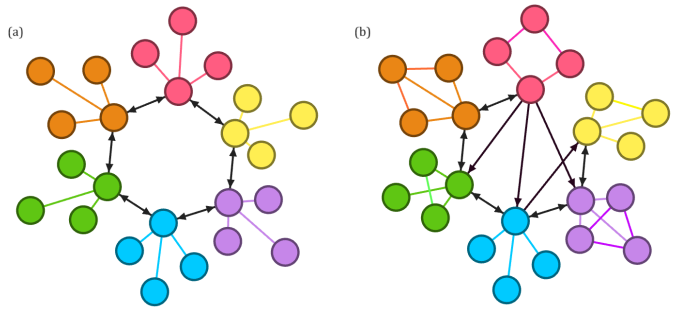

Figure 3 Two schematic illustrations of a network consisting of six subnetworks. Each subnetwork is represented by a color, and black lines represent the connections between subnetworks.

For complex dynamical networks, one of the most investigated collective behavior is synchronization, which occurs when the dynamics of its nodes are correlated over time (Chen *et al.* 2014; Pecora and Carroll 1998; Arenas *et al.* 2008). There are several definitions of synchronization among nodes in a network (Arenas *et al.* 2008). Even the definitions can be extended when considering the synchronization problem in a group of interconnected subnetworks.

In this paper, we will mainly focus on complete synchronization when discussing the subnetwork model. According to (Chen *et al.* 2014; Ruiz-Silva *et al.* 2021), a subnetwork of uniform, linearly, and diffusively coupled identical dynamical systems with a state equations description given by (2) is said to achieve (asymptotically) synchronization, if all the solutions converge to the same solution $s^{[k]}$ as t tends to infinity. For any initial condition in the neighborhood of the synchronization solution, one has that

$$\lim_{t\to\infty} \|\psi_i^{[k]} - s^{[k]}\| = 0, \text{ for } i = 1, 2, \cdots, r. \tag{6}$$

where $s^{[k]} \in \mathbb{R}^3$ satisfies the dynamics of an isolated multi-scroll attractor $\dot{s}^{[k]} = A(s^{[k]}) + B(s^{[k]})$.

To demonstrate that each subnetwork achieves the synchronization there are different methodologies. Following the proposal in (Ruiz-Silva *et al.* 2021) where they define the error as $e_i = \psi_i^{[k]} - s^{[k]}$ for each $i = 1, 2, \cdots, r$, and the error dynamics are linearized around the synchronization solution and diagonalized in terms of the eigenvalues of the Laplacian matrix for a subnetworks, resulting in the λ_2 criterion for the stability of the synchronized solutions. Therefore, the following Theorem has been reconstructed to establish *complete synchronization* on subnetwork:

Theorem 1 *(Ruiz-Silva et al. 2021) The RDS (2) achieves the complete synchronization (5). If the internal coupling matrix $\Gamma^{[k]} \in \Gamma_{cs}$ with*

$$\Gamma_{cs} = \{Diag(1,1,1),\ Diag(1,0,1),\ Diag(1,1,0),\ Diag(1,0,0)\}, \tag{7}$$

and the coupling strength, $g^{[k]} \in \mathbb{R}_+$ satisfies the condition:

$$g^{[k]} \geq \frac{|d^*|}{|\lambda_2^{[k]}|} \tag{8}$$

where d^* is a non-positive constant, and $\lambda_2^{[k]}$ is the largest nonzero eigenvalues of $L^{[k]} \in \mathbb{R}^{r\times r}$.

The above theorem is a useful result to simplify the analysis of the collective behaviors that can arise in a network of subnetworks. Therefore, when each subnetwork has completely synchronized the solution to (2) has r identical components $s^{[k]} \in \mathbb{R}^3$, which we write as $S^{[k]} = [s^{[k]}, s^{[k]}, \cdots, s^{[k]}]^T \in \mathbb{R}^{3r}$.

In this paper, our aim is to find sufficient conditions for the interconnected subnetwork to achieve different collective behavior. Since that we assume that each subnetwork achieves complete synchronization then the global analysis of collective behavior can be transformed into the synchronization problem for a weighted network. In this context, the complete and cluster synchronization between subnetworks is defined as follows:

Definition 1 *The network of subnetworks (4) is said to achieve identical synchronization, if*

$$\lim_{t\to\infty} \|S^{[k]} - S^{[l]}\| = 0, \text{ for } k, l = 1, 2, \cdots, M \tag{9}$$

where the symbols $\|\cdot\|$ is the Euclidean norm of a vector, and $S^{[k]}$ and $S^{[l]}$ are the synchronous solutions of the k-th and l-th subnetworks, respectively.

Definition 2 *The network of subnetworks (4) is said to achieve cluster synchronization, if nodes in the same subnetwork achieves the complete synchronization, in the sense of equation (6), and the differences among the synchronization solutions of different subnetworks do not converge to zero, i.e.,*

$$\lim_{t\to\infty} \|S^{[k]} - S^{[l]}\| = \epsilon, \text{ for } k, l = 1, 2, \cdots, M \tag{10}$$

where $\epsilon \in \mathbb{R}+$, and $S^{[k]}$ and $S^{[l]}$ are the synchronous solutions of the k-th and l-th subnetworks, respectively.

Synchronization stability analysis

To begin our analysis of the emergence of synchronized behavior in the network of subnetworks, we have the following assumptions:

A1. The interconnected subnetworks contain the same number of nodes.

A2. For simplicity, the inner connected matrices $H^{[l]}$ are the same throughout the network of the subnetworks model to be studied.

A3. From each weighted outer connected matrix D we obtain the unweighted matrix $\mathcal{B}$ whose elements are

$$b_{kl} = \begin{cases} 1 & d_{kl} \neq 0 \\ 0 & d_{kl} = 0 \end{cases}, \text{ for } k,l = 1,2,\cdots,M \text{ and } k \neq l. \quad (11)$$

and $b_{kk} = -\sum_{k=1,k\neq l}^{M} b_{kl}$. Also, these matrices satisfy the following condition

$$\lambda_2(D) \leq \tilde{d}\lambda_2(\mathcal{B}). \quad (12)$$

Similar to the case of a simple network, we need to find sufficient conditions to achieve complete synchronization or cluster synchronization. Firstly, we assume that there exists a global synchronization solution $S \in \mathbb{R}^{3rM}$, to which all subnetworks are synchronized so that analysis can be carried out. Here, the synchronization solution, S, may be an equilibrium point of the subnetwork, the average dynamics of all subnetworks, some periodic orbit, or a chaotic solution. Therefore, we define the error as $E_k = S^{[k]} - S$ for $k = 1,2,\cdots,M$, and its variational equation as follow

$$\dot{E}_k = F(E_k + S) - F(S) + \sum_{j=1}^{M} d_{kl} H E_l \quad (13)$$

The stability of the solution $S^{[k]}$ for the subnetwork interconnected in a weighted network can be established following a similar procedure as in (Ruiz-Silva *et al.* 2021; Ruiz-Silva and Barajas-Ramírez 2018). That is, by establishing stability conditions for an unweighted network, and the difference between the weighted and unweighted outer Laplacian matrices, we obtain sufficient conditions to guarantee synchronization. The result is stated in the following result:

Theorem 2 *Consider a dynamical network of M identical subnetworks (4), which satisfy conditions the Asssumptions **A1.** and **A2.**. If the elements of the outer connection matrix D satisfies*

$$d_{kl} \geq \frac{|d^*|}{|\mu_2|}, \quad (14)$$

*where d^* is a non-negative constant and μ_2 is the second largest eigenvalue of the unweighted outer connection matrix (Assumption **A3.**), then $E_k = 0$ for all $k = 1,2,\cdots,M$. Consequently, the network of subnetworks achieves synchronization.*

Proof: To prove the stability of the systems (13) a Lyapunov function is chosen as follows: $V = \frac{1}{2}\sum_{k=1}^{M} E_k^\top E_k > 0$. The time derivate of V along the trajectories of (13) gives:

$$\dot{V} = \sum_{k=1}^{M} E_k^T \left(F(E_k + S) - F(S) + \sum_{l=1}^{M} d_{kl} H E_l \right) \quad (15)$$

Assuming that each subnetwork is a connected graph, which achieves internal synchronization, it is considered that the dynamics of each subnetwork are bounded by

$$\|F(E_k + S) - F(S)\| \leq d\|E_k\|. \quad (16)$$

where d is a non-negative real number, which is related to a limit for the dynamics of each subnetwork in isolation. Due to the eigenvalues of the external coupling matrix D can be sorted in ascending order, this implies that $\bar{\mu}_k \leq \bar{\mu}_2$, and holds

$$\begin{aligned} \dot{V} &\leq \sum_{k=1}^{M} \left(dE_k^\top E_k + \sum_{l=1}^{M} E_k^\top (\bar{\mu}_2 H) E_l \right) \\ &\leq \sum_{k=1}^{M} \left(d\|E_k\|^2 - \bar{\mu}_2 h \sum_{l=1}^{M} \|E_k\|\|E_l\| \right) \end{aligned} \quad (17)$$

where $h > 0$ is the largest eigenvalue of the inner connection matrix. The right-hand side of (17) is quadratic in $p = (\|E_1\|, \|E_2\|, \cdots, \|E_M\|)^\top$, which can be written as $\dot{V} = -p^\top \Phi p$, whose elements are defined by

$$\phi_{kl} = \begin{cases} d - \bar{\mu}_2 h & l = k \\ -\bar{\mu}_2 h & l \neq k \end{cases} \quad (18)$$

If one choose $d \leq \bar{\mu}_2 h$, then $\Phi \geq 0$. If follows that $\dot{V} \leq 0$. Now to guarantee that the derivative of the Lyapunov function is strictly negative, we use the properties of the weighted and unweighted outer connection matrices.

Since the outer connection matrix satisfies the assumption **A3**. It follows that there exists a positive constant $\bar{d}$ such that the matrices satisfy $\bar{d}\mathcal{B} \geq D$. It is known that both matrices are negative semidefinite, which implies that their second largest non-zero eigenvalues are: $\mu_2 < 0$ for the weighted connection matrix and $\bar{\mu}_2 < 0$ for the unweighted connection matrix. Therefore,

$$\mu_2 \leq \bar{d}\bar{\mu}_2 \quad (19)$$

Additionally, individually the elements of the weighted matrix satisfy

$$d_{kl} > \bar{d} \; for \; k \neq l \;\; k,l = 1,2,\cdots,M \quad (20)$$

Now, defining a constant $d^* = d/h$ such that $d^* > d$, and using the (19)-(20), the condition (14) is obtained.

□

It is important to emphasize that the previous problem provides us with sufficient conditions for the error to be asymptotically stable. However, to achieve identical synchronization of the network of networks, the inner connection matrices of each subnetwork $H^{[l]}$ play a very important role because these matrices must be a combination of the matrices of the equation (7). So that the error in all states of the network is exactly zero. On the other hand, if the matrix H is made up of any linear combination that does not connect the first state of each node, then identical synchronization cannot be achieved, for these cases, the type of synchronization achieved is by cluster. To compactly express the previous discussion, the following two corollaries are extended from the theorem.

Corollary 1 *Ruiz-Silva* et al. *(2022b) The network of subnetworks (4) achieves the identical synchronization (9). If the elements of the outer connection matrix (14), and all inner connection matrix $H^{[l]}$ belongs to*

$$\{Diag(1,1,1),\ Diag(1,0,1),\ Diag(1,1,0),\ Diag(1,0,0)\} \quad (21)$$

for all $k = 1,2,\cdots,M$.

Corollary 2 *Ruiz-Silva* et al. *(2022b) The dynamical network (4) achieves the cluster synchronization (10). If the elements of the outer connection matrix (14), and some of the inner connection matrix $H^{[l]}$ belongs to*

$$\{Diag(0,1,0), Diag(0,0,1),\ Diag(0,1,1)\}, \quad (22)$$

for all $k = 1,2,\cdots,M$.

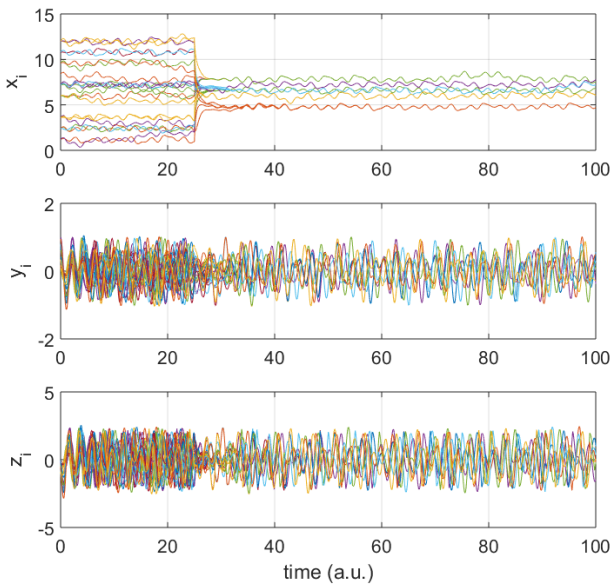

Figure 4 Numerical simulation of six decoupled subnetworks with an internal coupling matrix $\Gamma^{[k]} = Diag(1,0,1)$ for $k = 1,2,\cdots,M$, and the coupling strengths are: $g^{[1]} = 1$, $g^{[2]} = 2$, $g^{[3]} = 1.5$, $g^{[4]} = 3$, $g^{[5]} = 2.3$, $g^{[6]} = 4$

NUMERICAL SIMULATIONS

We consider a network of $M = 6$ subnetworks each made up of 4 identical multi-scroll systems (1). Thus, we describe the RDS model by equation (2) whose topology to use is a star graph (see Figure 3(a)).

First, it is necessary to ensure that identical synchronization is achieved within each RDS. In this example, let the internal coupling matrix $\Gamma = Diag(1,0,1)$ for each RDS. Consequently, condition (7) of Theorem 1 is satisfied, so it is necessary to obtain the appropriate critical value, d^*, associated with the internal matrix (see table 1). Finally, we calculate the minimum coupling strength to achieve synchronization, that is,

$$g^{[k]} > \frac{|d^*|}{|\lambda_2^k|} = \frac{0.9}{1}, \quad \text{for } k = 1,2,\cdots, M. \tag{23}$$

For this example, it is possible to choose the coupling strengths $g^{[1]} = 1$, $g^{[2]} = 2$, $g^{[3]} = 1.5$, $g^{[4]} = 3$, $g^{[5]} = 2.3$, $g^{[6]} = 4$, with which the conditions (7) of Theorem 1 are satisfied.

To illustrate the above in more detail, Figure 4 shows the time series of the subnetworks, with randomly chosen initial conditions. In numerical simulations, it is assumed that for t < 25 (a.u.) the nodes are decoupled so that each solution evolves its own attractor. While for t $\geq$ 25 (a.u.) the multi-scroll are connected in a subnetwork structure with a respective coupling strength. Moreover, for each subnetwork. In the first state of the nodes it is easy to observe how the trajectories collapse into six solutions, each one belonging to the synchronous state of each subnetwork.

Complete synchronization

Now, to illustrate complete synchronization in a network of subnetworks, we consider that the inner connection matrices described in Equation (21), particularly for $H^{[l]} = Diag(1,0,0) \in \mathbb{R}^{3\times 3}$ for $l = 1, 2, \cdots, M$, satisfying Corollary 1. Moreover, using the Table 1 we obtain the critical value for the entries of the outer Laplacian matrix, whose elements must satisfy the Theorem 2 equation (14), i.e.,

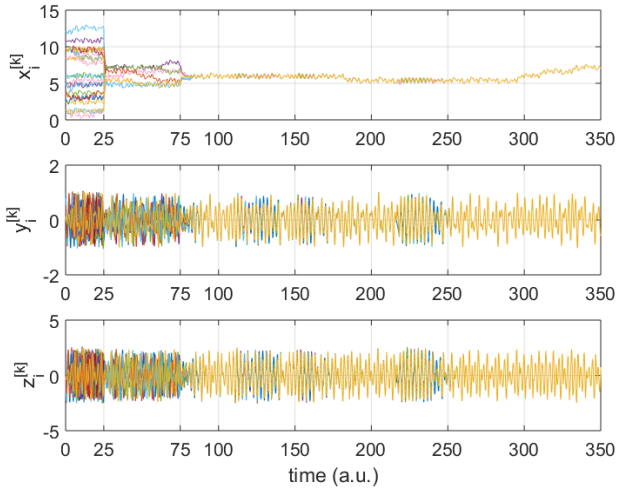

Figure 5 Numerical simulations of a network of six subnetworks interconnected in a ring structure, where the inner connection matrices are: $H^{[l]} = Diag(1,0,0)$ for $l = 1,2,\cdots,6$.

$$d_{kl} > \frac{|d^*|}{|\mu_2|} = \frac{3}{1}, \quad for \;\; k \neq l \tag{24}$$

and $k, l = 1,2,\cdots,M$. Consequently, we select the external connection matrix as:

$$\begin{pmatrix} -6.6 & 3.1 & 0 & 0 & 0 & 3.5 \\ 3.1 & -7.1 & 4 & 0 & 0 & 0 \\ 0 & 4 & -7.1 & 3.1 & 0 & 0 \\ 0 & 0 & 3.1 & -11.1 & 8 & 0 \\ 0 & 0 & 0 & 8 & -11 & 3 \\ 3.5 & 0 & 0 & 0 & 3 & -6.5 \end{pmatrix}. \tag{25}$$

The results of the numerical simulation are presented in Figures 5. First, for times less than 25, the 24 multi-scrolls of the global network are decoupled. At time 25, each of the subnetworks is individually connected with the aforementioned coupling strength, $g^{[k]}$. Furthermore, in the numerical simulation corresponding to the first state of the systems it is possible to observe how the 24 individual solutions collapse into six different solutions, that is, the synchronization solution of each subnetwork.

Finally, starting at time 75, the subnetworks are connected to each other, generating the entire network of the subnetworks model. Here, it can be observed how the trajectories of all subnetworks collapse in the three states, i.e., the nodes achieve complete synchronization. It is important to note that the synchronization solution location is related to the mean of each state for both cases: the subnetwork and the entire network (Ruiz-Silva *et al.* 2022b).

In Figure 6, we show the error synchronization between nodes that belong to different subnetworks. Since the subnetworks archive the complete synchronization, we can observe that the error converges to zero in the three states.

Table 1 Bounded of d^* for each internal coupling matrix

Γ	d^*	Γ	d^*
$Diag(1,1,1)$	0.6	$Diag(0,1,0)$	3.4
$Diag(1,0,1)$	0.9	$Diag(0,0,1)$	1.8
$Diag(1,1,0)$	0.32	$Diag(0,1,1)$	0.6
$Diag(1,0,0)$	3		

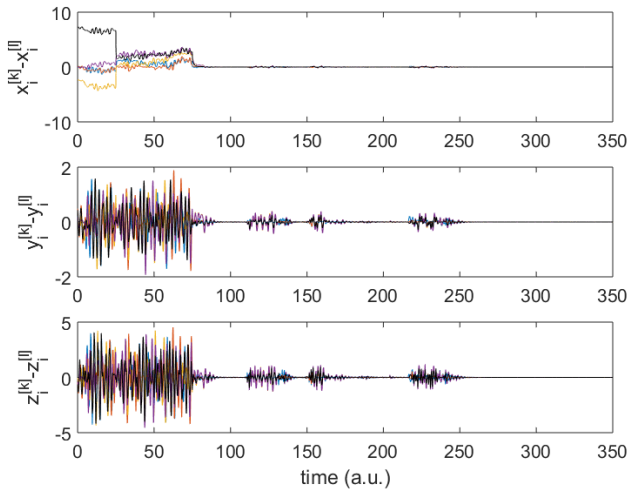

Figure 6 Evolution of the error synchronization between nodes of different subnetworks

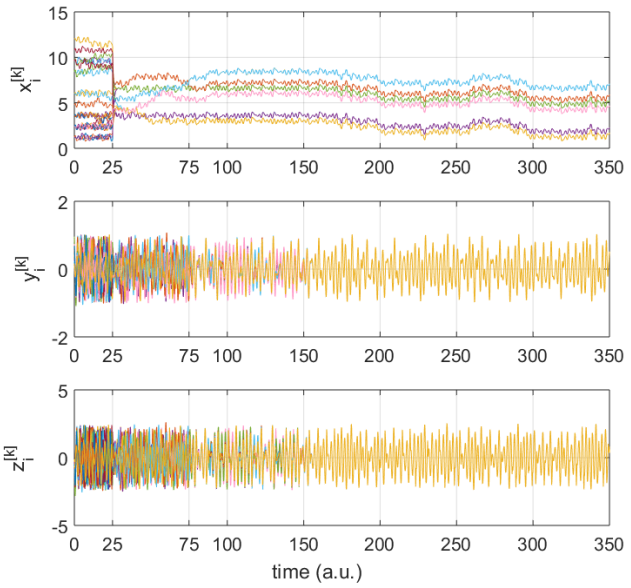

Figure 7 Numerical simulations of a network of six subnetworks interconnected in a ring structure, where the inner connection matrices are: $H^{[l]} = Diag(0,1,1)$ for $l = 1,2,\cdots,6$.

Cluster synchronization

For the cluster synchronization model, the same structure of the network of subnetworks is considered (see Figure 3 (a)), only that the association matrices between subnetworks described in eq. (22) particularly for $H^l = Diag(0,1,1)$ for $l = 1,2,\cdots,6$, satisfying Corollary 2.

Analogously to what is calculated in complete synchronization, the connection strength between the subnetworks can be calculated with Theorem 2, specifically with Equation (14). Under the proposed connection scheme, the critical value of d^* is 0.6 (see Table 1). Therefore, the elements of the external coupling matrix must satisfy

$$d_{kl} > \frac{|d^*|}{|\mu_2|} = \frac{0.6}{1}, \quad for \ k \neq l, \tag{26}$$

and $l = 1,2,\cdots,6$. It is easy to verify that the elements of the matrix (25) satisfy the previous condition. Therefore, it is the matrix that we will use for this scheme. The results of the numerical simulation are presented in Figure 7 where the dynamics of the six subnetworks are shown. First, for times less than 25, the 24 multiscrolls of the global network are decoupled. At time 25, each of the subnetworks is individually connected with the aforementioned coupling strength, $g^{[k]}$.

For simulation times less than 75 a.u., it is possible to observe the six synchronous solutions of each uncoupled subnetwork. Subsequently, starting at time 75 the subnetworks are connected to each other, it can be observed how the trajectories of all subnetworks collapse in two states, but they are kept separate in the first state, *i.e.* the complete synchronization in each subnetwork is preserved but the subnetworks reach partial synchronization between them. This can also be observed in Figure 8, note that the error between the nodes that connect the subnetworks are shown, where the error in the first state remains constant, and for the state two and three the error converges to zero.

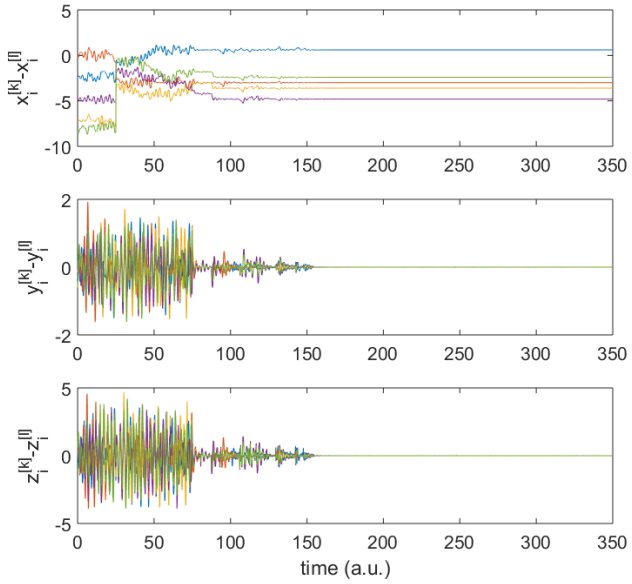

Figure 8 Evolution of the error synchronization between nodes of different subnetworks.

CONCLUSION

Our work focused on studying the synchronization of a set of coupled subnetworks and the emergence of collective behaviors in interconnected subnetworks when the coupling scheme changes. We considered subnetworks coupled by one, two, or three state variables and found two emerging behaviors in the synchronization state: complete and partial cluster synchronization. The results were validated using complex network theory and Lyapunov stability analysis and numerical simulations. In the first instance, we analyze a subnetwork of mutually coupled systems with uniform coupling strength, which must achieve complete synchronization to simplify the synchronization problem of a network of subnetworks. Furthermore, it is considered that the subnetworks have the same number of nodes and the same structure, so as not to have to perform an analysis to determine the node or nodes that should be interconnected between subnetworks. As a second instance, our analysis focused on the synchronization problem for subnetworks, where the outer connection matrix is crucial in determining the collective behavior of the network of subnetworks. In summary, this study delves into the emergence and characterization of collective behaviors in interconnected subnetworks. We strongly believe that the methodology discussed here can be applied to a subnetwork whose node dynamics are given by a broad class of PWL systems.

As future studies, it would be interesting to verify that the synchronization results can be extended to subnetworks with different structures or sizes, or even change the linear coupling between subnetworks.

Acknowledgments

Cassal-Quiroga B. B. (CVU:424203) acknowledges CONAHCYT financial support through the program "Estancias Posdoctorales por México 2022(1)".

Availability of data and material

Not applicable.

Conflicts of interest

The authors declare that there is no conflict of interest regarding the publication of this paper.

Ethical standard

The authors have no relevant financial or non-financial interests to disclose.

LITERATURE CITED

Arellano-Delgado, A., R. M. López-Gutiérrez, M. Á. Murillo-Escobar, and C. Posadas-Castillo, 2023 Master–slave outer synchronization in different inner–outer coupling network topologies. Entropy **25**: 707.

Arenas, A., A. Díaz-Guilera, J. Kurths, Y. Moreno, and C. Zhou, 2008 Synchronization in complex networks. Physics reports **469**: 93–153.

Ávila-Martínez, E. J., J. L. Echenausía-Monroy, and A. Ruíz-Sílva, 2022 Multi-scroll systems synchronization on strongly connected digraphs. Chaos Theory and Applications **4**: 205–211.

Boccaletti, S., G. Bianconi, R. Criado, C. I. Del Genio, J. Gómez-Gardenes, *et al.*, 2014 The structure and dynamics of multilayer networks. Physics reports **544**: 1–122.

Boccaletti, S., P. De Lellis, C. del Genio, K. Alfaro-Bittner, R. Criado, *et al.*, 2023 The structure and dynamics of networks with higher order interactions. Physics Reports **1018**: 1–64.

Campos-Cantón, E., 2016 Chaotic attractors based on unstable dissipative systems via third-order differential equation. International Journal of Modern Physics C **27**: 1650008.

Campos-Cantón, E., J. G. Barajas-Ramirez, G. Solis-Perales, and R. Femat, 2010 Multiscroll attractors by switching systems. Chaos: An Interdisciplinary Journal of Nonlinear Science **20**.

Campos-Cantón, E., R. Femat, and G. Chen, 2012 Attractors generated from switching unstable dissipative systems. Chaos: An Interdisciplinary Journal of Nonlinear Science **22**.

Chen, G., X. Wang, and X. Li, 2014 Fundamentals of complex networks : models, structures, and dynamics .

Cozzo, E., G. F. de Arruda, F. A. Rodrigues, and Y. Moreno, 2016 Multilayer networks: metrics and spectral properties. Interconnected networks pp. 17–35.

De Domenico, M., A. Solé-Ribalta, E. Cozzo, M. Kivelä, Y. Moreno, *et al.*, 2013 Mathematical formulation of multilayer networks. Physical Review X **3**: 041022.

Echenausía-Monroy, J. and G. Huerta-Cuéllar, 2020 A novel approach to generate attractors with a high number of scrolls. Nonlinear Analysis: Hybrid Systems **35**: 100822.

Gilardi-Velázquez, H. E., L. Ontañón-García, D. G. Hurtado-Rodriguez, and E. Campos-Cantón, 2017 Multistability in piecewise linear systems versus eigenspectra variation and round function. International Journal of Bifurcation and Chaos **27**: 1730031.

Huang, L., Y.-C. Lai, and R. A. Gatenby, 2008 Alternating synchronizability of complex clustered networks with regular local structure. Physical Review E **77**: 016103.

Katakamsetty, V. R., D. Rajani, and P. Srikanth, 2023 A study on community detection in multilayer networks. Journal of High Speed Networks pp. 1–13.

Kenett, D. Y., M. Perc, and S. Boccaletti, 2015 Networks of networks–an introduction. Chaos, Solitons & Fractals **80**: 1–6.

Liu, S., B. Xu, Q. Wang, and X. Tan, 2023 Synchronizability of multilayer star-ring networks with variable coupling strength. Electronic Research Archive **31**: 6236–6259.

Lu, R., W. Yu, J. Lü, and A. Xue, 2014 Synchronization on complex networks of networks. IEEE transactions on neural networks and learning systems **25**: 2110–2118.

Méndez-Ramírez, R., A. Arellano-Delgado, and M. Á. Murillo-Escobar, 2023 Network synchronization of macm circuits and its application to secure communications. Entropy **25**: 688.

Mucha, P. J., T. Richardson, K. Macon, M. A. Porter, and J.-P. Onnela, 2010 Community structure in time-dependent, multiscale, and multiplex networks. science **328**: 876–878.

Pecora, L. M. and T. L. Carroll, 1998 Master stability functions for synchronized coupled systems. Physical review letters **80**: 2109.

Ruiz-Silva, A., 2021 Synchronization patterns on networks of pancreatic β-cell models. Physica D: Nonlinear Phenomena **416**: 132783.

Ruiz-Silva, A. and J. G. Barajas-Ramírez, 2018 Cluster synchronization in networks of structured communities. Chaos, Solitons & Fractals **113**: 169–177.

Ruiz-Silva, A., B. Cassal-Quiroga, and H. Gilardi-Velázquez, 2022a Anti-synchronization in a pair of coupled multistable systems. In *Complex Systems and Their Applications: Second International Conference (EDIESCA 2021)*, pp. 23–37, Springer.

Ruiz-Silva, A., B. Cassal-Quiroga, G. Huerta-Cuellar, and H. Gilardi-Velázquez, 2022b On the behavior of bidirectionally coupled multistable systems. The European Physical Journal Special Topics **231**: 369–379.

Ruiz-Silva, A., H. Gilardi-Velázquez, and E. Campos, 2021 Emergence of synchronous behavior in a network with chaotic multistable systems. Chaos, Solitons & Fractals **151**: 111263.

Tang, F., X. Zhao, and C. Li, 2023 Community detection in multilayer networks based on matrix factorization and spectral embedding method. Mathematics **11**: 1573.

Wang, X. F. and G. Chen, 2002 Synchronization in small-world dynamical networks. International Journal of Bifurcation and chaos **12**: 187–192.

Zhou, L. and C. Wang, 2016 Hybrid combinatorial synchronization on multiple sub-networks of complex network with unknown boundaries of uncertainties. Optik **127**: 11037–11048.

How to cite this article: Ruiz-Silva, A., Cassal-Quiroga, B.B., Ávila-Martínez, E.J., and Gilardi-Velázquez, H.E. Emergent Behaviors in Coupled Multi-scroll Oscillators in Network with Subnetworks. *Chaos Theory and Applications*, 6(2), 122-130, 2024.

CHAOS
Theory and Applications
in Applied Sciences and Engineering

e-ISSN: 2687-4539
RESEARCH ARTICLE
Vol.6 / No.2 / 2024 / pp.131-143
Special Issue (EDIESCA 2023)
https://doi.org/10.51537/chaos.1372066

Opposition to Synchronization of Bistable State in Motif Configuration of Rössler Chaotic Oscillator Systems

J. H. García-López [1,α], **R. Jaimes-Reátegui** [2,α], **G. Huerta-Cuéllar** [3,α] **and D. López-Mancilla** [4,*]

[α]Optics, Complex Systems, and Innovation Laboratory, Centro Universitario de los Lagos, Universidad de Guadalajara, Lagos de Moreno, 47463, Jalisco, Mexico, [*]Control Laboratory, Centro Universitario de los Lagos, Universidad de Guadalajara, Lagos de Moreno, 47463, Jalisco, Mexico.

ABSTRACT This paper presents the study of the opposition to the synchronization of bistable chaotic oscillator systems in basic motif configurations. The following configurations were analyzed: Driver-response oscillator systems coupling, two driver oscillator systems to one response oscillator, and a three-oscillator systems ring unidirectional configuration. The study was conducted using the differential equations representing the piecewise linear Rössler-like electronic circuits; the initial conditions were changed to achieve a bistable characteristic Homoclinic **H**-type or Rössler **R**-type attractor. Analyzing a sweep of the initial conditions, the basin attractor was obtained. It can be observed that each system has a preferred Homoclinic chaotic attractor with any perturbation or change in initial conditions. A similarity analysis based on the coupling factor was also performed and found that the system has a preferentially Homoclinic chaotic attractor.

KEYWORDS
Rössler oscillator
Opposition to synchronization
Complex network
Coupled oscillators

INTRODUCTION

According to the Britain English dictionary, the meaning of the term synchronization is to occur at the same time. This phenomenon is now known as synchronization and represents the adjustment of the rhythm of the oscillations of two or more systems due to the weak interaction between them. Synchronization is commonly understood as a collective state of a coupled system. In general, it indicates the existence of some relation between functions of the different processes due to interaction (Boccaletti *et al.* 2001). Synchronization is also a process during which coupled system adjust their individual frequency in an organized fashion. Synchronization is a process where, due to their interaction or an external driving force, a dynamic system adjusts some properties of their trajectories so that they eventually operate macroscopically coherently.

The first studies on synchronization are historically attributed to the Dutch scientist Christian Huygens who invented two pendulum clocks attached to the same beam supported by two chairs in 1657. Studying synchronization in dynamic systems is extremely important in science and engineering and has numerous applications in many fields, from mechanics and electronics to physics, chemistry, biology, and even economics. Synchronization is ubiquitous in a natural and man-made system (Rosenblum and Kurths 2003; Boccaletti 2008). As examples of synchronization motion that are observed in a real-world system, we can mention a symphony orchestra is synchronized by the conductor, a school of fish changing its shape when attacked by sharks, the unison song of crickets, the synchronous rhythmic flash of fireflies observed in Borneo forest, the spontaneous synchronizations of clapping in a human platea.

Another manifestation of synchronization is the study conducted by Farkas *et al.* (2002) focusing on "La ola," which serves as an example illustrating how synchronization behaviors emerge within complex dynamical systems. Under specific initial conditions, this system transitions from a dormant state with sporadic fluctuations (where most individuals are seated, occasionally with a few raised hands) to a collective action phase. During this phase, the crowd synchronizes coherently by standing up with raised arms and sitting down, creating a phenomenon resembling a traveling wave – commonly known as "La ola" – that periodically traverses the stadium.

In man-made systems, physical devices exist where synchronous behavior enhances overall performance. An example is the Van der Pol electrical circuit (1889-1959), which employed vacuum tubes and discovered that they exhibit stable oscillations. When these circuits were driven by a periodic signal near the limit

Manuscript received: 6 October 2023,
Revised: 15 November 2023,
Accepted: 4 December 2023.

[1]jhugo.garcia@academicos.udg.mx
[2]rider.jaimes@academicos.udg.mx (**Corresponding author**)
[3]guillermo.huerta@academicos.udg.mx
[4]didier.lopez@academicos.udg.mx

cycle, their oscillation frequency became entrained by the external driven. This discovery had a great deal of practical importance because the vacuum tube was, at that time, the basic element of the radio communications systems (Pol and Mark 1927).

Furthermore, an arrangement of Josephson junctions exhibits heightened output power when these junctions oscillate in synchrony, as Barbara et al. (1999) demonstrated. Synchronous periodic states have been documented in numerous dynamic processes across diverse scientific and engineering domains. For a comprehensive exploration of this topic, we recommend readers consult the outstanding monograph authored by Pikovsky et al. (2001). Therefore, the examination of synchronization within complex systems holds a dual significance: from a theoretical standpoint, it provides valuable insights into understanding natural phenomena, and from a technological point of view, it proves to be advantageous for the development of high-performance devices and systems. During these years, chaotic synchronization has attracted great interest in applications such as the design of private and secure communication systems from the paper by Sharma and Ott (2000), to Méndez-Ramírez *et al.* (2023).

Currently, various forms of chaos synchronization can be distinguished. These include Complete Synchronization: The most robust form of synchronization where the state variables of two systems perfectly coincide Pikovsky *et al.* (2001); Phase Synchronization: Which involves a phase difference between chaotic oscillations locked within a range of 2π, representing the weakest manifestation of synchronization in chaotic systems Pecora and Carroll (1990); Antiphase Synchronization: Defines a state where the variables of two interacting systems have the same amplitude but differ in sign Rosenblum *et al.* (1996); Lag Synchronization: Characterized by the coincidence of two chaotic trajectories with a constant time lag Liu *et al.* (2006); Anticipating Synchronization: The opposite of lag synchronization, wherein chaotic trajectories coincide with a constant anticipated time Rosenblum *et al.* (1997); Generalized Synchronization: Involves trajectories of coupled systems that exhibit a specific functional dependence on each other, often utilized to describe synchronous behavior in coupled non-identical systems Rulkov *et al.* (1995). Additionally, there are unstable synchronization states like Intermittent Synchronization, which occurs when any form of synchronization is intermittently interrupted by asynchronous oscillations or the system changes synchronization type periodically, such as switching between phase synchronization and lag synchronization reported by Gauthier and Bienfang (1996); Buldú *et al.* (2006); Pisarchik and Jaimes-Reategui (2005).

Most research on synchronization has primarily focused on monostable systems, which are relatively straightforward dynamical systems characterized by a single attractor when they are uncoupled. However, the prediction of synchronization in multistable systems remains a topic of significant debate, even in seemingly uncomplicated systems like iterative maps. Multistability is a phenomenon that arises in dissipative systems when multiple stable attractors coexist for a specific set of system parameters. This phenomenon has been observed across various scientific domains, including electronics Maurer and Libchaber (1980), optics Brun *et al.* (1985), mechanics Stewart *et al.* (1986), and biology Foss *et al.* (1996). The mechanisms underlying multistability can be diverse, encompassing delayed feedback and homoclinic tangencies in weakly dissipative systems Boccaletti *et al.* (2018). Nonetheless, despite potential differences in the origins of multistability, multistable systems share several common traits. They all exhibit an extremely high sensitivity to initial conditions, where even the slightest perturbations can significantly change the final attractor state. Additionally, their qualitative behavior often undergoes dramatic shifts with only minor parameter variations Boccaletti *et al.* (2018).

Recently, Ahmed *et al.* (2016) conducted a study on robust synchronization in multistable systems evolving on manifolds within an Input-to-State Stability framework. Parallelly, Pm and Kapitaniak (2017) explored synchronization in coupled multistable systems featuring hidden attractors. Additionally, Khan *et al.* (2017) achieved the design of multistable systems through partial synchronization. It is noteworthy that highly multistable synchronized systems can be engineered, wherein all states of one system synchronize with their corresponding states in the other system, as demonstrated by Chakraborty and Poria (2019) and Khan *et al.* (2021). Furthermore, Dudkowski *et al.* (2021) illustrated that multistable synchronous states, encompassing in-phase, anti-phase, and phase-locked synchronization, can emerge based on parameters and initial conditions.

Moreover, Moskalenko *et al.* (2021) made a significant contribution by discovering multistability within the intermittent generalized synchronization regime in unidirectionally coupled chaotic systems. Additional noteworthy work on synchronization in multistable systems has been conducted by Ruiz-Silva *et al.* (2021); Vaidyanathan *et al.* (2022). Similarly, the synchronization of chaotic oscillator system with the application to new technologists has become an area of great importance as it allows us to perform information security analysis in various communication schemes, such as information encryption, data hiding, secure wireless communication, machine-to-machine communication, watermarking, synchronization of chaos, image encryption by Rodríguez-Orozco *et al.* (2018); García-Guerrero *et al.* (2020); Sarosh *et al.* (2022) and Trujillo-Toledo *et al.* (2023).

Nevertheless, developing the states within multistable systems when these systems are coupled remains a largely unresolved question, particularly when dealing with complex scenarios like the coupling of three chaotic bistable systems arranged in a motif configuration. One may naturally speculate about the behavior of the motif system as the coupling strength is increased. It might seem intuitive that the motif system would initially adjust its state to that of one of the bistable systems, transforming the problem into a well-understood case involving identical chaotic monostable systems. However, this simplistic view only captures part of the truth. In this context, the synchronization of multistable systems has received relatively little attention. In a preliminary investigation, we explored the synchronization of two identical chaotic bistable systems coupled in a driver-response oscillator configuration, exemplified by Homoclinic **H**-type or the Rössler **R**-type of the attractor Pisarchik *et al.* (2006).

A homoclinic orbit normally changes its period when the number of loops of the orbit increases or decreases by one saddle point by adding or omitting a loop while varying a control parameter by Pisarchik *et al.* (2005). Our findings revealed that the dynamics of coupled multistable systems are remarkably intricate, encompassing various forms of phase synchronization. The main objective of this work is to study of the opposition to synchronization of bistable chaotic oscillator systems. Our focus here is on synchronizing three coupled chaotic bistable systems arranged in a motif configuration. We examine electronic circuits that resemble Rössler-like systems as previously used by Pecora and Carroll (1990); Carroll and Pecora (1995) in their synchronization studies in chaotic systems.

The next sections of this manuscript are outlined as follows. In Section 2, we provide an overview of the mathematical model. Section 3 offers a detailed examination of the dynamics of an isolated Rössler oscillator, encompassing the bifurcation diagram and the system's time series. Section 4 investigates the synchronization stage of two coupled Rössler oscillators. Section 5 extends this analysis to three coupled Rössler oscillators, presenting the outcomes of numerical simulations and a comprehensive description of the synchronization stages observed. Finally, the conclusions derived from this numerical study are resumed in Section 6.

MATHEMATICAL MODEL

Presenting our analysis without generalization, let us consider the following case: **(a) First case** two identical unidirectional coupled chaotic oscillators, where the driver system is represented by Eqs. (1) and the response system by Eqs. (2), see Fig. 1; **(b) Second case** is shown in the Fig. 2: Three identical coupled chaotic oscillators in network motif configuration, two driver oscillators and one response oscillator represented by the systems of Eqs. (3), Eqs. (4) and Eqs. (5); **(c) Third case** in a ring configuration where all oscillators act together as a driver and response system, represented in this case by the systems of Eqs. (6), Eqs. (7) and Eqs. (8) and shown in the Fig. 3. For all cases, piecewise linear Rössler-like oscillators.

Two identical unidirectional driver-response coupled chaotic oscillators

$$\begin{aligned} \dot{x_1} &= -\delta x_1 - \beta y_1 - \lambda z_1, \\ \dot{y_1} &= x_1 + \gamma y_1, \\ \dot{z_1} &= g(x_1) - z_1, \end{aligned} \tag{1}$$

$$\begin{aligned} \dot{x_2} &= -\delta x_2 - \beta[y_2 - \epsilon(y_2 - y_1)] - \lambda z_2, \\ \dot{y_2} &= x_2 + \gamma[y_2 - \epsilon(y_2 - y_1)], \\ \dot{z_2} &= g(x_2) - z_2, \end{aligned} \tag{2}$$

where

$$g(x_{1,2}) = \begin{cases} 0, \text{ if } x_{1,2} \leq 3 \\ \mu(x_{1,2}), \text{ if } x_{1,2} > 3 \end{cases}$$

with $\delta = 0.05$, $\beta = 0.50$, $\lambda = 1.00$, $\gamma = \frac{R}{R_c}$, (in the experimental circuits $R = 10k\Omega$ and $R_c = 32k\Omega$) and $\epsilon \in [0, 1]$ is the coupling strength.

Three identical coupled chaotic oscillators, two drivers and one response

$$\begin{aligned} \dot{x_1} &= -\delta x_1 - \beta y_1 - \lambda z_1, \\ \dot{y_1} &= x_1 + \gamma y_1, \\ \dot{z_1} &= g(x_1) - z_1, \end{aligned} \tag{3}$$

$$\begin{aligned} \dot{x_2} &= -\delta x_2 - \beta y_2 - \lambda z_2, \\ \dot{y_2} &= x_2 + \gamma y_2, \\ \dot{z_2} &= g(x_2) - z_2, \end{aligned} \tag{4}$$

$$\begin{aligned} \dot{x_3} &= -\delta x_3 - \beta[y_3 - \epsilon(y_3 - y_2 - y_1)] - \lambda z_3, \\ \dot{y_3} &= x_3 + \gamma[y_3 - \epsilon(y_3 - y_2 - y_1)], \\ \dot{z_3} &= g(x_3) - z_3, \end{aligned} \tag{5}$$

where $g(x_{1,2,3}) = \begin{cases} 0, \text{ if } x_{1,2,3} \leq 3 \\ \mu(x_{1,2,3}), \text{ if } x_{1,2,3} > 3 \end{cases}$

with the same values for the parameters δ, β, λ, $\gamma = \frac{R}{R_c}$ and $\epsilon \in [0, 1]$ with similar coupling strength for all systems of equations.

Three identical coupled chaotic oscillators in a unidirectional ring configuration (or a motif configuration in which all oscillators act as driver and response form)

$$\begin{aligned} \dot{x_1} &= -\delta x_1 - \beta[y_1 - \epsilon_1(y_1 - y_3))] - \lambda z_1, \\ \dot{y_1} &= x_1 + \gamma[y_1 - \epsilon_1(y_1 - y_3)], \\ \dot{z_1} &= g(x_1) - z_1, \end{aligned} \tag{6}$$

$$\begin{aligned} \dot{x_2} &= -\delta x_2 - \beta[y_2 - \epsilon_2(y_2 - y_1)] - \lambda z_2, \\ \dot{y_2} &= x_2 + \gamma[y_2 - \epsilon_2(y_2 - y_1)], \\ \dot{z_2} &= g(x_2) - z_2, \end{aligned} \tag{7}$$

$$\begin{aligned} \dot{x_3} &= -\delta x_3 - \beta[y_3 - \epsilon_3(y_3 - y_2)] - \lambda z_3, \\ \dot{y_3} &= x_3 + \gamma[y_3 - \epsilon_3(y_3 - y_2)], \\ \dot{z_3} &= g(x_3) - z_3, \end{aligned} \tag{8}$$

where $g(x_{1,2,3}) = \begin{cases} 0, \text{ if } x_{1,2,3} \leq 3 \\ \mu(x_{1,2,3}), \text{ if } x_{1,2,3} > 3 \end{cases}$

in this third case was used same values for the parameters δ, β, λ, $\gamma = \frac{R}{R_c}$ and $\epsilon_{1,2,3} \in [0, 1]$ with similar coupling strength for all systems of equations.

DYNAMIC OF AN ISOLATED OSCILLATOR

When the driver and response chaotic oscillator, systems of Eqs.1 and Eqs.2 are not coupled ($\epsilon = 0$), each of them exhibits a complex dynamical behavior depending on the control parameter Rc and the initial condition. Fig. 4 (a) shows the bifurcation diagram of the local maximum of the variables x_1 of Eqs.1 as a function of the parameter Rc. This bifurcation diagram is computed under different initial conditions and shows different coexisting attractors. For large values of $28k\Omega < Rc < 141k\Omega$, the variable $x_1 < 3$ the dynamics of the system Eqs.1 or Eqs.2 similar to the classical Rössler oscillator. It exhibit route to the Rössler chaos from a limit cycle with one period and a period-doubling when R_c decreases.

An interesting result was found at relatively low values of the control parameter $R_c < 34k\Omega$, once the variable $x_1 > 3$, a second, different chaotic attractor appears, a Homoclinic-type chaotic attractor coexisting with Rössler-type chaotic attractors. The enlarged part of the bifurcation diagram in the region of small values of $Rc < 34k\Omega$ is shown in Fig. 4 (b). The diagram contains two branches, the red and blue dots, which are obtained by taking different initial conditions. The branch with the red dot corresponds to the typical dynamics of the classical Rössler chaotic attractor, while the branch with the blue dot corresponds to the Homoclinic chaotic attractor. The left column in Fig. 5 represents the Rössler chaotic attractor, in which we plot the time series in Fig. 5 (a), the phase space 5 (c), and the power spectra 5 (e). Fig. 5 right column shows the homoclinic chaotic attractor, where the time series Fig. 5 (b), the phase space 5 (d), and the power spectrum 5 (f) are shown.

In Fig. 6 we show the Poincare section for z_1 of the Eqs.1 or Eqs.2 without coupling. The initial condition for the system Eqs.1 or Eqs.2 representing a homoclinic chaotic attractor **H** is reached using I.C.: $x_{10} = 2.38019$, $y_{10} = -5.31956$ and $z_{10} = 2.32858$, see Fig. 6a and showing a Rössler chaotic attractor **R** is reached using I.C.: $x_{20} = 3.034636$, $y_{20} = -4.64063$ and $z_{20} = 0.00920$ see Fig. 6b. In this Poincare section, the basin attraction of the Rössler and Homoclinic chaotics attractors are presented in green and blue colors, respectively. In both plots of the Fig. 6 we can see that the basin attraction of the homoclinic-type chaotic attractor is much

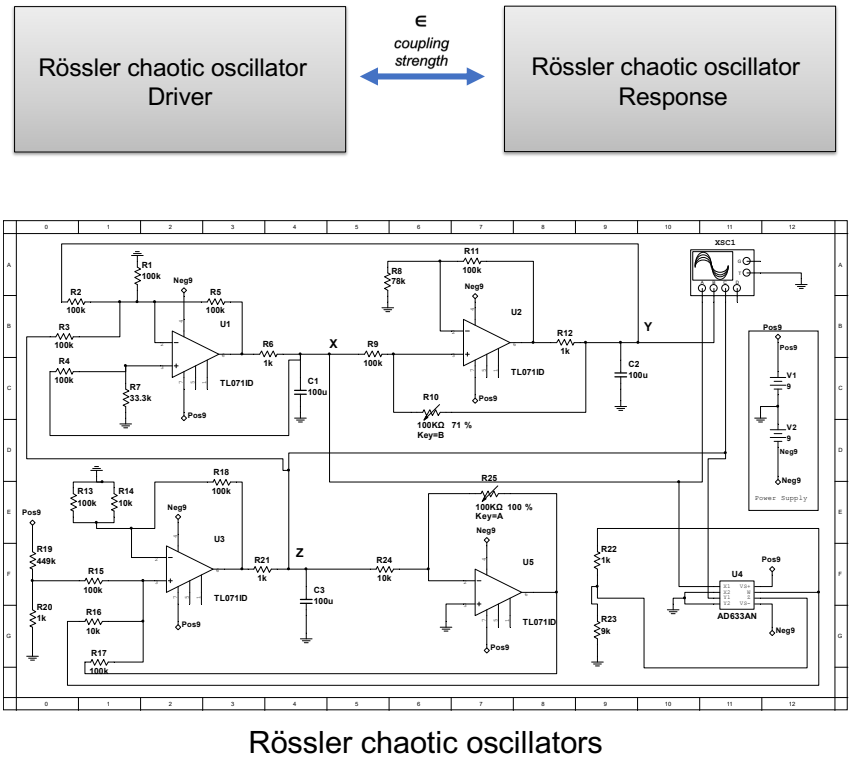

Figure 1 Two identical oscillators, unidirectionally coupled (up) and piecewise linear Rössler-like electronic circuits (down)

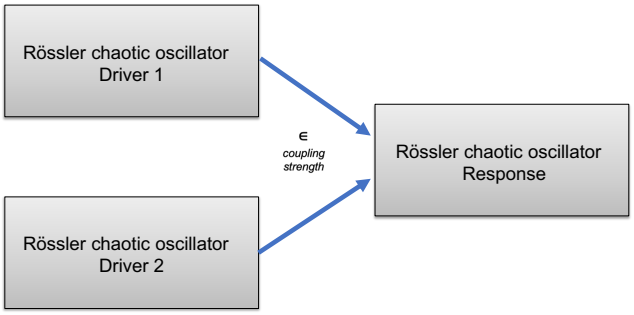

Figure 2 Two drives and one response motif configuration, unidirectionally coupled

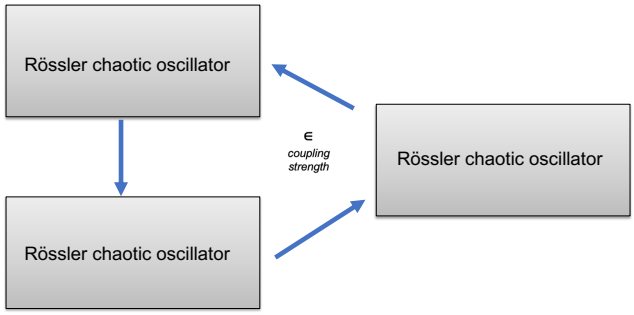

Figure 3 Rössler system unidirectional (A ring of three nodes) motif configuration

larger than the basin attraction of the Rössler-type chaotic attractor and while that the yellow region shows that the system of equation 1 or equation 2 without coupling has no solution.

To study the synchronization of multistable systems, we fixed the control parameter $Rc = 32k\Omega$, where our system exhibits the coexistence of two different chaotic attractors. Then we chose the initial condition for drive system Eqs.1 and response system Eqs.2 so that their chaotics state would be different without coupling $\epsilon_2 = 0$.

Quantitatively, phase synchronization between a pair of oscillators i and j can be characterized by the difference phase between their instantaneous phases Rosenblum and Kurths (2003),

$$\theta_{i,j} = \phi_i - \phi_j \tag{9}$$

$$\phi_{i,j} = arctan(\frac{y_{i,j}}{x_{i,j}}) \tag{10}$$

whereas identical or complete synchronization between a pair of Rössler chaotic oscillators can be determined by the synchronization error Euclidean norma as

$$\left\| e_{ij} \right\| = \sqrt{(x_i - x_j)^2 + (y_i - y_j)^2 + (z_i - z_j)^2} \tag{11}$$

As soon as the oscillator's phases have synchronized, synchronization quality can be characterized by comparing amplitudes

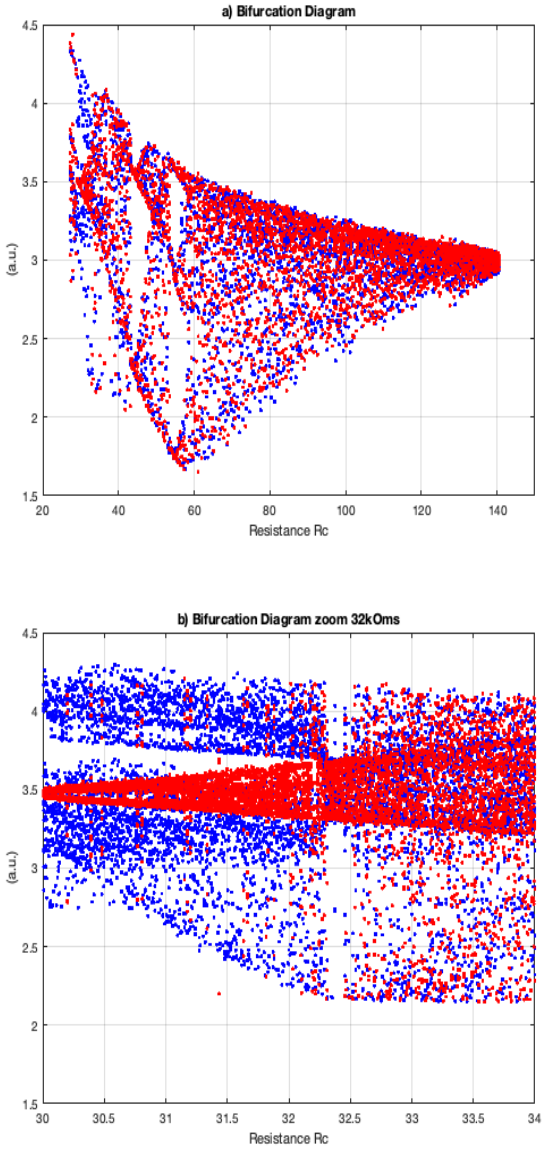

Figure 4 Bifurcation diagram for a Rössler circuit (a) Bifurcation diagram, In blue color from 140 to 0kΩ, and in red from 0 to 140kΩ, (b) A close up of 30 to 34kΩ in the Bifurcation diagram.

of coupled oscillators The commonly used measure for delay synchronization is similarity function S defined as

$$S^2_{i,j}(\tau) = \langle \frac{[x_j(t) - x_i(t+\tau)]^2}{\sqrt{\langle x_j(t)^2 \rangle \langle x_i(t)^2 \rangle}} \rangle \tag{12}$$

where τ is the time shift between two signals. The lower the minimum of similarity function S_{min}, means the better synchronization

SYNCHRONIZATION TWO IDENTICAL RÖSSLER CHAOTIC OSCILLATORS COUPLED

Within this section, phase synchronization in a system of two identical chaotic Rössler oscillators is shown. Specifically, a dynamic system comprising two Rössler chaotic oscillators coupled in a

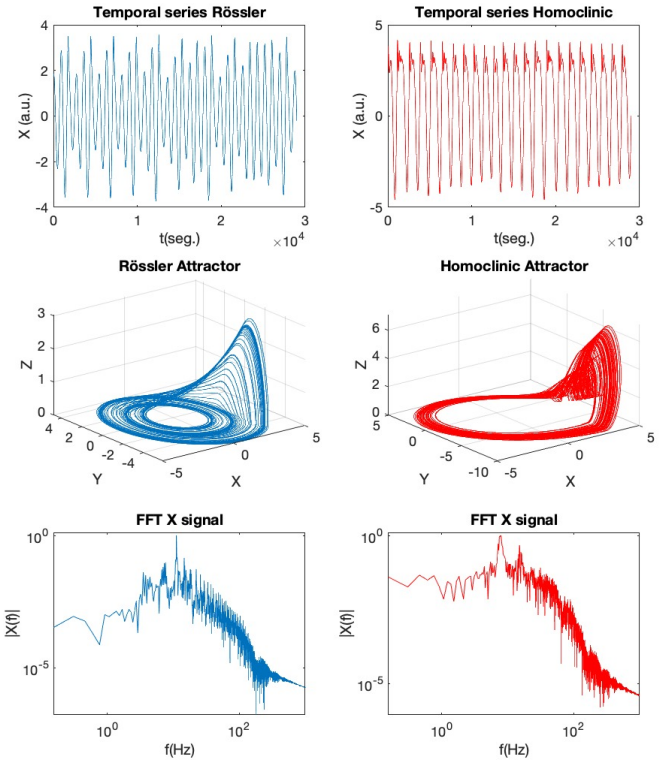

Figure 5 Dinamic of an isolated oscillator (left) Rössler type attractor: Temporal series, space state, and power spectrum, (rigth) Homoclinic type attractor: Temporal series, space state, and power spectrum.

unidirectional manner is examined, as described by Eqs. (1) and Eqs. (2), where $\epsilon \in [0, 1]$. In this setup, the response system, defined by Eqs. (2), is influenced by the variable y_1. It's important to note that the concept of phase lacks a precise definition for complex, chaotic systems, and thus, synchronization stages are interpreted as dimensions. In this context, we delineate three coupling ranges: (i) At very low coupling strength ($\epsilon \ll 1$), the driver signal given by Eqs. (1) is extremely small, resembling noise that doesn't significantly impact the overall structure of the phase space and the attractors in the response system described by Eqs. (2). (ii) the relatively robust chaotic driving from Eqs is at intermediate coupling strength. (1) increases the dimension of the phase space, potentially leading to the emergence of new attractors. And (iii) For very strong coupling ($\epsilon < 1$), the large amplitudes reduce the phase space dimension in the coupled identical multistable system.

To study the synchronization of multistable systems, the parameter R_c is set to $R_c = 32\Omega$, where the system has the coexistence of two different chaotic tractors. Then, we choose the initial condition for the system Eqs.1 representing a homoclinic chaotic or Rössler chaotic attractor. The analysis of synchronization is performed for two different cases: (a) driver system in Homoclinic **H** chaotic attractor and response system in Rössler **R** chaotic attractor, (b) driver system in Rössler **R** chaotic attractor and response system in Homoclinic **H** chaotic attractor.

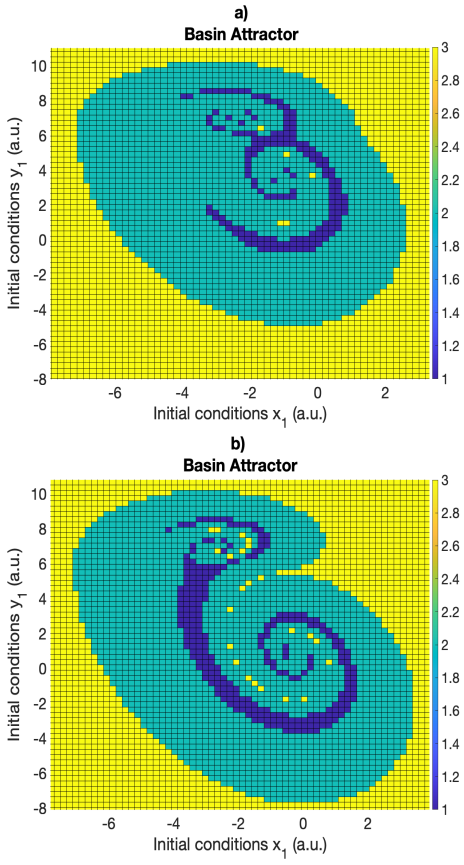

Figure 6 Basin attractor, the area for Homoclinic (green) is bigger than Rössler (blue) behavior. Using initial conditions to a) Homoclinic (**H**) and b) Rössler (**R**) attractor.

Case (a) driver system in Homoclinic chaotic attractor and response system in Rössler chaotic attractor

The time series of the coupled variables x_1 and x_2, the phase difference $\theta_{i,j}$ (see Eq.9) and similarity function $S_{i,j}(\tau)$ (see Eq.12 are shown in Fig. 7 (a)-(c) for a very low coupling strength ($\epsilon = 0.002$). $\theta_{i,j}$ increases linearly with time, indicating no synchronization. At a very low coupling strength ($\epsilon = 0.004$), the driven signal does not affect the response system, and the states are defined by the initial condition. Both oscillators are isolated, and their trajectory occupies a different space phase; see Fig. 5 and fig. 7 (d)-(f). There is a critical value of the coupling strength $\epsilon_c = \epsilon = 0.005$ at which the response oscillator system jumps from the Rössler chaotic attractor **R** to a new Homoclinic chaotic attractor $\mathbf{H}_2$ different from the Homoclinic chaotic attractor $\mathbf{H}_1$ of the driver oscillator system, i.e., the response oscillator system is sensitive to the driver when the response oscillator system switches to the attractors similar to the driver oscillator system, see Fig. 7 (g)-(i). This behavior for parameter $\epsilon_2 = 0.005$ is a precursor of phase synchronization in the multistable system. In Fig. 7 (h) we see how the phase looked $\theta_{i,j}$ approaches $\theta_{i,j} \approx 80$ and while Fig. 7 (i) the minimum S_{min} of the similarity function $S^2_{i,j}(\tau)$ is close to $S \approx 1.1$, which means that the response and the driven system are synchronized in the delayed phase synchronization, see time series 7 (g).

Further increasing the coupling parameter $\epsilon = 0.012$, the phase synchronization is most evident where the response oscillator system remains in the Homoclinic attractor, similar to the driver system's attractor. In the Fig. 7 (j)-(l) we can see that the phase looked $\theta_{i,j}$ decreases to $\theta_{i,j} \approx 20$, see Fig. 7 (k), just as the minimal similarity function S_{min} suffers a decrease Fig. 7 (k) and likewise the response time series is delayed for the driver oscillator time series Fig. 7 (j). While the coupling strength continues to increase at $\epsilon = 0.018$, Fig. 7 (m)-(p), the response oscillator system responds not only to the single peaks of the driver oscillator system, causing a change from the Rössler attractor to the Homoclinic attractor in the response oscillator system but also to the phase oscillation when the system remains in the similar attractors. It is noteworthy that phase synchronization is always accompanied by delay synchronization, where the shift time $\tau > 0$ of the similarity function is positive and the minimum S_{min} of this function also decreases $S \approx 1$, see Fig. 7 (p), which means that the response and drive oscillator systems reach phase synchronization, with the phase difference $\theta_{i,j}$ reaching $\theta_{i,j} \approx 0$, see Fig. 7 (n), and while the time series Fig. 7 (n) show that the delayed phase synchronization of the driver and response oscillator system has been achieved. For stronger coupling parameter $\epsilon_2 > 0.02$ the response oscillator system becomes unstable and there is no numerical solution the of the equation system (1).

Similar work on synchronization of a multistable system was done by Pisarchik *et al.* (2008). In this work, the authors show a detailed study of synchronizing two unidirectionally coupled identical systems with coexisting chaotic attractors and analyze the system dynamics observed on the route from asynchronous behavior to complete synchronization when the coupling strength is increased. In contrast to our work, they have studied two similar coexisting chaotic Rössler attractors. However, in the present work, we study the phase synchronization of two different chaotic attractors: the Homoclinic chaotic attractor and Rössler chaotic attractor. Because the system of equations (1) becomes unstable, complete synchronization was not found for the stronger coupling parameter $\epsilon > 0.02$. In Fig. 8 (a), the average synchronization error, see system equation (9) as a function of the coupling strength ϵ is shown. This figure shows that the synchronization error e increases when the control parameter ϵ is increased, i.e., complete synchronization between driver and response oscillator systems was not found. On the other hand, Fig. 8 (b) shows the average phase synchronization $< \theta_{i,j} >$ as a function of the coupling strength ϵ, where we can see that $< \theta_{i,j} >$ approaches zero when the control parameter ϵ is increased, indicating that phase or delay phase synchronization has been achieved.

Similarly, the bifurcation diagram of the local maximum of the state variables x_1 driver and x_2 response oscillator are shown in Figs. 9(a) and (b), respectively, as a function of the coupling strength ϵ. In this figure, we can see when the response oscillator system (Fig. 9 (b)) jumps from the Rössler chaotic attractor **R** to a new Homoclinic chaotic attractor $\mathbf{H}_2$, which is different from the Homoclinic chaotic attractor $\mathbf{H}_1$ of the driver oscillator system, i.e., there is a critical value of coupling strength $\epsilon_c = \epsilon = 0.005$ at which the response oscillator system changes its local maximum from $x_2^{max} \approx 3.6$ (Rössler attractor) to $x_2^{max} \approx 4.3$ (Homoclinic attractor $\mathbf{H}_2$).

Case (b) driver system in Rössler chaotic attractor and response system in Homoclinic chaotic attractor

Similar to the synchronization analysis performed in the Figs. 7 -9, in the Figs. 10- 12, a synchronization analysis is also performed, but in this case, we have the initial condition for the driver oscillator system equations.

The initial condition for the system Eqs.1 or Eqs.2 representing a

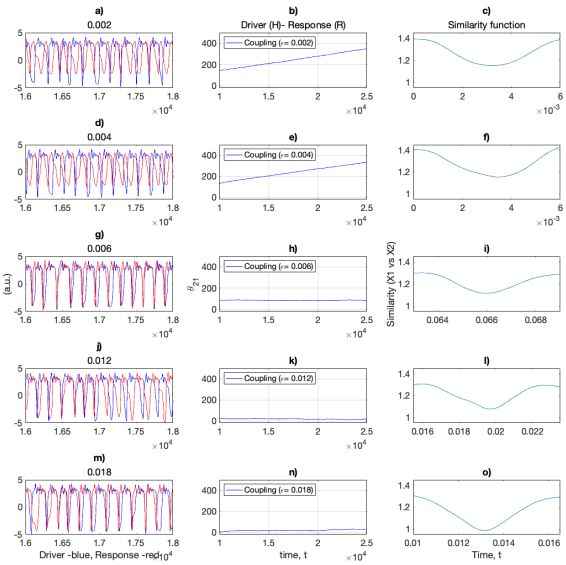

Figure 7 The time series of the coupled variables x_1, x_2 (left) and the phase difference $\theta_{i,j}$ (center) and Similarity Function (right).

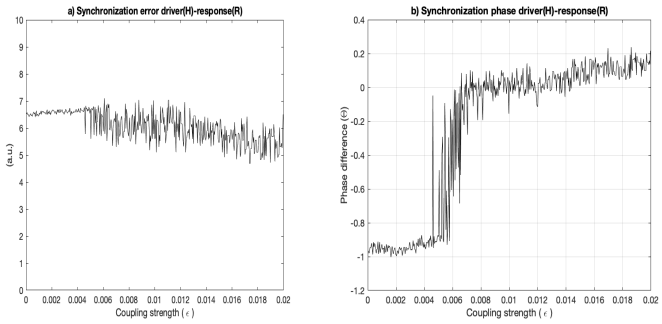

Figure 8 Show the average synchronization error equation system $< e_{i,j} >$ equation (9) as function of the coupling strength ϵ, the average phase synchronization $< \theta_{i,j} >$ as function of the coupling strength ϵ.

Homoclinic chaotic attractor **H** is reached using I.C.: $x_{10} = 2.38019$, $y_{10} = -5.31956$ and $z_{10} = 2.32858$, see Fig. 6a and showing a Rössler chaotic attractor **R** is reached using I.C.: $x_{20} = 3.034636$, $y_{20} = -4.64063$ and $z_{20} = 0.00920$ see Fig. 6b.

Eqs. 1 representing the Rössler chaotic oscillator **R** (I.C. $x_{20} = 3.034636$, $y_{20} = -4.64063$ and $z_{20} = 0.00920$) and while the initial condition of the response system represents a Homoclinic chaotic oscillator $\mathbf{H}_1$ (I. C. $x_{10} = 2.38019$, $y_{10} = -5.31956$ and $z_{10} = 2.32858$). The time series of the coupled variables x_1 and x_2, the phase difference $\theta_{i,j}$, and the similarity function $S_{i,j}(\tau)$ for different values of the coupling strength (ϵ) are shown in Fig. 10. In this figure, we can see that the phase synchronization was not achieved. Similarly, the average error synchronization $< e >$ and the average phase synchronization $< \theta_{i,j} >$ as a function of the coupling strength ϵ are shown in the Fig. 11 (a),(b) respectively, where no complete and no phase synchronization was found.

Also, the bifurcation diagrams of the local maximum of the state variables x_1 drive and x_2 response are shown in Fig. 12 (a)

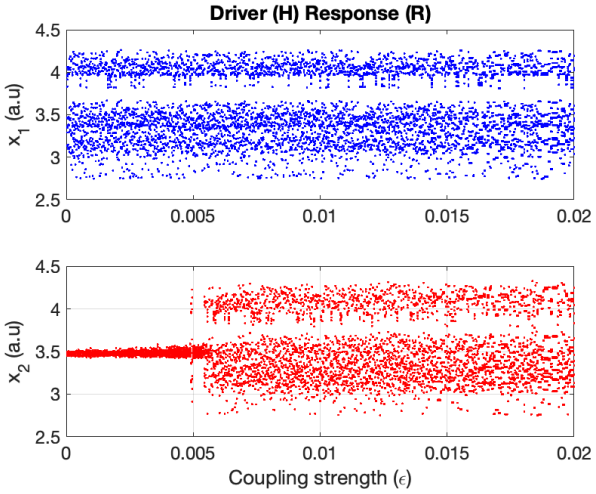

Figure 9 The bifurcation diagram of the local max of the state variables x_1 and x_2 as a function of the coupling strength ϵ.

and (b), respectively, as a function of the coupling strength ϵ. It can be observed that there is no critical value for the coupling strength ϵ_c at which the response oscillator system changes its local maximum from the x_2^{max} form of the Homoclinic attractor to the x_2^{max} Rössler attractor. It is worth noting that for larger values of the coupling strength ϵ the response oscillator system has no solution or it becomes an unstable system.

Thus, this result indicates an opposition to the synchronization of the response oscillator system when it operates as a Homoclinic chaotic attractor and the driver oscillator system operates as a Rössler chaotic attractor. Remarkably, to our knowledge, this is the first study of the opposition to the synchronization of bistable chaotic oscillator systems. In particular, the Homoclinic chaotic attractor of the response oscillator system resists entrainment or synchronization with the Rössler signal of the driver oscillator system. In contrast, in the cases where the response oscillator system is fixed in the Rössler chaotic attractor and the driver oscillator system is fixed in the Homoclinic chaotic attractor, there is a threshold coupling strength ϵ at which the Rössler chaotic attractor jump a new Homoclinic chaotic attractor and, depending on the coupling strength, the driver-response oscillator systems achieves delayed phase synchronization.

SYNCHRONIZATION OF THREE IDENTICAL RÖSSLER OSCILLATOR SYSTEMS COUPLED IN MOTIF CONFIGURATION.

In this work, we also study opposition to synchronization of multistable systems for another type of coupling, such as motif configuration of three identical bistable Rössler oscillator systems unidirectionally coupled. For example, two driver oscillator systems coupled to one response oscillator system, see equation systems Eqs.3, Eqs.4 and Eqs.5 where the two driver oscillator systems operate as a Rössler chaotic attractor and the response oscillator system operates in Homoclinic chaotic attractors, see the Fig.13.a) and Fig.14.a) for the average error synchronization $< e_{i,j} >$, and the average phase synchronization $< \theta_{i,j} >$ respectively, and also the Fig.15.a) the bifurcation diagrams of the local maximum of the state variables x_1 driver and x_2 response oscillator, as a function of the coupling strength ϵ. In these figures, it is clear that com-

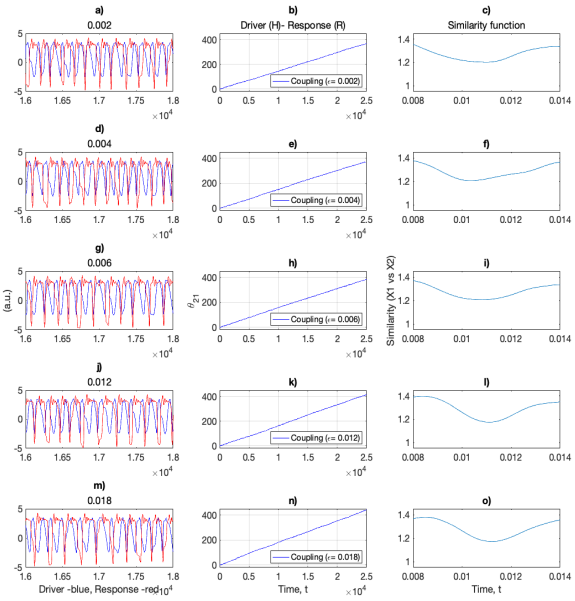

Figure 10 The time series of the coupled variables x_1 (left), x_2 and the phase difference $\theta_{i,j}$ (center) and Similarity Function (right).

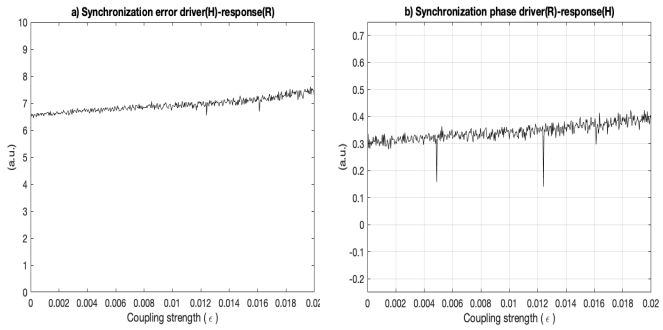

Figure 11 Show the average synchronization error equation system $< e_{i,j} >$ equation (9) as function of the coupling strength ϵ, the average phase synchronization $< \theta_{i,j} >$ as function of the coupling strength ϵ.

plete and phase synchronization between the driver and response oscillator systems has not been achieved.

In contrast, when the two driver oscillator systems operate in the Homoclinic chaotic attractor and the response oscillator system operates in the Rössler chaotic attractor, delayed phase synchronization between the driver and response oscillator systems is achieved since a value threshold of coupling strength ϵ. To observe these results, see Fig.13.b), Fig.14.b) and Fig.15.b) for the bifurcation diagrams, the average error synchronization $< e_{i,j} >$, and the average phase synchronization $< \theta_{i,j} >$ respectively.

In addition, this study also considered the opposition to synchronization of bistable chaotic oscillator systems in a configuration ring with unidirectional coupling schemes, where all oscillators act simultaneously as drivers and as response oscillator systems, see equation systems Eqs.6, Eqs.7 and Eqs.8. In this

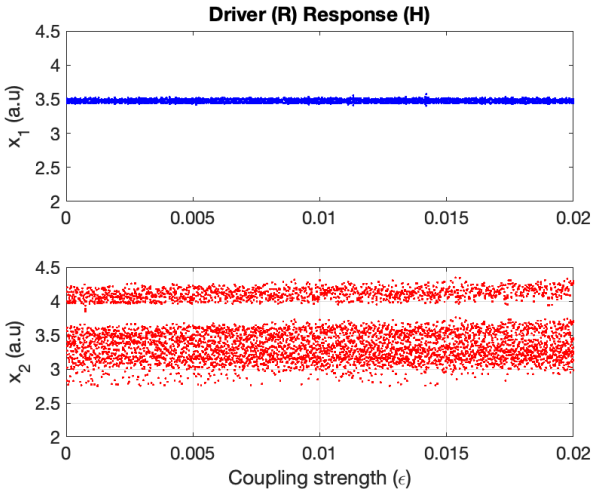

Figure 12 The bifurcation diagram of the local max of the state variables x_1 and x_2 as a function of the coupling strength ϵ.

configuration, it is sufficient for only one oscillator operating in Homoclinic chaotic attractors to trigger the entrainment of other two oscillators operating in Rössler chaotic attractors jump to new Homoclinic chaotic attractor since a value threshold of coupling strength ϵ.

The following figures show the dependence of the average error synchronization $< e_{i,j} >$ see Fig. 16 a), b), the average phase synchronization $< \theta_{i,j} >$ see Fig. 17 a),b), and the bifurcation diagrams of the local maximum of the state variables x_1 driver and x_2 response oscillator systems in Fig. 18 a), b), for the coupling strength ϵ. This means that all oscillators achieve synchronization in phase synchronization. This is an unexpected result since one might expect that these two oscillator systems operating in the Rössler chaotic attractor should cause the other oscillator operating in the Homoclinic chaotic attractor to jump to the Rössler chaotic attractor and that all oscillators should be able to synchronize in-phase synchronization.

The above result shows that the Homoclinic chaotic attractor opposes synchronization with Rössler chaotic attractor. In contrast, the homoclinic chaotic attractor is the one that stimulates the other two oscillators operating in the Rössler chaotic attractor to jump to the new Homoclinic chaotic attractor and then all these oscillators achieve phase synchronization.

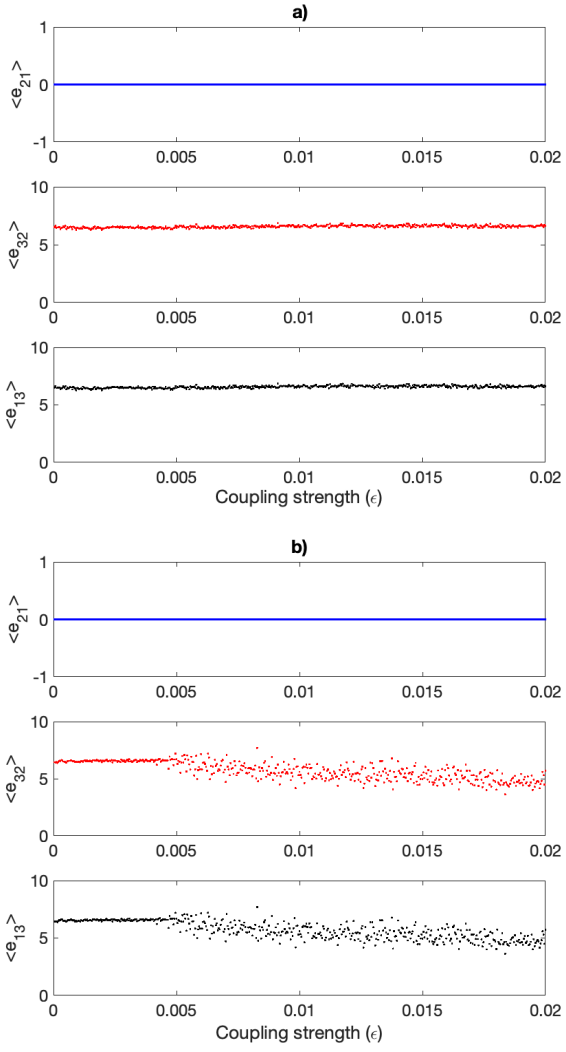

Figure 13 Synchronization error as function of the coupling strength (ϵ), a) Two drivers Rössler type, one response Homoclinic type, b) Two drivers Homoclinic type, one response Rössler type.

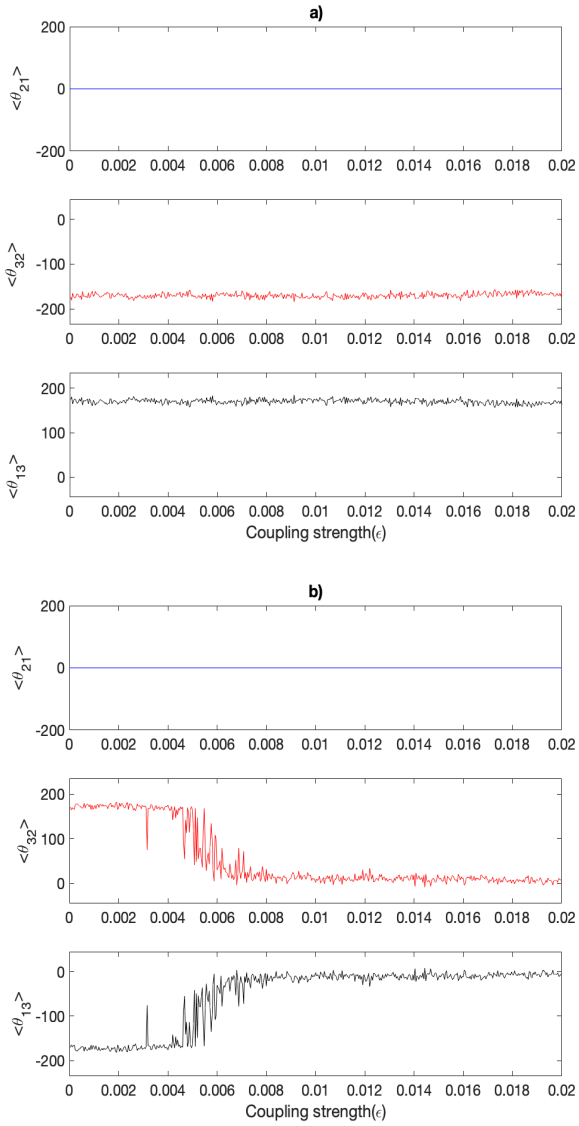

Figure 14 Phase synchronization as function of the coupling strength (ϵ), a) Two drivers Rössler type, one response Homoclinic type, b) Two drivers Homoclinic type, one response Rössler type.

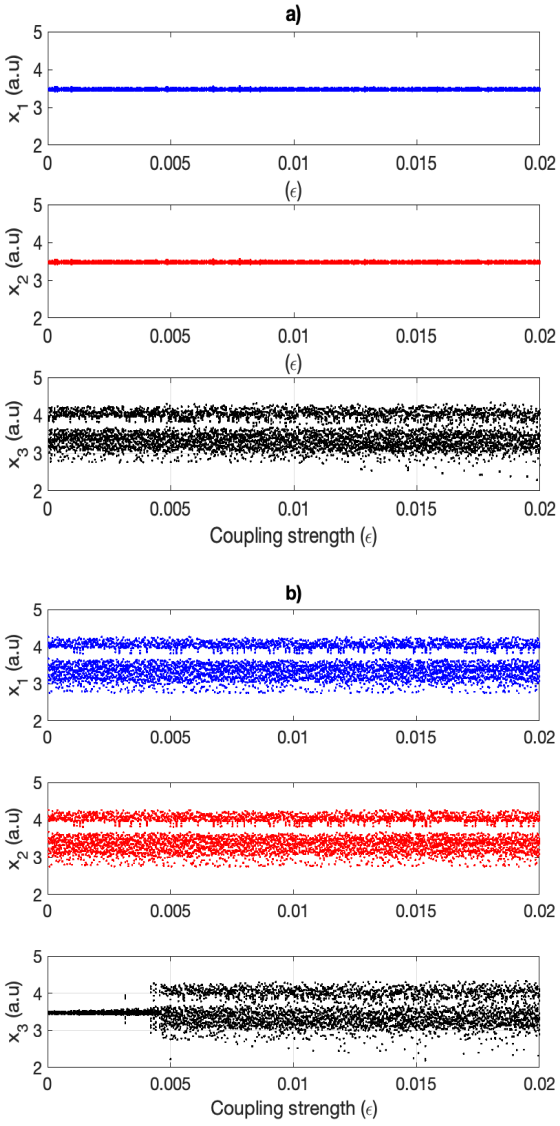

Figure 15 The bifurcation diagram of the local max of the state variables x_1, x_2 and x_3 as function of the coupling strengthϵ, a) Two drivers Rössler type, one response Homoclinic type, b) Two drivers Homoclinic type, one response Rössler type.

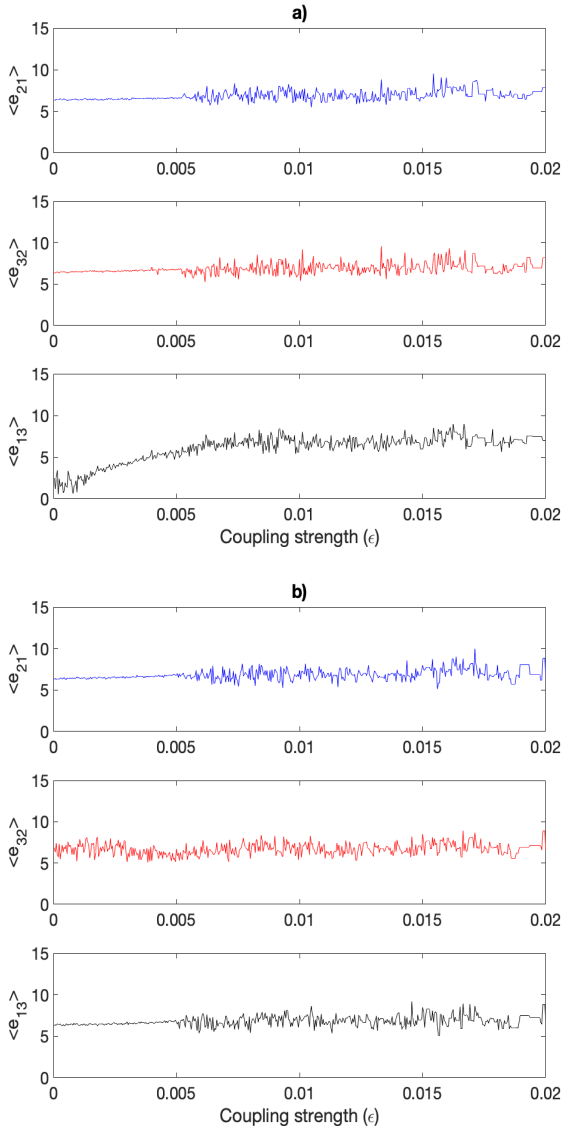

Figure 16 Synchronization error as function of the coupling strength (ϵ), a) Ring with two Rössler type, one Homoclinic type, b) Ring with two Homoclinic type, one Rössler type.

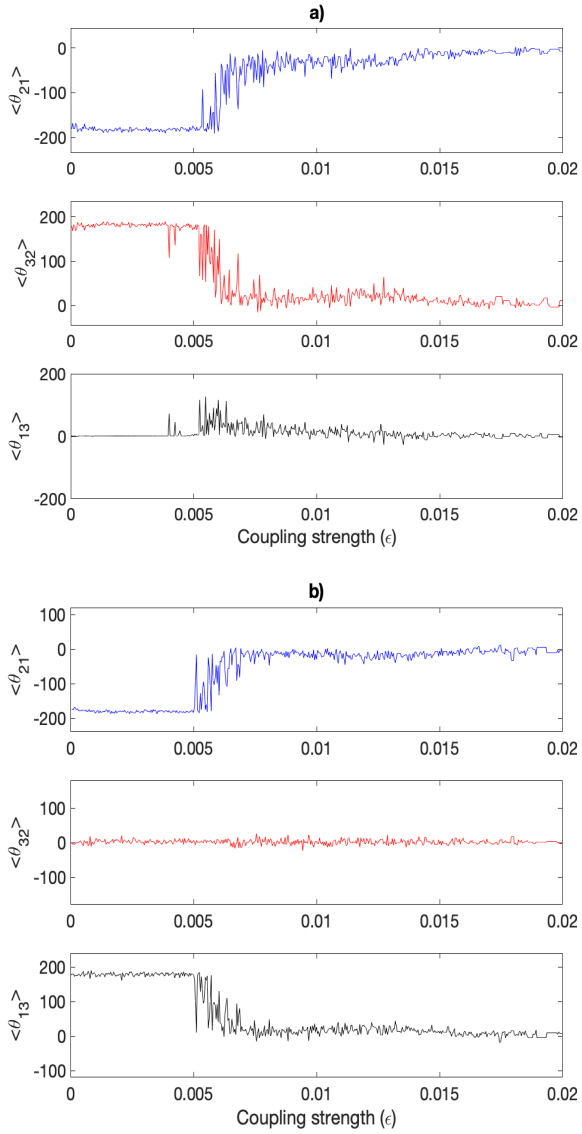

Figure 17 Phase synchronization as function of the coupling strength (ϵ), a) Ring with two Rössler type, one Homoclinic type, b)Ring with two Homoclinic type, one Rössler type.

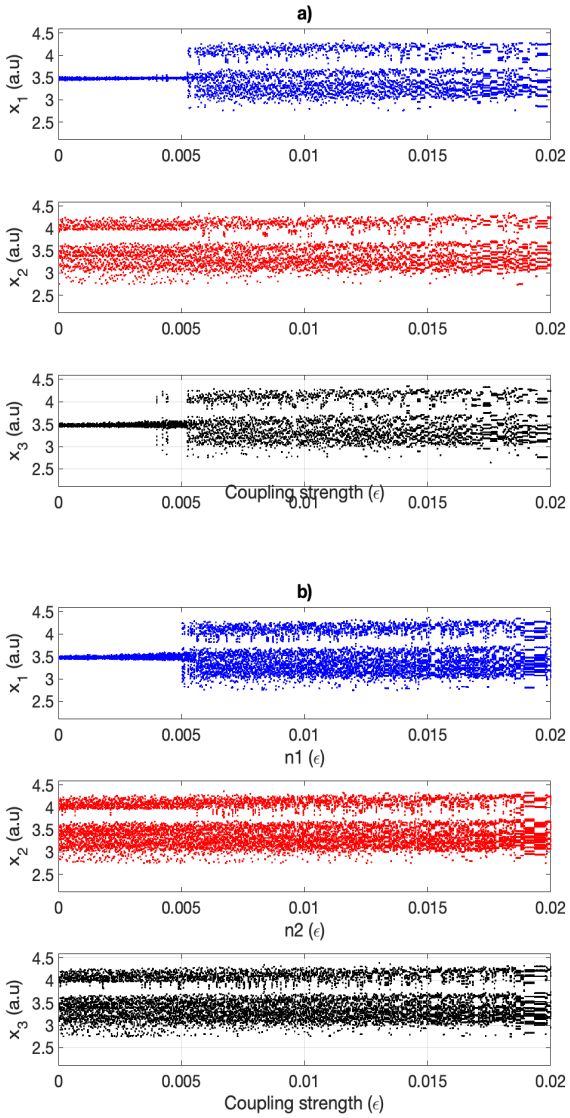

Figure 18 The bifurcation diagram of the local max of the state variables x_1, x_2 and x_3 as function of the coupling strengthϵ, a) Ring with two Rössler type, one Homoclinic type, b) Ring with two Homoclinic type, one Rössler type.

CONCLUSION

We have performed numerical investigations with Rössler oscillator system the opposition to synchronization of a bistable chaotic dynamical system coupled in different configurations: (a) two identical bistable chaotic oscillators coupled in a driver and a response system; (b) three identical bistable chaotic oscillators coupled in motif configuration; two drivers and one response oscillator, and (c) three identical coupled oscillators in a ring configuration where all oscillators act together as driver and response system. We have chosen the initial conditions of the driver or response oscillator system to be either a Homoclinic chaotic attractor or a Rössler chaotic attractor. In the first (a) case, when the driver oscillator system operates in the regime of the Homoclinic chaotic attractor and the response oscillator system in the regime of the Rössler chaotic attractor, there is a critical value of the coupling strength $\epsilon_c = \epsilon = 0.005$ at which the response oscillator system jumps from the Rössler chaotic attractor $\mathbf{R}$ to a new Homoclinic chaotic attractor $\mathbf{H}_2$ that is different from the Homoclinic chaotic attractor $\mathbf{H}_1$ of the driver oscillator system, i.e., the response oscillator system is sensitive to the driver signal.

Further increasing the coupling parameter $\epsilon > 0.005$, the phase synchronization is most evident where the response oscillator system remains into a homoclinic chaotic attractor, which is similar to the attractor of the driver oscillator system. An unexpected result was found when the driver oscillator system operates in the Rössler chaotic attractor regime and the response oscillator system operates into the Homoclinic chaotic attractor regime, as one might expect the driver oscillator system to cause the response oscillator system to jump to the Rössler chaotic attractor and the driver response oscillator system to be able to synchronize in phase, but this was not found. On the contrary, the result shows that the Homoclinic chaotic attractor opposes synchronization with Rössler chaotic attractor. The above results are because the basin attraction of the Homoclinic chaotic attractor is greater than the basin attraction of the Rössler chaotic attractor. When the response system operating in the homoclinic regime receives the signal of the Rössler chaotic attractor from the driver system, the response oscillator system does not change the attractor but maintains its original regime of the Homoclinic chaotic attractor, so that synchronization between the Homoclinic and Rössler chaotic attractors is not possible.

In contrast, the basin of attraction of the Rössler chaotic attractor is smaller than that of the Homoclinic chaotic attractor. When the response system operating in the Rössler chaotic attractor receives the homoclinic signal from the driver oscillator system, the response oscillator system is sensitive to the signal from the driver oscillator system, which acts like an external signal and causes the response oscillator system to jump from the Rössler chaotic attractor to the Homoclinic chaotic attractor, achieving the phase synchronization regime between the driver and response oscillator systems. A similar result was found regarding the opposition of the Homoclinic chaotic attractor to synchronization with the Rössler attractors when the network of three coupled bistable chaotic dynamical systems is considered: (b) three identical bistable chaotic oscillators coupled in motif configuration; two drivers and one response oscillator, and (b) three identical coupled oscillators in a ring configuration where all oscillators act together as driver and response oscillator system.

Acknowledgments

This work was supported by the University of Guadalajara, CU-Lagos, DCET. R.J.R. acknowledges to the National Council of Humanities, Science, and Technology (CONAHCYT), Project Number 320597.

Availability of data and material

Not applicable.

Conflicts of interest

The authors declare that there is no conflict of interest regarding the publication of this paper.

Ethical standard

The authors have no relevant financial or non-financial interests to disclose.

LITERATURE CITED

Ahmed, H., R. Ushirobira, D. Efimov, and W. Perruquetti, 2016 Robust synchronization for multistable systems. IEEE Transactions on Automatic Control **61**: 1625–1630.

Boccaletti, S., 2008 The synchronized dynamics of complex systems. Monograph series on nonlinear science and complexity **6**: 1–239.

Boccaletti, S., L. M. Pecora, and A. Pelaez, 2001 Unifying framework for synchronization of coupled dynamical systems. Physical Review E **63**: 066219.

Boccaletti, S., A. N. Pisarchik, C. I. Del Genio, and A. Amann, 2018 *Synchronization: from coupled systems to complex networks*. Cambridge University Press.

Brun, E., B. Derighetti, D. Meier, R. Holzner, and M. Ravani, 1985 Observation of order and chaos in a nuclear spin–flip laser. JOSA B **2**: 156–167.

Buldú, J. M., T. Heil, I. Fischer, M. C. Torrent, and J. García-Ojalvo, 2006 Episodic synchronization via dynamic injection. Physical review letters **96**: 024102.

Carroll, T. L. and L. M. Pecora, 1995 *Nonlinear dynamics in circuits*. World Scientific.

Chakraborty, P. and S. Poria, 2019 Extreme multistable synchronisation in coupled dynamical systems. Pramana **93**: 1–13.

Dudkowski, D., K. Czołczyński, and T. Kapitaniak, 2021 Multistable synchronous states of two pendulum clocks suspended on a swinging support. Mechanical Systems and Signal Processing **154**: 107549.

Farkas, I., D. Helbing, and T. Vicsek, 2002 Mexican waves in an excitable medium. Nature **419**: 131–132.

Foss, J., A. Longtin, B. Mensour, and J. Milton, 1996 Multistability and delayed recurrent loops. Physical Review Letters **76**: 708.

García-Guerrero, E., E. Inzunza-González, O. López-Bonilla, J. Cárdenas-Valdez, and E. Tlelo-Cuautle, 2020 Randomness improvement of chaotic maps for image encryption in a wireless communication scheme using pic-microcontroller via zigbee channels. Chaos, Solitons and Fractals **133**: 109646.

Gauthier, D. J. and J. C. Bienfang, 1996 Intermittent loss of synchronization in coupled chaotic oscillators: Toward a new criterion for high-quality synchronization. Physical Review Letters **77**: 1751.

Khan, M. A., G. Mahapatra, J. K. Sarkar, and S. D. Jabeen, 2021 Design of multistability of chaotic systems via self and cross coupling. The European Physical Journal Plus **136**: 1–12.

Khan, M. A., M. Nag, and S. Poria, 2017 Design of multistable systems via partial synchronization. Pramana **89**: 1–8.

Liu, W., J. Xiao, X. Qian, and J. Yang, 2006 Antiphase synchronization in coupled chaotic oscillators. Physical Review E **73**: 057203.

Maurer, J. and A. Libchaber, 1980 Effect of the prandtl number on the onset of turbulence in liquid 4he. Journal de Physique lettres **41**: 515–518.

Méndez-Ramírez, R., A. Arellano-Delgado, and M. Á. Murillo-Escobar, 2023 Network synchronization of macm circuits and its application to secure communications. Entropy **25**: 688.

Moskalenko, O. I., A. A. Koronovskii, A. O. Selskii, and E. V. Evstifeev, 2021 On multistability near the boundary of generalized synchronization in unidirectionally coupled chaotic systems. Chaos: An Interdisciplinary Journal of Nonlinear Science **31**: 083106.

Pecora, L. M. and T. L. Carroll, 1990 Synchronization in chaotic systems. Physical review letters **64**: 821.

Pikovsky, A., M. Rosenblum, J. Kurths, *et al.*, 2001 A universal concept in nonlinear sciences. Self **2**: 3.

Pisarchik, A., R. Jaimes-Reátegui, J. Villalobos-Salazar, J. Garcia-Lopez, and S. Boccaletti, 2006 Synchronization of chaotic systems with coexisting attractors. Physical review letters **96**: 244102.

Pisarchik, A. N. and R. Jaimes-Reategui, 2005 Intermittent lag synchronization in a nonautonomous system of coupled oscillators. Physics Letters A **338**: 141–149.

Pisarchik, A. N., R. Jaimes-Reátegui, and J. García-López, 2008 Synchronization of multistable systems. International Journal of Bifurcation and Chaos **18**: 1801–1819.

Pisarchik, A. N., A. V. Kir'yanov, Y. O. Barmenkov, and R. Jaimes-Reátegui, 2005 Dynamics of an erbium-doped fiber laser with pump modulation: theory and experiment. JOSA B **22**: 2107–2114.

Pm, G. and T. Kapitaniak, 2017 Synchronization in coupled multistable systems with hidden attractors. Mathematical Problems in Engineering **2017**.

Pol, B. and J. v. d. Mark, 1927 Frequency demultiplication. Nature **120**: 363–364.

Rodríguez-Orozco, E., E. E. García-Guerrero, E. Inzunza-Gonzalez, O. R. López-Bonilla, A. Flores-Vergara, *et al.*, 2018 Fpga-based chaotic cryptosystem by using voice recognition as access key. Electronics **7**.

Rosenblum, M. and J. Kurths, 2003 *Synchronization: a universal concept in nonlinear science*. Cambridge University Press.

Rosenblum, M. G., A. S. Pikovsky, and J. Kurths, 1996 Phase synchronization of chaotic oscillators. Physical review letters **76**: 1804.

Rosenblum, M. G., A. S. Pikovsky, and J. Kurths, 1997 From phase to lag synchronization in coupled chaotic oscillators. Physical Review Letters **78**: 4193.

Ruiz-Silva, A., H. Gilardi-Velázquez, and E. Campos, 2021 Emergence of synchronous behavior in a network with chaotic multistable systems. Chaos, Solitons & Fractals **151**: 111263.

Rulkov, N. F., M. M. Sushchik, L. S. Tsimring, and H. D. Abarbanel, 1995 Generalized synchronization of chaos in directionally coupled chaotic systems. Physical Review E **51**: 980.

Sarosh, P., S. A. Parah, and G. M. Bhat, 2022 An efficient image encryption scheme for healthcare applications. Multimedia Tools and Applications **81**: 7253–7270.

Sharma, N. and E. Ott, 2000 Exploiting synchronization to combat channel distortions in communication with chaotic systems. International Journal of Bifurcation and Chaos **10**: 777–785.

Stewart, H. B., R. Ghaffari, C. Franciosi, and H. Swinney, 1986 *Nonlinear dynamics and chaos: geometrical methods for engineers and scientists*. Wiley New York.

Trujillo-Toledo, D., O. López-Bonilla, E. García-Guerrero, J. Esqueda-Elizondo, J. Cárdenas-Valdez, *et al.*, 2023 Real-time medical image encryption for h-iot applications using improved sequences from chaotic maps. Integration **90**: 131–145.

Vaidyanathan, S., K. Benkouider, and A. Sambas, 2022 A new multistable jerk chaotic system, its bifurcation analysis, backstepping control-based synchronization design and circuit simulation. Archives of Control Sciences **32**: 123.

How to cite this article: García-López, J. H., Jaimes-Reátegui, R., Huerta-Cuellar, G. and López-Mancilla D. Opposition to Synchronization of Bistable State in Motif Configuration of Rössler Chaotic Oscillator Systems. *Chaos Theory and Applications*, 6(2), 131-143, 2023.

CHAOS
Theory and Applications
in Applied Sciences and Engineering

e-ISSN: 2687-4539
RESEARCH ARTICLE
Vol.6 / No.2 / 2024 / pp.144-151
Special Issue (EDIESCA 2023)
https://doi.org/10.51537/chaos.1381891

Hidden Attractors in Chaotic Systems with Nonlinear Functions

Hafiz Muhammad Zeeshan *,[1], **Rider Jaimes Reátegui** *,[2], **Juan Hugo García López** *,[3], **Safara Bibi** *,[4] and **Guillermo Huerta Cuellar** *,[5]

*Departamento de Ciencias Exactas y Tecnología, Centro Universitario de los Lagos, Universidad de Guadalajara, Enrique Díaz de León 1144, Colonia Paseos de la Montaña, Lagos de Moreno, Jalisco, México.

ABSTRACT In the present work, an interesting mini-review of hidden attractors in dynamical systems with associated nonlinear functions is carried out. Chaotic systems with nonlinear functions often possess hidden attractors due to their inherent complexity. These attractors can arise in various mathematical models, such as the Lorenz system, Rössler system, or Chua's circuit. The identification and comprehension of hidden attractors broaden our understanding of complex systems and provide new directions for future study and technological development. The discovery and characterization of hidden attractors in chaotic systems have profound implications for various scientific disciplines, including physics, biology, and engineering.

KEYWORDS
Hidden attractors
Chaotic systems
Nonlinear functions
Fixed points
Numerical simulations

INTRODUCTION

Bifurcation theory deals with the study of how certain behaviors or patterns in a system change as its parameters vary (Dueñas *et al.* 2023). One interesting phenomenon in this theory is the concept of a *hidden oscillation* (Ye and Wang 2023). This refers to a bounded back-and-forth movement that emerges in a system without causing the stationary points (equilibrium states) of the system to become unstable (Djorwe *et al.* 2023).

In nonlinear control theory, we focus on managing systems that do not have a simple linear relationship between their input and output (Gray *et al.* 2023). When we talk about the birth of a hidden oscillation in a time-invariant control system (meaning the system doesn't change over time) with bounded states (the system's variables remain within certain limits), it implies reaching a critical point in the parameter space (Kuznetsov 2020). At this critical point, the stationary states of the system switch from being locally stable (stable in the nearby region) to becoming globally stable (Kuznetsov *et al.* 2020) (stable across the entire system).

In simpler terms, when a system has hidden movements or vibrations that exist within a small part of its overall behavior, and these hidden motions draw in all the nearby movements, we call it a hidden attractor (Djorwe *et al.* 2023). This means that even though these movements may not be obvious at first glance, they have a strong influence on the nearby motions of the system.

The study of hidden attractors gained further momentum in the 21st century, with results obtained by researchers applying advanced analytical and computational techniques to uncover these elusive phenomena (Wang *et al.* 2021; Gong *et al.* 2022; Kuznetsov *et al.* 2023; Zaqueros-Martinez *et al.* 2023). Scientists have explored various mathematical models and physical systems to identify hidden attractors and understand their underlying mechanisms.

From a computational perspective, attractors can be classified into two categories: self-excited attractors and hidden attractors. Self-excited attractors can be easily localized using standard computational procedures and standard analytical procedures (Yang and Lai 2023). These attractors exhibit a transient process where a trajectory, starting from a point on the unstable manifold near an equilibrium, eventually reaches a state of oscillation (Lakshmanan and Rajaseekar 2012). Examples of systems with self-excited attractors include the Lorenz (Dubois *et al.* 2020), Rössler (Rybin *et al.* 2021), and Chua oscillators (Njitacke *et al.* 2020). The presence of self-excited attractors can be readily identified due to the observable oscillatory behavior.

In contrast, hidden attractors pose a greater challenge for localization. In these systems, the basin of attraction does not intersect with any small neighborhoods of equilibria (Cang *et al.* 2019). Hidden attractors can exhibit both chaotic and periodic behavior, such as the coexistence of a stable stationary point and a stable limit

Manuscript received: 26 October 2023,
Revised: 24 November 2023,
Accepted: 4 December 2023.

[1]zeeshan.hafiz9228@alumnos.udg.mx
[2]rider.jaimes@academicos.udg.mx
[3]jhugo.garcia@academicos.udg.mx
[4]safara.bi9231@alumnos.udg.mx
[5]guillermo.huerta@academicos.udg.mx (**Corresponding author**)

cycle. Unlike self-excited attractors, the existence of hidden attractors in the phase space is not easily predictable. Therefore, special procedures need to be developed to localize hidden attractors since there are no analogous transient processes leading to their emergence. If a hidden attractor is present in the dynamics of a system and happens to be reached, the system (such as an airplane or electronic circuit) can exhibit quasi-cyclic behavior (Zelinka 2016), which can potentially result in disastrous consequences depending on the nature of the device. Traditionally, dynamical systems without equilibrium points have been considered nonphysical or mathematically incomplete. However, empirical evidence shows that systems can possess hidden dynamical behavior without the presence of an unstable equilibrium state (Dudkowski *et al.* 2016).

In short, hidden attractors represent a unique challenge in the study of dynamical systems. Their existence is not easily predictable, and special procedures are required for their localization (Campos *et al.* 2020). While systems with hidden attractors have been viewed as nonphysical in the past, it is now evident that such behavior can occur even without an unstable equilibrium state.

The discovery and characterization of hidden attractors in chaotic systems have profound implications for various scientific disciplines, including physics (Kingni *et al.* 2019; Kuznetsov *et al.* 2023), biology (Chen *et al.* 2020; Lin *et al.* 2020), and engineering (Abdolmohammadi *et al.* 2018; Jasim *et al.* 2021). Hidden attractors are also found in nonlinear systems with applications considering fuzzy control and synchronization, as the works reported by (Tanaka *et al.* 1998; Zaqueros-Martinez *et al.* 2023)

In Section 2 of this short review, addressed the fascinating areas of hidden chaotic attractors in nonlinear dynamical systems. we explored the domain of hidden chaotic attractors without equilibria. Then we discussed hidden chaotic attractors that coexist with equilibria. We also ventured into the realm of hidden chaotic attractors that exhibit extreme multi-stability. Finally, we have studied hidden chaotic attractors with multi-scroll, a class of hidden attractors characterized by their complex multidimensional structure. Section 3, summarises the main discussion on these hidden chaotic attractors, which make a valuable contribution to combining the different studies for a better understanding of nonlinear dynamics.

HIDDEN ATTRACTORS IN NONLINEAR CHAOTIC DYNAMICAL SYSTEMS

In nonlinear chaotic dynamical systems, the region in phase space where a hidden attractor exerts its influence is not connected to any unstable equilibrium point. This phenomenon can be seen in systems where there are either no unstable equilibrium points at all or only one stable equilibrium point, which is a specific instance of having multiple stable equilibrium points. This characteristic defines the nature of hidden attractors in such systems.

In this section, we discuss hidden attractors with different aspects.

Hidden attractor in chaotic dynamical systems

The idea of hidden attractors has been proposed in relation to the identification of unforeseen attractors in Chua's circuit. These unexpected behaviors in the circuit's dynamics have been discussed in various studies (Wang *et al.* 2021; Wu *et al.* 2021; Kuznetsov *et al.* 2023).

We discuss hidden attractors in chaotic dynamical systems with an interesting example of the classical Lorenz system (Munmuangsaen and Srisuchinwong 2018). The classical Lorenz system is explained using three connected equations that represent simple mathematical relationships:

$$\begin{aligned} \dot{x} &= a(y-x), \\ \dot{y} &= -xz + rx - y, \\ \dot{z} &= xy - bz. \end{aligned} \tag{1}$$

Figure 1 shows a newly discovered chaotic attractor represented in red on a coordinate plane (x, y) with parameters $a = 4, r = 29$, and $b = 2$. This attractor is revealed using the starting values $L_1 = (x_0, y_0, z_0) = (5, 5, 5)$. The figure also displays two point attractors, one in blue and the other in pink. These point attractors move towards stable equilibrium points S_2 and S_3, respectively. The blue point attractor starts at $L_2 = (x_0, y_0, z_0) = (0.1, 0, 0)$, while the red point attractor starts and also in 3D is shown in Figure 2. The Runge-Kutta method of order 4 (RK4) is a numerical technique that is used to solve the nonlinear differential equations (ODEs) of system (1) with time step size 0.01 and total number of steps are 2^{16}.

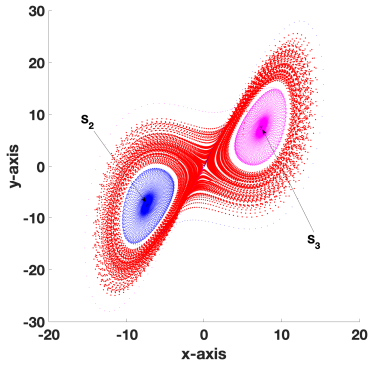

Figure 1 Classical Lorenz system plotted on a coordinate plane (x, y), a novel chaotic attractor, depicted in red, has emerged alongside two distinct point attractors, represented in blue and pink.

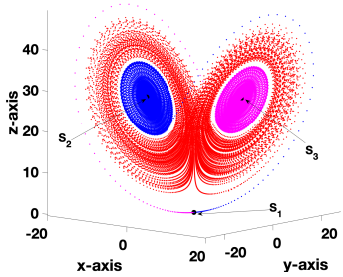

Figure 2 Classical Lorenz system plotted on coordinates (x, y, z), a novel chaotic attractor, depicted in red, has emerged alongside two distinct point attractors, represented in blue and pink.

Hidden chaotic attractors without equilibria

Hidden chaotic attractors without equilibria are a fascinating phenomenon in the field of nonlinear dynamics. Unlike well-studied chaotic systems with equilibria (such as the Lorenz system or the Rössler system), these attractors do not have stable fixed points.

Instead, they exhibit chaotic behavior with no underlying stable states. The discovery and study of such systems have challenged traditional notions of chaotic dynamics.

As an example, the Sprott case D system pioneered the investigation of a dynamical system that does not have equilibria, along with its various modifications (Wei 2011). The following is the system that has hidden chaotic attractors without equilibria/fixed points, as depicted in Figure 3.

$$\begin{aligned} \dot{x} &= -y, \\ \dot{y} &= x + z, \\ \dot{z} &= 3y^2 + xz. \end{aligned} \tag{2}$$

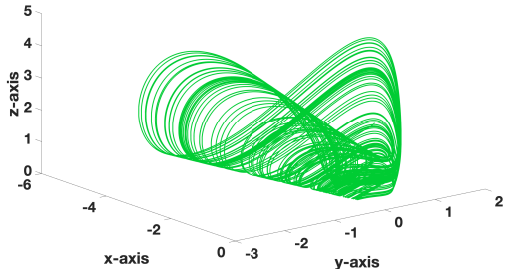

Figure 3 Hidden chaotic attractor of the system (2) with no equilibria in system plotted on coordinates (x, y, z) with the initial value (-1.6, 0.82, 1.9).

The chaotic system (2) has a single equilibrium point at $O(0,0,0)$. If we analyze the linearized version of the system at this equilibrium point, the characteristic values $(\lambda_1, \lambda_2, \lambda_3)$ of the Jacobian matrix are $\lambda_1 = 0$ and $\lambda_{2,3} = \pm i$.

Jafari and Sprott conducted a mathematical exploration to identify the most basic three-dimensional chaotic systems with hidden attractor without equilibria (Jafari *et al.* 2013). The following is the mathematical modeling and depicted in Figure 4.

The Runge-Kutta method of order 4 (RK4) is used for systems (2) & (3) with time step size 0.01 and total number of steps are 2^{16}.

$$\begin{aligned} \dot{x} &= -y, \\ \dot{y} &= -x + z, \\ \dot{z} &= -0.8x^2 + z^2 + 2. \end{aligned} \tag{3}$$

This system incorporated quadratic nonlinear and the absence of equilibria.

Many other researchers worked on hidden attractors that are chaotic systems with no equilibrium. Pham et al. discussed a novel autonomous system with a hidden attractor there is no equilibrium point in this system (Pham *et al.* 2017). Although their proposed system is simple with six terms, it exhibits complex behavior. Moving forward, Lai et al. have created a novel chaotic system and designed both the model and the circuit itself (Lai *et al.* 2020). This system behavuniquely way, it does not follow the usual patterns, and it has a hidden attractor with no equilibrium. Furthermore, Nag and Ghosh have developed an innovative 3D system that has some unique features (Nag Chowdhury and Ghosh 2020). In this

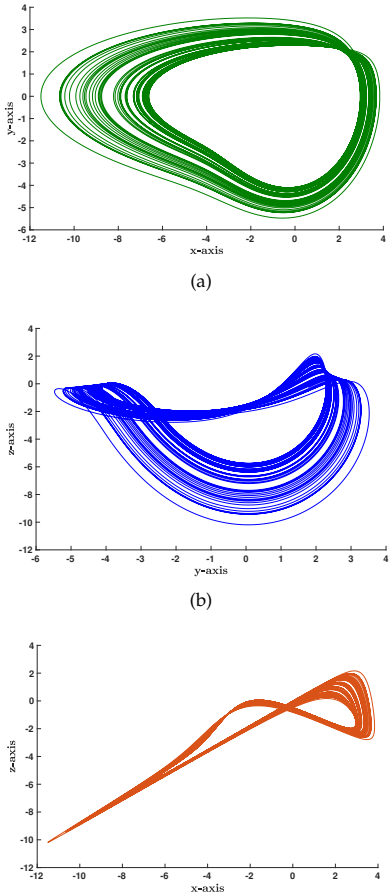

Figure 4 Hidden attractor of the system (3) without fixed-point (a) in xy-plane, (b) in yz-plane and (c) in xz-plane with the initial value (0, 2.3, 0).

system, there are certain hidden attractors with no equilibrium that cannot be predicted or tracked by conventional methods. The behavior of the system can be seen as a slow and steady trend by looking at its changes over time.

Hidden chaotic attractors with equilibria

The study of hidden chaotic attractors with equilibria remains a vibrant area of research. These systems exhibit a combination of stable equilibria and chaotic behavior.

We consider Wang and Chen's work as an example (Wang and Chen 2012). They introduced a chaotic system that operates in three dimensions. Within this system, there is a unique equilibrium point $p^\star = (0.25, 0.0625, -0.096)$ as shown in Figure 5 & 6.

$$\begin{aligned} \dot{x} &= yz + 0.006, \\ \dot{y} &= x^2 - y, \\ \dot{z} &= 1 - 4x. \end{aligned} \tag{4}$$

M. Molaie found twenty-three systems that have hidden attractors with one equilibrium point (Molaie *et al.* 2013). We found another fascinating example from one of those three-dimensional nonlinear systems. Following is the system and It is illustrated in Figure 7. The Runge-Kutta method of order 4 (RK4) is used to solve the

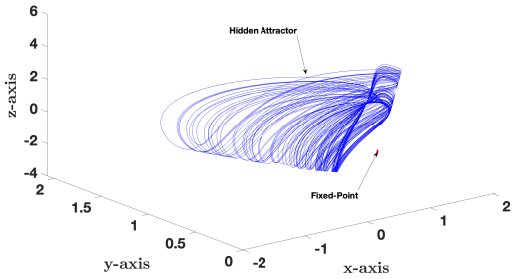

Figure 5 Hidden attractor of the system (4) with stable fixed-point in 3D with the initial value (0, 0, 0).

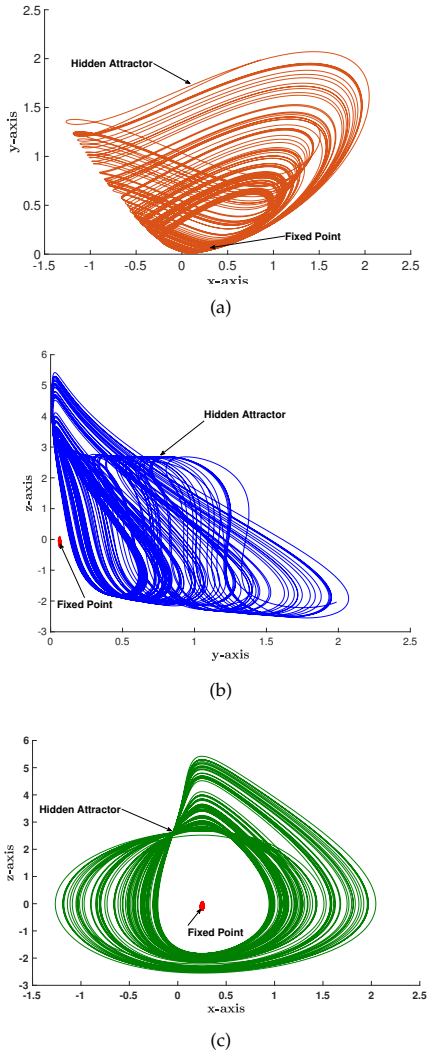

Figure 6 Hidden attractor of the system (4) with stable fixed-point in different phase spaces with the initial value (0, 0, 0). (a) in xy-axis, (b) in yz-axis, (c) in xz-axis.

nonlinear system (4) & (5) with time step size 0.01 and total number of steps are 2^{16}.

$$\begin{aligned} \dot{x} &= y, \\ \dot{y} &= -x + yz, \\ \dot{z} &= 2x - 2z + y^2 - 0.3. \end{aligned} \tag{5}$$

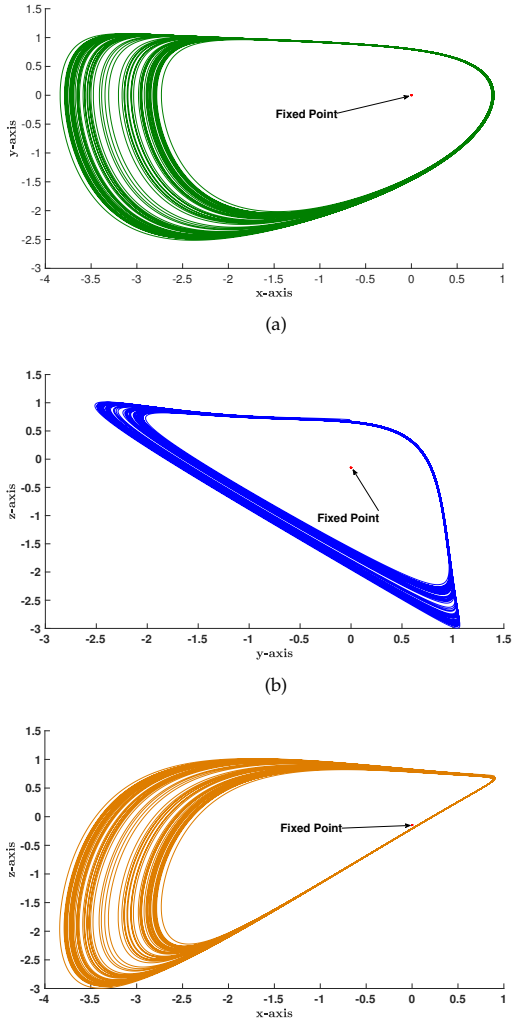

Figure 7 Hidden attractor of the system (5) with fixed-point in different phase spaces have initial value (0.9, 0, 0.7). (a) in xy-axis, (b) in yz-axis, (c) in xz-axis.

Other chaotic systems with equilibrium points were also explained.

Gong et al. have developed a chaotic system that generates both four-wing and single-wing hidden patterns, with only one stable node-focus equilibrium point (Gong *et al.* 2020). In addition, Cao and Zhao presented a unique chaotic system that exists in four dimensions and exhibits various interesting behaviors (Cao and Zhao 2021). The proposed system is characterized by three quadratic nonlinearity terms and exhibits various types of hidden attractors with equilibrium points. Further, Islam et al. studied a three-dimensional chaotic system that makes a hidden chaotic attractor with a line equilibrium in which a single non-bifurcation

parameter is used to control the amplitude and frequency (Islam *et al.* 2022).

Hidden chaotic attractor with extreme multi-stability

The study of multistability in the context of hidden chaotic attractors is crucial. Multistability with hidden attractors means that a system may have more than one stable state and that these stable states may not be directly observable or predictable without a detailed understanding of the underlying dynamics of the system.

The discovery of the hidden chaotic attractor with extreme multistability is a proof of the elusive nature of complex dynamical systems. It emerged in the late 20th century as researchers delved deeper into nonlinear dynamics.

The fascinating example of such type of work derived by Jafari (Jafari *et al.* 2018). They created a unique chaotic system with five dimensions. It's special because it has a hidden attractor and shows extreme multi-stability. These traits are quite rare in existing studies. The following is the mathematical model and illustration shown in Figures 8 & 9. To solve this nonlinear system (6) & (7) numerically with time step size 0.01 and total number of steps are 2^{16} the Runge-Kutta method of order 4 (RK4) is used.

$$\begin{aligned} \dot{x} &= y, \\ \dot{y} &= z, \\ \dot{z} &= w, \\ \dot{w} &= 4v + 1.7xz + 0.5xw, \\ \dot{v} &= y^2 + 1.1xy + xz. \end{aligned} \tag{6}$$

Let us consider another system as an example by Khalaf, A. J. M. (Khalaf *et al.* 2020):

$$\begin{aligned} \dot{x} &= y, \\ \dot{y} &= z, \\ \dot{z} &= w, \\ \dot{w} &= -0.16w^2 - 0.86w + v + 3.35xz - 0.36yz, \\ \dot{v} &= 1.09y^2 - 0.96y + 1.09xz - 1.92zw. \end{aligned} \tag{7}$$

Khalaf Analyzed a new 5D chaotic system that reveals hidden attractors with extreme multi-stability which is the modification of Jafari (Jafari *et al.* 2018) work shown in Figure 10.

In recent findings, researchers worked with chaotic systems that have hidden attractors with extreme multi-stability in nonlinear dynamics. Ahmadi et al. presented a rare chaotic system with extreme multistability and a unique equilibrium line (Ahmadi *et al.* 2020). Such systems are exceptionally rare. This newly developed chaotic system falls into the category of dynamical systems with hidden attractors. Its complete dynamical properties have been thoroughly investigated. This discovery expands our understanding of the hidden chaotic system's behavior. Additionally, Huang et al., derived a novel four-dimensional chaotic system from a known three-dimensional chaotic system that exhibits extreme multi-stability with an equilibrium point along a line (Huang *et al.* 2022). This system can generate innumerable symmetric and homogeneous attractors.

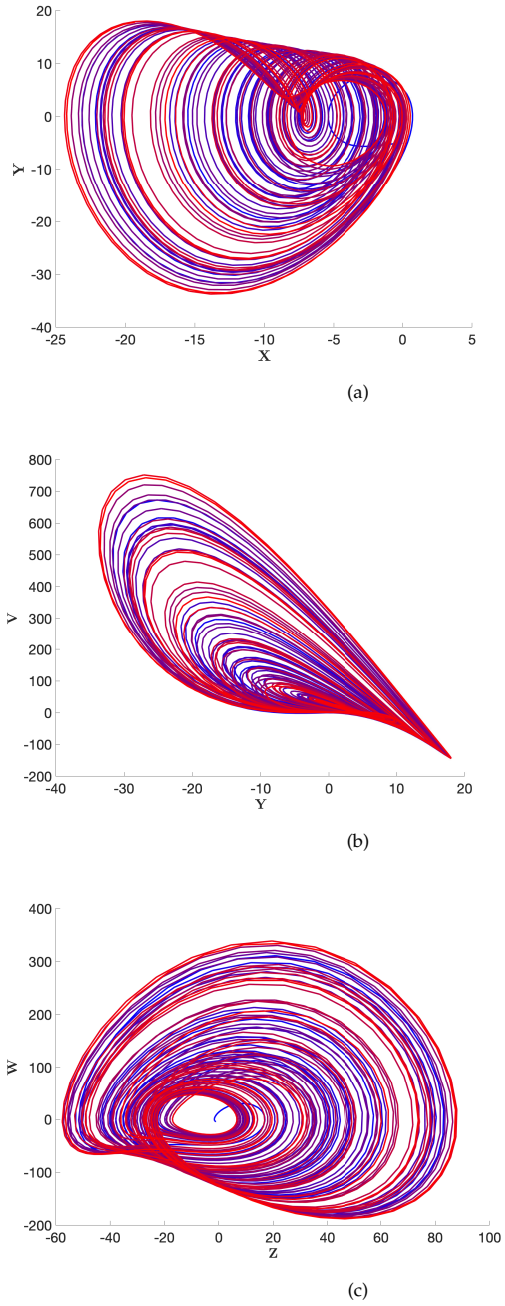

Figure 8 Strange attractor of the System (6) displays distinct shapes in three distinct projections when started from initial conditions (0,-5,-1,-4, 0).

Multi-scroll hidden chaotic attractors in nonlinear dynamics

Multi-scroll hidden chaotic attractors are a fascinating phenomenon in nonlinear dynamical systems. Unlike traditional attractors, these possess multiple basins of attraction, leading to complex, unpredictable trajectories.

An interesting example of multi-scroll hidden attractors has been derived by Xiaoyu Hu (Hu *et al.* 2017). They proposed the following novel 5-dimensional chaotic system in which hidden multi-scroll attractors and hidden multi-wing attractors can be observed at different phase levels as shown in Figure 11. The same as the previous RK4 method is used to solve the system (8)

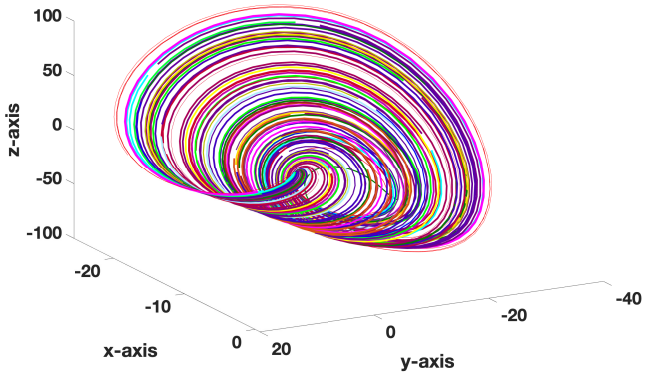

Figure 9 Strange attractor of the System (6) in 3D has initial conditions (0,-5,-1,-4, 0).

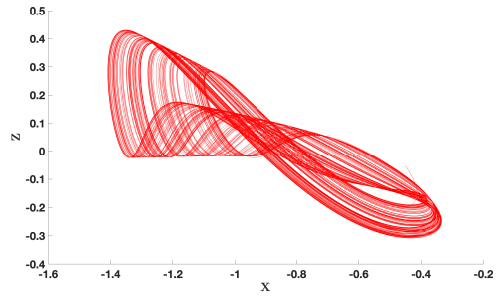

(a)

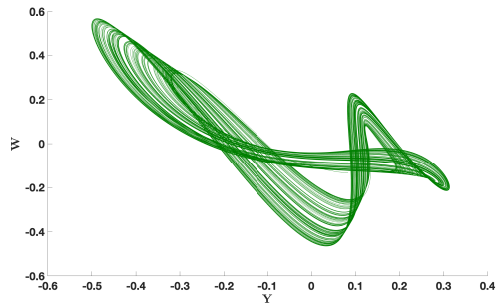

(b)

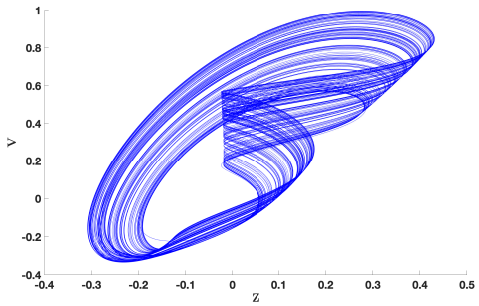

(c)

Figure 10 Visualize chaotic trajectories of system (7) with initial conditions (-1.44, 0.57, -0.82, -1.62, -0.75) through phase portrait projections of strange attractors. (a) in XZ, (b) in YW, (c) in ZV.

numerically.

$$\begin{aligned}
\dot{x} &= ay, \\
\dot{y} &= by - z + csin(2\pi dx), \\
\dot{z} &= y - ez, \\
\dot{u} &= -xy - (g + h\phi^2)u + k, \\
\dot{\phi} &= u.
\end{aligned} \tag{8}$$

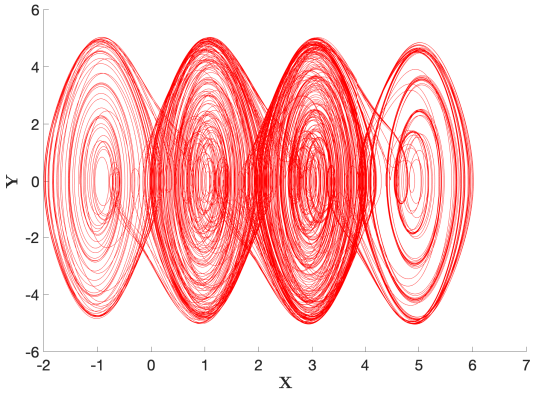

(a)

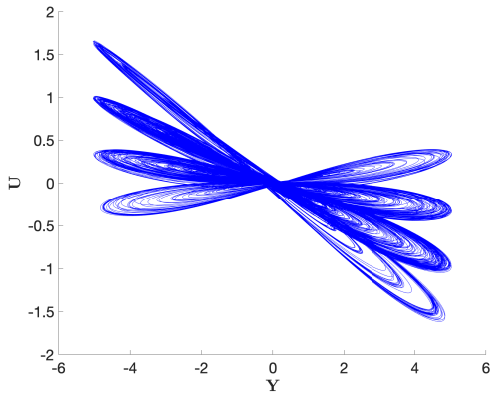

(b)

Figure 11 Hidden attractors of the system (8) with initial values $(x_0, y_0, z_0, u_0, \phi_0 = 0.2, 0, 0, 0.2)$, fascinating dynamics develop over a transient simulation period of 3000-time units. In (a) $x - y$ phase plane reveals the presence of 4 scroll hidden attractors, while in (b) $y - u$ phase plane reveals the presence of eight butterfly wings hidden attractors.

In this given scenario, the system parameters have been defined as follows: a = 0.25, b = 0.4, c = 2, d = 0.5, e = 0.5, g = 15, h = 0.01, and k = 0.05.

Some notable researchers have contributed to the study of multi-scroll hidden chaotic attractors. Escalante and Campos explored hidden attractors in addition to self-excitation (Escalante-González and Campos-Cantón 2019). First, a double-scroll attractor is generated from two equilibria connected by heteroclinic orbits. Hidden attractors arise when trajectories resembling these trajectories

break apart on a larger scale, increasing the complexity of the system. Pulido et al. have developed a method to generate dynamical systems with unique patterns, which they call bidirectional multiscroll hidden attractors (Pulido-Luna *et al.* 2021). These special attractors arise from piecewise linear systems, starting from their rest states, and can have both unidirectional (1D) and bidirectional (2D) lattice multiscroll patterns. This method opens up exciting possibilities for the design of complex and fascinating dynamical systems. In addition, Escalante and Campos have developed a method to generate complex systems with multiple hidden attractors (Escalante-González and Campos 2022). They use a nonlinear function to generate multiple self-excited attractors at specific points. Each pair of self-excited attractors leads to a hidden attractor, and these pairs combine to form larger hidden attractors. The number of self-excited attractors determines how many nested hidden attractors are created. These researchers have made significant strides in uncovering and studying multi-scroll hidden chaotic attractors, advancing our understanding of complex dynamical systems.

CONCLUSION

In this short review paper, we have addressed the fascinating area of hidden attractors in chaotic systems characterized by nonlinear functions. Through an extensive survey of various papers, we have discussed a variety of hidden chaotic attractors, each with particular features and behaviors.

First, we explored the realm of hidden chaotic attractors without equilibria. These fascinating phenomena challenge conventional wisdom and show that chaotic behavior can manifest in systems without stable equilibrium points. Moving forward, we have examined hidden chaotic attractors that coexist with equilibria. Furthermore, we have ventured into the realm of hidden chaotic attractors that exhibit extreme multiple stability. These systems exhibit a remarkable richness of dynamical behavior. This phenomenon has significant implications in the areas of control and synchronization, as it introduces a variety of possible states that the system can assume under different conditions. Lastly, we explored multi-scroll hidden chaotic attractors, a class of attractors characterized by their complex, multi-dimensional structure.

Collectively, this review underscores the profound importance of hidden attractors in nonlinear dynamics. These elusive phenomena challenge our conventional understanding of chaotic systems and offer new perspectives and avenues for research. Moreover, the diversity of hidden attractors discussed in this review provides fertile ground for further exploration and application in various scientific and engineering domains.

Acknowledgments

G.H.C. acknowledges the Fondo de Desarrollo Científico de Jalisco para atender Retos Sociales (2022), for the approved project 10304-2022. H.M.Z. acknowledges to the National Council of Humanities, Science, and Technology (CONAHCYT), Grant Number CVU 1290273.

Availability of data and material

Not applicable.

Conflicts of interest

The authors declare that there is no conflict of interest regarding the publication of this paper.

Ethical standard

The authors have no relevant financial or non-financial interests to disclose.

LITERATURE CITED

Abdolmohammadi, H. R., A. J. M. Khalaf, S. Panahi, K. Rajagopal, V.-T. Pham, *et al.*, 2018 A new 4d chaotic system with hidden attractor and its engineering applications: Analog circuit design and field programmable gate array implementation. Pramana **90**: 1–7.

Ahmadi, A., K. Rajagopal, F. E. Alsaadi, V.-T. Pham, F. E. Alsaadi, *et al.*, 2020 A novel 5d chaotic system with extreme multi-stability and a line of equilibrium and its engineering applications: circuit design and fpga implementation. Iranian Journal of Science and Technology, Transactions of Electrical Engineering **44**: 59–67.

Campos, E. *et al.*, 2020 Multistable systems with hidden and self-excited scroll attractors generated via piecewise linear systems. Complexity **2020**.

Cang, S., Y. Li, R. Zhang, and Z. Wang, 2019 Hidden and self-excited coexisting attractors in a lorenz-like system with two equilibrium points. Nonlinear Dynamics **95**: 381–390.

Cao, H.-Y. and L. Zhao, 2021 A new chaotic system with different equilibria and attractors. The European Physical Journal Special Topics **230**: 1905–1914.

Chen, H., S. He, A. D. Pano Azucena, A. Yousefpour, H. Jahanshahi, *et al.*, 2020 A multistable chaotic jerk system with coexisting and hidden attractors: Dynamical and complexity analysis, fpga-based realization, and chaos stabilization using a robust controller. Symmetry **12**: 569.

Djorwe, P., J. Yves Effa, and S. G. Nana Engo, 2023 Hidden attractors and metamorphoses of basin boundaries in optomechanics. Nonlinear Dynamics **111**: 5905–5917.

Dubois, P., T. Gomez, L. Planckaert, and L. Perret, 2020 Data-driven predictions of the lorenz system. Physica D: Nonlinear Phenomena **408**: 132495.

Dudkowski, D., S. Jafari, T. Kapitaniak, N. V. Kuznetsov, G. A. Leonov, *et al.*, 2016 Hidden attractors in dynamical systems. Physics Reports **637**: 1–50.

Dueñas, J., C. Núñez, and R. Obaya, 2023 Bifurcation theory of attractors and minimal sets in d-concave nonautonomous scalar ordinary differential equations. Journal of Differential Equations **361**: 138–182.

Escalante-González, R. and E. Campos, 2022 Multistable systems with nested hidden and self-excited double scroll attractors. The European Physical Journal Special Topics **231**: 351–357.

Escalante-González, R. and E. Campos-Cantón, 2019 Coexistence of hidden attractors and self-excited attractors through breaking heteroclinic-like orbits of switched systems. arXiv preprint arXiv:1908.03789 .

Gong, L., R. Wu, and N. Zhou, 2020 A new 4d chaotic system with coexisting hidden chaotic attractors. International Journal of Bifurcation and Chaos **30**: 2050142.

Gong, L.-H., H.-X. Luo, R.-Q. Wu, and N.-R. Zhou, 2022 New 4d chaotic system with hidden attractors and self-excited attractors and its application in image encryption based on rng. Physica A: Statistical Mechanics and its Applications **591**: 126793.

Gray, W. S., M. Palmstrøm, and A. Schmeding, 2023 Continuity of formal power series products in nonlinear control theory. Foundations of Computational Mathematics **23**: 803–832.

Hu, X., C. Liu, L. Liu, Y. Yao, and G. Zheng, 2017 Multi-scroll hidden attractors and multi-wing hidden attractors in a 5-dimensional memristive system. Chinese Physics B **26**: 110502.

Huang, L., W. Yao, J. Xiang, and L. WANG, 2022 Extreme multistability of a four-dimensional chaotic system with infinitely many symmetric homogeneous attractors. **44**: 390–399.

Islam, Y., C. Li, Y. Jiang, X. Ma, A. Akgul, *et al.*, 2022 A hidden chaotic attractor with an independent amplitude-frequency controller. Complexity **2022**.

Jafari, S., A. Ahmadi, A. J. M. Khalaf, H. R. Abdolmohammadi, V.-T. Pham, *et al.*, 2018 A new hidden chaotic attractor with extreme multi-stability. AEU-International Journal of Electronics and Communications **89**: 131–135.

Jafari, S., J. Sprott, and S. M. R. H. Golpayegani, 2013 Elementary quadratic chaotic flows with no equilibria. Physics Letters A **377**: 699–702.

Jasim, B. H., K. H. Hassan, and K. M. Omran, 2021 A new 4-d hyperchaotic hidden attractor system: Its dynamics, coexisting attractors, synchronization and microcontroller implementation. International Journal of Electrical & Computer Engineering (2088-8708) **11**.

Khalaf, A. J. M., H. R. Abdolmohammadi, A. Ahmadi, L. Moysis, C. Volos, *et al.*, 2020 Extreme multi-stability analysis of a novel 5d chaotic system with hidden attractors, line equilibrium, permutation entropy and its secure communication scheme. The European Physical Journal Special Topics **229**: 1175–1188.

Kingni, S. T., G. F. Kuiate, V. K. Tamba, V.-T. Pham, and D. V. Hoang, 2019 Self-excited and hidden attractors in an autonomous josephson jerk oscillator: analysis and its application to text encryption. Journal of Computational and Nonlinear Dynamics **14**: 071004.

Kuznetsov, N., 2020 Theory of hidden oscillations and stability of control systems. Journal of Computer and Systems Sciences International **59**: 647–668.

Kuznetsov, N., T. Mokaev, V. Ponomarenko, E. Seleznev, N. Stankevich, *et al.*, 2023 Hidden attractors in chua circuit: mathematical theory meets physical experiments. Nonlinear Dynamics **111**: 5859–5887.

Kuznetsov, N. V., M. Y. Lobachev, M. V. Yuldashev, R. V. Yuldashev, E. V. Kudryashova, *et al.*, 2020 The birth of the global stability theory and the theory of hidden oscillations. In *2020 European Control Conference (ECC)*, pp. 769–774, IEEE.

Lai, Q., Z. Wan, and P. D. Kamdem Kuate, 2020 Modelling and circuit realisation of a new no-equilibrium chaotic system with hidden attractor and coexisting attractors. Electronics Letters **56**: 1044–1046.

Lakshmanan, M. and S. Rajaseekar, 2012 *Nonlinear dynamics: integrability, chaos and patterns*. Springer Science & Business Media.

Lin, H., C. Wang, and Y. Tan, 2020 Hidden extreme multistability with hyperchaos and transient chaos in a hopfield neural network affected by electromagnetic radiation. Nonlinear Dynamics **99**: 2369–2386.

Molaie, M., S. Jafari, J. C. Sprott, and S. M. R. H. Golpayegani, 2013 Simple chaotic flows with one stable equilibrium. International Journal of Bifurcation and Chaos **23**: 1350188.

Munmuangsaen, B. and B. Srisuchinwong, 2018 A hidden chaotic attractor in the classical lorenz system. Chaos, Solitons & Fractals **107**: 61–66.

Nag Chowdhury, S. and D. Ghosh, 2020 Hidden attractors: A new chaotic system without equilibria. The European Physical Journal Special Topics **229**: 1299–1308.

Njitacke, Z., T. Fozin, L. K. Kengne, G. Leutcho, E. M. Kengne, *et al.*, 2020 Multistability and its annihilation in the chua's oscillator with piecewise-linear nonlinearity. Chaos Theory and Applications **2**: 77–89.

Pham, V.-T., C. Volos, S. Jafari, and T. Kapitaniak, 2017 Coexistence of hidden chaotic attractors in a novel no-equilibrium system. Nonlinear Dynamics **87**: 2001–2010.

Pulido-Luna, J. R., J. A. López-Rentería, N. R. Cazarez-Castro, and E. Campos, 2021 A two-directional grid multiscroll hidden attractor based on piecewise linear system and its application in pseudo-random bit generator. Integration **81**: 34–42.

Rybin, V., A. Tutueva, T. Karimov, G. Kolev, D. Butusov, *et al.*, 2021 Optimizing the synchronization parameters in adaptive models of rössler system. In *2021 10th Mediterranean Conference on Embedded Computing (MECO)*, pp. 1–4, IEEE.

Tanaka, K., T. Ikeda, and H. O. Wang, 1998 A unified approach to controlling chaos via an lmi-based fuzzy control system design. IEEE Transactions on Circuits and Systems I: Fundamental Theory and Applications **45**: 1021–1040.

Wang, N., G. Zhang, N. V. Kuznetsov, and H. Bao, 2021 Hidden attractors and multistability in a modified chua's circuit. Communications in Nonlinear Science and Numerical Simulation **92**: 105494.

Wang, X. and G. Chen, 2012 A chaotic system with only one stable equilibrium. Communications in Nonlinear Science and Numerical Simulation **17**: 1264–1272.

Wei, Z., 2011 Dynamical behaviors of a chaotic system with no equilibria. Physics Letters A **376**: 102–108.

Wu, X., H. Wang, and S. He, 2021 Localization of hidden attractors in chua's system with absolute nonlinearity and its fpga implementation. Frontiers in Physics **9**: 788329.

Yang, L. and Q. Lai, 2023 Construction and implementation of discrete memristive hyperchaotic map with hidden attractors and self-excited attractors. Integration p. 102091.

Ye, X. and X. Wang, 2023 Hidden oscillation and chaotic sea in a novel 3d chaotic system with exponential function. Nonlinear Dynamics pp. 1–10.

Zaqueros-Martinez, J., G. Rodriguez-Gomez, E. Tlelo-Cuautle, and F. Orihuela-Espina, 2023 Fuzzy synchronization of chaotic systems with hidden attractors. Entropy **25**: 495.

Zelinka, I., 2016 Evolutionary identification of hidden chaotic attractors. Engineering Applications of Artificial Intelligence **50**: 159–167.

How to cite this article: Zeeshan, H. M., Reátegui, R. J., García-López, J. H., Bibi, S., and Cuellar, G. H. Hidden Attractors in Chaotic Systems with Nonlinear Functions. *Chaos Theory and Applications*, 6(2), 144-151, 2024.

CHAOS
Theory and Applications
in Applied Sciences and Engineering

e-ISSN: 2687-4539
RESEARCH ARTICLE
Vol.6 / No.2 / 2024 / pp.152-158
Special Issue (EDIESCA 2023)
https://doi.org/10.51537/chaos.1376145

Flocking Behavior of Boids Driven by Hyperchaotic MACM System

Medina Galindo Ana C. [α,1], **Cardoza Avendaño Liliana** [α,2], **López Gutiérrez Rosa Martha** [α,3] **and Cruz Hernández Cesar** [*,4]
[α]Engineering, Architecture and Design Faculty, Autonomous University of Baja California (UABC), Ensenada 22860, Mexico, [*]Electronics and Telecommunication Department, Scientific Research and Advanced Studies Center of Ensenada (CICESE), Ensenada 22860, BC, Mexico.

ABSTRACT

In the present work a detailed study is presented, on the design, programming, and investigation of the behavior of flocking (Movement type flock), through the model of BOIDS, for its acronym in English "Bird Oid Object" (Object type bird), which was devised by Craig Reynolds in 1986. This complex flocking behavior that occurs arises from the interaction of simple local rules, in which complexity and sensitivity to initial conditions are present. A measure of chaotic compound will be introduced to the algorithm by means of a new four-dimensional autonomous hyperchaotic system based on the 3D Méndez-Arellano-Cruz-Martínez (MACM) system. The measures proposed herein, therefore, may have the potential to predict, control, and exemplify the behavior of group intelligence study systems that occur in nature, allowing the implementation of these systems in groups of robots through the implementation of hyperchaotic trajectories in the future, to obtain greater speed and efficiency, obstacle and collisions avoidance in their flights.

KEYWORDS

Flocking behavior
Boids
Hyperchaotic
MACM system

INTRODUCTION

The grouping of animals that occurs frequently in nature between different types of species; such as the behavior of bee swarms Karaboga *et al.* (2005), schools of fish (Pourpanah *et al.* 2023), flocks of birds (Duman *et al.* 2012), among others, has been an inspiration for different research groups in recent years, taking this behavior as an approach to solve very complex problems. By studying and simulating how animals behave, scientists hope to create powerful computational models that can solve challenging problems, optimize processes, and make decisions in ways inspired by the efficient and adaptive strategies found in nature.

Multi-agent-based simulation (MBS) is a valuable technique used to model flocking behavior, where collective behavior emerges from individual interactions. It helps understand complex interactions at a larger scale, which are often hard to predict, comprehend, and simulate. This difficulty arises because of the non-linear relationship between micro (individual agent) and macroscopic (overall group) properties. Small changes in an agent's environment or rules can result in vastly different outcomes in the simulation. Due to these complexities, MBS becomes a powerful tool for studying and analyzing emergent phenomena, providing insights into systems where traditional approaches might fall short.

One of the most commonly used methods to simulate the emergent behavior that occurs in different groups of animals in nature, are the so-called boids, devised by Craig Reynolds in 1987 (Reynolds 1987). This model was the first published way of simulating a fairly realistic flock simulation from an algorithm. It was developed into an artificial life program where each individual in the flock is called an agent, which has its own position, speed, and orientation, exhibiting complex flock behavior that arises from the interaction of three simple local rules:

- **Separation**. An agent must avoid collisions with other nearby agents. To avoid collisions, a separation factor is added. An agent will keep a certain distance from all other agents in his neighborhood. If the agent finds another agent too close, it will try to move away from them to avoid collisions.
- **Cohesion**. An agent must stick to the group or flock. To ensure this, a cohesive factor is added. The agent will move towards the average position of the neighboring agents. When

Manuscript received: 15 October 2023,
Revised: 23 February 2024,
Accepted: 9 March 2024.

[1]ana.medina.galindo@uabc.edu.mx
[2]lcardoza@uabc.edu.mx
[3]roslopez@uabc.edu.mx
[4]ccruz@cicese.mx (**Corresponding author**)

other agents are within the neighborhood, the agent will try to move to the midpoint of all the others.

- **Alignment**. The alignment rule is obtained by calculating a force directed at the average of the velocities of the neighbors.

The three rules of separation, alignment, and cohesion will result in different vector forces that must act on the agent to which they belong. Since animals cannot turn instantly in real life, a resultant force is calculated by adding the three effective vectors. The three forces can be applied differently by normalizing the individual vectors and then multiplying them with appropriate weights. Therefore, the specific behavior of each agent could be induced by the slight alteration of an aspect of the so-called flocking.

The resulting force is added to the velocity vector of the agent. Then the speed is normalized or limited to a maximum allowed speed. Finally, the agent's velocity is added to its position vector resulting in motion. The previous velocity can also be used as the base vector for the resultant, giving each agent a flow motion closer to what occurs in nature. Currently there are few works that can be found about the study of boids applied to chaotic systems, however there is great potential to use the dynamics of boids in relation to this type of systems, since adding rules can present behaviors that can be considered emergent, as was presented in previous work (Itoh and Chua 2007).

In this paper, we propose implement a new rules for the behavior of the boids, first with the introduction of a hyper MACM chaotic system (Méndez-Ramírez *et al.* 2021), where the boids are led in this trajectory. Emerging behavior was investigated through simulations implemented in MATLAB. After the analysis of the movement of each boid as well as the chaotic component of their trajectories, finally the conclusions obtained about the control of the boids are presented.

BASIC ANALYSIS AND MODELING OF BOIDS

We consider a network of N identical nodes that will be called *boids*, each node is considered like basic element with behavior depending on the nature of the network, which can be modeled by a set of nonlinear autonomous differential equations, with each boid being an n-dimensional dynamical system. The state equations of the entire network of boids are described as follows,

$$\dot{\mathbf{u}}_i = f_i(\mathbf{u}_1, \mathbf{u}_2, ..., \mathbf{u}_n), \quad i = 1, 2, ..., n \tag{1}$$

where $\mathbf{u}_i = (u_1, u_2, ..., u_n)^T \in \mathbb{R}^n$ is a state vector of boid i, and $\mathbf{f}(\mathbf{u}) = (f_1(\mathbf{u}), f_2(\mathbf{u}), ...f_n(\mathbf{u}))$ is a nonlinear vector function of $\mathbf{u}$. Given initial state ${u_i}^{\alpha}(0)$ at $t = 0$, the state ${u_i}^{\alpha}$ of each isolated boid B_α is assumed to envolve for all $t \geq 0$ via state equations,

$$\dot{u}_i^{\alpha} = f_i(u_1, u_2, ..., u_n), \quad i = 1, 2, ..., n. \tag{2}$$

For ease of modeling we will assume that all boids are identical, they are only influenced in their trajectories by those nearby neighboring boids which are located on a sphere described as S_α, if a boid moves in a random trajectory but in its trajectory the boid gets close to another boid they will be coupled as long as they are positioned at any distance inside the sphere S_α with radius ϵ as shown in Figure 1 a),

$$S_\alpha(\epsilon, t) = \left\{ B_\beta : r_{\alpha,\beta} \triangleq \sqrt{\sum_{i=1}^{n} (u_i{}^{\alpha}(t) - u_i{}^{\beta}(t))^2} \leq \epsilon \right\}, \tag{3}$$

at time t, where $r_{\alpha,\beta}$ indicates the distance between the boids B_α and B_β. We will usually delete ϵ and t from $S_\alpha(\epsilon, t)$ and simply write S_α to prevent confusions, see Figure 1 a.

Then, the dynamics of the nonlinear chaotic network of the locally coupled boids defined by

$$\dot{\mathbf{u}}_i^{\alpha} = f_i(u_1^{\alpha}, u_2^{\alpha}, ..., u_n^{\alpha}) + \sum_{B_\beta \in S_\alpha} D_i^{\beta} g_i(u_1^{\beta}, u_2^{\beta}, ..., u_n^{\beta}),$$
$$i = 1, 2, ..., n, \quad \alpha = 1, 2, ..., M \tag{4}$$

where D_i^{β} are coupling coefficients, and $\mathbf{g}(\mathbf{u}) = (g_1(\mathbf{u}), g_2(\mathbf{u}), ..., g_n(\mathbf{u}))$ is a nonlinear vector function of $\mathbf{u}$.

The dynamics of Equation (4) describes networks of boids with nonlinear behaviors, the number of boids belonging to S_α can change continuously as time t increases. Since at first, the boids can be found in random positions and speeds within some area, and as time passes they can get closer to a certain distance within the sphere S_α, continuously changing the number of boids in S_α.

The behaviors that make up the flock model are expressed in terms of "close flockmates". While a boid is in motion, it does not require full knowledge of the position and speed of each boid in the entire herd, it only knows the information of a small subset of it. This subset is composed of what we call the expression "near flockmates", often used in boid modeling of steering behavior, which refers to the awareness each boid has of the bodies of other nearby boids, based on the distance between them. Thus the boid has a range of perception of the world in the shape of the sphere around it, described in Equation (3). When different boids are within a very close distance of each other the boids perception spheres can overlap, influencing each other's behavior depending on their rule parameters.

In this section, we will describe the implementation of the boid rules. Based on the Reynolds model (Reynolds 1987), a model was made a boid swarm model in *MATLAB* software, the boid model has 5 rules: separation, cohesion, alignment, edge avoidance, and hyperchaotic MACM attractor, described as follows.

Cohesion

The cohesion force has the objective of keeping the flock of boids together. This means that this force will drive each agent to move towards the average position of its nearest neighbors which is in the volume of the sphere $S_\alpha(\epsilon, t)$ of each boid, as shown in Figure 1 b). This is expressed mathematically in the Equation (5). Boid cohesion is calculated using two steps.

First, the central position of the nearest neighbors of each agent is calculated by,

$$\overline{u_i^{\alpha}}(t) = \frac{\sum_{\beta \in S_\alpha} u_i^{\beta}(t)}{N_\alpha}, \tag{5}$$

where N_α indicates the number of nearby flockmates. Then the tendency of the boid to sail towards the visible flock center of density $\overline{u_i^{\alpha}}(t)$. Therefore the control dynamics is calculated as shown below,

$$\dot{u}_i^{\alpha} = f_i(u_1^{\alpha}, u_2^{\alpha}, ..., u_n^{\alpha}) + d_i^{\alpha}(\overline{u_i^{\alpha}} - u_i^{\alpha}), \tag{6}$$

where $d_i^{\alpha} > 0$.

There is a special case when there is no one around. The center of the nearby flockmates $\overline{u_i^{\alpha}(t)} = 0$. In this case, Equation (5) is not defined and the cohesion rule does not apply.

This principle encourages boids to stay close to their neighbors, leading to a sense of togetherness within the flock. By gravitating towards the average position of nearby companions, the cohesion

rule promotes collective movement, enabling boids to exhibit coordinated behaviors without any centralized leadership. As a result, the flock maintains a cohesive structure.

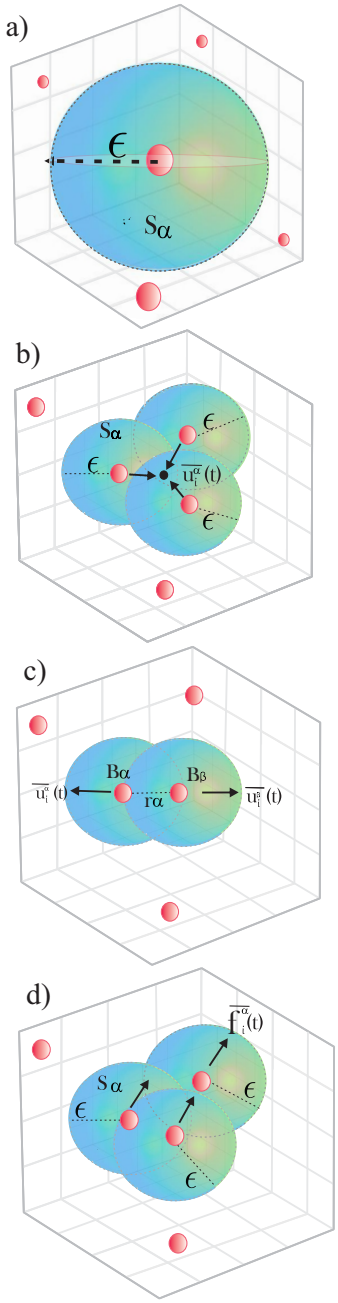

Figure 1 Graphic description of boids: a) Boid inside sphera S_α with radius ϵ. Rules governing the movement of boids, b) Cohesion, c) Separation, d) Alignment.

Separation

Separation force is the complementary force to the cohesion force as shown in Figure 1 c). Each member of a flock tends to avoid collision with its nearby neighbors. This tendency is called separation or collision avoidance. In the case where the distance $r\alpha$, between the boids B_α and B_β becomes less than $\delta > 0$, the boids will tend to disperse from the center of nearby flockmates. This is calculated by the following dynamics:

$$\left.\begin{aligned} \dot{u}_i^\alpha &= f_i(u_1^\alpha, u_2^\alpha, ..., u_n^\alpha) + e_i^\alpha(\overline{u_i^\alpha} - u_i^\alpha), \\ \dot{u}_i^\beta &= f_i(u_1^\beta, u_2^\beta, ..., u_n^\beta) + e_i^\beta(\overline{u_i^\beta} - u_i^\beta), \end{aligned}\right\} \tag{7}$$

where $e_i^\alpha, \quad e_i^\beta > 0$.

The separation rule in boids algorithm is a fundamental principle for simulating flocking behavior. Each boid maintains a minimum distance from its nearby flockmates, preventing collisions and promoting spacing within the group. By avoiding crowding, boids create a sense of personal space, enhancing overall flock stability and preventing individual boids from getting too close to each other.

Alignment

Alignment is the process by which each boid attempts to match its velocity and direction with that of its nearby flockmates as shown in Figure 1 d). It promotes the cohesive and coordinated movement of the group, leading to the emergence of flocking behavior. This rule is essential because it enables the boids to maintain alignment and unity without relying on any centralized control or explicit communication between individuals.

The alignment rule is implemented as follows: each boid examines its surroundings and identifies its nearby neighbors within a certain perception radius $S_\alpha(\epsilon, t)$, dictating how far it can "see" other flockmates. The boid then calculates the average velocity of its neighbors, which represents the average direction in which the neighboring boids are moving. The average velocity of nearby flockmates is defined by

$$\overline{f_i^\alpha} = \frac{\sum_{\beta \in S_\alpha} f_i(u_1^\beta, u_2^\beta, ..., u_n^\beta)}{N_\alpha}. \tag{8}$$

To align with the flock, the boid adjusts its own velocity to match the computed average velocity of its neighbors. However, it doesn't do this instantaneously; instead, it gradually changes its velocity over time to create a smooth and realistic alignment process. This gradual adjustment prevents sudden changes in direction that could disrupt the cohesion of the flock.

IMPLEMENTATION OF THE HYPERCHAOTIC MACM ATTRACTOR TO THE NETWORK OF BOIDS

The behavior of the boids is given by Reynolds (1987), and each of the behavioral rules is expressed as a vector. These rules are sorted by priority and added to an accumulator of the boids. This continues until the sum of the accumulated magnitudes increases the maximum acceleration value. In this work, the value of a new vector given by the new 4D hyperchaotic MACM system in the network of boids is prioritized, so that the boid has the priority to follow the hyperchaotic attractor trajectory, see Figure 2.

The implementation of a new rule consists of placing a new 4D hyperchaotic MACM system (Méndez-Ramírez *et al.* 2021), as a new rule in the behavior of the boids. This MACM attractor is obtained by modifying the 3D MACM system inspired by previous works (Méndez-Ramírez *et al.* 2017). A hyperchaotic system is a mathematical concept that extends the idea of a chaotic system. It has more than one positive Lyapunov exponent, see Table 1, this indicates greater complexity in its dynamic behavior in the projection of the phase space in the plane (Rajagopal *et al.* 2018). To create a hyperchaotic system, k chaotic systems can be coupled, resulting in an attractor with n positive Lyapunov exponents. This

Table 1 Analysis of stability of equilibrium points for a new hyperchaotic MACM system based on the Lyapunov exponents.

Point	Eigenvalues	Stability
P_0	$\lambda_1 = -0.5247$	λ_1,λ_2,$\lambda_4 < 0$, and $\lambda_3 > 0$
	$\lambda_2 = -1$	
	$\lambda_3 = 4.5361$	unstable saddle point
	$\lambda_4 = -6.5113$	
P_{1-4}	$\lambda_1 = -0.4939$	λ_1,$\lambda_4 < 0$, and the real part
	$\lambda_2 = 0.94767 - 3.4506i$	λ_2,$\lambda_3 > 0$
	$\lambda_3 = 0.94767 + 3.4506i$	unstable saddle point
	$\lambda_4 = -4.9014$	
P_{5-6}	$\lambda_1 = -0.4918$	λ_1,$\lambda_4 < 0$, and $\lambda_2, \lambda_3 > 0$
	$\lambda_2 = 1.5384$	
	$\lambda_3 = 2.7915$	unstable saddle point
	$\lambda_4 = -7.3381$	
P_{7-8}	$\lambda_1 = 0$	$\lambda_2 < 0$, and the real part
	$\lambda_2 = -1$	λ_2,$\lambda_3 < 0$
	$\lambda_3 = 1.25 + 0.9682i$	Spiral stable point
	$\lambda_4 = -1.25 - 0.9682i$	

coupling causes the dimension of the attractor to increase, leading to a transition from chaos to hyperchaos. As this transition occurs, the second Lyapunov exponent increases continuously (Kapitaniak *et al.* 2000), highlighting the greater complexity and richness of the system in its behavior compared to a normal chaotic system.

The dynamics of the hyperchaotic MACM system used is defined as follows (Méndez-Ramírez *et al.* 2021):

$$\begin{aligned} \dot{x} &= -ax - byz, \\ \dot{y} &= -x + cy + cw, \\ \dot{z} &= d - y^2 - z, \\ \dot{w} &= x - w. \end{aligned} \tag{9}$$

The given system in the Equation (9) is a mathematical representation with ten terms, including two quadratic nonlinearities. It also involves four parameters, denoted as a, b, c, and d, which must satisfy certain conditions: $a, b, c, d \in \mathbb{R}^+$ and $c < a + 2$. In this context, b and d are referred to as the bifurcation parameters, which influence the system's behavior. When the specific values $a = 2, b = 2, c = 0.5$, and $d = 14.5$ are used in the MACM system exhibits hyperchaotic behavior.

ALGORITHM IMPLEMENTATION HIERARCHY

The algorithm for the simulation of the boids was realized in MATLAB software.

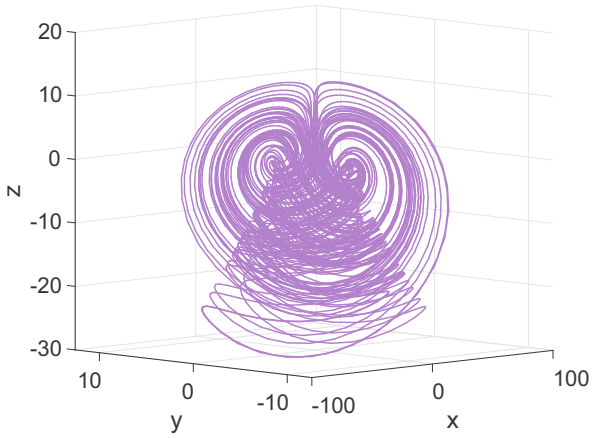

Figure 2 Hyperchaotic attractor of MACM system (9). Phase space x versus y versus z.

A boid can have conflicting requests as long as the matching algorithm is applied. The behavior is simply the result of the interaction of the aforementioned rules. For example, if two boids are moving in such a way that they are getting closer, with different speeds, the cohesion priority could override the spacing rule, since the boid cohesion request is opposite to the spacing rule, and therefore they could overlap, cancel directions, the boid could make only a small turn and crash into another boid. The highest priority should be to avoid collisions between the boids and the cohesion rule. Therefore, the behavior of the boids is modeled using a rule order priority as shown in Table 2.

Table 2 Rule Order Priority.

Priority	Order	Rule
High	1	Avoid edge
High	2	Cohesion
Medium	3	Separation
Low	4	Alignment
Low	5	MACM attractor

NUMERICAL SIMULATION RESULTS

This section shows the results obtained from the numerical simulation.

Numerical simulations for two boids

Figures 3 and 4 show the modeling of two boids following the trajectory of the hyperchaotic MACM attractor, Figure 3 show the projections of the phase space in the planes. Figure 4 shows the temporary states x, y, z, and w. Both figures show two boids modeled with the strange attractor of Equation (9) system by using the initial conditions $x(0) = 0.5$, $y(0) = 0$, $z(0) = -5$, $w(0) = 0.51$, the parameter values $a = 2$, $b = 2$, $c = 0.5$, and $d = 14.5$. The value of 80 has been added to each point of the solution of the Equation (9) system, because the attractor is located from -80 to 80

on the x axis, from -13 to 13 on the y axis, -30 to 13 on the z axis approximately.

Computer simulations use the following parameters.

Table 3 MACM´s oscillator.

Rule	Parameter
Flock centering	$d_i^{\alpha} = 5$
Velocity matching	$R_{max} = 2$
Collision avoidance	$\delta = 1.5$

Figures 3 and 4 show the trajectories followed by two boids, their cohesive movement as a flock. The distance between the two boids can be seen in Figure 5, it is shown that for 1000 iterations, the maximum distance does not exceed the value of 8, proving that the cohesion rule holds along the trajectory of the two boids.

The value of 80 has been added to each point of the solution of the hyperchaotic MACM system, because the attractor is located from -80 to 80 on the x axis, from -13 to 13 on the y axis, -30 to 13 on the the z axis approximately, to facilitate the implementation in robot trajectories in the future.

The synchronization behavior of the two boids is presented in Figure 6. However, it is important to note that exact synchronization is not achieved, leading to a certain thickness in the Lissajous figures. A thinner line would indicate perfect timing, but it can also lead to potential collisions.

In Figure 6 in particular, when considering the MACM oscillators, the two boids maintain a close distance of approximately $\delta = 1.5$.

Error analysis in trajectories of 2 boids

The separation measure was obtained in the trajectories of two boids, concerning the desired trajectory of the hyperchaotic MACM attractor employing the Root Mean Square Error, commonly referred to as RMSE, which is a statistical measure used to quantify the average magnitude of the error between predicted values and actual values. It is frequently employed to evaluate the precision of a predictive model. RMSE calculates the mean squared difference between forecasted numbers and subsequently observed numbers. the RMSE is defined by:

$$RMSE = \sqrt{\frac{1}{n}\sum_{i=1}^{n}(y_i - \hat{y}_i)^2} \tag{9}$$

where n represents the total number of data points or observations being considered, y_i represents the actual observed values, y represents the predicted values from the model. An RMSE = 7.54 was obtained for boid 1 and an RMSE = 8.56 for boid 2.

It is observed that there is a difference between the trajectory of the hyperchaotic MACM attractor and the trajectory of the boids, this is because of the order of priority shown in Table 2. is implemented so that the boids adjust their speed and position to the rules that define the boids, this implies that the distance between the trajectory of the boids and the trajectory of the MACM chaotic attractor will increase for certain coordinates, despite this, the ability of the boids to drive along the trajectory of the chaotic attractor is observed in Figure 3.

It is worth mentioning that RMSE gives greater weight to larger variations, as it squares off the differences before averaging. Consequently, larger variations between the position of the boids concerning the hyperchaotic MACM attractor trajectory have a greater impact on the RMSE than smaller gaps.

It is observed that the distance maintained between the trajectories of the two boids is less than the distance between the trajectories of the boids and the trajectory of the hyperchaotic attractor, this is because the rules of behavior are imposed, and it is the objective in this studio. If the boids give priority to following the trajectory of the hyperchaotic attractor, collisions could occur between them since the separation rule would be secondary. The scenario could also arise that the distance between them was greater than the parameter implemented in the cohesion rule and the boids would no longer remain together in the trajectory since they would not recognize each other as close neighbors.

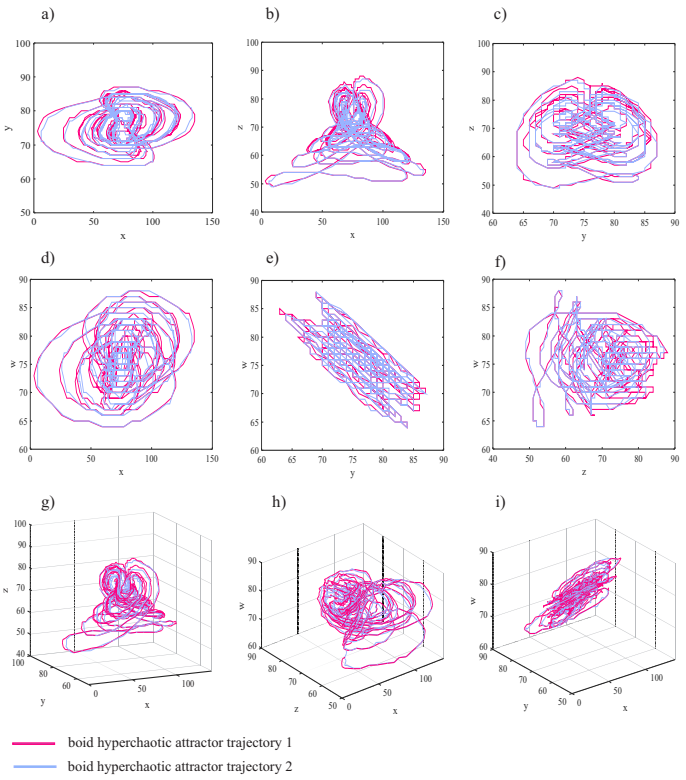

Figure 3 Projections of the phase space of flocking of two boids driven by hyperchaotic MACM attractor. a) (x,y), b) (x,z), c) (y,z), d) (x,w), e) (y,w), f) (z,w), g) (x,y,z), h) (x,z,w), and i) (x,y,w).

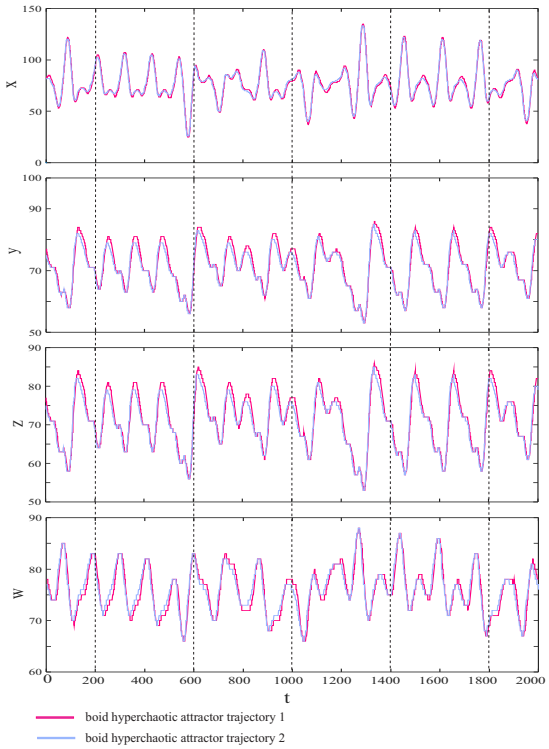

Figure 4 Temporary states x, y, z, and w, of two boids driven by hyperchaotic MACM attractor.

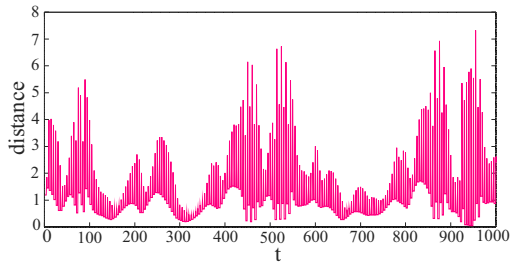

Figure 5 Distance between two boids (MACM's oscillators).

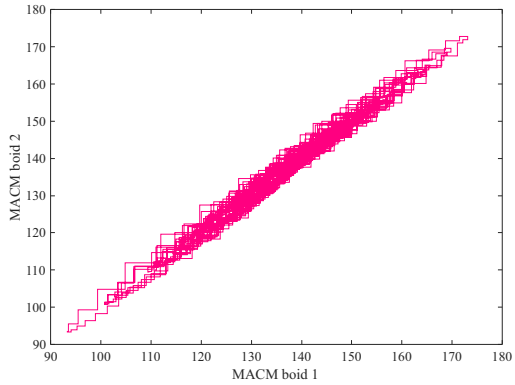

Figure 6 Synchronization of two boids (MACM's oscillators).

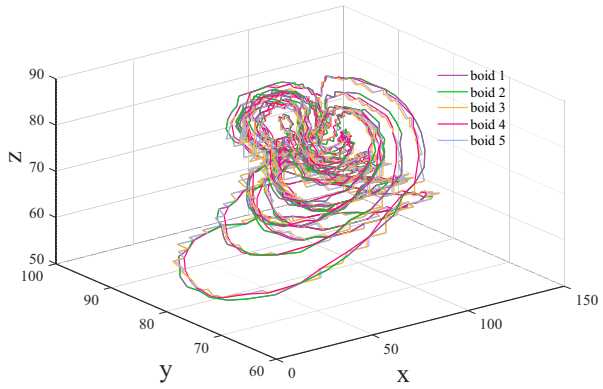

Figure 7 Synchronization of 5 boids (MACM's oscillators for $t \in [0, 50]$. MATLAB overwrites the existing graph in some sections and plots the trajectories in order of purple, green, yellow, orange, red, blue).

Computer simulations of the behavior of 5 boids controlled by the hyperchaotic MACM system is illustrated in Figure 7, it is observed that the flock of 5 boids that two boids are together all the way from the start and as time increases. In Figure 7, it can be seen that the trajectories are intertwined by observing the different colors throughout the entire journey. It is observed that in some sections the trajectories overlap over the same region in space, observing only two or three lines.

CONCLUSION

The investigation of a nonlinear system was carried out through the implementation of an algorithm that describes the behavior of the boids, which are controlled by a hyperchaotic MACM system, the implementation of this system forces the boids to follow their attractor trajectory, induce them to follow it. In this work a network formed by N identical nodes was considered, this behavior can be described using a set of nonlinear autonomous differential equations. The boids maintain the three rules of cohesion, alignment, and separation that define them while maintaining a hyperchaotic trajectory.

It is observed that the boids have characteristics that they share with complex systems with dynamic behavior, and emergent properties that arise from the interactions between the boids were presented.

For future work, tasks remain to be performed described below:

- Implementation of a rule for the introduction of one or more predators in the system, where the prey are the boids.
- Implementation of the rule to avoid obstacles, which prevent continuing with the trajectory, and the boids are forced to surround them to continue with the trajectory of the hyperchaotic attractor.
- Implement a rule to find specific targets.
- Implement a rule to adhere to a leader, the boid who is in front will take the position of leader and the others will follow.
- Implement this study in robots through the generation of hyperchaotic trajectories to directly influence the behavior of the robot's speeds, using the inputs to the system; as are the speeds of the engines. One of the advantages of this method is its simplicity and ease of being implemented in mobile robots

since it is only necessary to know the number of inputs handled by the robot to implement the algorithm. For a potential application in experimentation, we are considering the use of quadcopters. Each quadcopter would function as a boid, interconnected through wireless communication employing a Wi-Fi network, facilitating information exchange through sockets. The positional data for each boid would be acquired either through a Motion Capture System (Mocap, such as OptiTrack) or alternative methods like mounting cameras on each quadcopter, implementing infrared sensors, or utilizing radio frequency triangulation. To attain synchronization within a hyperchaotic MACM system, we propose the inclusion of an additional rule, assigned a lower priority compared to existing rules. This supplementary rule endows each boid with a distinct speed component, individually generated by a hyperchaotic trajectory generator algorithm as reported in (Cetina-Denis *et al.* 2022). This approach aims to provide each boid with a unique characteristic, similar to the individuality observed in a flock of birds, where differences in size, weight or, agility contribute to distinctive behaviors emerging from group interactions.

Acknowledgments

This work was supported by the CONAHCYT Research Project "Synchronization of complex systems and its applications" under grant number A1-S-31628. **In memory of Cornelio Posadas.**

Availability of data and material

Not applicable.

Conflicts of interest

The authors declare that there is no conflict of interest regarding the publication of this paper.

Ethical standard

The authors have no relevant financial or non-financial interests to disclose.

LITERATURE CITED

Cetina-Denis, J. J., R. M. Lopéz-Gutiérrez, C. Cruz-Hernández, and A. Arellano-Delgado, 2022 Design of a chaotic trajectory generator algorithm for mobile robots. Appl. Sci. **12**: 2857.

Duman, E., M. Uysal, and A. F. Alkaya, 2012 Migrating birds optimization: a new metaheuristic approach and its performance on quadratic assignment problem. Information Sciences **217**: 65–77.

Itoh, M. and L. O. Chua, 2007 Boids control of chaos. International Journal of Bifurcation and chaos **17**: 427–444.

Kapitaniak, T., Y. Maistrenko, and S. Popovych, 2000 Chaos-hyperchaos transition. Physical Review E **62**: 1972.

Karaboga, D. *et al.*, 2005 An idea based on honey bee swarm for numerical optimization. Technical report, Technical report-tr06, Erciyes university, engineering faculty, computer.

Méndez-Ramírez, R., A. Arellano-Delgado, C. Cruz-Hernández, R. Martínez-Clark, *et al.*, 2017 A new simple chaotic Lorenz-type system and its digital realization using a tft touch-screen display embedded system. Complexity **2017**.

Méndez-Ramírez, R. D., A. Arellano-Delgado, M. A. Murillo-Escobar, and C. Cruz-Hernández, 2021 A new 4d hyperchaotic system and its analog and digital implementation. Electronics **10**: 1793.

Pourpanah, F., R. Wang, C. P. Lim, X.-Z. Wang, and D. Yazdani, 2023 A review of artificial fish swarm algorithms: Recent advances and applications. Artificial Intelligence Review **56**: 1867–1903.

Rajagopal, K., S. Vaidyanathan, A. Karthikeyan, and A. Srinivasan, 2018 Complex novel 4d memristor hyperchaotic system and its synchronization using adaptive sliding mode control. Alexandria Engineering Journal **57**: 683–694.

Reynolds, C. W., 1987 Flocks, herds and schools: A distributed behavioral model. In *Proceedings of the 14th annual conference on Computer graphics and interactive techniques*, pp. 25–34.

How to cite this article: Ana, C. M. G., Liliana, C.A., Martha, L. G. R., and Cesar, C. H. Flocking Behavior of Boids Driven by Hyperchaotic MACM System. *Chaos Theory and Applications*, 6(2), 152-158, 2024.